School of Applied Chemistry

DISTRIBUTION AND AGGLOMERATION OF GOLD IN ARSENOPYRITE AND PYRITE

Mark Graham Aylmore
BSc University of Western Australia
BSc (Hons) Murdoch University

This thesis is presented as part of the
requirements for the award of the
Degree of Doctor of Philosophy
of
Curtin University of Technology

1995

Abstract

The form and location of gold in the structure of arsenopyrite and pyrite minerals, and the mechanisms for the mobility agglomeration of gold in arsenopyrite during thermal treatment, have been studied using a combination of Rietveld X-ray diffraction refinement, Convergent Beam Electron Diffraction (CBED) and Atomic Location by Channelling Enhanced Microanalysis. The basic structure of all the arsenopyrite compositions studied, has been shown to be monoclinic $P2_1/c$, regardless of the variation in stoichiometry. An increase in the arsenic to sulfur ratio in the natural arsenopyrites was found to be associated with an increase in unit cell dimensions accompanied by expansions within the iron-centred octahedra along the [101] direction of the monoclinic cell and concommitant contractions of the octahedra in the (101) plane. There was no obvious relationship between variation in stoichiometry and structure of arsenopyrite which could provide information as to possible substitution of gold in its structure. However, atomic displacements caused by twinning or disorder, may help to incorporate gold.

The synthesis of auriferous arsenopyrites showed that gold has to be in an ionic form to be taken up in the structure. The form of the gold species affects the distribution of gold in the structure, being chemically zoned when derived from a dichloro complex and more evenly distributed when derived from a hydrosulfido complex. It is suggested that rapid crystallisation, with resultant displacement faults along the b-axis, may contribute to higher concentrations of gold in the natural arsenopyrite structure. Electron probe microanalysis showed a possible slight iron-deficiency in some of the auriferous arsenopyrite grains analysed. However, the errors in the analyses were too high to provide conclusive evidence of gold substitution on the iron sites, as has been proposed in the literature.

Analyses of natural and synthetic pyrites showed no deviations in structural parameters which could indicate possible substitution of gold or other impurities within the structure.

Electron channelling experiments showed that gold was located on the sulfur sites in pyrite. In arsenopyrite, there was some evidence for gold located on the iron sites, however, most gold was interstitial, probably situated between the octahedra. This location is probably facilitated by the presence of displacement faults as observed by CBED in the synthetic auriferous arsenopyrite.

Breakdown of arsenopyrite under thermal treatment was topotactic along its b-axis, which converts to the a-axis in the pyrrhotite structure, following a reconstruction mechanism based on the preferential removal of arsenic over sulfur. Gold was visually recorded exsolving from the arsenopyrite structure and agglomerating as liquid metal globules as the arsenopyrite was chemically altered during thermal treatment under the Transmission Electron Microscopy electron beam. Gold became mobile on the decomposition of arsenopyrite, but this was not observed until a temperature of approximately 470°C was reached. Above this temperature both solid solution and particulate gold became mobile. The interaction of arsenic vapour and gold reduced the melting point of gold.

The observations on the effects of arsenic residence time, and the relative mobility of solid solution and particulate gold during the thermal decomposition of auriferous arsenopyrite and pyrite, have significant implications for improved industrial extraction of gold from these minerals.

TABLE OF CONTENTS

LIST OF FIGURES[1]

---

[1] f stands for following page

LIST OF TABLES

Chapter 1

1.0 INTRODUCTION

With the depletion of auriferous oxide ore in mining areas, the processing of deeper auriferous sulfide ores has become increasingly important. In many sulfide-bearing refractory gold ores, submicroscopic gold ("invisible gold") may account for the majority of the gold present and this is most often located in the minerals arsenopyrite (FeAsS) and pyrite (FeS$_2$). The successful processing of these ores is difficult and will undoubtedly be enhanced by a better understanding of the mineralogy of the "invisible gold" and its distribution within and among coexisting common sulfide minerals (Cook and Chryssoulis, 1990).

The gold may be in the form of metallic gold or, as recent studies have demonstrated, also in solid solution in sulfide minerals. The main difficulty in the determination of solid solution gold has been the limits of detection by available procedures. Only recently have analytical techniques been pioneered that allow the accurate and precise quantitative determination of gold abundant at less than 1ppb in solid solution within the sulfide matrix. Little is known about the location and chemical state of gold in the sulfide structures. Part of this problem, as shown by a number of authors (Buerger, 1936; Morimoto and Clark, 1961; Fuess *et al.*, 1987), is that the arsenopyrite structure is complex and difficult to determine. This is largely due to the presence of multiple twinning and the fact that arsenopyrites can have a large variation in chemical composition even within a single grain.

Wu *et al.* (1990) have suggested that gold is only taken up in solid solution in arsenopyrite which is rapidly crystallised. A rapidly crystallised arsenopyrite will possibly be less ordered than a well crystallised sample. A comparison of the structure of an auriferous arsenopyrite sample with the structure of a 'gold free' arsenopyrite may thus provide some detail as to the environment in which Au is taken up in arsenopyrite and lead to better methods of processing.

The metallurgical problems associated with the treatment of refractory gold arsenopyrite ores, are directly related to the mode of occurrence of the gold in the ores and to the minerals they contain. Direct cyanidation of arsenopyrite may give low gold recoveries even after fine grinding and the common practice has been to roast arsenopyrite to form a porous iron oxide product which is inert to cyanide and gives high gold recoveries. Other oxidation processes have also been tried including bacterial oxidation (Swash, 1988). A factor which has become of increasing concern is the environmentally active products resulting from the roasting process, in particular the SO_2 and As_2O_3 emissions. In addition, disposal of the recovered arsenic may present problems. In recent years, new methods have been sought in order to make extraction cheaper. Techniques need to be developed where gold can be mobilised to sites where it can be easily separated with little poisonous by-products to be managed. The first step in the development of such techniques is a detailed understanding of the mineralogy of arsenopyrite and pyrite containing gold.

Heat treatment of arsenopyrite containing submicroscopic gold has been shown to cause the gold to aggregate and become microscopically observable (Swash and Ellis, 1986; Graham et al., 1988). The mechanism for this process is as yet not well understood and its elucidation is of substantial scientific interest and economic importance. It has been suggested (Swash and Ellis, 1986) that roasting via the formation of pyrrhotite is a prerequisite for the successful extraction of gold from arsenopyrite and pyrite. The pyrrhotite formed is however a cyanicide so normally a complete roast to iron oxide is carried out.

The alteration that occurs during the roasting process appears to be dominated to a large extent by the local environment in proximity to the ore grain, where reducing conditions may exist, even when the bulk atmosphere is an oxidising one. It is at this level that the rate-controlling processes occur and that detailed understanding is essential. An understanding of the crystal structure of arsenopyrite and the form of the gold in the arsenopyrite is also essential to an understanding of the mechanism of movement of gold through the arsenopyrite structure when heated. In

addition, the environment in which the gold is made mobile will depend on the behaviour of different host arsenopyrites under thermal conditions.

The present studies were aimed at a more detailed resolution of the structures of arsenopyrite and pyrite, the form and location of gold in these minerals and the mechanisms of gold mobilisation and agglomeration during thermal treatment. An innovative combination of analytical and experimental techniques were used. These techniques included the application of the Rietveld Refinement Method (Rietveld, 1969) to powder X-ray diffraction data, convergent beam electron diffraction (CBED) and atomic location by channelling enhanced microanalysis (ALCHEMI) to transmission electron microscopy.

A review of the relevant literature on the composition and structure of arsenopyrites, the nature of the bonding and form of gold in arsenopyrite together with studies on the conditions of formation of auriferous arsenopyrite and its thermal behaviour is presented in Chapter 2 to define the specific deficiencies in knowledge.

In the first experimental section (Chapter 3) the compositions and crystal structures of a number of natural arsenopyrites have been examined. The aim of these studies was to determine the variations in the stoichiometry of the arsenopyrite structure and its implications for the location of gold in solid solution. It was essential to establish the most appropriate orientations for subsequent channelling experiments used in locating gold in the arsenopyrite structure.

Because of the uncertainty in the abundance of solid solution gold in the natural arsenopyrites available, a number of experiments were carried out (Chapter 4) to produce synthetic arsenopyrites containing gold in solid solution from appropriate arsenic, sulphur and iron constituents. These experiments were also aimed at providing information on the mechanism by which gold is taken up into the arsenopyrite structure.

Pyrite simultaneously formed during some of these experiments was also found to contain solid solution gold and was examined (Chapter 5) to provide detailed information on the nature of the solid solution process.

In Chapter 6 both the natural and synthetic arsenopyrite and pyrite compounds were examined in detail using ALCHEMI to determine the specific location of the gold in the structures.

Having established the form and distribution of the gold in the arsenopyrites, the thermal behaviour of the arsenopyrites and its relationship to the mobility and agglomeration of both solid solution and metallic gold were examined under different environmental conditions (Chapter 7).

The final Chapter 8 summarises the results of the thesis and the general conclusions. Suggestions for further studies and relevance to industry are also provided.

Chapter 2

2.0 LITERATURE REVIEW

In the following review of literature, the stoichiometry, possible structure and bonding mechanisms occurring in arsenopyrites and to a lesser extent in pyrites are first discussed. Information on the conditions under which gold is taken up in arsenopyrite and pyrite is then reviewed. This is followed by an outline of knowledge on the form and location of gold in arsenopyrite and pyrite. Finally the thermal behaviour of these sulfides and the mobility of gold through thermally altered sulfides are reviewed.

2.1 Habit and Morphology of Arsenopyrite

Arsenopyrites have a silver-white colour with a metallic lustre (H 5.5-6,G 6.07). Crystals of arsenopyrite are commonly prismatic, elongated on the c and less commonly on the b axes (based on marcasite pseudo-cell Figure 2.1). However the habit of arsenopyrite varies considerably in different geological environments (Lacroix, 1913). Wu *et al.* (1990) suggested from their work on arsenopyrite from the Le Chatelet gold mine in Creuse, France, that needle-like habit, small crystal size (1-350μm) and complex twinning were frequently associated with gold-substituted arsenopyrite. In contrast, the morphology of gold-poor arsenopyrites from gold deposits from the French Central Massif was generally characterised by a pyramidal habit. Cook and Chryssoulis (1990) in their detailed analyses of a number of gold ore bodies, found high contents of 'invisible' gold associated with small arsenopyrite grains where more than one generation of arsenopyrite was present.

2.2 Composition and Structure of Arsenopyrite

The ideal formula of arsenopyrite is FeAsS. However, significant variation in structure, composition and the bonding and oxidation states of the various atoms in each site, have been observed.

2.2.1 Stoichiometry

Arsenopyrite exhibits considerable nonstoichiometry, the ratio As:S ranging from 1.22 to 0.82 (Kostov, 1981). Determinations of the crystal structure of FeAsS (Buerger, 1936; 1937; Fuess *et al.*, 1987) have indicated the existence of mixed populations on As and S sites. Morimoto and Clark (1961) found that the monoclinic cell constants for six analysed arsenopyrites were related linearly to their arsenic content and inversely to their sulfur contents, indicating the mutual solid solution of these elements in arsenopyrite. The unit cell volume became larger with increasing arsenic content. They noted that changes in the position of the X-ray (131) peak of arsenopyrite was a sensitive indicator to the differences in arsenopyrite compositions. Morimoto and Clark (1961) first derived a linear equation relating d_{131} and arsenopyrite composition which apparently has been misprinted in their paper. Kretschmar and Scott (1976) have refined it using natural arsenopyrites with less than 1 wt% Co, Ni and Sb and a few synthetic samples. Their equation is :

$$As \text{ (at\%)} = 866.67d_{131} - 1381.12$$

with an estimated one standard deviation of ±0.45 % in As

Kretschmar and Scott (1976) and subsequent workers have used the variation of the As:S ratio in arsenopyrite as a geothermometer. That is, the stoichiometry of arsenopyrite is temperature controlled.

Cathelineau *et al.* (1988), Johan *et al.* (1989) and Marcoux *et al.* (1989) carried out systematic electron microprobe analyses on arsenopyrites from samples taken from gold mines or other deposits in Western Europe. Their results showed that crystals of arsenopyrite can exhibit extreme chemical variations, especially in As, Sb and S contents. Backscattered scanning electron microscopy indicated strong chemical zonation with increasing average atomic number from the centre to the periphery of the crystals, controlled by the chemical changes occurring from one growth zone to another. Such increase is due to a progressive enrichment in As,

correlated with a decrease in the S content. As and S were strongly anticorrelated following roughly the classical substitution :

Fe As$_{1-x}$S$_{1+x}$
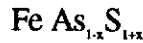
These workers found that the arsenic content in a single crystal varied from 0.27 to 0.33 atomic fraction, whilst trace element contents (e.g. Au,(Co,Ni)) varied largely among the different growth zones.

In some cases, microprobe analyses of natural and synthetic arsenopyrites have revealed a fairly systematic deficiency in Fe (up to 1 at %), but these results have not always been taken into consideration in the past (Kretschmar and Scott, 1976). Buerger (1936) first suggested that Fe sites can be partly occupied by As. Morimoto and Clark (1961) compared the chemical compositions of 16 published arsenopyrite data and found the variation in iron content to be about ±0.6 at% of the mean value. They found the errors consistent with a built-in bias derived from some of the analytical techniques and concluded that arsenopyrite does not vary measurably from a 1:2 cation:anion ratio. Several authors (Marcoux *et al.*, 1989; Johan *et al.*, 1989; Wu *et al.*, 1990) have subsequently postulated a deficiency of iron (e.g. 31.46-33.11 at%) in the arsenopyrite structure particularly associated with auriferous arsenopyrites (see Section 2.5.6). Thus, the question remains as to whether arsenopyrites can be iron deficient.

2.2.2 Space group and Symmetry

The crystal structure of arsenopyrite is closely related to the orthorhombic marcasite (FeS$_2$) structure. Figure 2.1 represents the unit cell of marcasite P2$_1$/m 2$_1$/n 2$_1$/n lattice constants A, B, and C projected down the c-axis together with different settings of the arsenopyrite cell presented by Morimoto and Clark (1961), Buerger (1936) and Fuess *et al.* (1987). The non-standard setting of the space group Pnnm is used for marcasite in order to compare it with that reported for the arsenopyrite structure.
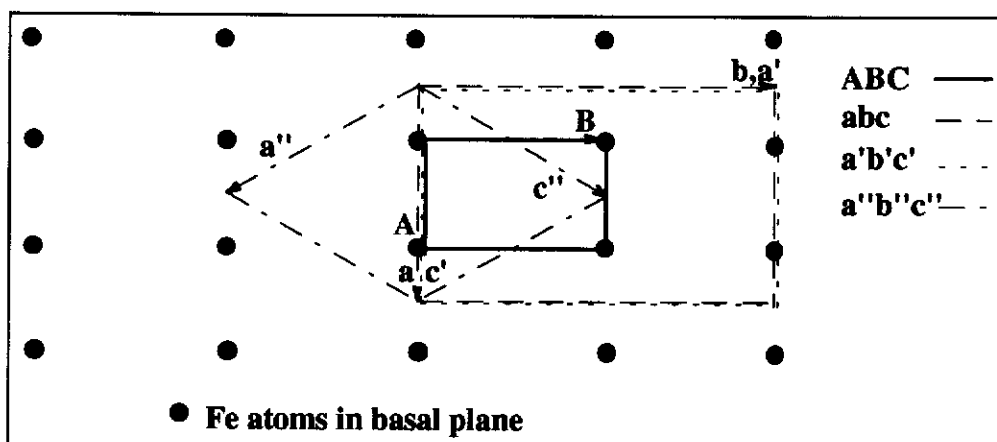
A.B.C marcasite-cell (FeS$_2$) Pmnn

$\underline{A}$, $\underline{B}$, $\underline{C}$

a, b, c arsenopyrite-cell (Fe,Co)(As,S)$_2$ C112$_1$/d

    monoclinic, pseudo-orthorhombic (Fuess *et al.*, 1987)

    $\underline{a}$ = 2$\underline{A}$, $\underline{b}$= 2$\underline{B}$, $\underline{c}$ = $\underline{C}$ γ=90°

a',b',c' arsenopyrite-cell (Fe,Co)(As,S)$_2$ B12$_1$/d

    monoclinic, pseudo-orthorhombic (Buerger, 1936)

    $\underline{a}$' = 2$\underline{B}$, $\underline{b}$' = $\underline{C}$', $\underline{c}$' = 2$\underline{A}$ β = 90°

a", b", c" arsenopyrite-cell, primitive setting P2$_1$/c

    monoclinic (Morimoto and Clark, 1961)

    $\underline{a}$" = $\underline{A}$ - $\underline{B}$, $\underline{b}$" = -$\underline{C}$, $\underline{c}$" = $\underline{A}$+$\underline{B}$ β = 110°

Figure 2.1 Projections of the arsenopyrite structure chosen by various authors (after Fuess *et al.*, 1987).

The arsenopyrite cell was first determined by de Jong (1926) using the powder and rotation methods on arsenopyrite from Sulitjelma, Norway, which contained 7 wt % cobalt. The orthorhombic cell constants were a=6.45, b=9.54, c=5.72Å and Z=8. The space group from the indices of 17 powder reflections was Pmmm or Pmmn.

Buerger (1936) determined the crystal structure of arsenopyrite using the Weissenberg method and derived a model by analogy to related compounds. The apparent symmetry of that crystal was orthorhombic with cell dimensions a=6.43, b=9.57 and c=5.72Å, but the structure could not be solved in one of the possible orthorhombic space groups Cmmm, Cmm2 or C222. Buerger (1936) concluded that the true symmetry of arsenopyrite must be monoclinic or even triclinic and derived a model by trial and error based on the marcasite and gudmundite (FeSbS) structures and on symmetry considerations. Buerger's work was hampered by crystal twinning.

The crystals of arsenopyrite are monoclinic holohedral but tend to grow together in twins. The twinned composition has orthorhombic pseudo-symmetry and therefore gives orthorhombic diffraction effects which give rise to misleading symmetry data. Buerger defined a monoclinic cell with $\beta=90°$ and the orthorhombic axes rotated according to the transformation 001/100/010, with space $B2_1/d$ and $B\overline{1}$, in order to compare the structure with manganite and rutile respectively.

Huggins (1937) criticised the structures of marcasite and arsenopyrite as determined by Buerger (1931,1936), on the grounds that the structures led to interatomic distances not in agreement with those calculated from electron-pair bond radius sums. Buerger (1937) refined the structure of marcasite and confirmed its abnormal interatomic distances. From this, he concluded that the interatomic distances in the arsenopyrite group are different from those in the pyrite group minerals. Buerger attributed the deviations from monoclinic symmetry in 'common' arsenopyrite to variations from the ideal chemical formula (FeAsS).

Morimoto and Clark (1961) refined the structure of arsenopyrite from Freiberg (Germany) based on 172 h0l reflections in space group $P\overline{1}$. The agreement, however was poor (R = 0.29). Using the Buerger precession method they observed that the intensities of the h0l reflection with l odd, decreased with increasing arsenic content in the arsenopyrite analysed. From additional powder data, these authors proposed that an excess of sulfur in arsenopyrite tends to lower the symmetry to triclinic, whereas a high amount of arsenic favours monoclinic symmetry. A primitive monoclinic cell, derived from Buerger's (1936) double monoclinic, but metrically orthorhombic cell by transformation ½0½/0 10/½0½, was used to give a space group of $P2_1/c$ with cell dimensions a=c=5.76, b=5.66Å and $\beta=111°47'$. They concluded that most natural arsenopyrites are sulfur-rich.

Fuess et al. (1987) studied arsenopyrite crystals from Hakansboda (Sweden) by single crystal diffraction and analytical transmission electron microscopy. Their material contained an excess of sulfur and some cobalt. They chose the space group $C112_1/d$, a non-standard space group, to emphasise structural relationships containing

the reflections h=2n, k=2n coinciding with the marcasite lattice, while those with h=2n+1, k=2n+1 were considered as due to the doubling of the cell volume. Reflections they obtained with h+k=4n+2, forbidden by the d glide were observed on precession photographs for h=2n+1. These symmetry elements were lost due to symmetry reduction. The "forbidden" hk0 reflections were interpreted as the result of twinning in arsenopyrite.

The ideal structure of arsenopyrite is depicted in Figure 2.2. In this, each iron atom has six neighbours at the corners of a distorted octahedron. One face of the octahedron is a triangle of three arsenic atoms, while the opposite face is a triangle of three sulfur atoms. The sulfur atom is surrounded by three iron atoms and one arsenic atom at the corners of a distorted tetrahedron. In a corresponding manner, the arsenic atom is surrounded by three iron atoms and one sulfur atom at the corners of a distorted tetrahedron (Buerger, 1936).

The early structure determinations described were frequently confounded by problems associated with varying As and S compositions, and twinning present in the arsenopyrite grains studied.

2.2.3 Substitution of Impurities

Some arsenopyrites have been reported to contain Ni, Co, Sb, Mn, Se or Bi within their structures (Klemm, 1965; Morimoto and Clark, 1961). Most detailed structural studies have been carried out on arsenopyrites containing impurities and consequently the structure can be influenced by their presence. Morimoto and Clark (1961) considered that the monoclinic structure for arsenopyrite could be attained if minor amounts of elements such as cobalt or antimony were incorporated. The Ni, Co, and Mn replace some Fe, Bi and Sb replace some As, and Se replaces S on their respective sites. Figure 2.3 shows the relationship between arsenopyrite and various other minerals. As a result of changes in structure there is no complete solid solution series between any of these minerals.
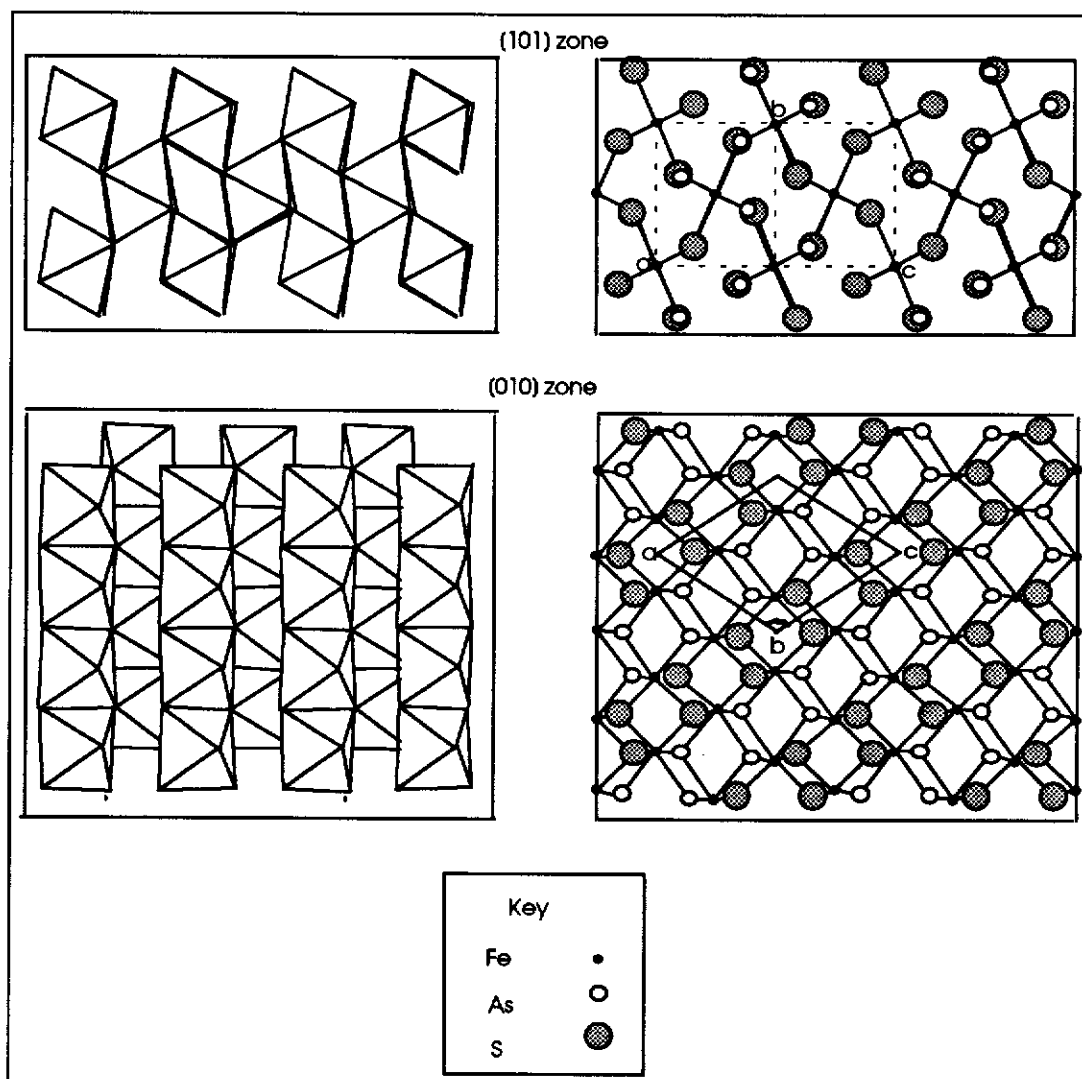
Figure 2.2 The octahedra and stick and ball model of [101] and [010] zones of the ideal arsenopyrite structure. The unit cell based on P2$_1$/c space group is also shown.
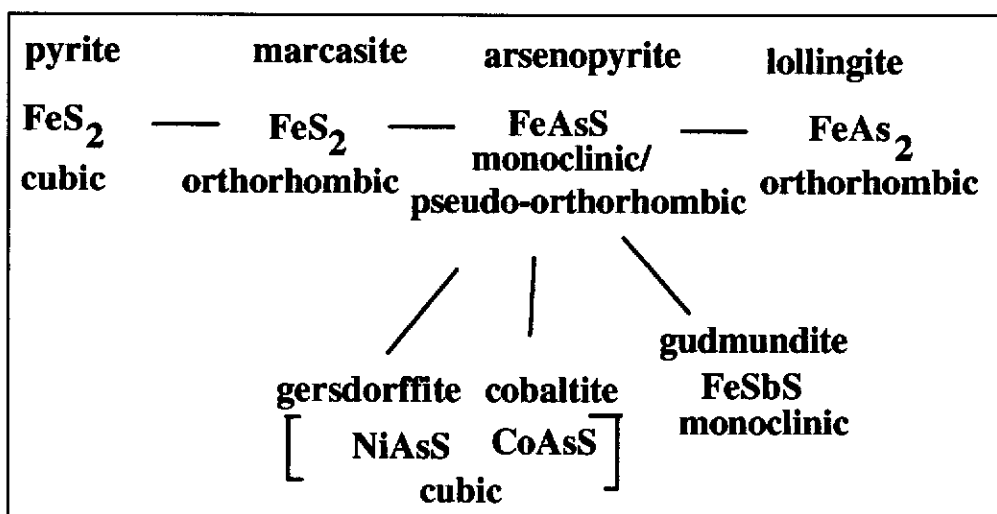
Figure 2.3 The relationship of arsenopyrite to various sulfides.

The influence of the cations on arsenopyrite structure was examined by Klemm (1965) using various natural samples and synthetic specimens. This author elucidated the system FeAsS-CoAsS-NiAsS by microprobe analyses and X-ray powder patterns. He observed that the amount of impurities in the arsenopyrite increased with increasing temperature of formation and that arsenopyrite can accommodate up to 14 mol% of nickel or up to 25 mol % of cobalt or a combination. However, the monoclinic arsenopyrite structure becomes unstable for large metal atoms due to the close iron to iron approach near their shared octahedral coordination edge. The cubic structure of cobaltite or gersdorffite then becomes the favoured structure (Buerger, 1936).

Fuess et al. (1987) observed exsolutions of Co-rich and Co-poor lamellae of arsenopyrite in their TEM studies. The microstructure in the $(Fe, Co)(As,S)_2$ system is similar to that in the marcasite-pyrite system. These two polytypes of FeS_2 may occur with {110} of marcasite parallel to {001} of pyrite (Fleet, 1970). TEM observations by Fuess et al. (1987) confirm that the (001) plane of arsenopyrite is intergrown with parallel (001) planes of cobaltite. The values $d(002) = 2.712\text{Å}$ in arsenopyrite and $d(002) = 2.791\text{Å}$ in cobaltite are similar as well. This model is based on the similarity of the cobaltite structure projected on (001) and the [001] projection of the arsenopyrite structure. A similar transformation may occur for gersdorffite.

^{121}Sb Mössbauer studies on arsenopyrite containing 1wt% of antimony and gudmundite (FeSbS), which has the arsenopyrite type structure, showed similar measurements which strongly suggests that antimony in arsenopyrite replaces arsenic (Friedl *et al.*, 1992). Thus it appears there may be a total solid solution series between arsenopyrite and gudmunite.

Gold substitution in arsenopyrite is discussed in a later section (2.6.4).

2.2.4 Twinning

One of the difficulties encountered in structural analyses has been the ubiquitous twinning and/or antiphase domains. Morimoto and Clark (1961) found splitting of some reflections on the single-crystal photographs in many arsenopyrites studied. In order to explain the splitting, at least two types of twinning were inferred. The first one in reference to the chosen primitive monoclinic space group P2$_1$/c has twin plane (10$\bar{1}$) or (101) or has twin axis [10$\bar{1}$] or [101] respectively (designated type I). This type of twinning was described in detail by Buerger (1936). The second type of twinning (type II) requires the assumption that arsenopyrite is triclinic. Morimoto and Clark postulated that it has a twin axis [010], which is equivalent to a twin plane (010). Evidence for this twinning was observed in the intensities of some (hk0) reflections being different from those corresponding to (h$\bar{k}$0) reflections. The twinning could be associated with change in chemical composition.

High resolution transmission electron microscope images obtained by Cabri *et al.* (1989) also showed domain structures corresponding to (101) twin domains. The *a* and *c* cell dimensions are sufficiently different to cause a slight misfit between adjacent (101) twin domains.

TEM studies carried out by Fuess *et al.* (1987) have revealed the presence of antiphase domains and microtwins. The microtwins seen were similar to type I twins. Fuess *et al.* (1987) also observed an antiphase domain corresponding to the vectors ½[100] (=a marcasite) and ½[010] (=b marcasite). These submicroscopic defects were interpreted on the basis of group-subgroup relationships devised by Van

Tendeloo and Amelinckx (1974) to relate the marcasite to the arsenopyrite structure.

The symmetry reduction from marcasite type Pmnn to arsenopyrite $C112_i/d$ is demonstrated in Figure 2.4 (Fuess *et al.*, 1987 fig. 7). The loss of symmetry is compensated by characteristic crystal defects. The reduction t2 leading from Pmnn to $P112_i/n$ causes two kinds of twin domains with twofold twin axes parallel to A and B. $P112_i/n$ is a maximal subgroup of Pmnn. The reduction k2 is responsible for the formation of antiphase domains with displacement vectors A or B (lattice vectors of marcasite), which compensate for the loss of translational symmetry. $C112_i/d$ is a maximal subgroup of $P112_i/n$. The sample used by Fuess *et al.* (1987) did not however, correspond to the ideal formula of arsenopyrite, containing high S, and Co substituted for Fe.
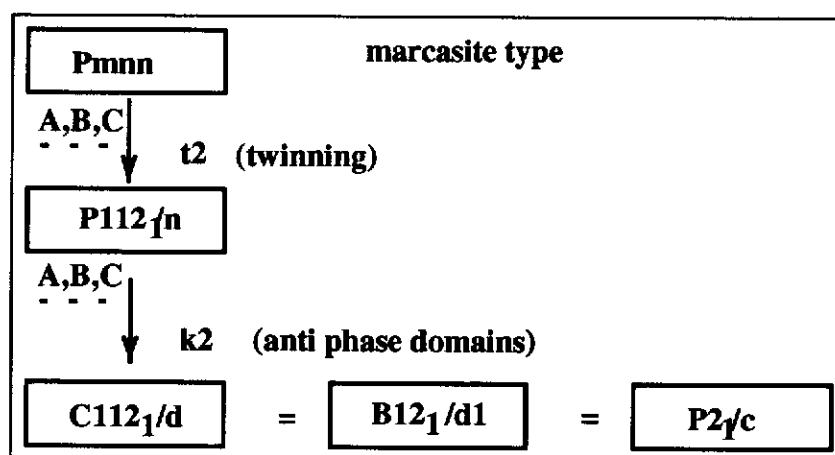
Figure 2.4 Group-subgroup relationships between the space-group of marcasite and the space-groups of arsenopyrite. t2 means "translationengleiche" symmetry reduction and k2 stands for "klassengleiche" symmetry reduction (after Fuess *et al.*, 1987).

2.2.5 Strain

Little attention has been given to strain in arsenopyrite and this may be an important feature in some interpretations of the structure of arsenopyrite. Studies by Campa-Vineta (1980) on polished sections of previously stressed arsenopyrite samples indicated high temperature deformation by twinning on [100], [101] and [201] (presumably $P2_i/c$) and low temperature deformation by elastic compliance or

fracture. In some cases, he reported that arsenopyrite may deform by exfoliation along the (110) plane.

2.3 Composition and Structure of Pyrite

Pyrite has the general formula of FeS_2. However, natural pyrites are nonstoichiometric containing FeS_n with n ranging from 1.93 to 2.01 (Finklea et al., 1976). In addition, pyrite can contain As, Ni and Co in its structure (Klemm, 1965). Based on synthesis experiments, the maximum amount of arsenic that can be incorporated in pyrite is about 0.1 wt% (Clark, 1960). However, Fleet et al. (1989) have reported up to 8 wt% arsenic in natural pyrites.

Pyrite was one of the earliest crystal structures to be solved by X-ray diffraction (Bragg, 1913; Parker and Whitehouse, 1932) and is cubic with the octahedrally coordinated metal atoms at the corners and face centres of the cube unit cell. Pyrite can be considered as a modified sodium chloride structure in which the iron is situated on the sodium site and two sulfurs are situated on the chlorine site. The systematic absences from X-ray studies of isotropic pyrite agree with the cubic space group Pa3. Brostigen and Kjekshus (1969) refined pyrite in the space group Pa3 to an R factor of 0.075, while Finklea et al. (1976) refined it to an R factor of 0.036.

Klemm (1962) observed weakly anisotropic zoned pyrite as well as clearly zoned isotropic pyrite. The crystal structure of a weakly anisotropic pyrite was defined by Bayliss (1977) to be pseudo-cubic. Based on similar degeneracy observed in the pyrite-type structure of arsenian ullmannite, he postulated that pure pyrite (FeS_2) has a triclinic crystal structure. Several of the minerals with pyrite type crystal structures, notably cobaltite (Giese and Kerr, 1965), gersdorffite (Bayliss and Stephenson, 1968), willyamite (Cabri et al., 1970) and arsenian ullmanite (Bayliss, 1977; 1989), have been recognised as pseudo-cubic. Schneiderhöhn (1930) has observed that arsenian pyrite is often weakly anisotropic, although Klemm's (1962) findings suggest that no general relationship exists between anisotropy and chemical

variations. Pyrite subjected to severe deformation and also when formed at high temperatures, is isotropic, whereas weakly anisotropic pyrite forms at low temperatures (Smith, 1942).

2.4 Bonding in Pyrite and Arsenopyrite

In pyrite and arsenopyrite, as with other sulfide minerals, the bonding is essentially covalent. The outer electron configuration of sulfur ($3s^2$ $3p^4$) leads to the possibility of more diffuse delocalised bonding systems than in oxides or silicates. The metal-metal interactions observed in many sulfides also influence the metal-sulfur bond distances and hence the radius. Because of the structural complexity and the variety of chemical bonds in sulfides, variations in crystal chemistry, stereochemistry and the presence of delocalised bonding, it is not possible to approach substitution in sulfides in the same way as for silicate minerals by comparing ionic radii (Vaughan and Craig, 1978). The conflicting views on structure make it difficult to determine what the oxidation states of the various elements within arsenopyrite are and how impurities such as gold are bonded in the sulfide structure.

2.4.1 Relationship of Pyrite-Marcasite-Arsenopyrite-Löllingite

The stability of pyrite and arsenopyrite structures can be explained by relating it to the pyrite (FeS_2) -marcasite (FeS_2) -arsenopyrite (FeAsS) -löllingite ($FeAs_2$) transition.

The difference between pyrite and the other three minerals can be seen in Figure 2.5. This shows the relationship of the metal coordination octahedra in each of the structures. In the pyrite structure, the octahedra only share corners. In the structures of marcasite, arsenopyrite and löllingite, the octahedra share edges lying in the 001 plane of the marcasite orthorhombic cell. As a consequence, the intermetallic distances across the shared edges are reduced and this provides a greater possibility for direct metal-metal interaction along the c-axis. In arsenopyrite, the metal atoms are displaced along the c-axis in such a way that short metal-metal distances ($\sim 2.89 \text{Å}$)

filled bonding orbitals with the following closed-shell configurations: $[S_2]^{2-}$ in pyrite, $[AsS]^{3-}$ in arsenopyrite and $[As_2]^{4-}$ in löllingite. In recent years with the availability of new spectroscopic data and quantum mechanical calculations the electronic structures of these anions (e.g. Tossell, 1980) have become available.

In these structures, each nonmetal atom is bonded to one other anion (its pair) and to three metal atoms. The formal negative charges on $[S_2]^{2-}$, $[AsS]^{3-}$, and $[As_2]^{4-}$ dianions require formal positive charges on the metal atoms of equal valency. In the case of pyrite (or its dimorph, marcasite), Fe is present as Fe^{2+}, and in arsenopyrite, as Fe^{3+} ions (Wood and Stren, 1979). However arsenopyrite is a semiconductor with a very low magnetic moment, implying that adjacent pairs of Fe^{3+} ions are bonded, resulting in the observed alternating long and short Fe-Fe bond distances.

For arsenopyrite, with alternating short and long Fe-Fe distances along the c-axis, the Fe-As-Fe angles subtending the short Fe-Fe distance are about $75°$ while the Fe-S-Fe angles subtending the long Fe-Fe distances are about $97°$, suggesting that the As end of the AsS groups is slightly more positive, while the S end is more negative. Analyses of safflorite ($CoAs_2$) which is isoelectronic with arsenopyrite, and has a similar structure with similar electrical and magnetic moments to that of arsenopyrite, (Kjekshus and Rakke, 1977) have shown that the effective bond types for safflorite are Co^{+3}-As and Co^{+2}-As, explaining why there are alternating large and small Co-As-Co angles. Similar bond types may occur in arsenopyrite.

2.5 Conditions in which Gold is taken up in Arsenopyrite and Pyrite

Factors which control the concentration of structurally bound gold in a sulfide mineral include the gold content of the ore-forming solution, the prevailing physicochemical parameters during ore genesis or metamorphism, the chemistry of the host, and the simultaneous formation of such gold minerals as native gold, electrum and gold tellurides. The presence of submicroscopic intracrystalline inclusions of gold in a sulfide depends on the suitability of the host substrate for gold nucleation, initial gold solubility and solubility variation with changing conditions.

Hydrothermal gold deposition in which arsenopyrite and pyrite occur may therefore take place over a wide range of temperature, pressure and fluid composition, comprising diverse environments extending from amphibolite facies metamorphism to lower temperature epithermal mineralisation and the formation of sea floor massive sulfides.

2.5.1 The Transport and Precipitation of Gold as Complexes

Gold may be taken up in, or associated with, arsenopyrite and pyrite by precipitation reactions involving the destabilisation of gold-bearing species in solution (Seward, 1992; Groves and Foster, 1992). It has been recently proposed by several authors that the adsorption of aqueous gold-bearing species on to earlier-formed sulfides occurs via conductivity, and then autocatalytic reduction of the aqueous species to metallic gold (Jean and Bancroft, 1985; Hyland and Bancroft, 1989; Starling et al., 1989).

Most workers have been concerned with the role of chloride and reduced sulfur (e.g. HS⁻) in hydrothermal gold chemistry because both chloride and hydrosulfide ions are known to form complexes with gold (I) and both are present in appreciable concentrations in hydrothermal ore fluids. For these reasons, almost all of the experimental work conducted at elevated temperatures and pressures has focused on gold solubility and complexing in chloride and reduced sulfur-containing solutions. The relevant literature for this study is reviewed below. A more detailed review on the gold complexes has been given by Seward (1982, 1992).

2.5.1.1 Halide Complexes

The solubility of gold in chloride solutions (HCl, NaCl, KCl) has been demonstrated over a wide range of temperatures and pressures (Anderson and Burnham, 1967; Glyuk and Khlebnikova, 1982; Henley, 1973; Rytuba and Dickson, 1977; Wood et al., 1987). Recently, Zotov et al. (1989) obtained thermodynamic data for the solubility of gold (as $AuCl_2^-$) from 350 to 500°C and 500 to 1500 bar. The

most important of these investigations has been recalculated in terms of the equilibrium reaction

$$Au_c + 2Cl^- + H^+ = AuCl_2^- + 1/2H_2(g) \quad\text{...(2.1)}$$
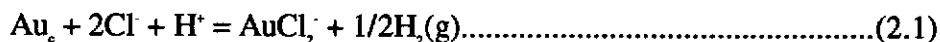
The solubility of gold increases with temperature (Henley, 1973). Gold deposition may occur as a response to a decrease in temperature, increase in pH, as well as a decrease in chloride activity caused by dilution (Seward, 1982).

2.5.1.2 Hydrosulfido and Sulfido Complexes

The existence of sulfide complexes of gold(I) were first demonstrated by Seward (1973) and he showed that three complexes, $AuHS^0$ (acid pH), $Au(HS)_2^-$ (near neutral to weakly alkaline pH), and $Au_2(HS)_2^{2-}$ (alkaline pH) were present in high-temperature, high-pressure aqueous sulfide solutions. Experiments by Belevantsev *et al.* (1981) confirmed the presence of the $Au(HS)_2^-$ complex in the neutral pH region and they have also suggested the presence of the protonated species $HAu(HS)_2^0$ in acid solutions. Shenberger (1985) and Shenberger and Barnes (1989) have measured the solubility of aqueous sulfide solutions from 150 to 350°C and at the equilibrium saturated vapour pressure of the system for the reaction

$$Au +H_2S(aq) + HS^- = Au(HS)_2^- + H_2(g) \quad\text{...(2.2)}$$
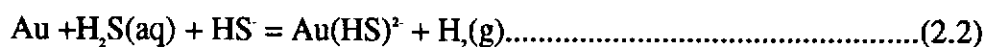
For the $AuHS^0$ complex, there are no experimentally based thermodynamic data pertaining to its stability at high temperatures, although Renders and Seward (1989a,b) have reported thermodynamic data at 25°C. For gold deposition a decrease in temperature would destabilise these complexes.

2.5.1.3 Thioarsenite and Thioantimonite Complexes

The role of thioarsenite and thioantimonite complexes in the complexing and transporting of gold is not well understood. Romberger (1986) described the possible mechanism of gold deposition using fO_2-pH, fO_2-fS_2 diagrams which give the stability

fields of minerals and other species in solution. Assuming a stoichiometry of $AuAsS_2^0$ Romberger proposed different hypothetical reactions which suggested that both oxidation and pH increase could result in gold deposition.

The solubility of arsenic in hydrothermal sulfide solutions is extremely high (Heinrich and Eadington, 1986). Ballantyne and Moore (1988) evaluated the published fluid analyses from geothermal systems for arsenic and found that the arsenic content in reservoir fluid varied inversely with P_{H_2S} and directly with temperature. As^{III} (not As^V) also forms bisulfide complexes in some sulfide bearing solutions (Mironova and Zotov, 1980; Robins, 1985; Heinrich and Eadington, 1986). The relative stabilities of the hydroxide and sulfide species have been predicted for 90 °C and 250°C and some arsenic sulfide complexes ($H_3As_3S_6$, $H_2As_3S_6^-$ and $HAs_3S_6^{2-}$) can be found at low temperatures (25-300°C) (Spycher and Reed, 1989). At higher temperatures, both As^{III} and As^V can occur as the complexes H_3AsO_3 (arsenious acid) and H_3AsO_4 (arsenic acid) and dissociation products (Nakagawa, 1971; Mironova et al., 1984; Heinrich and Eadington, 1986). Calculations by Heinrich and Eadington (1986) on the Fe-As-S-O-H system suggest that at neutral to acid pH, the aqueous species $H_3AsO_3^0$ can account for the transport of adequate concentrations of arsenic to explain the association of many hydrothermal arsenic minerals. Chloride complexes are unlikely, although As^{III} chloride may exist in extremely acid, highly saline conditions (Cobble, 1985)

A number of workers (Grigor'yeva and Sukneva, 1981; Nekrasov et al., 1982a; Nekrasov and Konyshok, 1982b) have measured the solubility of gold in aqueous sulfide solutions in the presence of stibnite and orpiment in the temperature range from 200 to 300°C in order to determine the effect of thioantimonite and thioarsenite species on gold solubility. However, uncertainties in the hydrogen fugacities prevailing in these experiments together with ambiguities in the stoichiometry of the thioantimonite and thioarsenite complexes, make their results inconclusive.

Thus it is not possible to say whether gold(I) thioarsenite complexes exist and whether they are of any importance in the formation of auriferous sulfides (Seward, 1992).

2.5.2 Temperature, Pressure and fO_2 of Arsenopyrite Formation

Based on fluid inclusion studies carried out on host quartz in two auriferous arsenopyrite ore bodies, Wu et al. (1990) found that the temperatures of formation of auriferous arsenopyrite at two deposits were different and concluded that temperature is not a major factor in incorporation of gold in arsenopyrite. They suggested that non-equilibrium rapid crystallisation may induce gold trapping under an extended range of $T-P-fO_2$ conditions.

Conditions of crystallisation of arsenopyrites have been estimated at Marche - Combrailles and Limousin deposits, France, by combined studies of mineral associations, alteration minerals in the host-rocks and fluid inclusion studies on the arsenopyrite-bearing quartz. Results indicated that most arsenopyrite crystallised at low fO_2, around that fixed by the pyrite-arsenopyrite-pyrrhotite triple point and by the Ni-NiO oxygen buffer; at low pH; and frequently at low temperatures (180-250°C) (Cathelineau et al., 1988: Boiron et al., 1989).

So far no experimental data on the hydrothermal solubility of arsenopyrite, or theoretical investigations of the solution transport of arsenic and its precipitation as arsenopyrite have been reported. In the absence of experimental data for the speciation of arsenic in high temperature aqueous solution equilibria, Heinrich and Eadington (1986) predicted it by extrapolation of the available low-temperature thermodynamic data to the high-temperatures. They also suggested that the solubility of arsenopyrite is more strongly dependent on oxygen fugacity than most other ore minerals.

2.5.3 Experimental Studies on Arsenopyrite Synthesis

The solid solution behaviour of arsenopyrite and its stability relative to other solid phases have been established experimentally (Clark, 1960; Barton, 1969;

Kretschmar and Scott, 1976; Scott, 1983) and are discussed in section 2.7. Attempts to recrystallise or grow crystals of arsenopyrite in high pressure vessels in gold tubes by several workers (Clark, 1960; Kretschmar and Scott, 1976; Scott, 1983; Wu and Delbove, 1989) have failed due to the reaction of arsenic with gold. Wu and Delbove (1989) tried to introduce gold into the arsenopyrite structure by the reaction of Fe, As and S mixtures. However, gold introduced as Au^o (metallic gold) or as Au^{3+} ($AuCl_3.2H_2O$) with the starting materials, was not incorporated into the arsenopyrite structure and appeared systematically as metallic gold in the products. None of these studies, however, has conclusively demonstrated that some gold was not taken up in solid solution. Auriferous arsenopyrite has been recently synthesised by the reaction of Fe_2O_3 with As and S in $NaCl-H_2O$, $HCl-H_2O$ solutions or in pure water at 500°C and 2kbars in gold capsules (Wu and Delbove, 1989). In this case gold present in the starting materials in the form of Au^o (metallic gold) or as Au^{3+} ($AuCl_3.2H_2O$) was regularly detected in zoned arsenopyrite formed in this way, with maximum contents of about 1.7 wt% gold in the enriched zones.

2.6 The Form and Location of Gold in Arsenopyrite and Pyrite

Gold ores that do not yield their gold content when treated by the standard gravity and cyanidation processes are classified as 'refractory'. Such ores are generally sulfidic, in particular, containing arsenopyrite and pyrite. The reason why refractory gold ores are not readily amenable to conventional cyanidation is usually because the gold is 'locked' inside the sulfide. To understand the response of ores to subsequent methods of treatment the form and location of gold within arsenopyrite and pyrite is of importance.

Gold occurs in association with most of the common rock-forming minerals and its manner of occurrence in the host mineral is very varied. Harris (1990) listed 26 accepted gold-containing minerals, three unpublished minerals, two doubtful and 13 unnamed compounds. Of these, the most important are native gold and its varieties as a result of metal substitution, in particular silver. There are also gold tellurides which

are abundant in several deposits and aurostibite which is rare but can cause problems in processing.

Several papers have reviewed recent advances in instrumental techniques and their application to understanding the nature and location of gold in minerals and in considering approaches which aim to quantify the distribution of gold among various mineralogical sites in ores and mill products. These topics have been reviewed by Henley (1992); Chryssoulis and Cabri (1990); Cook (1990); Harris (1990); Petruk (1989); Henley (1989); and Cabri (1988a, 1988b).

In recent years, increasing interest has focussed on what is known as "invisible gold", a term introduced by Bürg (1930). "Invisible gold" is that which cannot be observed by optical or electron microscopy, which may occur either in solid solution or as submicroscopic inclusions in sulfide minerals and which can not be recovered by cyanide solution (Chryssoulis *et al.*, 1987).

The incorporation of gold into sulfide minerals has long been inferred by several investigators (Boyle, 1979). However, Gasparrini (1983) and others noted that the analytical techniques used to detect gold are bulk in nature and fail to determine conclusively whether the gold is in solid solution or present as discrete inclusions of submicroscopic size. Boyle (1979) has extensively reviewed the evidence for both structurally bound and submicroscopic gold, and concluded that both types can exist. A more recent review has been given by Harris (1990).

2.6.1 Distribution of Gold in Arsenopyrite and Pyrite

Tables 2.1 and 2.2 show the amount of "invisible gold" in pyrite and arsenopyrite reported in the literature. The most extensive study has been carried out by Cook and Chryssoulis (1990) who observed that the amount of gold in sulfide minerals varies considerably from deposit to deposit. The "invisible gold" content is generally higher in arsenopyrite than pyrite. The maximum gold in arsenopyrite is 1.5 wt% for natural samples and 1.7 wt% in synthetic samples. In pyrite the maximum reported is 8100 ppm (Table 2.1).

Table 2.1 - Invisible Gold Content in Pyrite				
Sample, Location	Type	average (SD) (ppm)	Range (min-max)	Reference
Windy Craggy, British Columbia	coarse	0.15(0.10)	<0.25-0.6	Cook & Chryssoulis (1990)
Windy Craggy, British Columbia	fine	1.37(0.50)	<0.43-2.7	Cook & Chryssoulis (1990)
Lara, British Columbia	coarse	0.16(0.12)	<0.25-1.4	Cook & Chryssoulis (1990)
Golden Pond, Quebec				
Ore A	coarse	1.10(0.90)	<0.5-4.1	Cook & Chryssoulis (1990)
Ore B	coarse	0.23(0.24)	<0.25-1.4	Cook & Chryssoulis (1990)
HW, British Columbia	coarse	0.25(0.09)	<0.25-2.8	Cook & Chryssoulis (1990)
Estrades, Quebec	coarse	0.67(0.53)	<0.25-12.0	Cook & Chryssoulis (1990)
Trout Lake, Manitoba	coarse	0.72(0.38)	<0.25-6.8	Cook & Chryssoulis (1990);
Congress, British Columbia	coarse	1.2(0.61)	<0.25-21.0	Cook & Chryssoulis (1990)
Mobrun, Quebec	fine	1.41(0.23)	<0.25-5.6	Cook & Chryssoulis (1990)
Unspecified, Canada	fine	3.3(0.9)	0.8-9.4	Chryssoulis (1990)
Olympias, Greece	As poor	3.6(2.0)	1.0-12.0	Cook & Chryssoulis (1990)
Olympias, Greece	As rich	36(12)	4.1-110	Cook & Chryssoulis (1990)
Unspecified, Australia	As poor	9.0(?)	<5-74	Sie et al. (1989)
Elmtree, New Brunswick	As poor	24.1(5.3)	0.9-107.8	Cook & Chryssoulis (1990)
Unspecified	As rich	68.8(20)	?-320	Chryssoulis (1990)
Cortez, Nevada	coarse	700(?)	<600-1500	Wells &Mullens (1973)
Cortez, Nevada	Rims	1200(?)	<600-2200	Wells &Mullens (1973)
Carlin, Nevada	coarse	900(?)	<600-1500	Wells &Mullens (1973)
Carlin, Nevada	Dissemin-ated	4200(?)	2100-8100	Wells &Mullens (1973)
Banqui, China	<10μm	1400(?)	<500-4600	Shui (1991)
Unspecified	rims	288		Marion et al. (1991)
	core	44		Marion et al. (1991)
Fairview Mine, Barberton, S. Africa		488(?)		Swash (1988)
Banqi, China	As- rich rims	257	<0.3-108 <82-600	Chryssoulis (1989) Mao (1991)

Sample, Location	Type	average (SD) (ppm)	Range (min-Max)	Reference
Lara, British Columbia	coarse	10(4.7)	1.9-22	Cook & Chryssoulis (1990)
Ketza River, British Columbia		11.9(2.2)	1.3-46	Cook & Chryssoulis (1990)
Golden Pond, Quebec				
Ore A	coarse	13.2(5.0)	0.3-72.8	Cook & Chryssoulis (1990)
Ore A	fine	39.1(13.2)	17.5-77.4	Cook & Chryssoulis (1990)
Ore B	coarse	23.1(10.3)	1.3-158	Cook & Chryssoulis (1990)
Ore B	fine	98.9(16.2)	10.6-402	Cook & Chryssoulis (1990)
Trout Lake, Manitoba	coarse	30.2(8.6)	2.0-112	Cook & Chryssoulis (1990);
Congress, British Columbia	coarse	38(17)	1.7-100	Cook & Chryssoulis (1990)
Congress, British Columbia	fine	1630(1330)	25-13000	Cook & Chryssoulis (1990)
Olympias, Greece	fine	49(24)	2.3-370	Cook & Chryssoulis (1990)
Estrades, Quebec	fine	54(36)	<0.3-170	Cook & Chryssoulis (1990)
Elmtree, New Brunswick	fine	123(61)	0.4-912	Sie et al. (1989)
Unspecified, Australia	fine	162(?)	<40-405	Sie et al. (1989)
Unspecified, Canada	fine	360(139)	1.3-5600	Chryssoulis (1990)
Sheba, South Africa	fine	929(150)	81-1900	Cook & Chryssoulis (1990)
Sheba, South Africa	fine	1046(154)	440-1900	Cabri et al. (1989)
Sheba, South Africa	fine		<350-4400	Cabri et al. (1989)
Unspecified, France		1300(2400)	<800-3600	Cathelineau et al. (1989)
Cortez, Nevada	fine	2600(?)	<600-6800	Wells &Mullens (1973)
Le Chatelet, France	fine	3500(6980)	<200-11500	Johan et al. (1989); Marcoux et al. (1989)
Villerange, France	fine	6820(9680)	<200-15200	Johan et al. (1989); Marcoux et al. (1989)
Fairview Mine, Barberton, S. Africa		2700(?)		Swash (1988)
			0.5-2500	Chryssoulis (1989)
Synthetic arsenopyrite	zoned crystals		0-17000	Wu et al. (1990)
Griffin's Find Aust	core		2.8-3.36	Neumayr et al. (1993)
Mt York Australia	core		20-33	Neumayr et al. (1993)

Table 2.2 - Invisible Gold Content in Arsenopyrite

The distribution of "invisible gold" within individual sulfide crystals is commonly highly irregular, with wide variations in gold concentrations as shown by point analyses and secondary ion mass spectrometer imaging (SIMS) (Cathelineau *et al.*, 1988; Boiron *et al.*, 1989; Graham *et al.*, 1989; Johan *et al.*, 1989; Marcoux *et al.*, 1989; Chryssoulis, 1990; Chryssoulis and Cabri, 1990; Stephens *et al.*, 1990; Wu *et al.*, 1990).

Microprobe analyses of pyrite and arsenopyrite grains from the Fairview Mine, South Africa, showed that gold was present in both sulfides (Swash and Ellis, 1986). Wells and Mullens (1973) have used the electron microprobe to study gold-bearing arsenian pyrites from the Cortez and Carlin gold mines in Nevada, USA. They concluded that in the sulfide ore, gold is concentrated along with arsenic in tiny ($\leq 5\mu$m) pyrite grains and in the rims of larger pyrite grains. Gold is also concentrated in arsenopyrite which is sparsely distributed in the Cortez ore. Robinson (1983) using both an electron and ion microprobe also reported a large proportion of gold to be submicroscopic in the Porgera deposit in Papua New Guinea.

Recent studies with the electron microprobe and some work done with an ion probe microanalyser have confirmed that arsenopyrite may contain gold in appreciable concentrations (Cathelineau *et al.*, 1988; Graham *et al.*, 1989; Johan *et al.*, 1989; Marcoux *et al.*, 1989; Cook and Chryssoulis, 1990). The detection limit for electron microprobe analyses for gold in sulfides is normally about 200 ppm (Cabri, 1988a,b), however, Graham *et al.* (1988) have obtained a detection limit of 10 ppm by using a very high beam current and accelerating voltage.

Chryssoulis *et al.* (1987) developed an *in situ* microanalytical technique using an ion microprobe or secondary ion mass spectrometer (SIMS) to quantitatively measure the gold content of sulfides. Calibration procedures, accurate to 15% in the quantification of 1 ppm, were discussed by Chryssoulis *et al.* (1989). The in-depth profiling capability of the ion microprobe permits subsurface, submicrometer-scale inclusions as small as 100Å to be detected, thus leading to more accurate determination of the gold that is dispersed in the crystal structure of sulfides. Their

results have shown that enrichment in arsenic and gold occurs from core to margin in several crystals observed in arsenopyrite samples from Sheba, South Africa and Le Chatelet, France. Johan *et al.* (1989) obtained data suggesting that Au may be incorporated in arsenopyrite when As occupies the Fe sites in the arsenopyrite structure but this may be an artifact of the stoichiometry assumed.

Cook and Chryssoulis (1990) found a positive correlation between the concentration of As and Au in pyrite, suggesting that substitution of Au into that structure is facilitated by the presence of As. SEM backscattered electron images of pyrite crystals show complex chemical zoning (Marion *et al.*, 1991; Cathelineau *et al.*, 1988; Fleet *et al.*, 1989). Mao (1991) found similar occurrences of up to 600ppm gold in pyrite associated with arsenic-rich rims.

2.6.2 Inclusions

Gold commonly occurs as discrete macroscopic or microscopic grains of the native metal either in vein quartz or occupying fractures or inclusion sites within certain sulfide minerals, particularly pyrite and arsenopyrite. The grain size of native gold varies with the mode of origin of the mineral. Where the gold has been deposited contemporaneously with quartz and other gangue and ore minerals, much of it is generally very finely divided, occurring as minute particles disseminated in other minerals. Gold deposited later than the associated minerals has a tendency to occupy small fissures in the pre-existing minerals, with the result that the bulk of it is of coarser grain size (Harris, 1990). Schwartz (1944) reviewed the association of native gold with various sulfides in 115 deposits and observed that the number of deposits with gold intergrown with different sulfides was pyrite 48, arsenopyrite 45, galena 30, sphalerite 26 and chalcopyrite >23. For these associations, metallurgical treatment of the gold ore yields good recoveries with proper grinding and direct cyanidation. In some gold ores, either the gold inclusions are submicroscopic or the gold occurs in solid solution in which case the ore is considered refractory.

Dissolution of Brazilian arsenopyrites containing gold inclusions, has revealed grains of gold with botryoidal textures, indicating the presence of colloidal precipitation of gold (Michel, 1989). The late precipitation of gold among well-formed arsenopyrites led Michel to suggest that gold was liberated from the lattice of arsenopyrites by fracturing and carried as a colloid over short distances before precipitation took place. The transport of gold by soluble complexes over long distances could not explain why the gold precipitation always occurred within the already-formed arsenopyrites.

Amosov and Gureev (1970) and Amosov et al. (1975) observed epitaxial growth of gold on pyrite. They suggested that co-crystallisation of gold and pyrite occurs on the surface of the growing pyrite crystals.

Studies by Starling et al. (1989) and Knipe et al. (1992) on several Precambrian mesothermal lode-gold deposits have revealed the site specific nucleation of precious metals on the surface of the sulfide minerals, in particular pyrite. Gold is typically located at sites of increased surface charge density and focused conductivity, such as grain edges, grain junctions, growth terraces and fracture surfaces. Serial sectioning through oriented gold cling-on deposits attached to pyrite showed that the contact is planar, which indicates that the mechanism is not one of diffusion through the crystals.

2.6.3 Colloidal Gold

The existence of colloidal gold (less than 200Å in diameter) has recently been confirmed in unoxidised Carlin type ores using high-resolution transmission electron microscopy and Aüger spectroscopy (Bakken et al., 1989). They found gold present as discrete particles varying from 50 to 200Å in diameter which were encapsulated primarily in pyrite. Hochella et al. (1988) have also used transmission electron microscopy to locate and identify similar types of gold in partially oxidised ore.

2.6.4 Solid Solution Gold in Pyrite and Arsenopyrite

Spectrographic techniques have recently been developed which prove that in some cases, gold is chemically combined within sulfide minerals rather than being discrete mineral inclusions. In studies of gold ores using Mössbauer spectroscopy, Wagner et al. (1986), Cathelineau et al. (1988) and Marion et al. (1991) have shown conclusively that gold present in concentrates of pyrite and arsenopyrite may be either metallic (i.e. present as inclusions) or structurally bound even though its chemical state (Au^0, Au^{1+}, Au^{3+}) is not known. Results obtained on a number of Au-rich arsenopyrites show that gold is mostly present in the samples as combined gold which exhibits a reproducible large absorption peak that is easily distinguished from the spectra of metallic gold (Friedl et al., 1992). This peak is due to the presence of Au-X(As?) bonds which can be attributed either to solid solution within the arsenopyrite lattice or solid inclusions being too small in size to be detected by conventional methods (Cathelineau et al., 1988). Zhang et al. (1987) found several hundred ppm gold in solid solution in arsenopyrite and pyrite from the Wuxi deposit, Hunan province, China, using electron paramagnetic resonance spectroscopy.

In [197]Au Mössbauer spectroscopic studies carried out by Marion et al. (1991) on arsenian pyrite, a significant amount of the gold was found to be intimately associated with the mineral in a combined chemical state with only a small peak corresponding to the metallic gold position. However the absorption peak corresponding to the combined gold did not have the same position as for gold combined in arsenopyrite. This suggests the gold bonding environments are different between pyrite and arsenopyrite. Boyle (1979) considered that some gold may substitute in the iron sites of pyrite and arsenopyrite mainly because of similar octahedral radii, a certain affinity for sulfur and the isostructual relationship of the two minerals pyrite and aurostibite.

The argument for structurally bound gold in arsenopyrite has also been tested by electron and ion probe microanalysis, coupled with high-resolution transmission electron microscopy (Cabri et al., 1989). Visible segregations of gold of a few

Angstroms in diameter were not observed in grains containing up to 2000 ppm gold and it was therefore concluded that gold was in solid solution.

Marcoux *et al.* (1989) and Johan *et al.* (1989) using electron microprobe analyses mapped the distribution of gold, antimony, arsenic and iron in gold-bearing arsenopyrite crystals from the Le Chatelet and Villerange ore deposits in France. Their analyses showed clear chemical zoning with enrichment in arsenic and gold from core to margin in several crystals (e.g. 31.2 to 36.7 atom % As and 0 to 1.22 wt% gold). Antimony and sulfur and to a lesser degree iron showed an inverse distribution. They found no correlation between the total As content and Au and/or Sb in arsenopyrite. However, examination of variations in the Fe site occupancy revealed an inverse linear correlation between As and Au +Sb. Their correlations indicated that each growth zone for arsenopyrites from the Le Chatelet and Villerange deposits is characterised by a minimum value of Fe/(Fe+As) on the Fe site, corresponding to the maximum Fe deficiency. Within each of these zones, the incorporation of Au and Sb becomes possible due to the substitution mechanism

$$2As[Fe] = (Au,Sb)+Fe$$
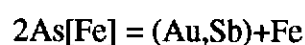
where As[Fe] is As on the Fe site. Buerger (1936) concluded that the existence of Fe(III) in the non-polar state in the FeAsS crystal structure, explains the As(III) = Fe(III) substitution, implying that gold and antimony replacing iron in arsenopyrite are in the Au(III) and Sb(III) state. Swash (1988) and Graham *et al.* (1988) also suggested that submicroscopic gold could be accommodated within arsenopyrite, owing to its suitable atomic spacing, crystal chemistry, and closure temperature with respect to gold. Based on bonding mechanisms described in section 2.4, Cook and Chryssoulis (1990) proposed that arsenopyrite which can be expressed $[Fe]^{3+}[AsS]^{3-}$, could easily contain trivalent metal cations (e.g. $As^{3+}, Au^{3+}\ Sb^{3+}$ etc.) substituting for Fe^{3+}.

In the pyrite structure, Kuranti (1941) was the first to consider that gold replaces iron. Kuranti (1941) synthesised auriferous pyrite and observed that the lattice constant progressively decreased with increasing gold content (up to 2000g/t), indicating some possible relationship of gold with the pyrite structure. However, Stillwell and Edwards (1946) considered that gold occupied vacancies in the pyrite lattice rather than replacing iron. Kravtsova and Solomonova (1984), Mironov and Geletiy (1978) and Mironov et al. (1986) hydrothermally synthesised various sulfides in the presence of radioactive gold and then studied them by optical microscopy, electron and laser microprobe and autoradiography. In pyrite, they concluded that gold is not structurally bound but occurs as micro-inclusions at the boundaries of crystals. In contrast to Kuranti (1941) findings, Chang and Zhang (1991) found that gold-rich pyrites have larger unit cell than pyrites containing no gold. They attributed this to gold substitution or a defective structure in pyrite grains, but did not characterise the form of gold present.

Cook and Chryssoulis (1990) proposed that in pyrite expressed as $[Fe]^{2+}[S_2]^{2-}$, the addition of arsenic, commonly found in the structure, would result in $[AsS]^{3-}$ pairs. This would result in a charge imbalance with the metal. If such an imbalance of charge exists because of the incorporation of As in the structure, it can be met by trivalent cations replacing the divalent iron. This would imply that the presence of the $[AsS]^{3-}$ species would appear to be necessary before substantial quantities of gold can enter the sulfide structure (Cook and Chryssoulis, 1990).

There is, however, no direct evidence to date as to the location of solid solution gold in either the arsenopyrite and pyrite structures.

2.7 Thermal Behaviour of Arsenopyrite and Pyrite

When the gold is intimately associated with sulfide minerals and fine grinding of the ores does not increase the extraction of gold by cyanidation to the desired extent, pretreatment by either roasting, hydrometallurgy or biological leaching is required. These processes have been described in detail by various workers (e.g.

Robins and Jayaweera, 1992; La Brooy *et al.*, 1994). Roasting of sulfide ores to liberate gold has been well documented and in the past has been one of the most cost-effective options. This process generally involves arsenopyrite and pyrite being oxidised to hematite via an intermediate formation of pyrrhotite at temperatures in the range of 500 to 700°C, resulting in gold becoming accessible to the cyanidation process. However, with regulations being introduced in some countries to reduce emissions of SO_2 and As_2O_3, this process is becoming more costly.

Detailed knowledge of the behaviour of gold in its host sulfide under thermal conditions, the composition of arsenopyrite and pyrite, their associations with other phases in the system and possible variations as related to different physical and chemical environments, is an essential prerequisite to an understanding of the possible mechanisms of gold incorporation and extraction. In addition, the solubilities and possible reactions of gold with the decomposition products have to be considered.

2.7.1 Phase Diagram of Fe-As-S systems

A thorough investigation of the Fe-As-S system was initially carried out by Clark (1960). His study was undertaken to correlate the physical conditions of formation for both sulfide and arsenide deposits. Equilibrium phase relations in the Fe-As-S system were determined at 600°C and changes in assemblages were studied in the 400°C to 800°C temperature range. At 600°C he found that a very narrow liquid field lies along the arsenic-sulfur side of a ternary system between 100 and 22±0.2 wt%.

Synthetic arsenopyrite produced at temperatures above 600°C has the approximate composition of $FeAs_{1.1}S_{0.9}$. Compositions that are sulfur rich relative to ideal FeAsS become stable at lower temperatures and under high confining pressures. Changes in the phase assemblages at various temperatures are governed by the reactions pyrite + arsenopyrite = pyrrhotite + liquid or vapour, arsenopyite + arsenic = löllingite + liquid or vapour; and arsenopyrite = pyrrhotite + löllingite + liquid or

vapour. The invariant temperatures at which both liquid and vapour are present in these assemblages are $491°\pm12°C$, $688°\pm3°C$ and $702°\pm3°C$ respectively.

Barton (1969) using the results of Toulmin and Barton (1964) for the Fe-S system combined with data on arsenic-bearing assemblages, derived the free energies, enthalpies and entropies of formation of arsenopyite, löllingite, orpiment and realgar.

Kretschmar and Scott (1976) extended the phase relations of the Fe-As-S system below 400°C. Clark (1960) and Kretschmar and Scott (1976) showed that at low temperatures (circa 300°C) the As:S ratio in arsenopyrite is lower than at higher temperatures (400-600°C). Kretschmar and Scott (1976) devised an arsenopyrite geothermometer which has been utilised by several authors (Beglund and Ekstrom, 1980; Sharp et al., 1985) in determining the conditions of rock formation. The technique requires that the system is buffered and equilibrium has been reached (Scott, 1983). Arsenopyrite synthesed by Wu and Delbove (1989) contained chemically zoned arsenopyrite grains containing up to 40 at% of arsenic which can not be explained by the Kretschmar and Scott (1976) diagram. The nonstoichiometry of arsenopyrite has been discussed in an earlier section.

2.7.2 Decomposition of Arsenopyrite

The thermal decomposition of arsenopyrite follows roughly the simplified endothermic reaction

$$4FeAsS \rightarrow 4FeS(s) + As_4(g) \dots\dots\dots\dots\dots\dots\dots\dots\dots\dots\dots\dots\dots\dots\dots\dots\dots\dots (2.3)$$

In addition to arsenopyrite varying in As:S ratio, the final iron sulfide product also has a Fe:S ratio less than one (Grimsey and Aylmore, 1990). Furthermore, thermodynamic calculations and experimental data confirm that in an inert atmosphere, apart from As_4, there is As_2 and some S_2 vapour species present in the Fe-As-S system (Chakraborti and Lynch, 1985). Many researchers have reported that there is only As_4 and no As_2 gas species below 800°C (Shigematsu, 1986). The reaction followed is more likely to reflect the unbalanced equation

$$FeAsS \rightarrow Fe_{1-x}S + FeAs_2 + As_4(g) + S_2 \ldots\ldots\ldots\ldots\ldots(2.4)$$

Thus, even stoichiometric arsenopyrite will not decompose to FeS but rather to a pyrrhotite with an Fe/S ratio less than one. The formation of $FeAs_2$ (or some FeAs compound) would appear necessary to maintain the stoichiometry; however in many studies no löllingite is found (Swash and Ellis, 1986; Swash, 1988; Graham *et al.*, 1988; Grimsey and Aylmore, 1990).

The amounts of the above product species as well as their compositions will vary according to the composition of the initial arsenopyrite phase and period of roast. The composition of pyrrhotite formed is temperature dependent as well as being a function of sulfur activity (Toulmin and Barton, 1964). The vapour pressure of arsenic over arsenopyrite never exceeds 1 atmosphere at temperatures below 1080°C.

Strathdee and Pidgeon (1969) measured the dissociation pressure of arsenic in equilibrium with arsenopyrite, $As_4S_4(l)$, and pyrrhotite at temperatures between 473 and 923 K by a quartz spoon gauge. They assumed the total pressure in the gauge to be the sum of the partial pressures of As_4 and As_4S_4. Their assumption that arsenopyrite, $As_4S_4(l)$ and pyrrhotite were the only condensed phases present, appears to be in error. Barton (1969) has shown that these phases are in equilibrium only at temperatures between 764 and 962 K and not between 473 and 923 K as suggested by Strathdee and Pidgeon (1969). At lower temperatures pyrite, not pyrrhotite is in equilibrium with the other phases. In addition, Barton (1969) has shown that the As-S liquid in equilibrium with arsenopyrite and pyrrhotite is not As_4S_4 but a liquid of variable composition which is rich in arsenic. Shigematsu (1986) measured the equilibrium vapour pressure of arsenic or arsenic compound gases formed from the thermal dissociation of each synthesised compound by the Knudsen method. Shigematsu's results indicated that the temperature of dissociation of arsenopyrite in Ar atmosphere was 500°C. The relationship between log Pe and 1/T for arsenopyrite is

Log Pe(atmos) = - 6530(±30)/T + 6.50(±0.05)

Arsenopyrite has been reported to dissociate slightly at temperatures as low as 220°C (Hausen, 1991). Thus the thermal behaviour of arsenopyrite is not clearly defined.

2.7.3 Phase Diagram of Fe-As-S-Au systems

A scan of the literature shows that data on As-Fe-S-Au systems are not well defined. However, examination of phase diagrams of Au-S, Au-As and As-S provide some information and these are shown in Figure 2.6(a to c). In the Au-S system no interaction of gold and sulfur occurs at temperatures below 1048°C (Okamoto and Massalski, 1985). Although Au$_x$S can be prepared from solutions (Cardile et al., 1993), it is however, a metastable compound. None of the gold sulfides are stable above 240°C.
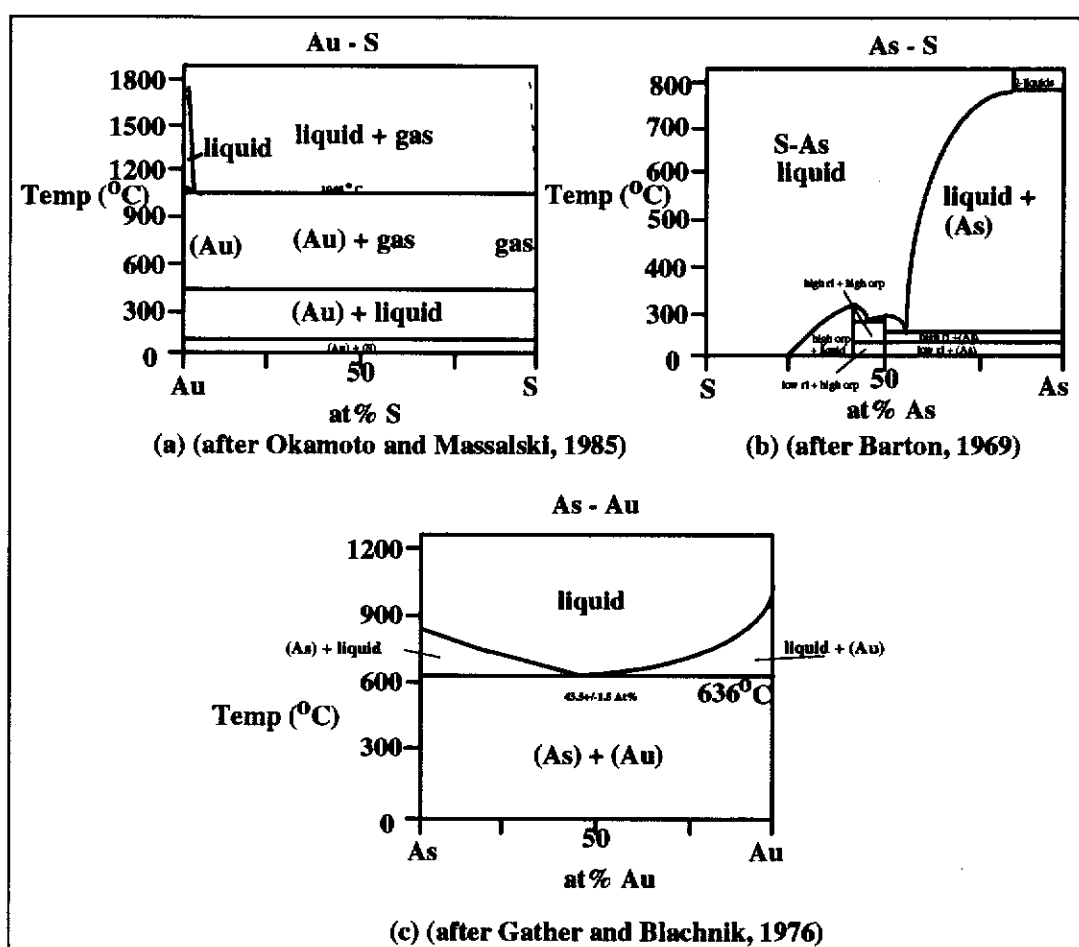
Figure 2.6 Binary phase diagrams of As, S and Au systems. *Elements in brackets correspond to solid phases.

For the As-Au system (Figure 2.6c), a eutectic is formed between As and Au at 636°C with minimal solution of gold in arsenic and vice versa. Gold is mobile in the presence of arsenic at temperatures of 636°C and above (Gather and Blachnik, 1976). Gold arsenides are unstable above 120-130°C. Hansen and Anderko (1958) showed a portion of the Au-As system with a eutectic at about 78 wt% gold at 665°C. Owen and Roberts (1977) reported that 0.2 at% arsenic is soluble in gold at 610°C.

In the As-S system, arsenic dissolves in sulfur to form a liquid at temperatures above the melting point of sulfur (115°C), but sulfur does not dissolve in arsenic at any temperature, although the vapours are miscible (Barton, 1969). The As-S system is characterised by an extensive liquid field, a two-liquid field on the arsenic-rich side and two binary compounds orpiment (As_2S_3) and realgar (As_2S_2). Barton (1969) studied the sulfur activities of sulfur-arsenic liquids by measuring the temperature at which sulfur-arsenic liquids of known composition were simultaneously in equilibrium with pyrite and pyrrhotite (Toulmin and Barton, 1964). The solubility of arsenic in the liquid increases with vapour pressure of As_4, thereby decreasing both the vapour pressure of S_2 in equilibrium with the liquid and the sulfur content of the liquid.

Little iron is soluble in any As-S liquid (Clark, 1960; Barton, 1969) and an $AuFe_2$ compound exists. However, iron will have preference over gold to combine with sulfur or arsenic. In the Au-Fe diagram, Hansen and Anderko (1958) showed about 12 wt% iron soluble in gold at 600°C.

Under hydrothermal conditions, orpiment and realgar melt at 312°C and 307° C respectively, and liquids of variable As/S ratio are stable at lower temperatures (Barton, 1969). Solid + liquid arsenic sulfide melts coexisting with hydrothermal solution are unlikely to occur under geological conditions as the arsenic sulfides are soluble above 200°C. (Heinrich and Eadington, 1986). However, the formation of melts and As-Fe-S liquid will have an impact on gold mobility under other conditions.

2.7.4 Mobility of Gold in Pyrite and Arsenopyrite

Early studies on auriferous pyrite and arsenopyrite have shown exsolution of gold on heating the host mineral. Maslenitsky (1944) prepared pyrite containing 300g/t gold by adding auric chloride or colloidal gold during the synthesis. Gold could not be seen at a magnification of x1200. By heating the pyrite *in vacuo* at 600°C, the pyrite altered to pyrrhotite and gold aggregates were exsolved.

Sakharova *et al.* (1972) found that when various gold bearing sulfides from East Transbaikal, Russia were heated around 250 to 300°C, the finely dispersed ("invisible") gold aggregated into larger visible gold particles. A disintegration of some of the larger gold particles was also observed. They concluded that over a long period of time gold can be redistributed at relatively low temperatures. Kalitkina (1971) also found that gold migrated relatively rapidly by diffusion in the solid state along fracture and grain boundaries in both pyrite and arsenopyrite. Similar results were seen by Klempert *et al.* (1973). Narseev and Starova (in Petrovskaya, 1974, *cited by* Boyle, 1979) noted that heating auriferous pyrite for 20 mins at 250°C enlarged gold particles and decreased the cell parameter from 5.4275 to 5.4095Å. They suggested that point defects in the lattice of pyrite occur at the sites of the dispersed gold. A decrease in micro hardness found in the auriferous pyrite was considered to result from linear dislocations. For the auriferous arsenopyrite the investigators noted a tendency to fine acicular to finely prismatic habit, increased cell parameters *a* and *b* and a decrease in micro-hardness. Morimoto and Clark (1961) observed no such sluggish high-low polymorphic inversion in their structural analysis of arsenopyrite.

McPheat *et al.* (1969) and Boyle (1979) have suggested that, in arsenical ores formed at elevated temperatures, gold may be incorporated into the lattice of pyrite or arsenopyrite. This would be largely in solid solution, or as atomic layers on the growing crystal faces of the sulfide minerals. When these minerals have cooled, the gold in the structure distorts the sulfide lattice and, consequently, there is a rise in the strain energy of the system.

When these sulfides are subjected to a later thermal event, the submicroscopic gold may then migrate to sites of lower potential such as fractures, grain boundaries, and other micro- and macro- structural sites; the strain energy of the system is thus reduced. This movement of gold may be enhanced by temperature gradients and may also be reorganised into a new thermodynamically stable assemblage that is characterised by the presence of pyrrhotite. The arsenopyrite may change from an n-type to a p-type sulfide after it has been remobilised and reconstituted (Swash, 1988).

The formation of gold particles has been attributed to the removal of arsenic from the arsenopyrite lattice. Swash and Ellis (1986) proposed that as the localised shrinking cores of arsenopyrite diminish in size, so does the molten As-S interface which is thought to form during the topochemical dissociation. As this molten interface is reduced in size, the gold concentration is increased. During heating, the free energy of the new system is minimised by the postulated As-S interface which is a site of lower energy where gold is readily soluble in arsenic and sulfur liquid. The liquid under a confining pressure within the grain and is released to the outer atmosphere. When arsenic and sulfur are totally removed the gold remains behind in the form of a 'blob' situated adjacent to the pore in the calcine microstructure.

This process was first observed in arsenopyrite by Clark (1960) who found that gold diffused rapidly through arsenopyrite at temperatures of 660°C and higher. Clark was looking for the curve that would define the effect of pressure at which the breakdown reaction

$$FeAs_{1.1}S_{0.9} \rightarrow Fe_{1-x}S + FeAs_2 + Liquid \dots\dots\dots\dots\dots(2.6)$$
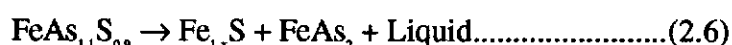
could proceed and when projected to very low pressure, would originate in the arsenopyrite invariant point at 702°±3°C defined earlier in his experiments. In the presence of excess gold arsenopyrite breaks down at about 670°C under pressure of invariancy (~1 bar). That is, the curve is offset about 30°C towards lower temperatures. In his experiment where arsenopyrite decomposed, the results indicated that gold was transported by an arsenic rich sulfur-arsenic fluid. Graham *et al.* (1988)

observed exsolution of gold from auriferous arsenopyrite heated *in vacuo* at temperatures around 600°C.

The breakdown in pyrite may be different to that in arsenopyrite due to the differences in atomic spacing and crystal chemistry. Swash and Ellis (1986) postulated that during the breakdown of auriferous pyrite, gold grains or atoms in a metastable state migrate by solid state diffusion to a site of lower energy, so that the exsolution phenomenon is possibly largely the result of diffusion processes.

The exsolution of gold from pyrite and arsenopyrite structures has been confirmed by Wagner *et al.* (1986) from Au^{197} Mössbauer measurements. A peak shift in the spectra was observed from a gold peak associated with gold bonding in the sulfides to a gold peak position associated with metallic gold after heating.

Chapter 3

3.0 COMPOSITION AND STRUCTURE OF NATURAL ARSENOPYRITE

3.1 Introduction

Previous attempts to accurately determine the composition and structure of arsenopyrite have been hindered by uncertainties in the stoichiometry and difficulties associated with the occurrence of crystal twinning. The following chapter details analyses that were carried out on natural arsenopyrite samples using the electron microprobe, convergent beam electron diffraction analyses and the Rietveld (1969) method of analysis applied to X-ray powder diffraction data, in an attempt to overcome these difficulties and to provide accurate information as to the possible mechanism for the retention of gold in solid solution in arsenopyrite. In the first instance the morphology and composition of the arsenopyrites were characterised. Trace gold analyses were then carried out to determine whether suitable arsenopyrite crystals could be found which contained sufficient gold to be used in detailed analyses for determining the types of structural environment suitable for gold uptake in the lattice of arsenopyrite. In particular it was important to establish any potential association of gold and arsenic substitution on iron deficient iron sites. In addition, the most appropriate orientations for subsequent channelling experiments used in locating gold in the arsenopyrite structure required identification.

3.2 Materials and Methods

3.2.1 Habit and Morphology of Arsenopyrite Samples

The morphology and grainsize of the arsenopyrites used in these studies are shown in Table 3.1. Most of the arsenopyrite samples obtained were already separated from their gangue and the actual location within the deposit is unknown. The

arsenopyrites described in Table 3.1 do not necessarily represent all arsenopyrites within a particular ore deposit.

Table 3.1 Arsenopyrite Samples Analysed			
Sample	Habit	grainsize	Form of gold
Sheba Mine, S. Africa	acicular crystals	≤50μm	inclusions and invisible
Salsigne, France	massive, acicular	~10μm	invisible
Le Chatelet, France	acicular	10-20μm	invisible
Harbour Lights W.A	massive	10-20μm	invisible
Paddington W.A.	massive, rhombohedral	1cm	inclusions
Coolgardie, W. A	rhombohedral	≤1mm	inclusions
Southern Cross W.A.	acicular	10-20μm	invisible
Goodall WA	massive	2cm	-
Mexican, Mexico	rhombohedral	~1cm	-
Greenbushes, W.A.	massive to rhombohedral	2mm	-
Wuhan, China	massive, rhombohedral	1cm	-
Pine Creek, W.A.	massive, tabular	~1cm	-
Portugal	massive, tabular	~1cm	-
Utah, U.S.A	massive	2cm	-

invisible - denotes gold which cannot be observed by optical or electron microscopy, which may occur either in solid solution or as submicroscopic inclusions

Polished sections revealed characteristic silver-white colour and metallic lustre under an optical microscope. Samples containing acicular crystals existed as aggregates or were finely disseminated in the gangue matrix of quartz or phyllosilicates. Others consisted of large, mainly singular crystals, massive, rhombohedral in habit and striated along several crystal faces. Examination under cross polarised light revealed distinctive twin lamellae in some large crystals that were much more extensive in the Coolgardie sample. Rotating the polariser revealed non-uniformity in the interference colours indicating strain in some crystals. Generally the large crystals were uniform. Faint shades of striated colour were observed in the Portugese and Chinese crystals corresponding possibly to twin lamellae similar to those observed by Morimoto and Clark (1961).

3.2.2 Sample Preparation

Natural arsenopyrite samples were concentrated by initial light crushing and where necessary, dissolution of surrounding material in hydrofluoric acid for two days following the method of Neverburg (1975). In some cases residual quartz was still present.

Grains of liberated arsenopyrite were checked under a Scanning Electron Microscope (SEM) for evidence of dissolution. Residual quartz was removed by flotation in bromoform. Finally, pyrrhotite was removed using a hand magnet. Fine grained samples were sized into two fractions; less than 63μm and greater than 63μm. Small proportions of each fraction were made into polished sections. Subsamples were crushed for X-ray diffraction analyses (XRD) and thermal analyses, as described in Chapter 7.

Polished sections were prepared by placing the arsenopyrite in 30 mm diameter plastic moulds and adding epoxy resin. Air was removed by evaculating and the epoxy left to set. For synthetic arsenopyrite (discussed in Chapter 4) epoxy resin mounts were first made and a small hole (5mm diameter 3mm thick) was drilled into the mount. The sample was then added to the mount. Additional epoxy resin was then added to the hole, evacuated and then left to set. Once set, the epoxy resin grain mounts were removed from the plastic moulds and ground to provide sections of arsenopyrite grains. Electron microprobe samples were carbon coated.

3.2.3 Optical and Scanning Electron Microscopy

Polished sections were analysed initially under an optical microscope and features of interest marked. Samples were observed under either the ISI or Jeol GeoSEM partial vacuum scanning electron microscopes (Robinson and Nickel, 1979). The scanning electron microscopes are equipped with energy dispersive spectrometers, TV displays and Robinson backscattered electron detectors. The backscattered electron image obtained gives compositional information in the images so that phases are clearly differentiated. Initially, each polished section was rapidly

scanned to evaluate the different forms of minerals present. Typical grains of interest were photographed and analysed qualitatively using the energy dispersive analysis equipment. Backscatter images revealed gold inclusions present in the Sheba, Coolgardie and Paddington arsenopyrites. High contrast backscatter images did not reveal strong chemical zoning. Weak zoning was observed in some Le Chatelet and Sheba arsenopyrite grains. Generally, the grains appeared uniform and this was confirmed by chemical compositions obtained by electron microprobe analyses described in the next section.

3.2.4 Electron Microprobe Analyses

3.2.4.1 Major Elemental Analysis Technique

The compositions of all natural and subsequently, synthetic arsenopyrite samples, were determined by electron microprobe analyses using a Cameca SX-50 electron microprobe with three spectrometers. Several analysing conditions were used as well as several different standards. Samples of natural pyrite and indium arsenide were initially used as standards for Fe and S, and for As respectively. Sb, Cu, Bi, Pb, Ni, Co and Ag were also analysed in natural samples using pure or sulfide standards. A sample of arsenopyrite characterised by Kretschmar and Scott (1976) and known as ASP200 was later obtained and used as a standard for Fe, As and S analyses. Data were collected and corrected for ZAF (atomic number, absorption and fluorescence) matrix corrections using WANUSX software. Data were generally collected using an accelerating voltage of 20 kV and a beam current of 20nA analysing As Lα, Fe Kα and S Kα. Some data were collected using As Kα X-rays at voltages of 25 kV and 30 kV. The use of higher voltages meant moderate amounts of counts for Au Lα X-rays could also be collected along with the other elements. For all analyses a counting time of 20 or 40 seconds was used.

Data were collected by traversing across every grain within each carbon-coated polished section. Using the electron beam, lines were drawn in the epoxy resin

from grain to grain so that any grain of interest could be found after analysis. Several traverses were made on different parts of the polished sections. In addition, some grains were analysed at several positions in order to check homogeneity. The standards were analysed at intervals during collection of data from unknowns in order to check for instrumental drift.

3.2.4.2 Calibration of Microprobe Conditions

For quantitative electron microprobe analyses, characteristic X-ray intensities from the specimen are compared with those from standards of known composition. Matrix corrections are applied to allow for differences in absorption and backscattering between the specimen and the standard. These corrections can be calculated with reasonable accuracy. Errors exceeding 1% may occur when the specimen and standard are of vastly different composition. If the standard used is similar in composition to the analysed specimens, the matrix corrections are not required. For these standards, errors due to chemical effects are negligible and errors due to dead time and other count rate dependent effects are eliminated.

To determine whether there is an iron deficiency, a number of factors need to be considered. These include (i) X-ray wavelength, (ii) the amount of instrumental drift, (iii) the current and voltage of electron beam (iv) the type of standard to be used, and (v) reproducibility of data,

X-ray Wavelength

The critical excitation energy of the As Kα line (10.53 KeV) is much higher than As Lα line (1.28 KeV). The excitation efficiency is dependent on the overvoltage ratio (U), defined as E_0/E_c where E_0 is the incident electron energy and E_c is the critical excitation energy of the relevant shell. A high U is desirable as it gives a greater count rate for the As Kα line. However, electron penetration increases rapidly with E_0 and the electrons spread out further from the point of input reducing spatial resolution. Because of the small size of many of the natural (and subsequently the

synthetic) arsenopyrite crystals together with the need to determine chemical zonation, a small probe size was desirable and spatial resolution was essential. In addition, absorption corrections increase as the accelerating voltage increases due to an increase in the electron penetration to greater depth. A higher accelerating voltage which is suitable for As Kα excitation will have a detrimental effect on the S Kα line (2.3 KeV). Furthermore, measurement of the S Kα line at high accelerating voltage appeared to cause some wandering of the peak position. For the measurement of the As Lα line, the thallium hydrogen phthalate (TAP) crystal on one spectrometer was used, whereas for the As Kα line, the lithium fluoride crystal (LiF) detector was used. While there is a higher background on TAP crystals compared with LiF crystals, the peak to background ratio is better for TAP crystals. Therefore the As Lα line was mostly used.

Variations in Current and Voltage

The composition of several arsenopyrites with varying stoichiometries were obtained under various electron beam conditions (see Appendix A). In all cases, pyrite and indium arsenide were used as standards. Each beam condition was tried on different days and on different locations on the samples. The results for accelerating voltages 20 kV and 25 kV were similar for each type of arsenopyrite. However at 30 kV, the iron values were always higher (0.01 at%) relative to the pyrite standards. In the case of the lower accelerating voltage, the arsenopyrites' iron values were generally lower (0.002 at%) than the pyrite standard.

Arsenopyrite Standard

Detailed analyses were carried out on the ASP 200 arsenopyrite standard to check the chemical homogeneity and establish its suitability as a probe standard, rather than pyrite and indium arsenide. Scanning and transmission electron microscopy and qualitative energy dispersive analyses revealed inclusions of pyrrhotite and quartz. Stray radiation may produce a contribution from these minerals and result in incorrect values. Also, electron microprobe analyses showed that

although the average composition of the sample gave similar results to the published data (Kretchsmar and Scott, 1976), there were regions in which the sample was not homogeneous. Consequently, in obtaining the composition of other arsenopyrites, the ASP 200 sample was re-analysed and used as a guide as to the validity of these results. Any significant deviations in composition of the ASP200 sample from its published values during analyses resulted in the data being deemed incorrect.

Reproducibility of Data

Figure 3.1 shows the variation in chemical composition of the arsenopyrite (ASP200) standard for analyses obtained in conjunction with those analyses obtained for all the arsenopyrites. The average and standard deviations, as well as the published data are shown and are in good agreement with each other. Figure 3.1 also shows the distribution of points about the average. Disregarding the inhomogeneities mentioned above, it would appear that, under the analytical conditions chosen, the precision for iron would be ±0.002, and for arsenic and sulfur would be ±0.005 atomic fraction.

3.2.4.3 Trace Gold Analysis Technique

Trace gold analyses were carried out following the method of Graham *et al.* (1989). For maximum trace sensitivity, maximum counts are obtained by using a high current and voltage. The analytical conditions used for the natural arsenopyrite were an accelerating voltage of 40 kV and a beam current of 500nA. Calibration was carried out by analysing a standard containing 20% gold in a gold-silver standard using the two LiF crystal spectrometers fitted on the Cameca SX-50, set at the position for the Au Lα line. On the standard, the beam current was reduced to 30nA to prevent overloading the detectors with X-ray counts, and counted for 10 seconds. Background counts included the negative peak in the background caused by diffraction of general radiation planes in the LiF crystal (Self *et al.*, 1988; Graham *et al.*, 1989). Arsenopyrite and pyrite samples were then analysed at the same points

Arsenopyrite Standard (ASP200) for various analyses

Atomic ratio of various elements

0.38
0.37
0.36
0.35
0.34
0.33
0.32
0.31
0.3

0.3   0.31   0.32   0.33   0.34   0.35   0.36   0.37   0.38

Fe(Atomic ratio)
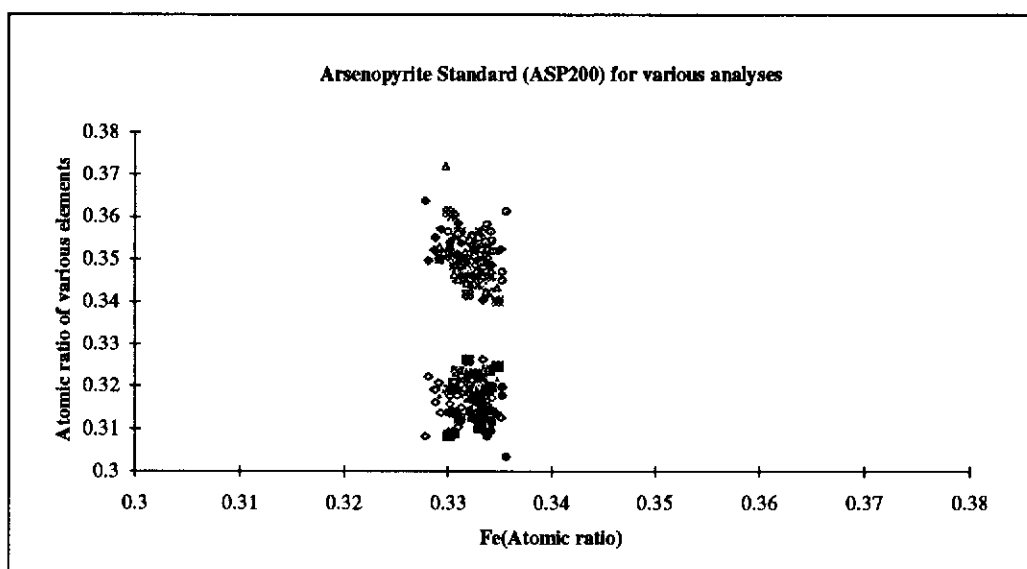
Variation in Composition of Asp200 from Different Analysis Runs (atomic fraction, sd)			
	Fe	As	S
average (this study)	0.3314±0.0019	0.3174±0.0045	0.3512±0.0047
Kretchsmar and Scott (1976)	0.331	0.318	0.352

Figure 3.1 A plot of all arsenic and sulfur values versus iron content for arsenopyrite standard (ASP200). The symbols represent different analyses, the upper group being sulfur and the lower arsenic. The table shows average and standard deviation values of all data points.

across polished sections as described for the major elemental analyses (Section 3.2.4.1). A counting time of 10 minutes gave the method a detection limit of 10 ppm.

3.2.5 Wet Chemical Analyses

Wet chemical analyses from several arsenopyrites were obtained and compared with those obtained by electron microprobe analyses. For the wet chemical analyses 0.1 g of arsenopyrite was placed into a zirconia crucible. 0.5 g of sodium peroxide and 0.3 g of sodium carbonate were added to the arsenopyrite. The crucible was then heated in a muffle furnace at 500°C. After 30 minutes the crucible was removed from the furnace and left to cool. 20ml of hydrochloric acid was added to the fused product. The melt was then dissolved in water making sure that all instruments used were thoroughly washed. The solution was transferred to a 1L volumetric flask. Arsenic and sulfur were determined by the inductively coupled plasma technique using emission lines at 193.760 nm and 180.731 nm respectively. The iron content was determined by Atomic Absorption Spectroscopy.

3.2.6 X- ray Diffraction Powder Studies

Most detailed investigations of the structures of crystalline materials have been carried out by single crystal diffraction studies using the well known Weissenberg and the Buerger precession methods (Klug and Alexander, 1974). However, difficulties associated with X-ray studies on single crystals of arsenopyrite, due to twinning, are well documented (Buerger, 1936; Morimoto and Clark, 1961).

Until recently, conventional wisdom held that powder XRD data were unsuitable for crystal structure studies primarily because of problems of peak overlap and the difficulty of measuring accurate Bragg intensities (Post and Bish, 1989). With the introduction of computer-automated diffractometers to collect routinely digitised data using a step-scan procedure and in particular, the application of the Rietveld (Rietveld, 1967,1969) refinement method to powder XRD data, the refinement of a number of crystal structures previously unavailable has become possible.

3.2.6.1 Sample Preparation for X-ray Diffraction Powder Studies

One of the critical stages of any structural study based on powder XRD data is the sample preparation. In particular, most minerals exhibit some cleavage and therefore are prone to yield powder samples having nonrandomly oriented crystallites. Consequently, relative peak intensities will be modified to an unknown degree resulting in an incorrectly refined structure. Klug and Alexander (1974) found that accurate and reproducible peak intensities were obtained for quartz only when samples were ground to particles less than $15\mu m$.

The natural arsenopyrite samples were finely ground for 10 mins in a Tema mill with acetone to prevent heat damage to the crystals and mounted in aluminium holders. Several patterns of each of these samples were recorded and compared to determine whether preferred orientation of arsenopyrite occurred.

Natural arsenopyrite samples were examined using two different diffractometers, a Siemens D500 X-ray diffractometer and a Philips X-ray diffractometer. Both used Cu $K\alpha$ radiation and a graphite monochromator. Patterns were recorded from 10 to 130° 2θ using a stepsize of 0.04° 2θ and a scan speed of $0.25^\circ 2\theta/min$. The patterns were recorded over this range in order to make the determination of site occupancy and isotropic temperature factors more accurate for Rietveld analysis. X-ray powder data was stored on a PC computer using Sietronics™ software. X-ray patterns were examined and peak positions measured using a software package called XPAS (Singh and Gilkes, 1992).

3.2.6.2 Rietveld Method

There are two methods for extracting structural information from powder diffraction data. One is the procedure where the integrated intensities of individual Bragg reflections are measured and converted to structure factors and the structure solved or refined similarly to single crystal data (Will et al., 1983). This method works well for high symmetry structures that have minimal peak overlap in their diffraction patterns. However complex structures with low symmetry gives patterns with many

Bragg reflections and severe peak overlap, and it is not possible to resolve individual Bragg reflections.

One of the important strengths of the Rietveld method (Rietveld, 1967,1969) is the capability of refining precise and accurate unit cell parameters even for materials having complex diffraction patterns with severe peak overlap, since it does not require decomposition of patterns into component Bragg reflections. It also can model multiphase systems. Powder pattern X-ray intensities are unaffected by twinning. During a Rietveld refinement, structural parameters (atom positions, temperature and occupancy factors), scale factor, unit cell parameters and background coefficients, along with profile parameters describing peak widths and shape, are varied in a least-squares procedure until the calculated powder pattern, based on the structural model, best matches the observed pattern. This method was first applied to powder neutron diffraction data where peak shapes, arising from constant-wavelength powder neutron diffraction experiments, are close to Gaussian and can be easily modelled. It was later adapted for use with X-ray data (Malmros and Thomas, 1977;Young et al., 1977). Rietveld refinements on powder XRD data have only recently been more widely used with the advent of improved functions to describe powder XRD peak shapes which are more complex and difficult to model than neutron data. The easy accessibility of XRD opposed to neutron diffraction has also increased the use of XRD over neutron experiments. The method has been described by Hill and Howard (1986) and is presented in detail in Appendix B. In the present work the structure of arsenopyrite was refined from X-ray diffraction data on powder samples using the Rietveld method (Rietveld, 1967,1969).

Rietveld Procedure Used in this Study

Calculations were performed using Rietveld software (LHPM10 version) devised by Hill and Howard (1986) which has been adapted for use on an IBM compatible PC.

The structural parameters obtained by Fuess *et al.* (1987) were used as a starting point and a Pseudo-Voigt peak shape function (see Appendix B) was used in the refinement. Peak base was taken to be 5x full width at half maximum (FWHM). Five background parameters were refined; the background was assumed to have the form

$$I_{bkg}(2\theta_i) = B_0 + B_1 2\theta_i + B_2 2\theta_i^2 + B_3 2\theta_i^3 + B_4 2\theta_i^{-1}$$

where B_i is the ith background parameter.

Several refinement cycles were carried out on the scale factor, unit cell dimensions and 2 theta zero shift parameters on all XRD powder patterns of arsenopyrite. This was followed using a sequence of background, atomic coordinates, preferred orientation, peak half width, profile shape and finally isotropic thermal parameters for separate elements atomic coordinates. The fit improved dramatically on the introduction of occupancy of sites interchanging between As and S sites with the Fe site remaining fixed. As a result the Bragg-R factor was reduced by a factor of two. Site occupancy parameters were refined followed by the preferred orientation parameter. The weak cleavage direction on arsenopyrite (101) was used as the preferred orientation direction of which the contribution was very small. At the end of each refinement, the observed and calculated patterns were examined to check for any deviations in order to detect problems such as an improper fit of background or peak shape irregularities. The goodness of fit, weighted and unweighted profile fit parameters were monitored as well as the Durbin-Watson parameter (see Appendix B for definition) within the program (Hill and Madsen, 1987) to check for convergence of fit.

3.2.6.3 Bond Lengths and Angles Calculations

Using atomic coordinates from the refined Rietveld data , the bond lengths and angles between an iron atom and its surrounding three arsenic and three sulfur sites

were calculated using a program written in Pascal (see Appendix C) and using the formula set out in Boisen and Gibbs (1985).

3.2.6.4 Measurement of 131 d-spacing

To determine the arsenopyrite composition the position of the (131) X-ray peak of arsenopyrite was measured and then corrected against the internal standard (311) peak of calcium fluoride using the equation (Morimoto and Clark, 1961; Kretschmar and Scott, 1976):

$As = 866.67d_{131}$ - 1381.12 with an estimated one standard deviation of ±0.45 wt% in As

The d-spacings were compared with those obtained in the Rietveld analyses.

3.2.6.5 Structures Modelled using ATOMS^{TM} Software

To help interpret structural data in relation to twin planes, anti phase domains and the best directions in the arsenopyrite structure for ALCHEMI experiments, a program called "ATOMS" devised by Dowty (1989) was used to plot projections for a number of zone axes. Models of the arsenopyrite structure were also constructed to help interpretation.

3.2.7 Transmission Electron Microscopy

3.2.7.1 Convergent Beam Electron Diffraction and Selected Area Diffraction

The use of electron diffraction techniques provides accurate information on crystal system, unit cell dimensions and Bravais lattice. In particular, convergent beam electron diffraction can uniquely identify the space group of a crystal structure. The use of electron diffraction techniques provides crystallographic information at a high spatial resolution (potentially 50-100Å) which means problems associated with twinning or antiphase domains are reduced and where present, can be interpreted better than by X-ray techniques.

Convergent beam electron diffraction (CBED) has only become widely used in recent years. Reviews on the topic have been presented by Cowley (1978) and Williams (1984). Tanaka and his co-workers (Tanaka and Terauchi, 1985; Tanaka *et al.*, 1988) have published two volumes on applications of various types of CBED.

Convergent beam as a function of the inclination between the incident electrons and a particular crystal direction and selected area electron diffraction patterns are two dimensional maps of diffraction intensity. They are normally composed of discs for convergent beam and points for selected area electron diffraction patterns with each disc or point corresponding to a different Bragg reflection. The difference between selected area electron diffraction (SAED) and CBED is illustrated in Figure 3.2.

To obtain the normal SAED pattern an almost parallel electron beam is directed along a zone axis of the crystal, and the diffraction pattern produced in the back focal plane of the objective lens is an array of spots. For CBED, the incident electron beam is focussed on the specimen to a probe of finite diameter by the prefield of the condenser objective lens. If the illumination convergence angle 2α is appropriately chosen, the diffraction pattern consists of an array of non-overlapping discs. The angle of convergence is directly proportional to the diameter of the second condenser aperture. For thick specimens dynamic contrast is observed in each disc. The intensity variation within the discs carries important information about the specimen orientation and thickness as well as other properties of the specimen, one of which is crystal symmetry. Crystal symmetry information can be obtained by observing the internal structure of the 000 and hkl discs (Goodman, 1975; Steeds, 1979).
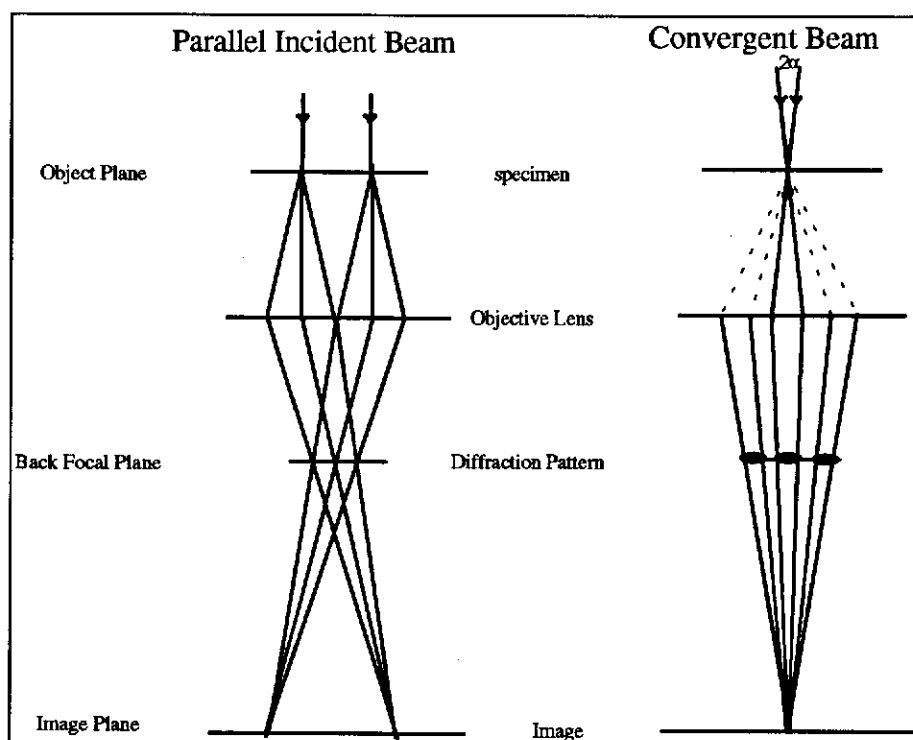
Figure 3.2 Ray diagram illustrating the difference between Selected Area and Convergent Beam Diffraction.

Electron diffraction is normally considered in terms of the Ewald sphere construction (sphere of reflection, relating real and reciprocal space) in the reciprocal lattice. Because of the small wavelength of high energy electrons the radius of the Ewald sphere is much greater than the spacing of the reciprocal lattice points. When an electron beam is incident along a zone axis, a reciprocal lattice plane perpendicular to the axis is a tangent to the nearly planar surface of the Ewald sphere and many reflections are excited. Figure 3.3 shows a schematic zone-axis electron diffraction pattern. This plane of excited reflection is known as the zero-layer plane or zero order Laue zone (ZOLZ). As the separation between the Ewald sphere and the reciprocal lattice points in the zero layer plane increases with distance from the origin (at the point of contact), the zero-layer reflections in this plane are no longer excited and eventually diminish in intensity and there is consequently an annular region without reflections. At greater scattering angles the Ewald sphere crosses the next plane of reciprocal lattice, exciting a ring of reflections in what is known as the first order Laue zone (FOLZ). Successive planes are intersected in a series of concentric circles of

increasing diameter known in turn as the second order Laue zone, third order Laue zone and so on. The FOLZ and higher reflections are collectively known as high order Laue zones (HOLZ).
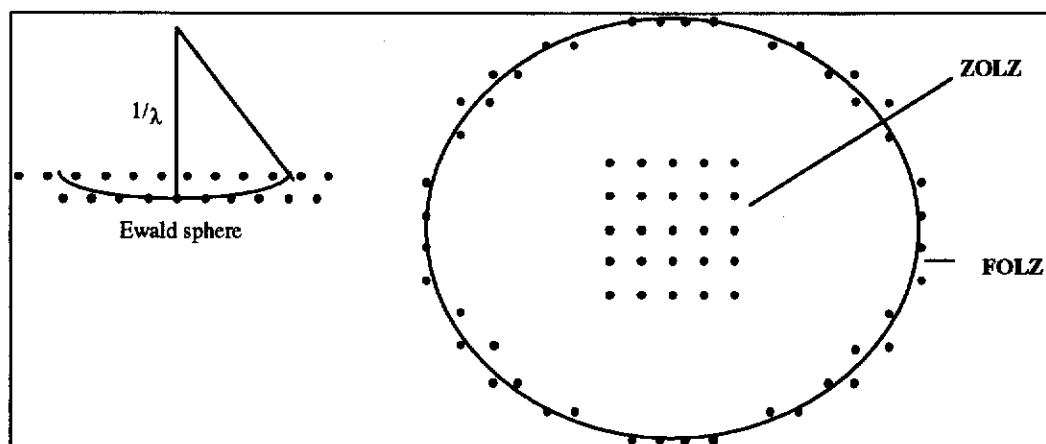
Figure 3.3 Schematic zone axis electron diffraction pattern showing the zero order and first order Laue zones in plane view.

3.2.7.2 Determination of Symmetry and Space Group

The symmetry of CBED patterns has been discussed by several authors (Goodman, 1975; Buxton et al., 1976, Steeds and Vincent, 1983). Buxton et al. (1976) found relationships between the 32 crystal point groups and the 31 possible symmetries (diffraction groups) of CBED patterns from ideal plane foils with normal electron incidence. The diffraction groups are described by the symbols of ten two dimensional point groups together with an inversion operation through the Bragg position of the dark field discs. Steeds and Vincent (1983) devised a sequence of steps using information available on convergent beam electron diffraction patterns from high symmetry zone axes for crystal point and space group determination. Their principle is to tilt the crystal until a mirror line is seen in the diffraction pattern. The crystal is then tilted so that the line remains visible, i.e. about an axis normal to the mirror line, until another mirror line or lines are observed. The intersection of these mirror lines is then a principal zone axis and will display symmetry in the zero Laue zone reflections and in some cases in the higher Laue order zones. In some cases it is

possible to determine the space group from patterns recorded at one zone axis if clear HOLZ reflections are present. Examples of point group determination have been given by Champness (1987) and Steeds and Morniroli (1992).

When a crystal structure contains screw axes or glide planes so called 'forbidden reflections' occur, according to kinematic diffraction theory, whenever the structure factor vanishes. When a reflection, forbidden by kinematical diffraction theory appears on a principal line of a zone axis pattern that has 2mm symmetry it generally reveals a central line of absent intensity in a well oriented pattern. The existence of such a line of absence indicates that the electron beam is incident on the crystal either parallel to a glide plane or perpendicular to a screw axis (Gjonnes and Moodie, 1965). The two forms can easily be distinguished by obtaining patterns with 3 dimensional diffraction information in them, i.e. deficiency HOLZ lines in the bright field disc. The symmetry of the zero order pattern is then reduced to m and if the mirror lies as m_1 in Figure 3.4 then the zone axis is perpendicular to a screw axis in the crystal, while a mirror m_2 indicates that the zone axis is parallel to a glide plane. The width of the GM lines increase with decreased crystal thickness.
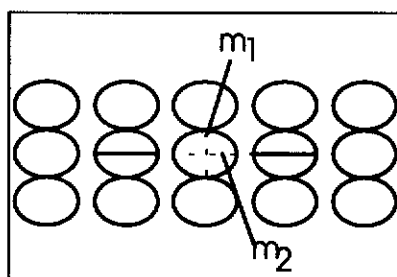
Figure 3.4 Schematic diagram of CBED for axial illumination parallel to a glide plane or perpendicular to a screw axis showing orientation of mirrors m_1 and m_2 with respect to the line of dynamic absences (after Steeds, 1979).

3.2.7.3 High Order Laue Zones

The dark lines within the bright field disk are called deficiency (or defect) HOLZ lines. Bright lines observed in HOLZ reflections under certain conditions are known as excess lines. The intensity initially present in the direct beam at the entrance

surface of the specimen is Bragg reflected away to each of the reflections excited in the FOLZ for orientations corresponding to the portion of the dark line. The length, orientation and positions in the bright field CBED disc of each deficiency line is exactly matched by corresponding excess lines in each FOLZ reflection. These excess lines consist of a number of plane wave excess lines of Bloch wave branches of the dispersion surface branch structure, corresponding to solutions of Schrodinger's equation for fast electrons travelling through a periodical potential. The intensity variations of the branch structure in the HOLZ ring are very sensitive to atomic location and in some cases can be used for accurate structure determinations (Vincent *et al.*, 1984).

Although CBED studies have been used in a wide variety of applications, very few sulfides have been analysed. Some detailed structural analyses have been carried out on pyrite (Steeds and Vincent, 1983). Marcasite and nickel arsenide type structures have also been analysed. Studies on niccolite minerals have shown that the classical NiAs structures are modulated (Vincent and Pretty, 1986; Vincent and Withers, 1987). The true symmetry of these minerals as a result of these modulations is in fact orthorhombic and not hexagonal. The primary purpose for using CBED in the present studies was to determine the space group and crystal structure of arsenopyrite. It was also used in the interpretation of ALCHEMI experiments (see Chapter 6).

3.2.7.4 Sample Preparation

For transmission electron microscopic studies, samples of arsenopyrite were crushed under liquid nitrogen and then dispersed on a holey carbon coated copper grid. To analyse grains in the polished sections, the grains were scraped out using a fine needle in a droplet of water and then pipetted onto a holey carbon coated copper grid. The instrument used for these studies was a Philips EM 430 analytical transmission electron microscope fitted with an EDAX PV9900 energy dispersive X-ray system. The instrument was operated at 300kV. To obtain diffraction data a tilt

and rotating liquid nitrogen cold stage holder (Gatan™) was used, as arsenopyrite samples readily decomposed under the beam.

The method used in these studies for determining space group symmetry using CBED patterns, was that outlined by Steeds and Vincent (1983). CBED patterns were obtained for major zone axes for several arsenopyrite samples with differing compositions. The 30μm second condenser aperture was required to produce a convergence angle small enough to prevent overlap of discs for all zone axes. Selected area electron diffraction patterns were also taken and the d-spacings were accurately measured after corrections from calibrated patterns of silicon. In auriferous arsenopyrite samples electron diffraction patterns were also checked for spacings corresponding to metallic gold.

3.3 Results and Discussion

3.3.1 Chemical Composition of Natural Arsenopyrites

Table 3.2 shows the chemical compositions (based on approximately a hundred data points for each sample) of all natural arsenopyrites analysed by electron microprobe. Generally the samples analysed contained few impurities in the crystals of arsenopyrite and where present, these were sparsely distributed. These included impurities of Ni, Bi, Co, and Cu in some grains . In samples from Sheba, Le Chatelet and Southern Cross, impurities, in particular antimony, were more abundant. Fine inclusions of bismuth, lead, and tin sulfide minerals were also present in many of the arsenopyrite samples, in particular, the China and Goodall samples. The concentration of these minerals was less than 0.2 wt%.

Large variations in chemical composition occurred in arsenopyrites from different generations within the same ore body. This is illustrated by comparing two different arsenopyrites obtained from the Southern Cross mine. One obtained from a mica schist was arsenic rich whereas those obtained from the quartz lenses were sulfur rich.

Table 3.2 Chemical Composition of Arsenopyrites, Microprobe analyses			
Natural Arsenopyrite Samples (Atomic ratios, sd)			
	Fe	As	S	Other abundant impurities
Le Chatelet	0.332±0.003	0.288±0.02	0.379±0.02	Sb 0.0006±0.0004
Salsigne	0.333±0.005	0.304±0.03	0.355±0.03	Au 0.00002,Sb, Cu 0.0006±0.0004
Sheba	0.331±0.002	0.318±0.008	0.352±0.008	Au 0.00072,Sb
Harbour Lights	0.330±0.002	0.321±0.005	0.348±0.005	nd
Southern Cross	0.334±0.002	0.322±0.01	0.344±0.01	Sb 0.0003±0.0002
Paddington	0.332±0.002	0.322±0.007	0.346±0.006	
Coolgardie	0.329±0.002	0.323±0.006	0.347±0.006	Cu
Goodall	0.331±0.001	0.326±0.003	0.343±0.004	
Mexican	0.332±0.004	0.333±0.003	0.335±0.003	
Greenbushes	0.331±0.002	0.339±0.007	0.331±0.007	
China	0.331±0.004	0.351±0.007	0.319±0.006	
Southern Cross	0.333±0.004	0.355±0.02	0.311±0.02	Ni 0.001±0.002 Co 0.0002±0.0003
Utah	0.331±0.002	0.360±0.007	0.309±0.007	
Pine Creek	0.331±0.002	0.361±0.008	0.308±0.008	
Portugal	0.332±0.002	0.363±0.006	0.305±0.006	

nd- not determined,

The arsenopyrites analysed are presented in increasing order of arsenic content. Although the As:S ratio changed, generally, the iron content did not vary more than ±0.002 from 0.331. Ideally, the iron value should be 0.3333 representing no substitution of any other elements, particularly arsenic. However based on the fact that the standard arsenopyrite (ASP200) used to check the validity of the data had an iron value of 0.331, this value is acceptable (Kretchsmar and Scott, 1976). This value does not deviate too far from the ideal 0.3333 within errors (±0.002) and suggests that no other element is substituted on the iron site. To illustrate the lack of variation in iron value with As:S ratio, Figures 3.5a and b show probe analyses of various arsenopyrite iron, arsenic and sulfur values respectively. The distribution of data
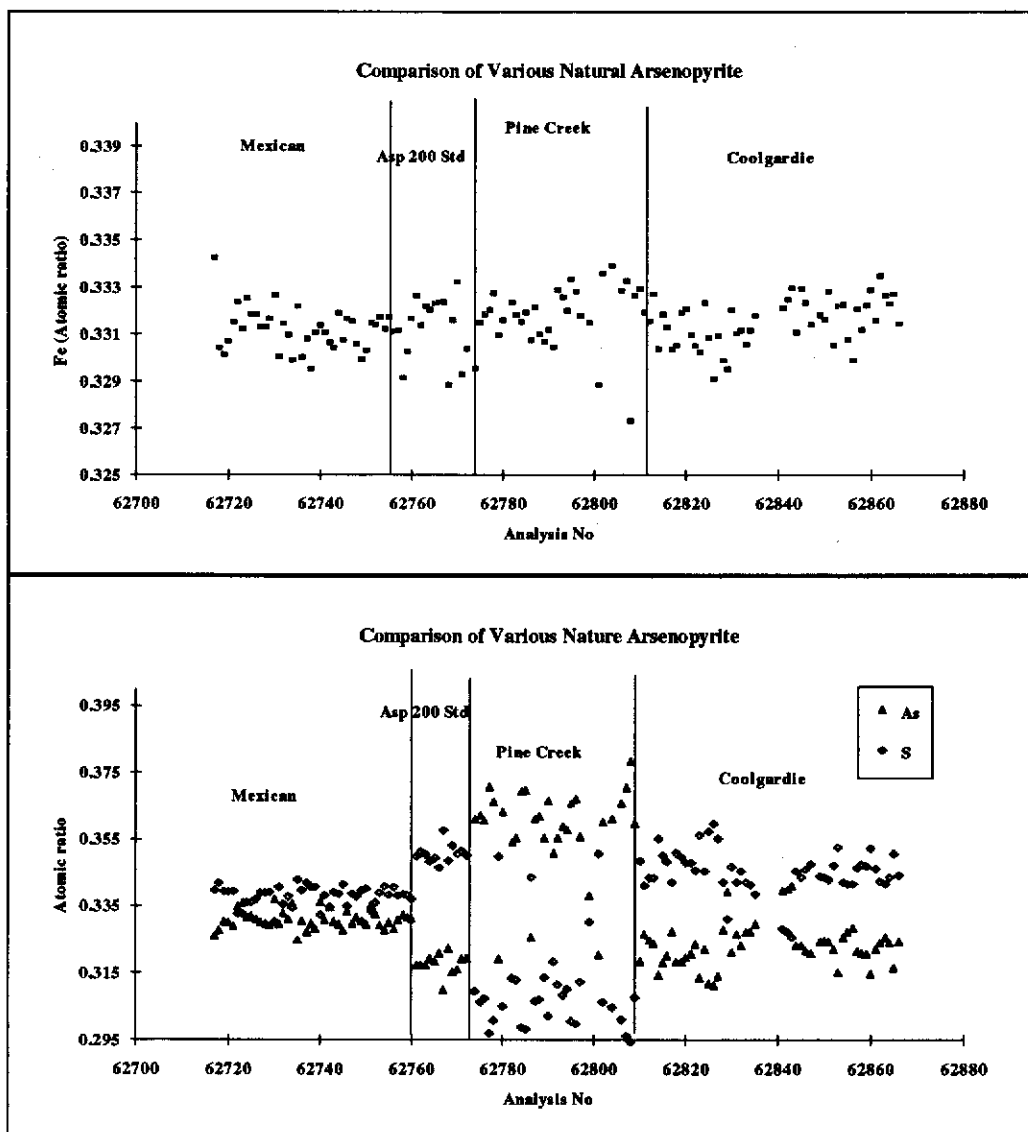
Figure 3.5 The variation of iron (a) and arsenic and sulfur (b) for various arsenopyrite analysed. The graphs show that the iron does not vary with composition.

points indicates that the iron values do not vary from one arsenopyrite to the next despite the variation in stoichiometry. A plot of all the data as arsenic to sulfur ratio versus iron showed no relationship with iron. The arsenic and sulfur values did not vary by more than ±0.008 atomic ratio within one sample except for the Le Chatelet, Southern Cross, Pine Creek and Salsigne arsenopyrite samples. These samples tended to be more abundant in other impurity elements. The impurity elements (e.g.. Ni, Bi, Co, Cu) may substitute for iron on the iron site (Klemm, 1965) or be part of inclusions from other minerals. The presence of impurities such as Ni, Co and Cu in some of the arsenopyrites showed a positive correlation with arsenic content. According to Klemm (1965) and Kretschmar and Scott (1976), the amount of impurities in the arsenopyrite increases as the As:S ratio increases with increasing temperature of formation. Figure 3.6 shows a plot of copper content versus arsenic to sulfur ratio for Salsigne arsenopyrite.

Wet chemical analyses for several arsenopyrites are shown in Table 3.3 and are in general agreement with electron microprobe analyses. However, the iron value for the China and sulfur value for the Mexican are slightly high.

3.3.2 Trace Gold Analysis

All selected samples were analysed for trace gold by electron microprobe analyses. Very little gold was found in the natural samples, with the exception of the Sheba sample. Some of the Southern Cross samples contained 24 to 123 ppm of gold, whereas gold contents in the Salsigne and Le Chatelet samples were less than 50 ppm. The distribution of gold in the Sheba sample is shown in Figure 3.7. It contained up to 0.79 wt% gold with the majority of the sample containing significantly less. Gold inclusions were also observed in the Sheba samples ($\leq 5\mu m$) and this may account for some of the gold content. This increased slightly with increasing As:S ratio (Figure 3.8), indicating an association of gold with arsenic richer areas. Also present in the sample were trace amounts of antimony, which showed no general correlation with any of the other elements.
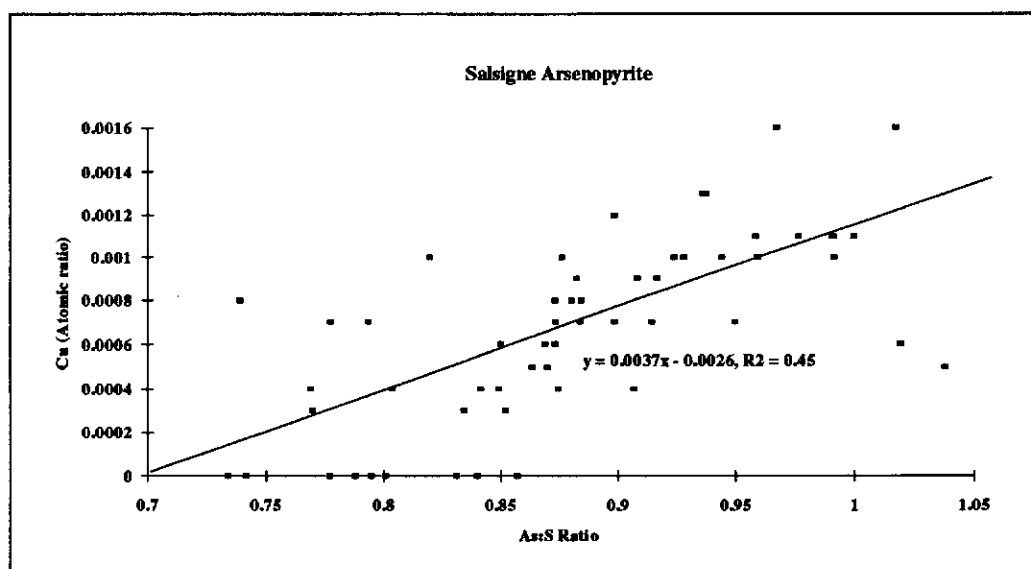
Figure 3.6 Relationship of copper content versus arsenic to sulfur ratio in Salsigne arsenopyrite.

Table 3.3 Wet Chemical Analyses of Several Arsenopyrite Studied			
	Fe	As	S
Greenbushes Wt%	34.5±1.0	46.4±1.2	19.8±1.2
at	0.333	0.333	0.333
Mexican Wt%	32.7±0.4	42.0±0.4	19.4±0.2
at	0.334	0.320	0.345
China Wt%	34.4±0.5	46.6±0.4	18.2±0.4
at	0.342	0.344	0.315
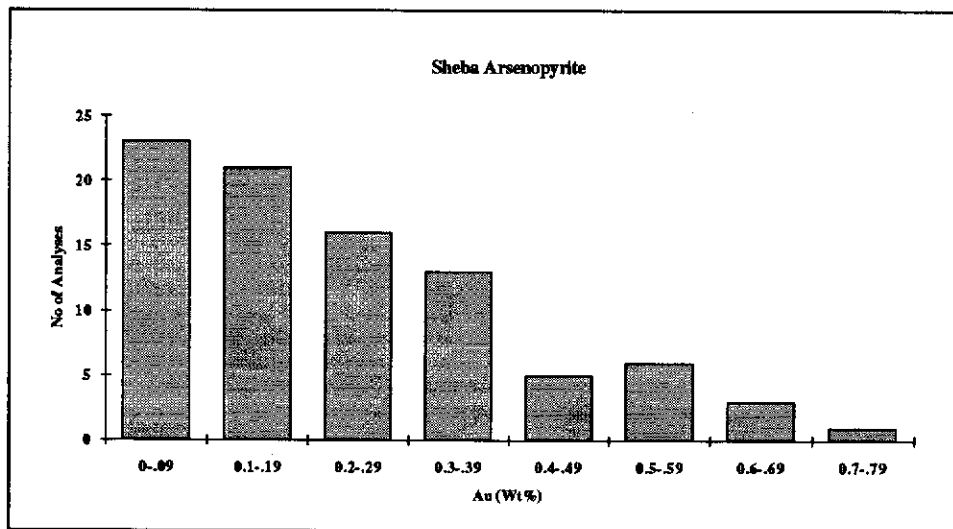
Figure 3.7 Distribution of gold in Sheba arsenopyrite sample.
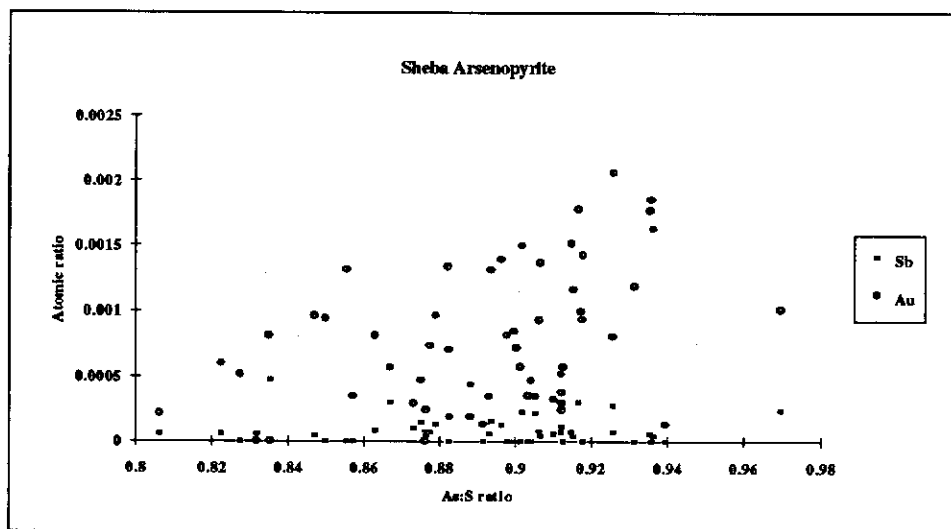
Figure 3.8 Relationship of gold and antimony content to arsenic to sulfur ratio in Sheba arsenopyrite sample.

To assess the possibility of gold and antimony occurring in solid solution, rules devised by Johan *et al.* (1989) were used for allocating elemental concentrations to the Fe, As and S sites. Excess arsenic was calculated and the gold and antimony content correlated with possible iron deficient iron sites. Figure 3.9a shows the correlation of calculated arsenic excess against the iron content for the Sheba arsenopyrite. Within experimental error (for Fe ±0.002, impurities ±0.0002) the majority of points did not differ from 0.3333 for iron and so the scatter of points on either side of this value represent the error in the analyses. The trend observed in Figure 3.9a reflects the assumption that all sites are fully occupied and that no sites are vacant, rather than indicating the presence of excess arsenic on the iron deficient site. The correlation between the antimony and gold content and excess arsenic observed by Johan *et al.* (1989) in their analyses of Le Chatelet arsenopyrites was not observed (Figure 3.9b) for Sheba arsenopyrite. According to Johan *et al.* (1989) antimony can also be accommodated on the iron site. Mössbauer measurements on Sheba arsenopyrite containing 1 wt% of antimony suggest that antimony is on the arsenic site (Friedl *et al.*, 1992). Antimony was assigned to the arsenic sites and the excess arsenic obtained from the calculations was correlated with the iron content. The correlation coefficient calculated for this fit was 0.95 whereas arsenic excess calculated without antimony substituted on the arsenic site, resulted in a correlation coefficient of 0.94.

The correlation coefficients obtained for both possibilities were not markedly different from each other and the results are therefore inconclusive. This is most probably due to a lack of range of data points at the low iron values. Figure 3.10 shows the correlation of excess arsenic obtained with and without antimony substitution on the arsenic site against iron content for the Le Chatelet sample. The iron values cover a larger range than those for the Sheba sample. However the substitution of antimony on the arsenic site also appeared to have little effect on the correlation. Some data points for both the Sheba and Le Chatelet arsenopyrites indicated a possible deficiency in iron. However the assumption made that all sites are
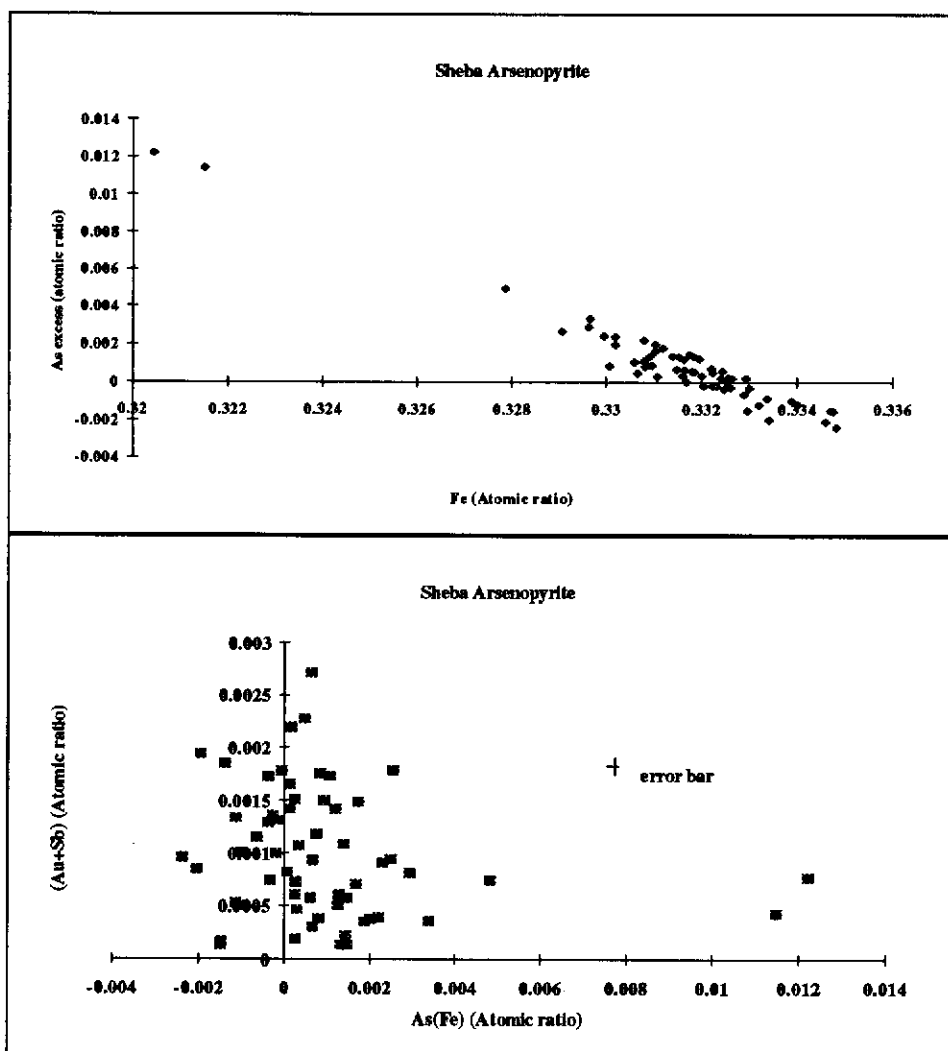
Figure 3.9 (a) Calculated excess arsenic versus iron content and (b) Gold and Antimony content versus calculated excess arsenic for Sheba arsenopyrite sample.
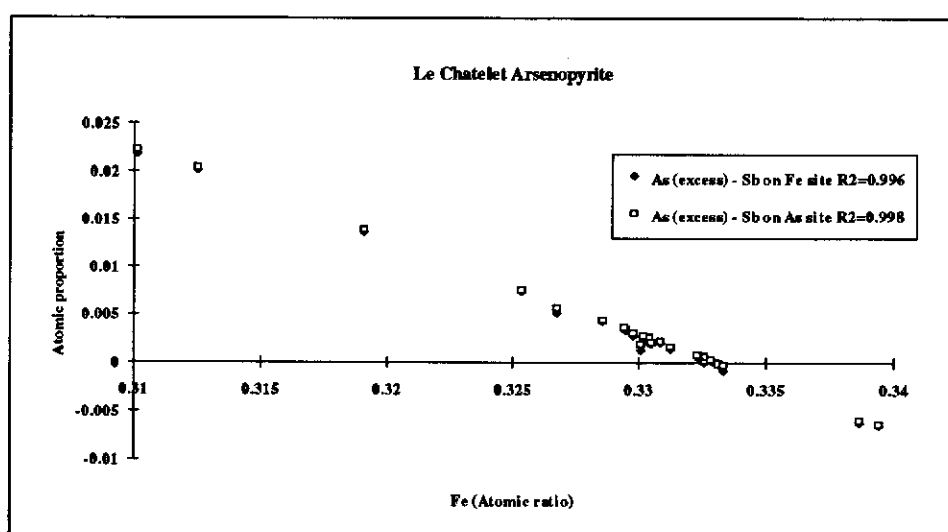
Figure 3.10 Correlation of arsenic excess obtained with and without antimony substitution on the arsenic site against iron content for the Le Chatelet sample.

occupied as well as the small range of iron values obtained for most data points make any correlation observed inconclusive. In the method described by Johan *et al.* (1989) the possibilities of vacant sites within the structure are not considered.

One of the reasons why little gold was observed in some of these samples may be the fact that high gold contents are normally associated with high As:S ratios. The Sheba and Le Chatelet arsenopyrites analysed had low As:S ratios.

For structural analyses in the next section, arsenopyrite samples were selected which were easily separated and for which chemical compositions did not vary and contained less than trace amounts of transitional metal impurities.

3.3.3 Structure of Natural Arsenopyrites

The powder X-ray diffraction patterns of arsenopyrites analysed from 2-theta angles of 20° to 65° are shown in Figures 3.11a to 3.11i in order of increasing As:S ratio based on chemical analyses from electron microprobe studies, with the exception of the Mexican arsenopyrite for reasons discussed later.

As the Rietveld method is primarily a refinement technique, for unknown structures it must be preceded either by a structural determination involving indexing and measuring intensities of individual Bragg reflections, or a confirmation of the structural model by other methods such as electron diffraction from TEM studies.

3.3.3.1 Indexation of Stoichiometric Arsenopyrite

The composition of one sample of Greenbushes arsenopyrite shown in Table 3.4 approached stoichiometric arsenopyrite with the ideal composition of FeAsS. Hence the structure of this sample was examined first.

X-ray diffraction patterns from the powder sample were compared with data observed in the literature. There are several space groups recorded in the literature and all can be related by some form of transformation (Fuess *et al.*, 1987). Fuess *et al.* (1987) adopted a non-conventional monoclinic setting (C112$_1$/d) to describe the arsenopyrite structure in relation to the orthorhombic marcasite structure but

Figures 3.11 X-ray diffraction powder patterns of (a) Sheba, (b) Coolgardie and (c) Southern Cross arsenopyrite samples in increasing order of As:S ratio.
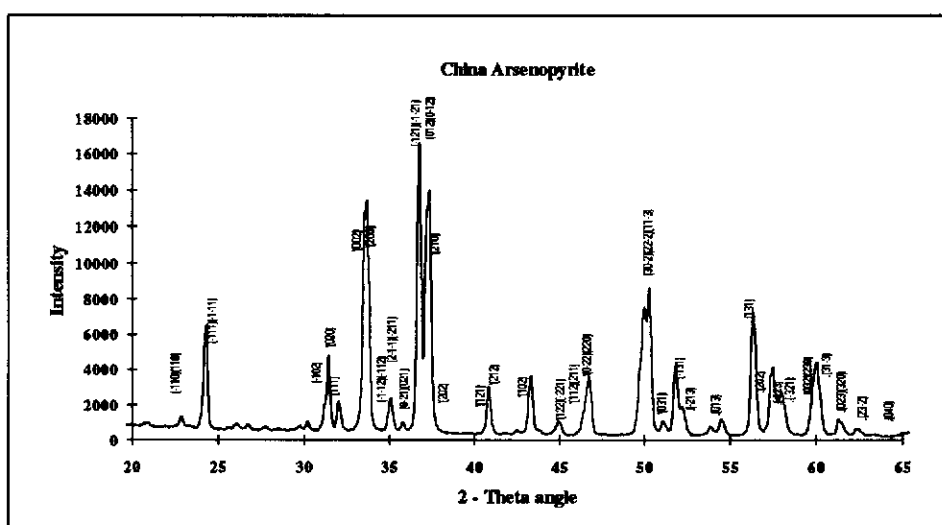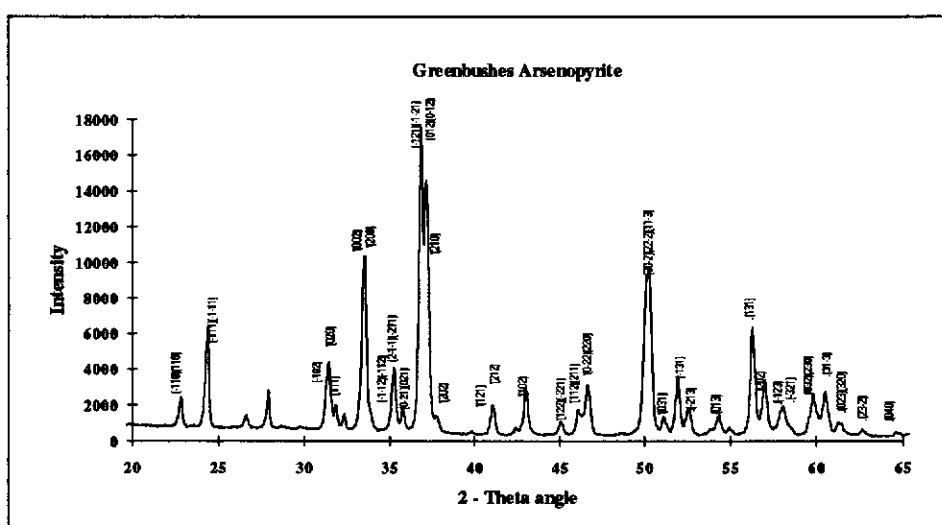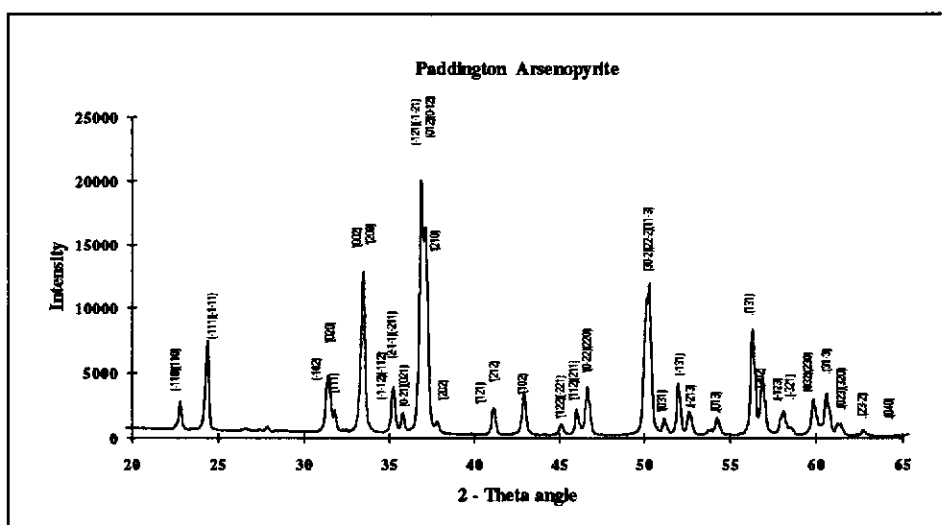
Figures 3.11 X-ray diffraction powder patterns of (d)Paddington (e) Greenbushes, (F) China arsenopyrite samples in increasing order of As:S ratio.
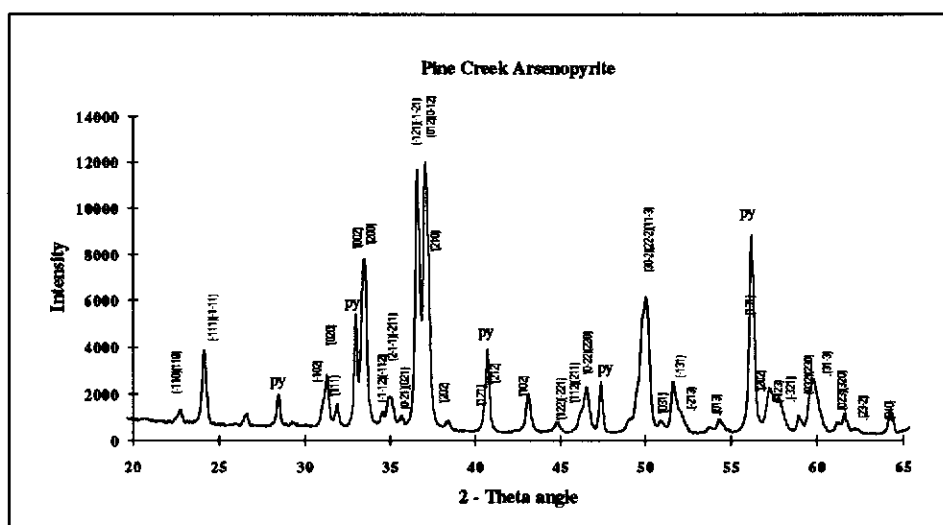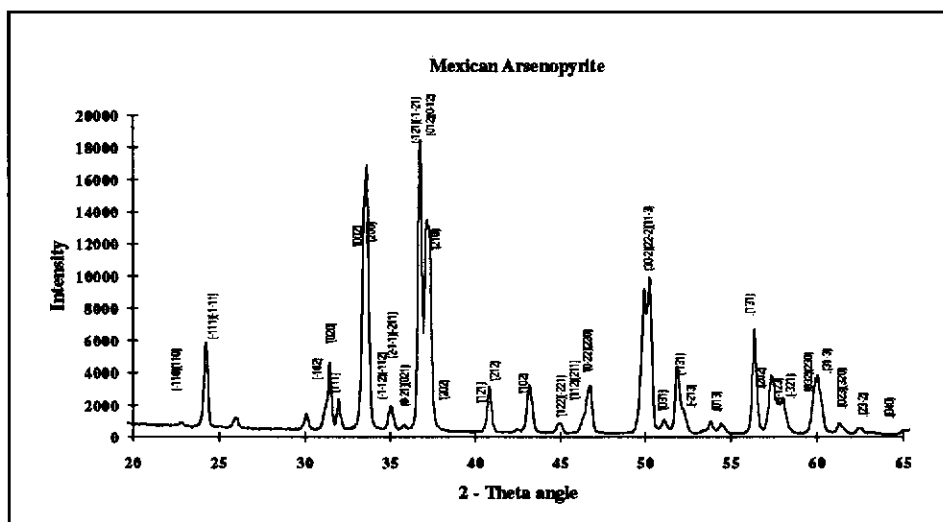
Figures 3.11 X-ray diffraction powder patterns of (g) Mexican; and (h) Pine Creek arsenopyrite samples in increasing order of As:S ratio.
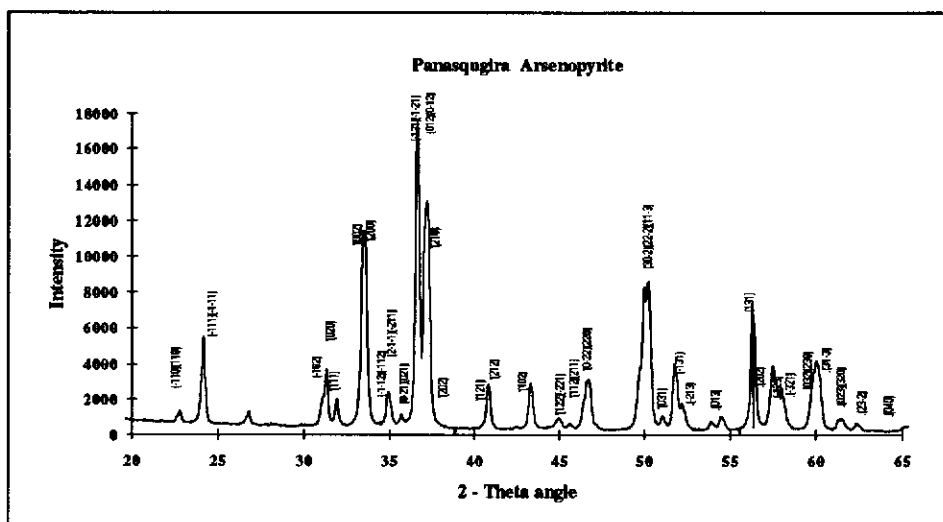
Figures 3.11 X-ray diffraction powder patterns of (i) Utah and (j) Panasqugira arsenopyrite samples in increasing order of As:S ratio.

considered the arsenopyrite symmetry to be monoclinic based on Morimoto and Clark's (1961) statement that cobalt stabilises the monoclinic symmetry. Their arsenopyrite contained 10% cobalt, whereas the Greenbushes sample analysed here contained no detectable impurities within the structure. For this sample, the conventional monoclinic symmetry (P2$_1$/c) was found adequate to describe the structure. Application of the automatic indexing program called UNITCELL to 54 reflections with 2 theta angles ranging from 15° to 70° produced a good fit for a monoclinic cell with a = 5.741, b = 5.679, c = 5.758Å and β = 111.75°. Seven lines were unindexed and these were found to correspond to an impurity of pyrrhotite. This rationalises the difference between microprobe and wet chemical analyses in Tables 3.3 and 3.4. The powder diffraction pattern is shown in Figure 3.11e together with the indexed reflections. The X-ray pattern is similar to that observed by Morimoto and Clark (1961). However, they did not observe or report the reflections (100) or ($\bar{1}$ 10,110) in their study. The (100) reflection is not shown in Figure 3.11e but was observed at a d-spacing of 5.379Å.

3.3.3.2 Effect of Stoichiometry on Arsenopyrite Structure

The structure of arsenopyrites with As:S ratios varying from low to high were analysed by XRD and compared with the essentially ideal structure, represented by the Greenbushes arsenopyrite.

Marked differences in the XRD patterns between the different stoichiometries are evident (Figure 3.11a to 3.11i). In the Sheba, Pine Creek and Utah arsenopyrite samples pyrite is also present as indicated by the reflections 3.12Å, 2.709Å and 2.428Å. In some of the patterns, a splitting of some of the major reflections was observed, e.g. for (210) and (012). Morimoto and Clark (1961) observed similar splitting of these peaks in their sulfur rich arsenopyrite sample from Freiberg, Germany. In contrast to their findings, the results reported here show that the splitting of these peaks increases as the As:S ratio increases towards stoichiometry. No splitting of these peaks was observed in the Sheba arsenopyrite sample with the

lowest As:S ratio. As the As:S ratio increases beyond one, the major peaks remain split. There are also differences in the d-spacings of other reflections between the different stoichiometries. The intensities of the $(\bar{1}10)$, (110) and (021), $(0\bar{2}1)$ reflections are reduced in the Mexican and China arsenopyrites compared with the other samples. The intensities of these reflections appear to be a function of site occupancy. In the subsequent Rietveld refinements (Section 3.3.3.4), adjusting the site occupancy parameter increased or reduced the intensities of these reflections in the calculated patterns. The variations in d-spacings of the powder patterns are due to variations in the cell constants which reflect compositional differences.

No characteristic löllingite reflections (2.605, 2.599, 2.37Å) were found in the Panasqugira, Pine Creek or Utah arsenopyrite arsenic rich samples. It is normally difficult to differentiate arsenopyrite and löllingite by optical microscope as their optical properties are similar.

3.3.3.3 Structure Determination by Convergent Beam Electron Diffraction

To supplement the results of the XRD analyses the crystal point and space group were determined from Convergent Beam Electron Diffraction (CBED) patterns, following the method of Steeds and Vincent (1983).

For the space group $P2_1/c$, there are kinematically forbidden reflections for Bragg reflections $0k0 \neq 2n$, due to a 2-fold screw axis in the b direction of the monoclinic unit cell and for reflections $h0l \neq 2n$, as a result of a glide plane perpendicular to b in the c direction. The presence of a glide plane and screw axis in the crystal structure would be seen in a crystal aligned precisely on certain zone axes in a CBED pattern. The condenser aperture used in the TEM was small, and 3D diffraction data in the zero order pattern, in the form of fine lines crossing the zero order Laue zone (ZOLZ), could not be deciphered to determine the difference between glide and screw axis. Consequently, extra information was obtained by analysing the first order Laue zone (FOLZ) individual reflections for symmetry.

Examination of CBED patterns for the Greenbushes arsenopyrite sample at low camera lengths revealed a mirror line in the Kikuchi line arrays and in the diffraction pattern. Tilting along the mirror line revealed no other mirrors in the whole pattern. Examination of diffraction disks in the zero order Laue zone (ZOLZ) revealed dark bands along mirror lines in CBED patterns taken to two major zone axes. The CBED patterns for the major zone axes for Greenbushes arsenopyrite, which where subsequently found to be [101] and [100] in P2$_1$/c were obtained and recorded.

[101] zone axis

Figure 3.12 shows a CBED pattern for a typical [101] zone axis observed in the Greenbushes arsenopyrite crystals. The d-spacings correspond to the b axis and ($10\bar{1}$) values obtained by XRD and recorded in ICDD (International Centre for Diffraction Data) files. In Figure 3.12 the kinematically forbidden reflections (band of negligible intensity within disks) are observed for both the b* direction (2-fold screw axis) and [$10\bar{1}$]* direction (glide plane along c) in the ZOLZ. Examination of the first order Laue zone (FOLZ) indicated a mirror line along the [$10\bar{1}$] direction in the whole pattern. No mirror line was observed along the other direction in the FOLZ. This indicated that the dynamic absences represent a glide plane along the [$10\bar{1}$] direction and a two fold screw axis along b*, which is what is expected for the P2$_1$/c space group. The two fold screw axis was perpendicular to the glide plane.

[100] zone axis

Figure 3.13 shows a CBED pattern of a [100] zone axis for the Greenbushes arsenopyrite. Measurement of d-spacings from micrographs agreed well with the d-spacings of b and c axes from XRD analysis. GM lines are observed orthogonal to each other in ZOLZ patterns with a mirror line observed in the FOLZ along the c* direction.
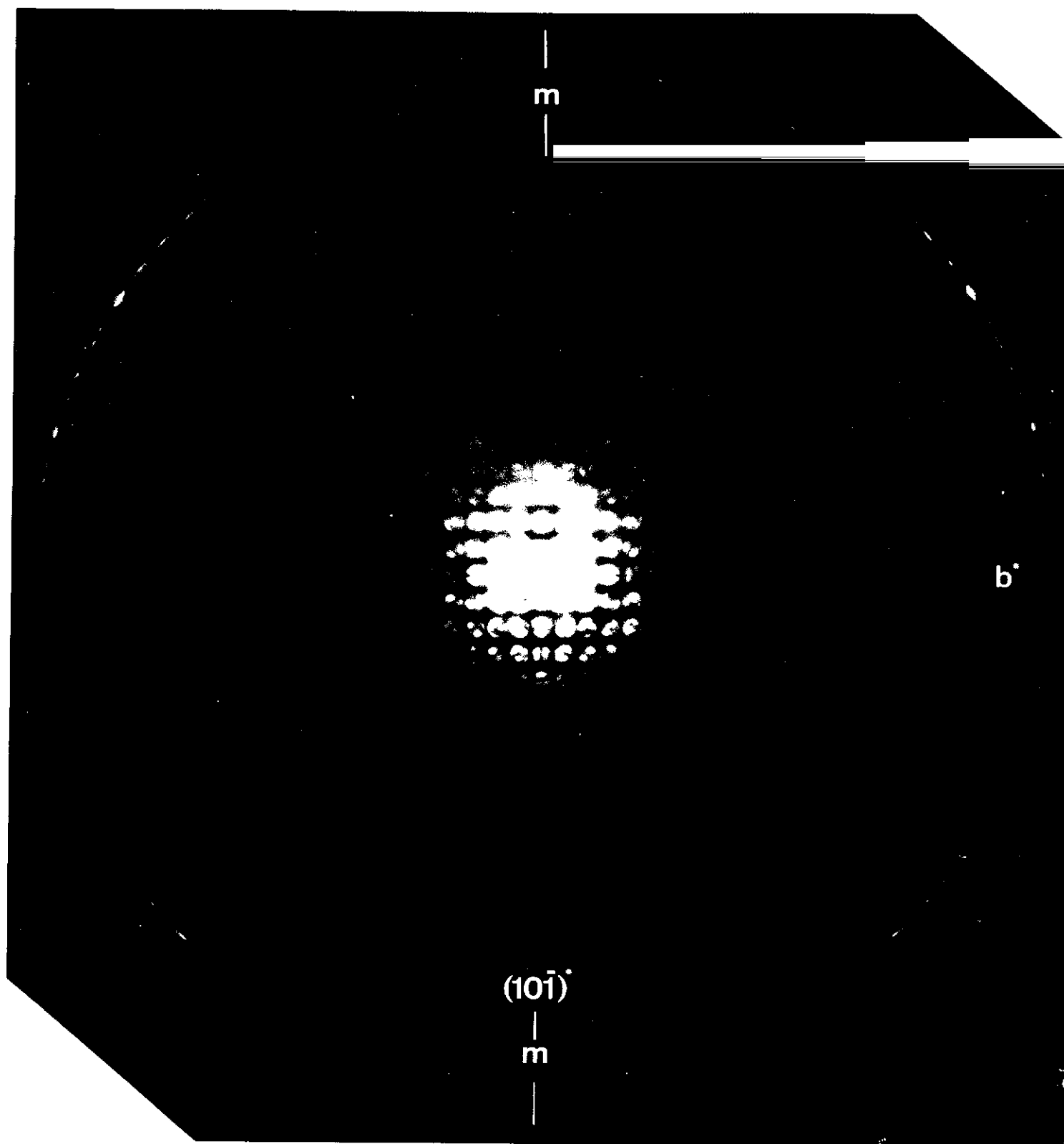
Figure 3.12 Convergent beam electron diffraction pattern of Greenbushes arsenopyrite along the [101] zone axis indicating m symmetry in the whole pattern along the (10$\bar{1}$) in the FOLZ with GM lines orthogonal in the ZOLZ corresponding to a two fold screw axis in the b direction and a glide in the c direction
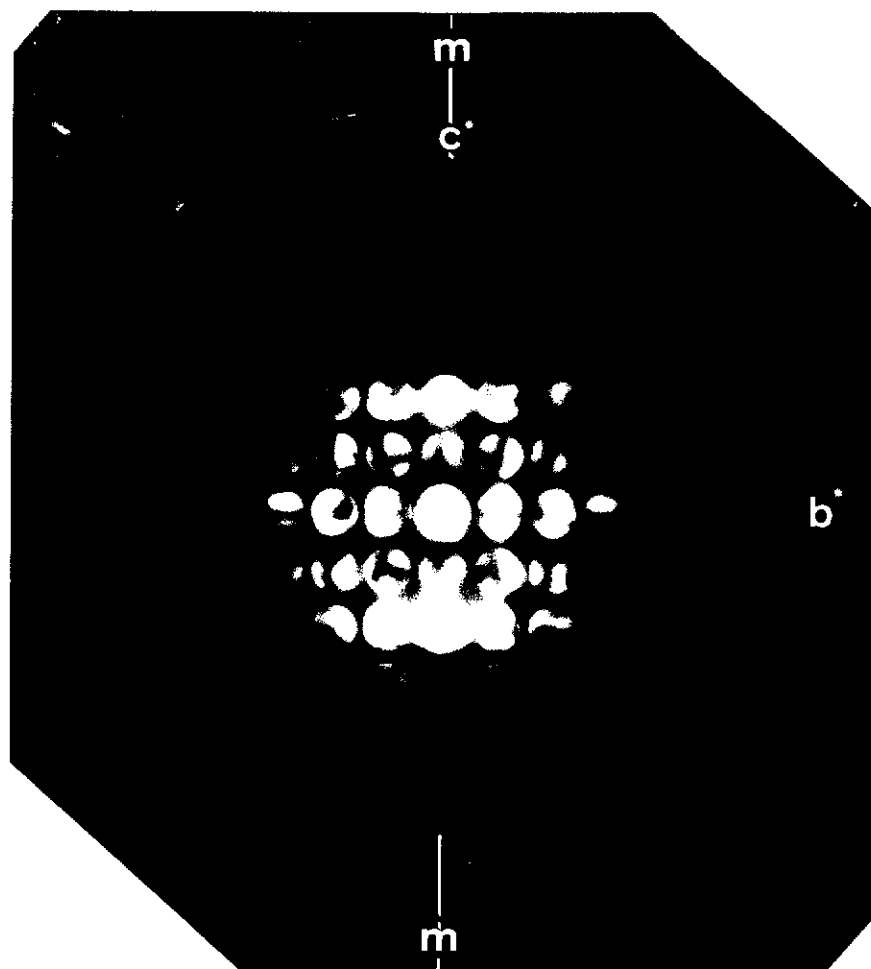
Figure 3.13 Convergent beam electron diffraction pattern of Greenbushes arsenopyrite along the [100] zone axis indicating m symmetry in the whole pattern along the c axis in the FOLZ with GM lines orthogonal in the ZOLZ corresponding to a two fold screw axis in the b direction and a glide in the c direction.

The Greenbushes arsenopyrite crystals adopted a preferred orientation of the [101] zone and observation of the [010] zone was not always possible in many of these crystals. Rotation to other zone axes was also made difficult because the goniometer on the TEM was only able to tilt $\pm 40°$.

CBED patterns of the [001] were not readily attainable. The difference between the a* and c* directions was not readily distinguishable (a = ~5.74, c = ~5.78Å). However in the a * direction GM lines would not be expected as they are in the c* axis.

The CBED patterns of stoichiometric arsenopyrite confirmed Buerger's (1936) hypothesis that the ideal arsenopyrite structure is monoclinic P2$_1$/c.

3.3.3.3.1 Relationship to Marcasite Structure

The structure of arsenopyrite has often been compared to that of marcasite (FeS$_2$). However for the marcasite structure, 2mm symmetry would be seen on major zone axes in the whole pattern and also GM lines in the (001) and (0k0) reflections of the [100] pattern for h and l odd, corresponding to glide planes in its Pmnn structure (Vincent and Pretty, 1985). From the discussion above, the presence of m whole pattern symmetry and a screw axis perpendicular to a glide plane in [101] and [100] patterns confirms the space group P2$_1$/c. The [101] zone in arsenopyrite is equivalent to the [001] of marcasite except for differences in symmetry as a result of arsenic replacing half the sulfur sites. Thus the structure of the Greenbushes arsenopyrite determined here is different to marcasite. The similarities observed in the literature are presumably the result of the presence of twinning (Fuess *et al.*, 1987).

3.3.3.3.2 Comparison of Non-stoichiometric Arsenopyrites by CBED

Clear CBED patterns of nonstoichiometric arsenopyrite generally corresponding to [101] zones were similar to those obtained for Greenbushes over the range of As:S ratios examined and some examples are illustrated below.

Low As:S ratio Arsenopyrite - Sheba and Southern Cross Arsenopyrites

Figure 3.14 for Sheba arsenopyrite shows a [101] zone CBED pattern revealing GM lines in the ZOLZ and a mirror in the whole pattern similar to that observed for the Greenbushes sample. A [100] zone pattern (Figure 3.15) observed by tilting the crystal along the ($10\overline{1}$) direction, revealed GM lines corresponding to the glide along c* and 2-fold screw axis along b* as confirmed in the Greenbushes arsenopyrite. As found with the Greenbushes sample, the [100] zone was not stable under the electron beam for long periods of time even with a cold stage.

Information on structure was not readily obtainable for crystals orientated on the [010] zone (Figure 3.16) and GM lines expected along the c* axis are not readily distinguishable.

Figure 3.17 shows the [101] zone axis pattern of a Southern Cross arsenopyrite crystal also showing similar symmetry to the Sheba and Greenbushes crystals. By tilting the crystal in the direction of the glide (i.e. rotating about the b* axis) to a minor axis (Figure 3.18) the presence of GM lines in the ZOLZ pattern confirmed the existence of the glide and 2-fold screw axis in the arsenopyrite structure. Alternatively, by tilting along the screw axis direction (i.e. rotating the crystal about ($10\overline{1}$)) the GM lines were lost, which indicated that there was no additional symmetry. The results indicate that low As:S ratio arsenopyrite are not triclinic as deduced by Morimoto and Clark (1961).

High As:S ratio Arsenopyrite- Pine Creek and China Arsenopyrite

Figures 3.19 and 3.20 show CBED patterns of the [101] and [100] zones respectively for the Pine Creek arsenopyrite. Similar patterns were seen in the China arsenopyrite crystals. Again the symmetry elements were present.

In comparison of various arsenopyrites, the CBED patterns indicate that the basic monoclinic $P2_1/c$ structure is always present for all stoichiometries.
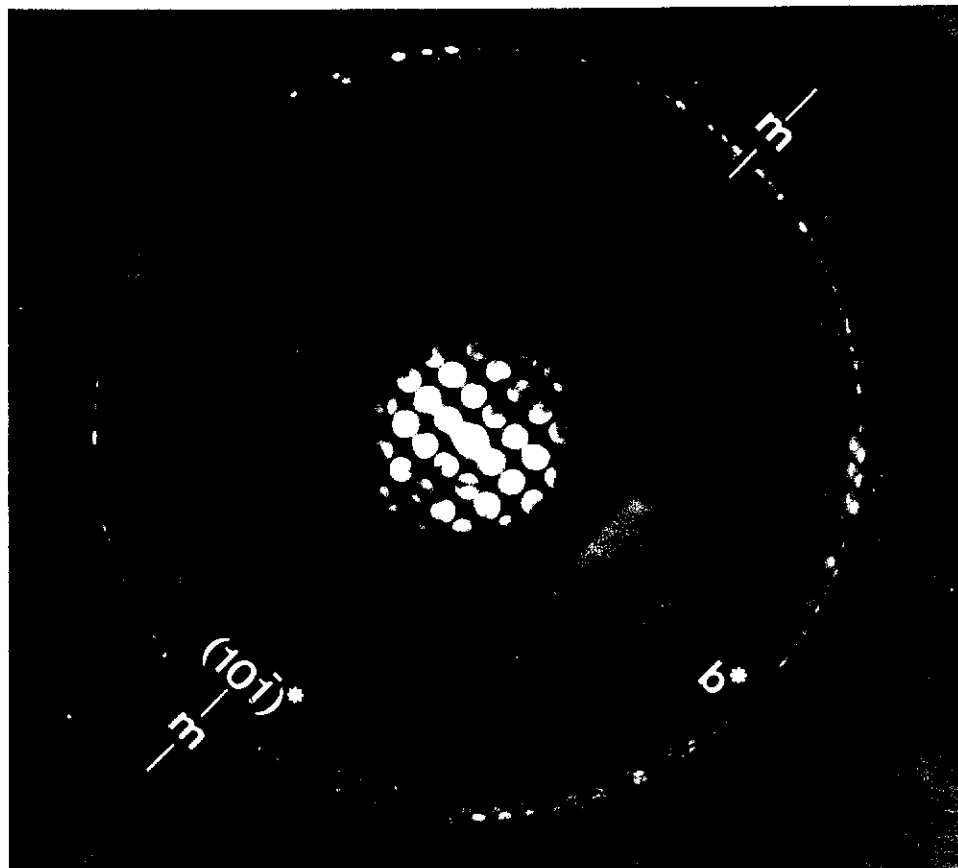
Figure 3.14 Convergent beam electron diffraction pattern of Sheba arsenopyrite along the [101] zone axis. Extinction Conditions are 0k0 ≠ 2n due to a 2-fold screw axis in the b direction of the monoclinic unit cell and for reflections h0l ≠ 2n as a result of a glide plane.
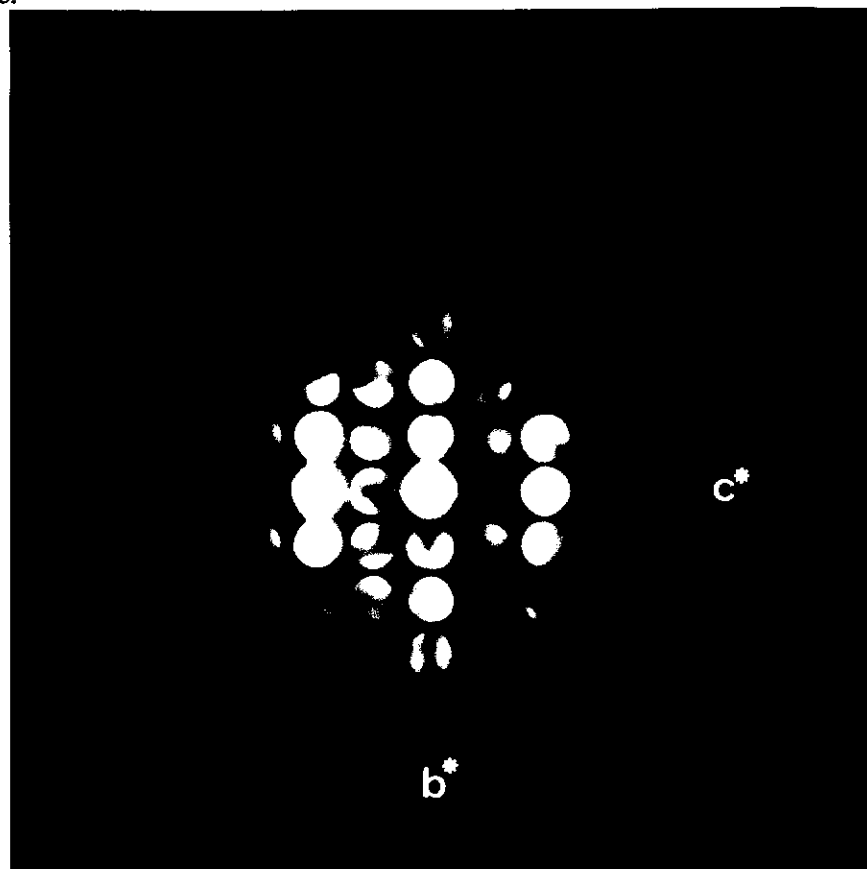
Figure 3.15 Convergent beam electron diffraction pattern of Sheba arsenopyrite along the [100] zone axis. Extinction Conditions are 0k0 ≠ 2n due to a 2-fold screw axis in the b direction of the monoclinic unit cell and for reflections 00l ≠ 2n as a result of a glide plane.
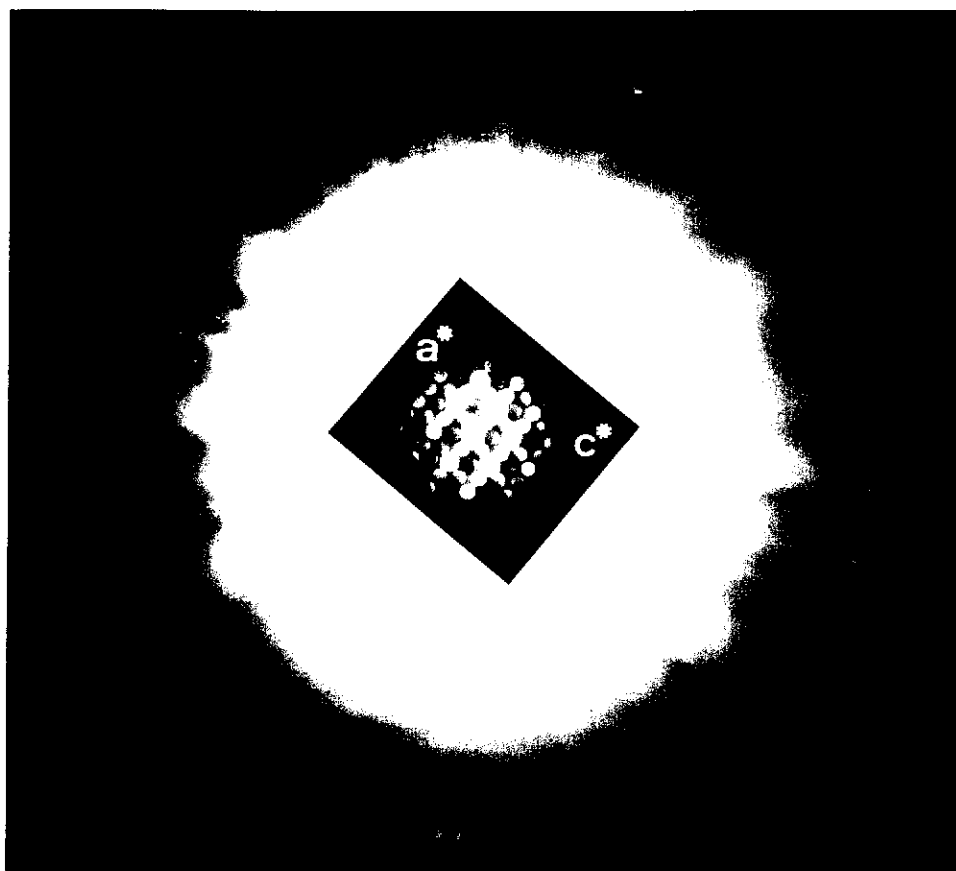
Figure 3.16 Convergent beam electron diffraction pattern of Sheba arsenopyrite along the [010] zone axis.
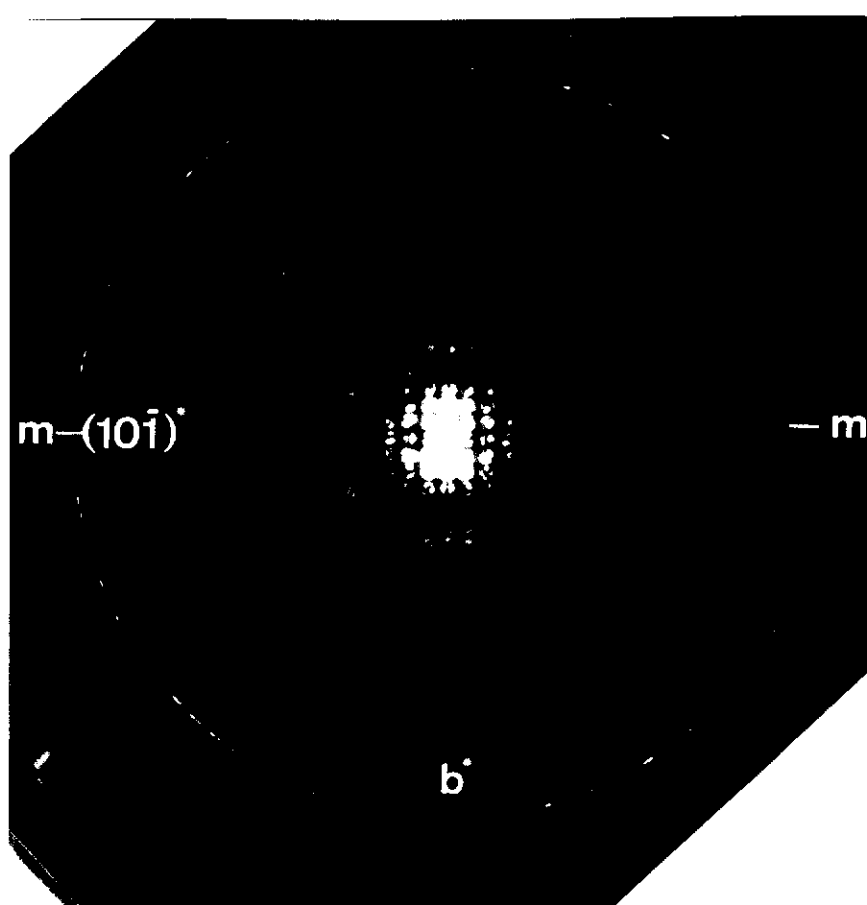
Figure 3.17 Convergent beam electron diffraction pattern of Southern Cross arsenopyrite along the [101] zone axis. Extinction Conditions are $0k0 \neq 2n$ due to a 2-fold screw axis in the b direction of the monoclinic unit cell and for reflections $h0l = 2n$ as a result of a glide plane.
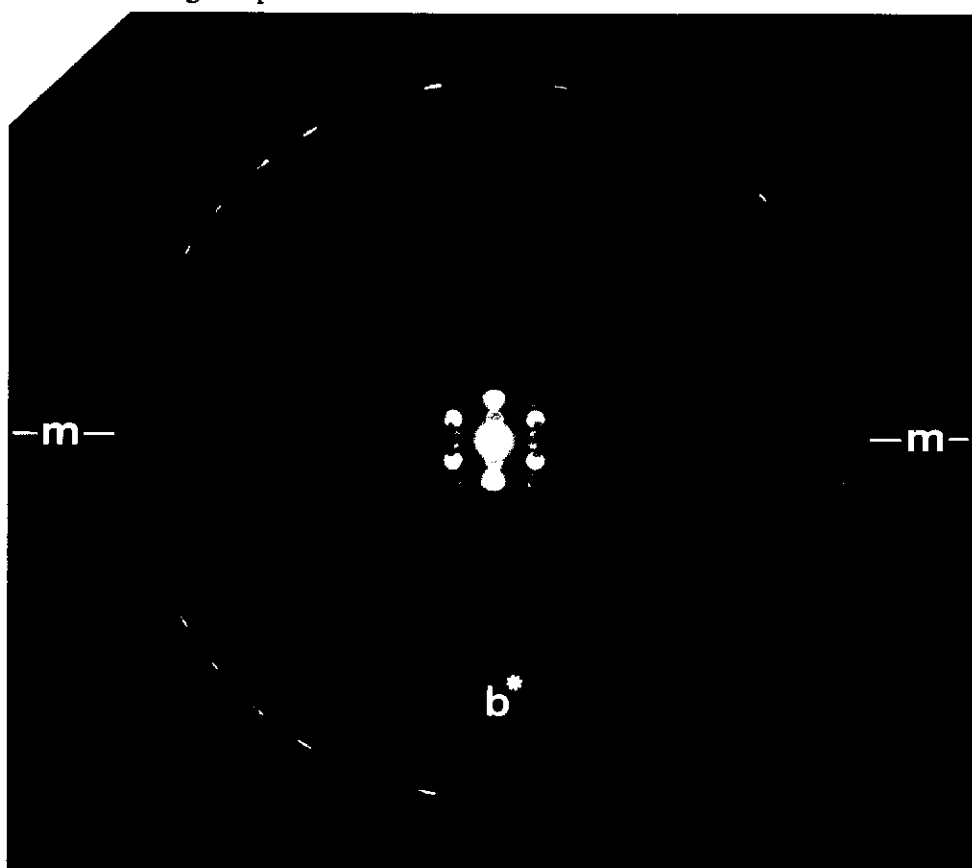
Figure 3.18 Convergent beam electron diffraction pattern of Southern Cross arsenopyrite along a minor zone axis.
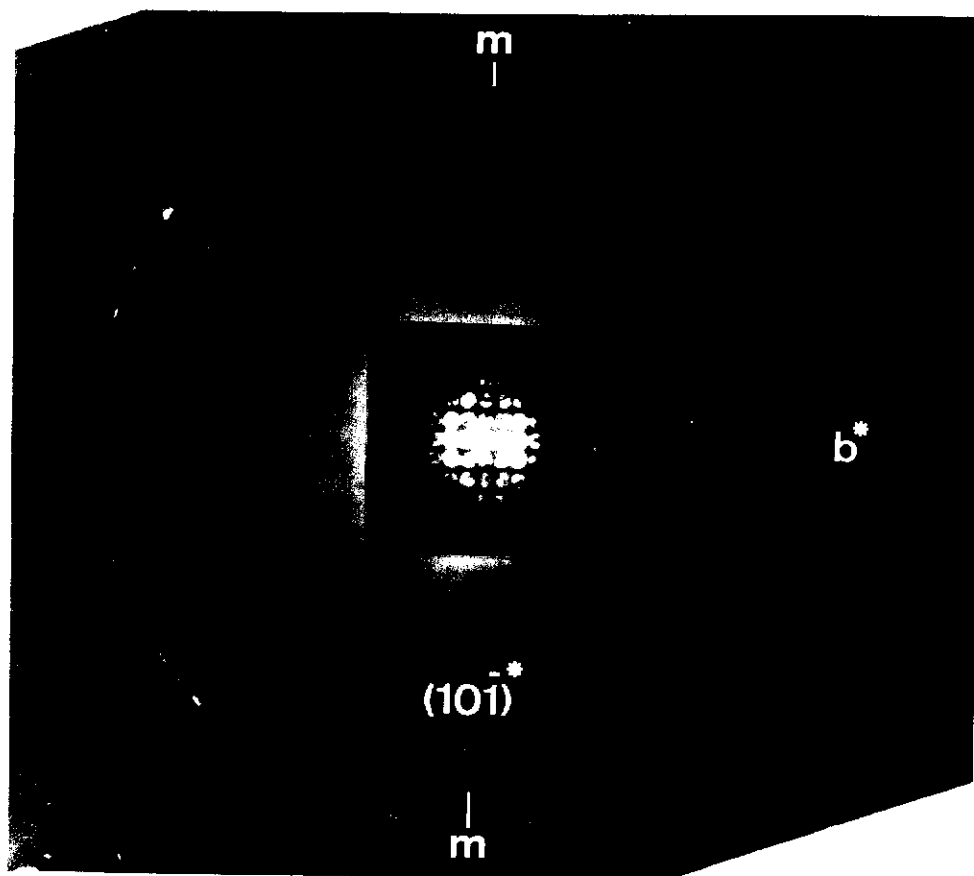
Figure 3.19 Convergent beam electron diffraction pattern of Pine Creek arsenopyrite along the [101] zone axis.
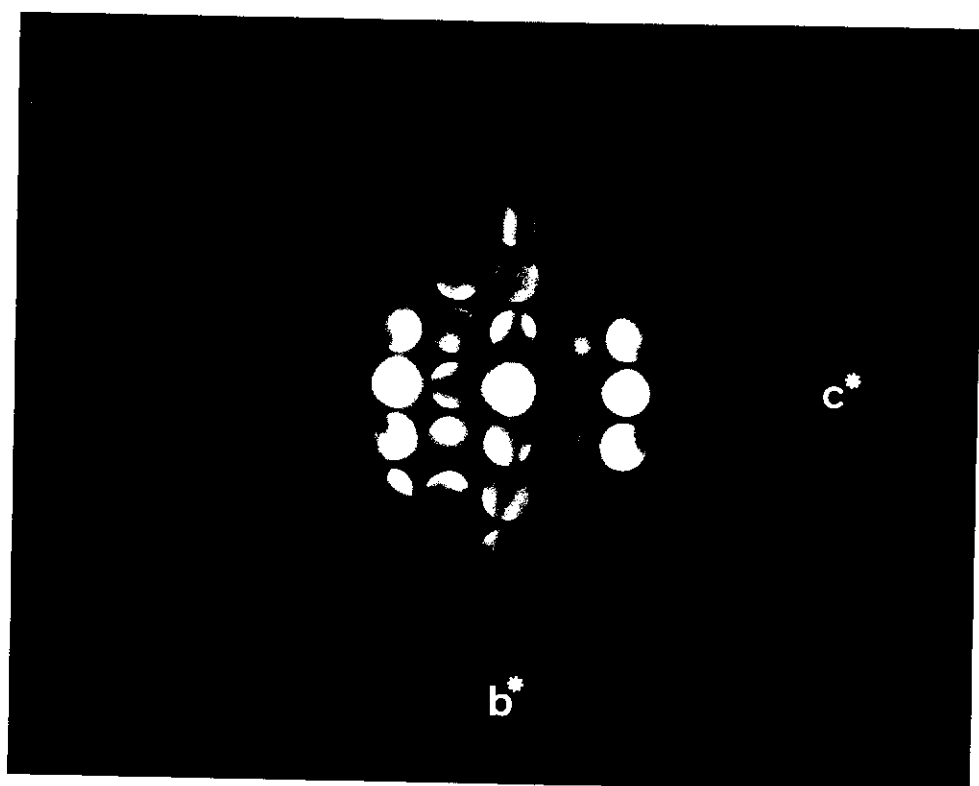
Figure 3.20 Convergent beam electron diffraction pattern of Pine Creek arsenopyrite along the [100] zone axis.

3.3.3.3.3 Distorted CBED Patterns

Deflecting the electron beam on all samples analysed above resulted in the GM lines within the CBED discs moving, indicating some bending in the crystal (Figure 3.21). CBED patterns of the [101] zones showed less distortion than patterns obtained in the [100] zones. The bending appears more of a problem in other zone axes and generally appeared anisotropic. However, in the [100] patterns the bending varied along the c axis. Despite the bending observed in the crystals, the GM lines were confirmed to be real not only because alternate reflections along the systematic line showed the characteristic lines of absence, but also by the presence of a line of absence observed orthogonal to the first line of absence (black cross) for a reflection satisfying the Bragg condition. The bending may be as a result of disorder or strain in the crystal structure.

The distortions observed in some crystals may have resulted from stress produced during sample preparation for TEM studies. Alternatively, they could result from deviations in the structure from the monoclinic setting. The replacement of arsenic on a sulfur site and vice versa may cause either shortening or lengthening of the bond lengths. For example, arsenic replacing sulfur on the sulfur site would increase the bond length between the closest iron atom and the sulfur site because the bond length between an arsenic and iron (~2.40Å) is longer than an iron to sulfur bond length (~2.25Å) in the arsenopyrite structure (Buerger, 1936; Morimoto and Clark, 1960; Fuess et al., 1987). EDS spectra obtained at intervals across crystals in which GM lines were moving showed no major variation in arsenic and sulfur composition. Variations in stoichiometry may however, be different on a finer spatial interval and this requires more investigation. Thus, it is not clear whether the distortions are a result of variation in stoichiometry. The question of the effect of stoichiometry on the structure is discussed later. Twinning observed in arsenopyrite provides a mechanism for interchange of arsenic and sulfur on their sites and perhaps would result in strain or disorder. However no obvious twinned crystals were observed. The effect of twinning is discussed in section 3.3.3.5.
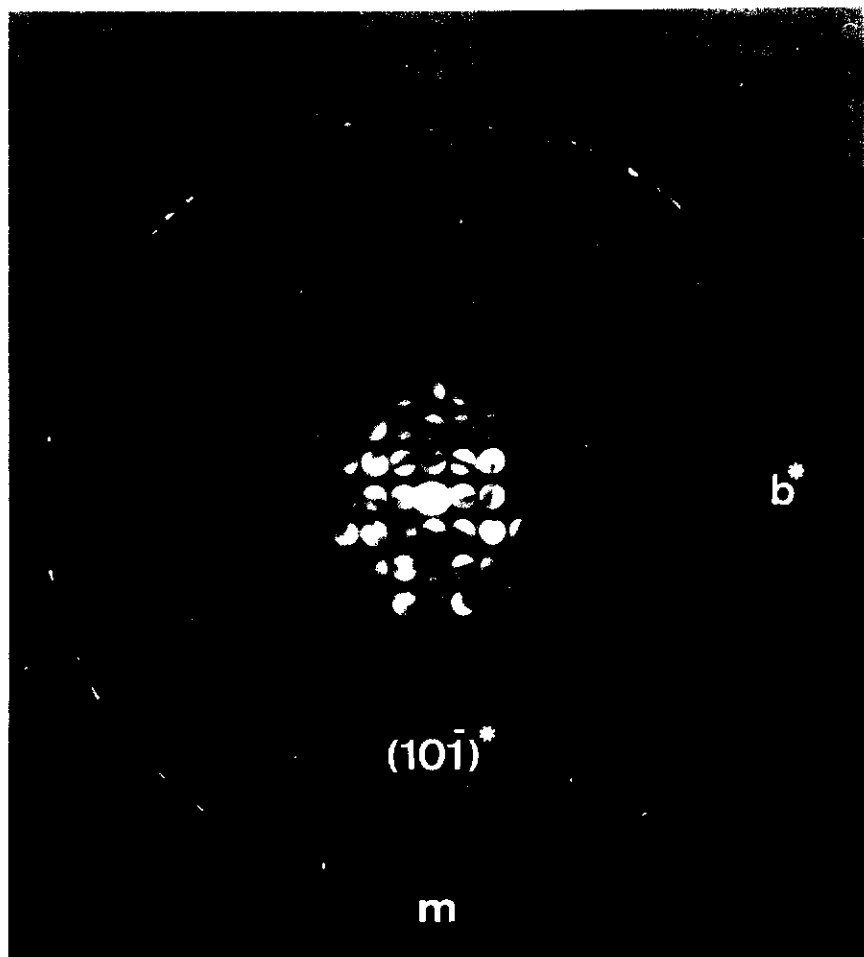
Figure 3.21 A distorted Convergent beam electron diffraction pattern of Sheba arsenopyrite along the [101] zone axis.

Another factor which would contribute to strain or disorder is the geological environment. Arsenopyrite crystals examined in polished sections from some samples (e.g. Sheba) contain crystals which have literally been fragmented as a result of some geological grinding process in the post crystallisation stage. Campa-Vineta (1980) observed twinning as a result of deformation by elastic compliance fractures. This would explain why the strain or disorder observed in CBED patterns of all arsenopyrites is not related to composition.

3.3.3.4 Rietveld Refinements of Arsenopyrite Structures

The structure of Greenbushes arsenopyrite was refined using the Rietveld method on XRD patterns from powdered samples. For the first refinement the unit cell dimension and atomic coordinates obtained by Fuess *et al.* (1987) were transformed (from $C112_1/d$) and used for the space group $P2_1/c$.

The observed, calculated and difference patterns obtained from the Rietveld analysis are shown in Figure 3.22. The results show a good fit with the space group $P2_1/c$, with the refinement resulting in a Bragg-R factor less than 3.0 and profile fits less than 10. The data is collated with the data for other arsenopyrites in section 3.3.3.4.2 and the interpretation is discussed later. The unit cell dimension and atomic coordinates obtained from several XRD patterns recorded and refined by the Rietveld method, were in excellent agreement with each other with only small differences in the values obtained.

3.3.3.4.1 Model of Ideal Structure of Arsenopyrite

Using the Rietveld refined data for Greenbushes arsenopyrite, a model of the structure was made using the program ATOMS. Diagrams showing the ideal structure of arsenopyrite obtained from projection down the [101], [010], [001] and [100] zone axes are shown in Figure 3.23.

For the ideal model each iron atom has six neighbours at the corners of a somewhat distorted octahedron. One face of the octahedron is a triangle of three
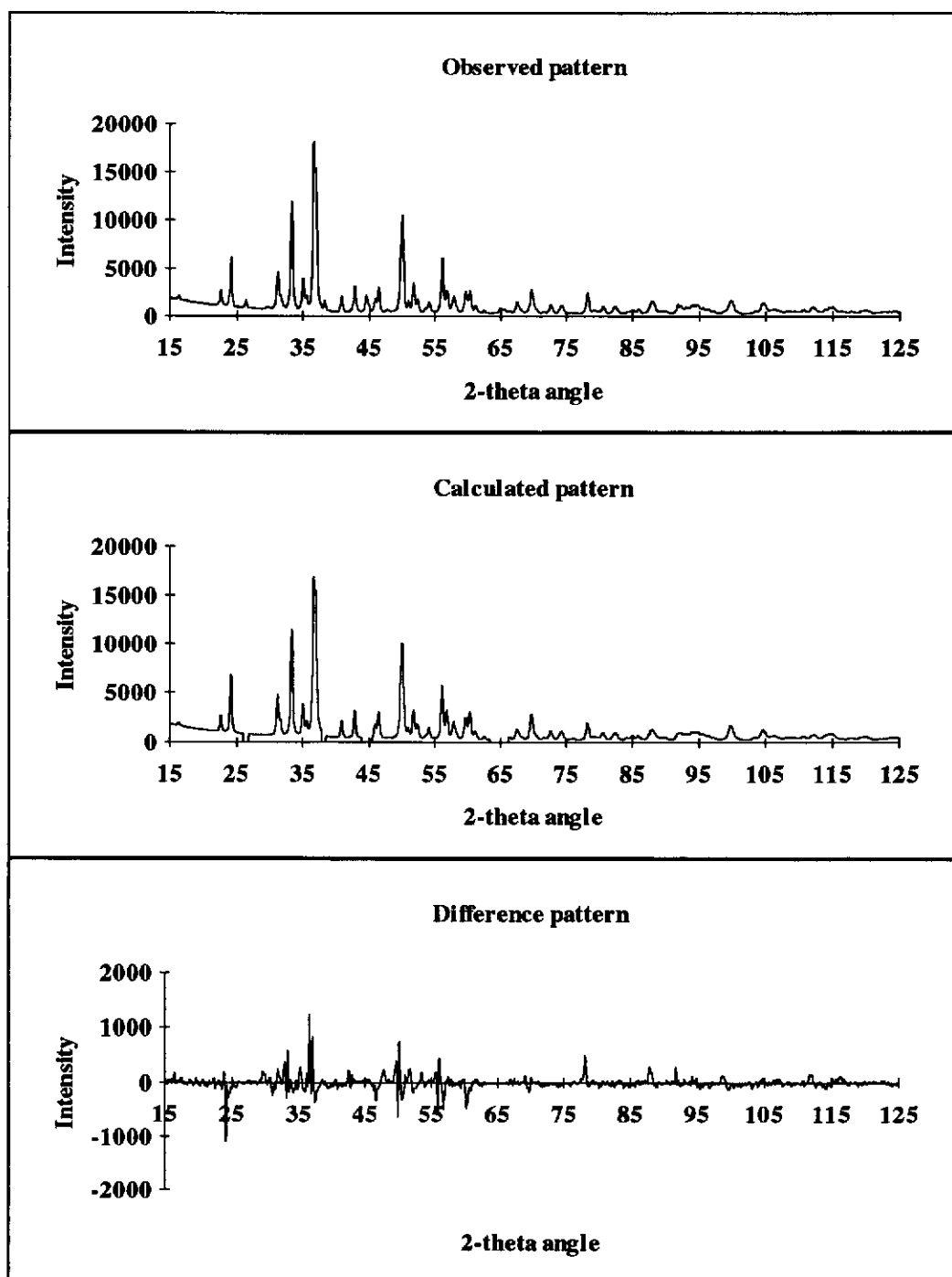
Figure 3.22 X-ray Diffraction patterns of (a) observed, (b) calculated and (c) difference of observed and calculated patterns for Greenbushes arsenopyrite.
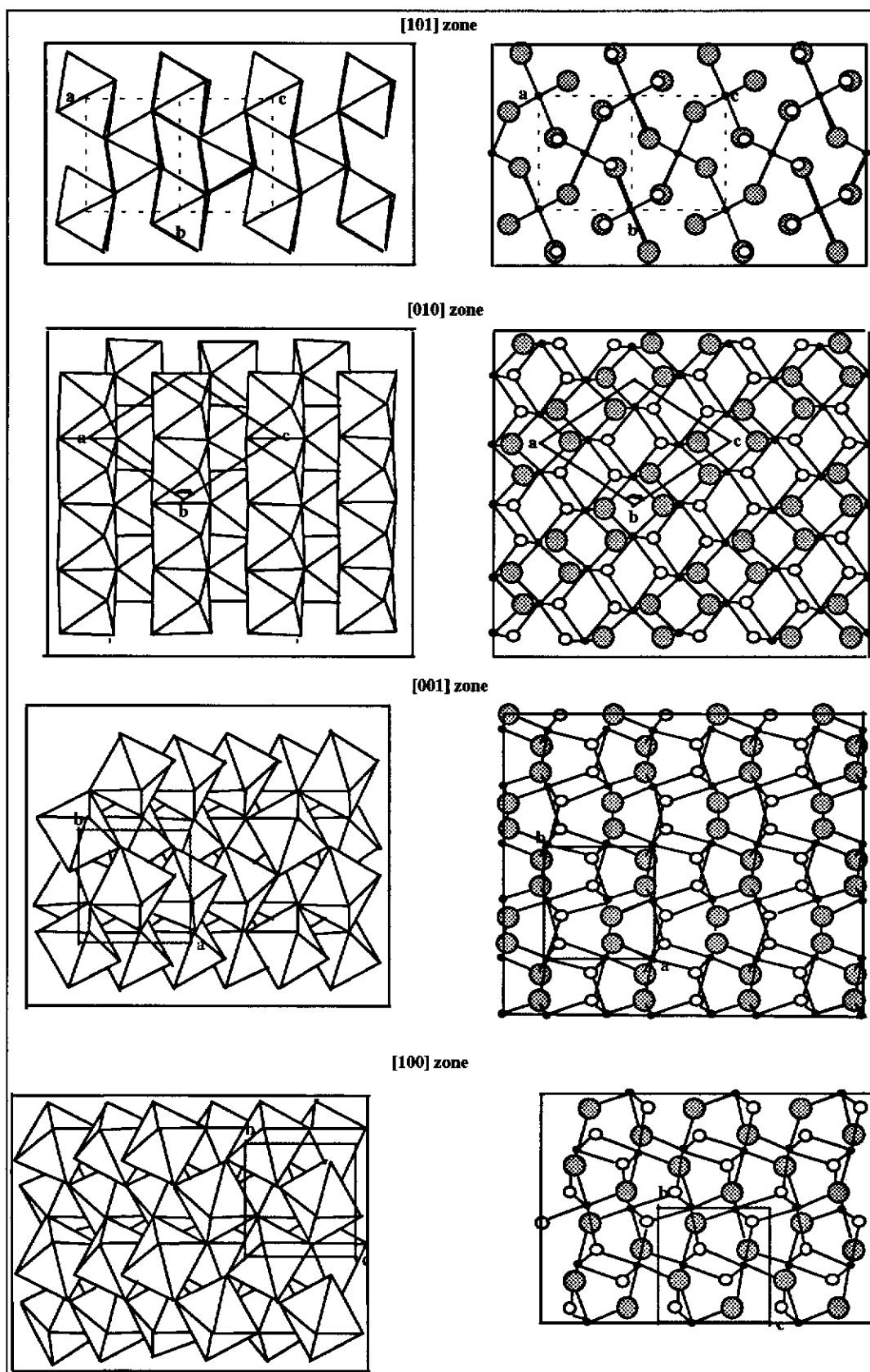
Figure 3.23 The [101,] [010], [001] and [100] zone projections of the ideal structure of arsenopyrite as octahedra model as well as an atoms model. Fe - small black circles, As - white circles, S - large grey circles. The lines correspond to iron to arsenic or sulfur bonding.

arsenic atoms while the opposite face is a triangle of three sulfur atoms. Each octahedron is joined to another along edges in the (101) direction (i.e. into the page for the [101] zone or down the page for the [010] in Figure 3.23). Each chain of octahedra is joined to another by corners. The sulfur atom is surrounded by three iron atoms and one arsenic atom at the corners of a somewhat distorted tetrahedron. In a corresponding manner, the arsenic atom is surrounded by three iron atoms and one sulfur atom at the corners of a somewhat distorted tetrahedron. Thus, the combined CBED patterns and XRD data obtained here confirm Buerger's (1936) hypothesis that the ideal arsenopyrite structure is monoclinic $P2_1/c$. However, this is a simple model of arsenopyrite as experimentally there is interchange of As and S on the As and S sites.

3.3.3.4.2 Comparisons of Non-stoichiometric Arsenopyrite

To facilitate subsequent discussion of likely sites for gold incorporation, the structures of the non-stoichiometric arsenopyrites were then refined using the Rietveld method on the XRD patterns from powdered samples. The data refined were from 2-theta angles $15°$ to $125°$ for the space group $P2_1/c$ using the starting parameters obtained for the Greenbushes arsenopyrite. The final refinement values are illustrated in Figures 3.24 to 3.30 and tabulated in Appendix D. The various agreement indices obtained and refined structural parameters were then compared for possible trend with composition.

Agreement Indices

The agreement between observed and calculated data is shown in Figure 3.24. The results show a good fit with the space group $P2_1/c$ with most refinements containing Bragg-R factors (R_B) less than 3.0 and profile fits less than 10. The profile fit ($R_{expected}$) is based on counting statistics only and is an estimation of the minium R_{wp} obtained for a given problem. For perfect refinement with correctly weighted data, the final R_{wp} would equal $R_{expected}$ and goodness of fit (GOF) would be 1.0 (see Appendix

B for definition of agreement indices). Generally the GOF values achieved (5 to 7) can be considered to be good. Significantly high GOF values occur in systematic errors, instrumental limitations (Hill, 1992) and when not all phases present are taken into account in the refinement. Although every attempt was made to remove impurities, many arsenopyrites contained some inclusions of either quartz, pyrrhotite or pyrite which were refined along with the arsenopyrite. In general, better fits were obtained for sulfur rich arsenopyrites, except for the Mexican arsenopyrite which appeared not to have been modelled as well as the other arsenopyrites.

With the exception of the Mexican sample, the agreement indices obtained support the concept of monoclinic symmetry across the range of arsenopyrite studied.
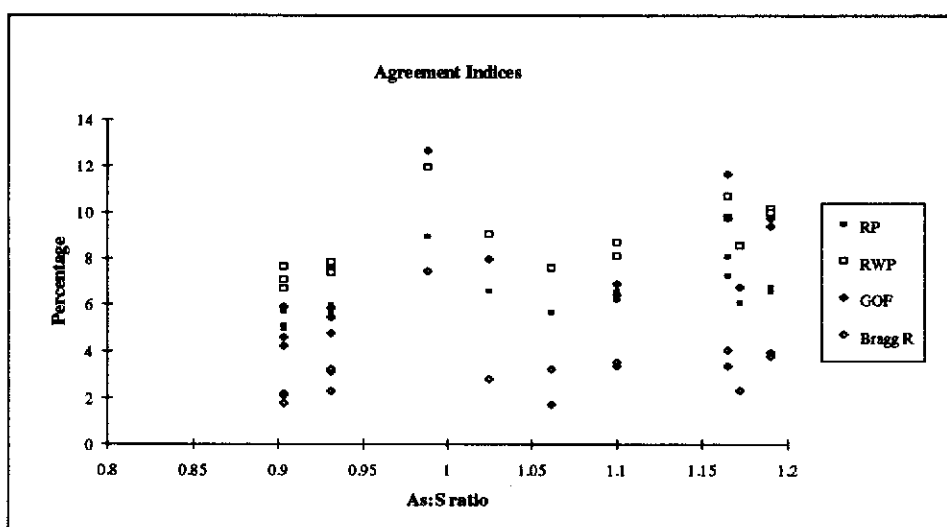
Figure 3.24 Plot of the Rietveld agreement indices versus As:S ratio obtained for all arsenopyrites.

Unit Cell Parameters

Figures 3.25a to c show plots of the unit cell dimensions versus As:S ratio. With an increase in the arsenic to sulfur ratio, an increase in the unit cell dimensions first reported by Morimoto and Clark (1961) is observed. The volume of the unit cell also increases with higher arsenic content. That is, the arsenopyrite structure expands with increasing arsenic replacement of sulfur in the arsenopyrite lattice. An expanded structure could accommodate higher amounts of impurities such as gold
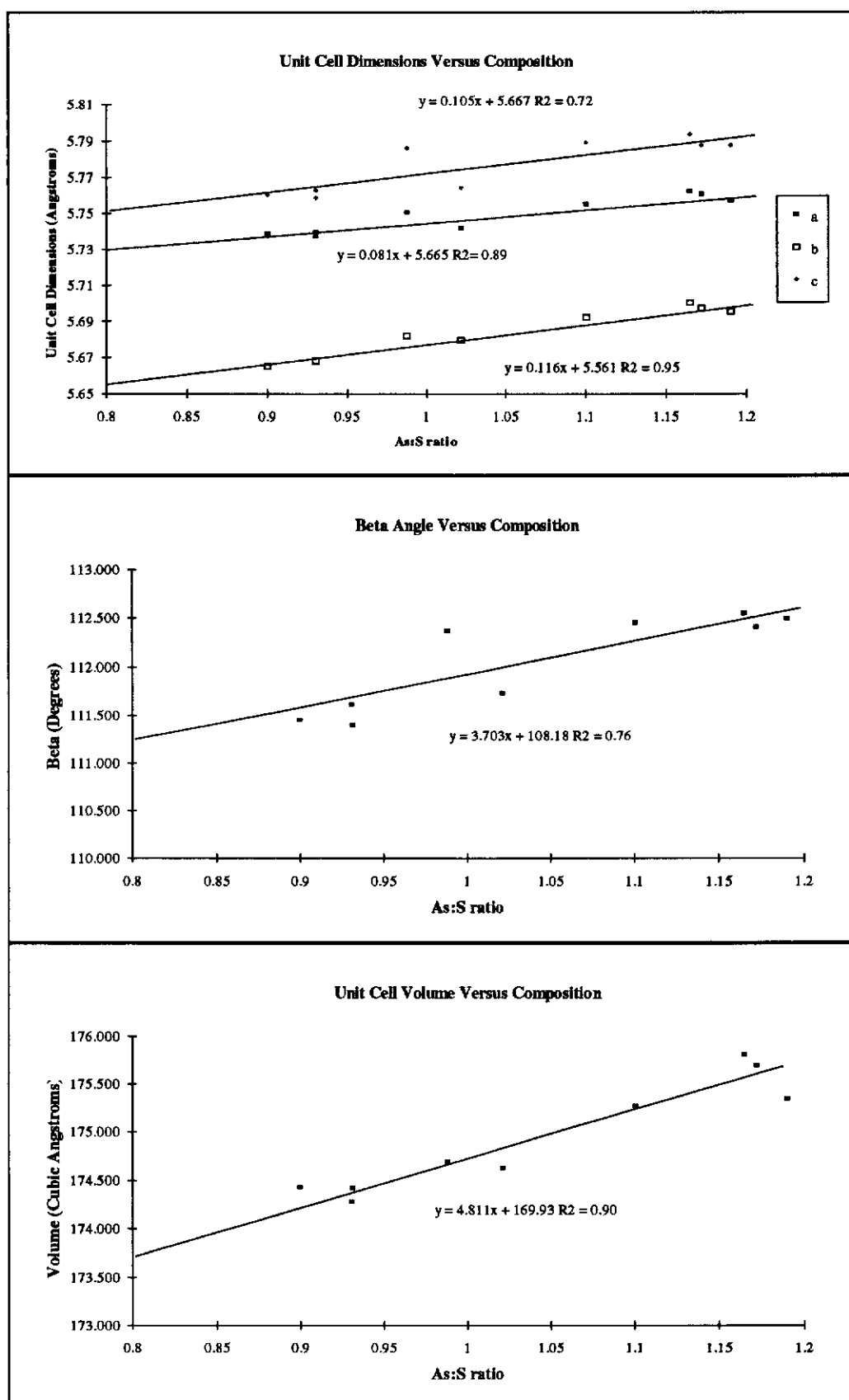
Figure 3.25 The unit cell parameters versus As:S ratio.

The chemical composition obtained for the Mexican arsenopyrite indicates an As:S ratio below 1.0 whereas the crystallographic data from the Rietveld refinement indicates that it should be more arsenic rich than sulfur rich. The deviation of the Mexican samples from the relationship between arsenic content and unit cell dimensions indicates that other factors can influence the structure. This problem is discussed in section 3.3.3.3.

Atomic Coordinates

The atomic coordinates for iron, arsenic and sulfur with variation in stoichiometry are shown in Figures 3.26a to i. Generally there is little variation in the values and the slight scatter represents the error in the Rietveld refinement. No correlation occurs between atomic coordinates and stoichiometry.

Site Occupancy

The interchange of arsenic and sulfur in arsenopyrite has been documented (Morimoto and Clark, 1960; Fuess *et al.*, 1987). The site occupancies for arsenic and sulfur were refined in the Rietveld refinement and generally resulted in an improved fit. The site occupancy values for all the arsenopyrites were less than 1.0 for As and greater than 1.0 for S which is interpreted as indicating a mixed population at both As and S sites. The refinement of site occupancies showed a tendency for more interchange of arsenic and sulfur in the high As:S ratio arsenopyrites as reflected in the lower values of the ratio As occupancy: S occupancy (Figure 3.27). These corresponded to changes in intensity of several reflections in XRD powder patterns in the low angle range with increasing arsenic content as discussed in section 3.3.3.2.1. The difficulty in refining site occupancies is that they correlate with refinement of isotropic temperature factors and large angle ranges of data are required to obtain reliable values for both variables. The range of 10° to 130° two theta used in the refinement was the maximum that could be evaluated using the software available and so the errors in site occupancy determination are somewhat higher. The data point at
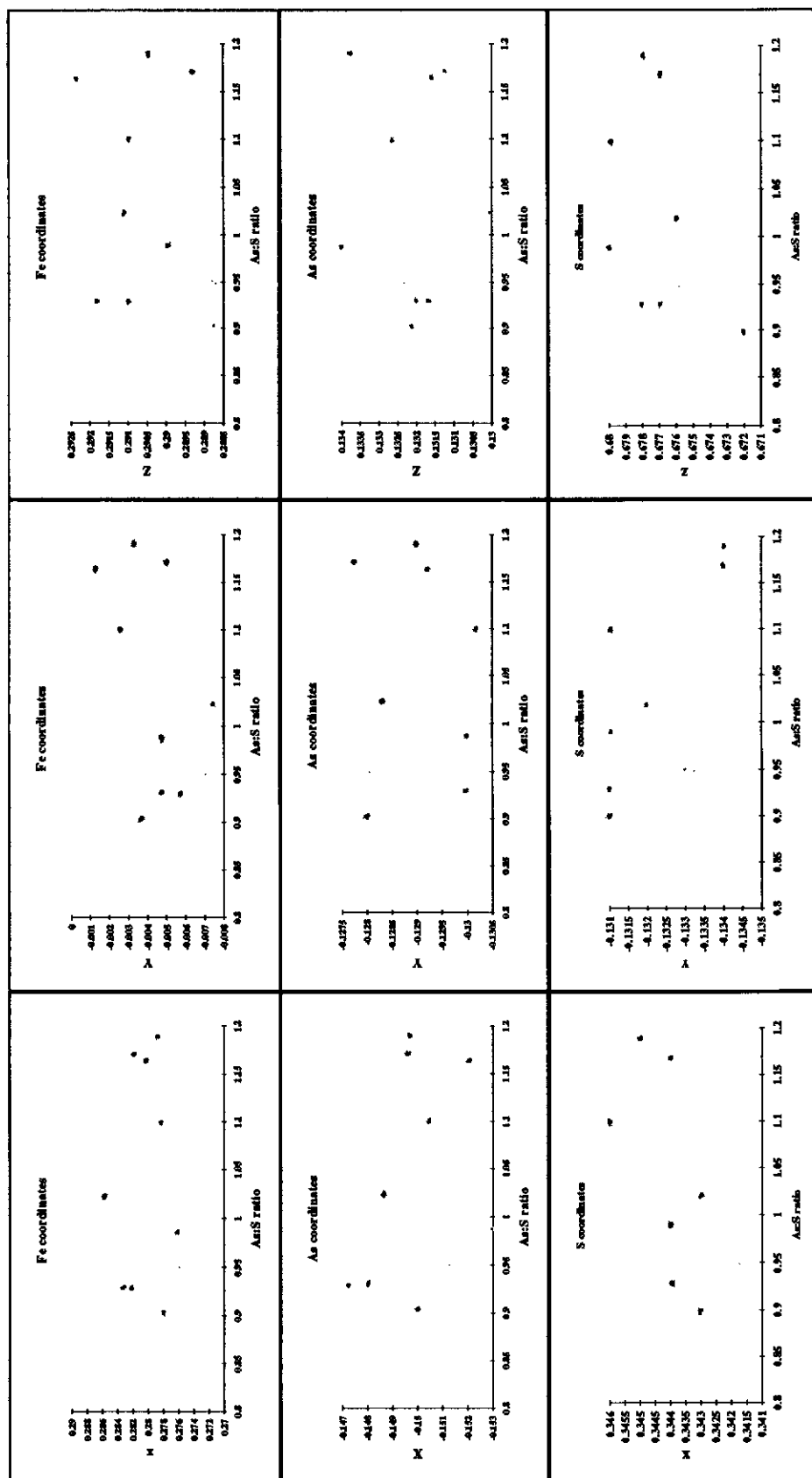
Figure 3.26 Atomic coordinates for iron, arsenic and sulfur with variation in stoichiometry.

0.99 corresponds to the Mexican arsenopyrite, which structure could not be modelled as well as the other arsenopyrites. The Greenbushes sample (1.02) has site occupancy values significantly different from one, indicating interchange of arsenic and sulfur even though the arsenopyrite is close to the stoichiometric formula (FeAsS).
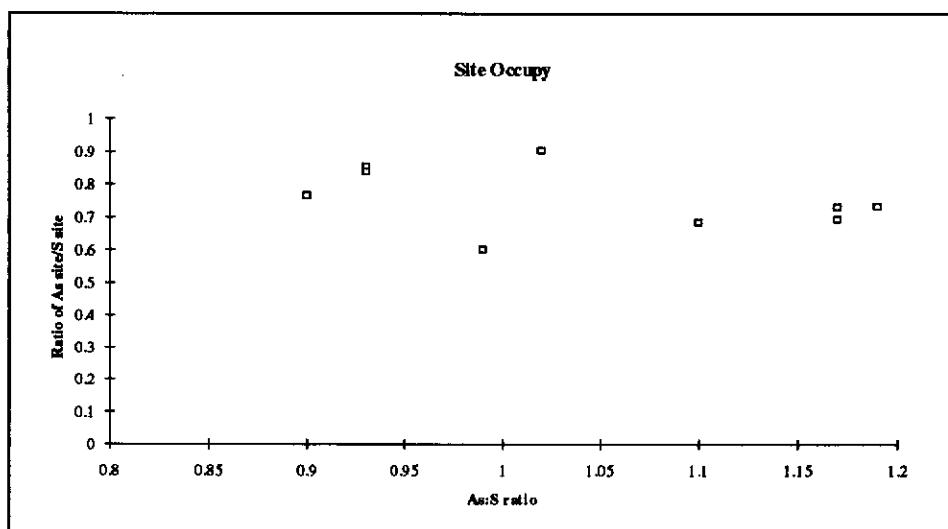
Figure 3.27 Plot of variation of site occupancy ratios versus As:S ratio for all arsenopyrites.

Isotropic Temperature Parameters

The isotropic temperature factors relate to the vibrations of the atoms in the lattice due to heat motion. These were refined separately for iron, arsenic and sulfur (Figure 3.28). The iron generally varied from 0.4 to 0.65Å^2, arsenic from 0.2 to 0.4Å^2, and sulfur from 0.1 to 0.3Å^2. The temperature factors tend to include accumulated errors in refinement and thus are among the least reliable parameters. Possible explanations for variations in values are that some of the sites are disordered and that some sites may not be fully occupied. The bonding in arsenopyrite is covalent.

Thus the charge distribution is not evenly distributed on the atoms. In fact the As and S are strongly bonded. The Fe - Fe interactions influence Fe - S and Fe - As distances and hence the effective radii of arsenic, sulfur and iron. The uncertainty associated with the variety of chemical bonds, variations in crystal chemistry,

stereochemistry and the presence of delocalised bonding in arsenopyrite (Tossell *et al.*, 1981) remains the subject of controversy.
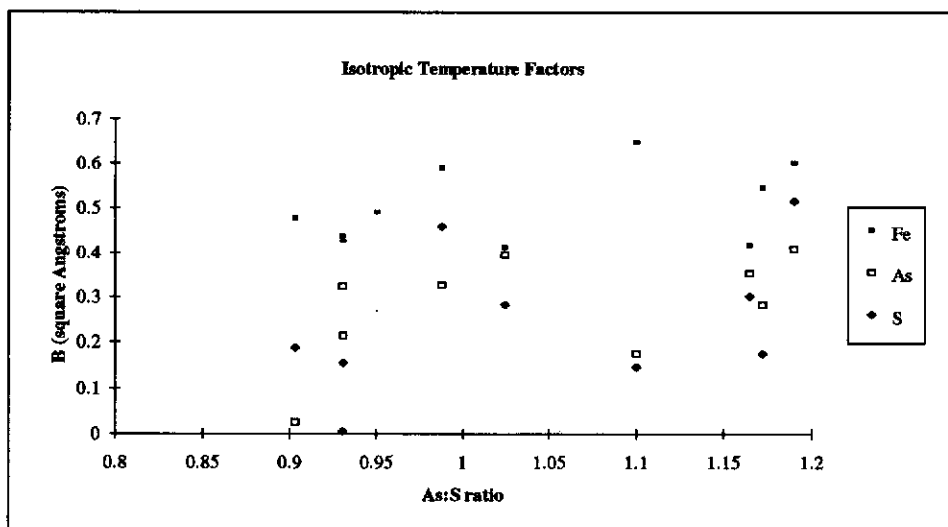
Figure 3.28 Variation of the isotropic temperature parameters determined by Rietveld refinements with As:S ratio for all arsenopyrites.

Profile Parameters

The refined peak shape and peak width parameters can provide information about strain in the arsenopyrite structure. The peak shape of all the arsenopyrites examined tended to be more Lorentzian in character then Gaussian as would be expected for XRD powder data (Hill, 1992). The sulfur rich arsenopyrites tended to have more Lorentzian character than the arsenic rich samples (Figure 3.29). That is, the peaks were broader at the base for sulfur rich arsenopyrites while the arsenic rich arsenopyrites peaks were sharper.

Generally the peak widths for all the arsenopyrites refined were similar and appeared independent of chemical composition (Figure 3.30). The Utah arsenopyrite appeared to be much broader at the high angle than the other arsenopyrites. The Coolgardie and Paddington on the other hand tend to be less broad at the high angle end. The lower values obtained for peak shape for the high As:S ratio arsenopyrites may reflect more disorder in these samples.
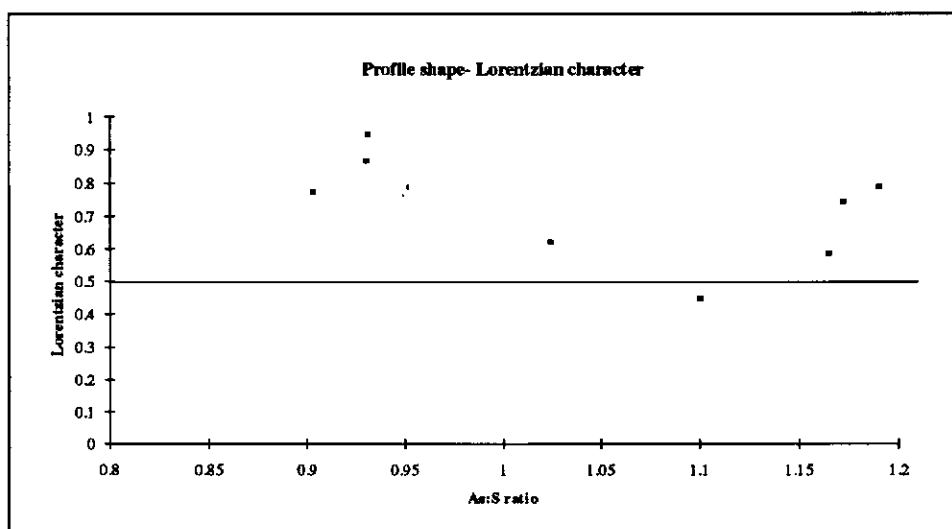
Figure 3.29 Plot of the variation in percent Lorentzian character with As:S ratio for all arsenopyrite analysed by Rietveld.
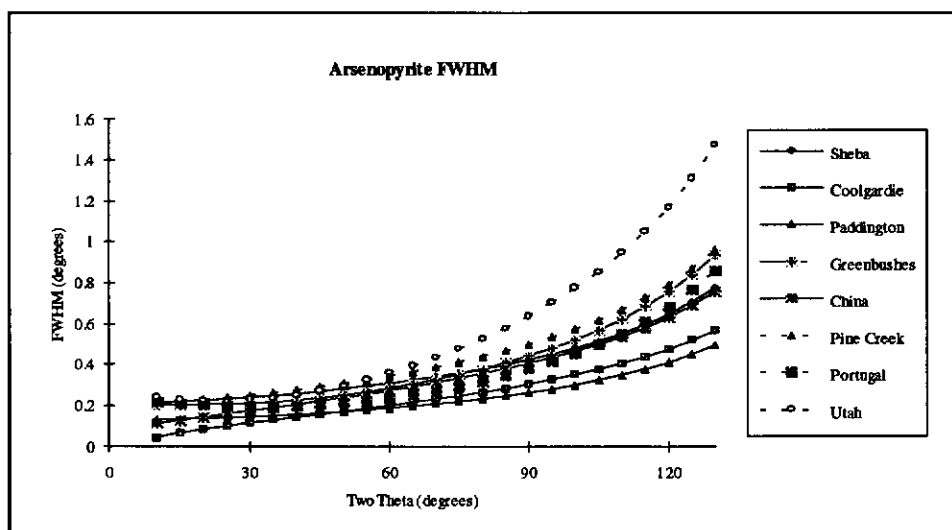
Figure 3.30 Plots of the peak full width at half maximum (FWHM) as a function of diffraction angle calculated from the values of parameters U,V and W in the Caglioti *et al.* (1958) relationship for all arsenopyrites.

Estimation of Errors

One of the problems in the Rietveld analysis is to determine the accuracy of the results and there has been much discussion about the reliability of the estimated standard deviations. The error estimates for Rietveld refinement are correct if counting statistics is the sole source of errors (Prince, 1981, 1985). However, long counting times ensure that errors arising from counting variance are insignificant and the cause of deviation in final structure parameters are systematic errors such as preferred orientation of sample crystallites, inadequate peak shape or atomic structure model, or poor background fit and the presence of unaccounted for phases in the sample (Bakarie and Pawley, 1983). To minimise errors several patterns were obtained and refined. The estimated errors in the structural parameters were taken to be the standard deviations of the results in several patterns. Generally the standard deviations were small (see Appendix D).

In their studies Fuess *et al.* (1987) concluded that their sulfur rich arsenopyrite was monoclinic even though it contained 10% cobalt. Data here also support the conclusion that sulfur rich arsenopyrites are not, as proposed by Morimoto and Clark (1961), triclinic. The deviation of reflections from monoclinic to triclinic structure observed by them, may be attributed to disorder or strain associated with the arsenopyrite structure and the presence of twinning.

3.3.3.5 Arsenic Concentration Determined by X-ray Diffraction Peak Measurements

The d_{131}- spacing taken from the Rietveld refined data as well as measured d_{131}- spacings from the same arsenopyrites containing calcium fluoride as an internal standard, shown in Table 3.4 are in good agreement. In the Sheba, Pine Creek and Utah samples the d_{131}-spacing was masked by the presence of a pyrite 311 reflection and so could not be measured. As a consequence only the Rietveld refined value was obtained. Generally, as expected, the d_{131}-spacing increased as the As:S ratio increased in the arsenopyrite structure. The chemical analysis data obtained by EPMA are also

presented and are, within experimental error, in good agreement with those obtained by XRD measurements. For the Mexican arsenopyrite, the observed and Rietveld refined d_{131} spacing value indicate a sulfur rich arsenopyrite as did the electron microprobe data. However, as indicated earlier the structure refinement indicates larger unit cell dimensions that are more consistent with an arsenic rich arsenopyrite.

Table 3.4 Chemical Composition from measured d(131) spacing				
Sample	As At% from EPMA	Rietveld		Measured with CaF, std
		d-spacing	As At%	
Sheba	31.8±0.8	1.6312	32.59±0.45	-
Coolgardie	32.3±0.6	1.6315	32.85±0.45	1.6320
Paddington	32.2±0.7	1.6313	32.68±0.45	-
Greenbushes	33.9±0.7	1.6332	34.33±0.45	1.6333
China	35.1±0.7	1.6332	34.33±0.45	1.6333
Mexican	33.3±0.3	1.6313	32.68±0.45	1.6319
Portugal	36.3±0.8	1.6337	34.76±0.45	-
Pine Creek	36.1±0.8	1.6347	35.63±0.45	-
Utah	36.0±0.7	1.6348	35.71±0.45	-

Thus, although measurements of the d-spacing of the arsenopyrite (131) reflections and other structure factors agree reasonably well with the expected arsenic composition in arsenopyrite, the results here show that the chemical composition is not the only factor affecting the structure. Close examination of Morimoto and Clark's (1961) data shows that there is some deviation of d-spacing with chemical composition. Their structure information obtained for the Freiberg arsenopyrite (a = 5.744, b = 5.675, c = 5.785Å, β = 112.17°) indicated that this is stoichiometric or arsenic rich whereas their composition and measurement of the d_{131} spacing indicated sulfur rich. They attributed the deviations to fractional impurities in their arsenopyrite sample. However, impurities in the Mexican arsenopyrite constitute less than 1% by weight.

3.3.3.6 Comparison of Bond Lengths and Angles in Natural Arsenopyrites

To facilitate subsequent discussion of likely sites for gold incorporation, the average bond lengths and angles between iron and the surrounding closest three arsenic and three sulfur sites in the ideal monoclinic structure were calculated for all the arsenopyrites refined. Figures 3.31a and b show the projection of the arsenopyrite structure along the [010] and [101] zones indicating the positions of the atoms in the structure referred to in this study. Polyhedra with iron centrally located between the three arsenic and three sulfur sites are superimposed. The top striated triangular face shows the positions of the sulfur sites (S1, S2 and S3) and the bottom striated triangular face shows the positions of the arsenic sites (As1, As2 and As3).

3.3.3.6.1 Bond Lengths

Table 3.5 shows the iron to arsenic and iron to sulfur bond lengths. The bond lengths are similar to those for the iron and arsenic bond lengths found in löllingite ($FeAs_2$) and also similar to those reported in the literature. Generally there appears to be no relationship between the iron and arsenic bond lengths and composition. Except for the Fe to S2 there is no relationship observed between Fe and S bond lengths. The average bond length is similar to that for marcasite and those reported for arsenopyrite in the literature. The replacement of arsenic by sulfur on the sulfur sites does not result in an increase in bond length with increasing arsenic content. There may be some difference, however, since the accuracy in this method is not sufficient to detect small changes. Calculating bond lengths from powder X-ray diffraction patterns is not as accurate as from single crystal studies. Fuess *et al.* (1987) found that the Fe-S distance in their arsenopyrite (2.249Å) was similar to that found in marcasite (FeS_2) of 2.246Å whereas the average Fe-As distance of 2.367Å in arsenopyrite was shorter than the 2.40Å found in löllingite ($FeAs_2$) (Brostigan and Kjekshus, 1970a,b). These differences may be attributed to the high cobalt content of their sample. The Fe to As bond lengths calculated in the present series of arsenopyrites are close to those of löllingite.
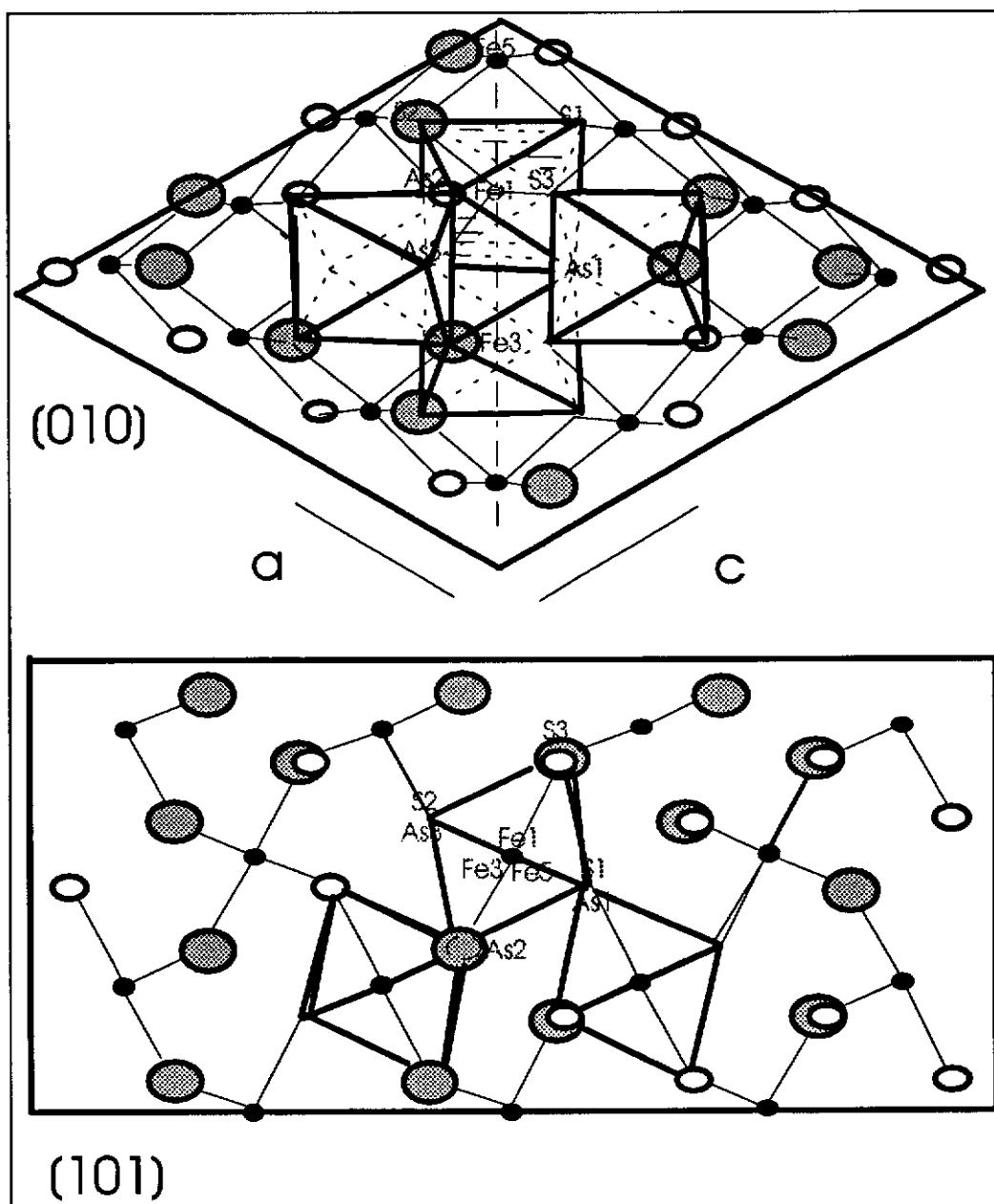
Figure 3.31 Projection of arsenopyrite structure along the [010] and [101] zone axes. The atom positions used in the calculation of bond lengths and angle are also shown. Octahedral units are superimposed. Grey circles are sulfur atoms, white circle are arsenic atoms and the small black circles are iron atoms.

3.3.3.6.2 Bond Angles

The bond angles between arsenic and sulfur sites with respect to the central iron site are shown in Table 3.6. The bond angles are similar to those reported by Fuess *et al.* (1987). Figure 3.32 shows a marked decrease in the S1-Fe-As1 bond angle with increasing arsenic in the arsenopyrite structure. As a result the S1-Fe1-S2 bond angle increased with increased arsenic content (Figure 3.33). The S2-Fe1-As3 bond angle (Figure 3.34) also showed a slight tendency to decrease with increasing arsenic content, however the data obtained from the Mexican arsenopyrite sample do not follow this trend. There appeared to be no detectable relationship for any of the other bond angles.

The results indicate a slight compression of the octahedra as a result of the shift in the S1 atom position in each octahedron, mainly along the (101) direction. A plot of the octahedra volume versus arsenic to sulfur ratio (Figure 3.35) shows that the slight contraction of the octahedra in the (101) direction does not markedly affect the volume of each octahedron.

3.3.3.6.3 Inter Octahedral Distances

The distances between the Fe atoms along the (101) direction were also calculated. These distances corresponding to Fe1-Fe3 (longest) and Fe1-Fe5 (shortest) are marked in Figure 3.31. In this direction the Fe atom distance alternates between being short and long (see section 2.3.1). In Figures 3.36a and b the differences between the short and long distances respectively are plotted against variation in As:S ratio. In both figures the scatter of the data indicates no relationship, although there tends to be a slight decrease in the Fe1-Fe3 distances with increasing arsenic content in the (101) direction. Excluding the Mexican value would enhance this trend. It could be expected that as more arsenic is included in the structure the distance would approach that between iron to iron in the löllingite (FeAs$_2$) structure, that is, the longest iron to iron distance would approach the same length as the

Table 3.6 Bond Angles for Arsenopyrites

Sample	Sheba	Coolgardie	Paddington	Greenbushes	Mexican	China	Pine Creek	Portugal	Utah
As1-Fe									
-As2	89.37±0.06	88.67±0.06	88.40±0.10	87.93±0.06	89.95±0.07	89.73±0.06	88.80±0.28	89.40±0.01	90.70±0.28
-As3	79.70±0.61	78.77±0.23	78.37±0.06	78.27±0.06	81.20±0.28	80.60±0.10	79.80±0.14	80.53±0.06	80.60±0.28
S1-Fe									
-S2	101.93±0.15	103.20±0.01	103.90±0.10	104.10±0.20	103.80±0.01	104.50±0.10	104.35±0.07	104.20±0.17	104.35±0.07
-S3	89.30±0.26	89.83±0.92	89.67±1.07	90.37±1.53	89.85±0.35	90.63±0.67	90.25±0.07	89.97±0.12	89.50±1.27
As2-Fe									
-As3	84.88±0.08	84.10±0.01	83.93±0.06	83.93±0.06	85.10±0.42	84.82±0.13	84.88±0.11	84.83±0.15	86.35±0.49
S2-Fe									
-S3	94.83±0.32	95.33±0.25	95.50±0.26	96.33±0.06	93.85±0.07	94.00±0.17	95.50±0.28	94.57±0.12	94.20±0.42
S1-Fe									
-As1	93.10±0.26	92.97±0.06	92.87±0.15	92.57±0.06	92.50±0.14	92.37±0.12	91.90±0.14	91.93±0.12	91.50±0.42
-As2	92.90±0.20	92.57±0.06	92.30±0.10	91.83±0.12	93.25±0.21	92.80±0.17	92.95±0.64	93.53±0.23	94.55±0.78
-As3	172.17±0.23	171.00±0.17	170.67±0.23	170.10±0.01	173.45±0.35	172.57±0.23	171.50±0.01	172.20±0.17	171.15±0.49
S2-Fe									
-As1	164.73±0.23	163.57±0.12	163.03±0.12	163.23±0.12	163.60±0.14	162.77±0.12	163.70±0.01	163.63±0.12	164.20±0.01
-As2	91.97±0.12	92.50±0.10	92.63±0.15	91.97±0.12	91.65±0.21	92.53±0.06	91.45±0.49	91.90±0.01	93.50±1.56
-As3	85.57±0.21	85.20±0.26	84.93±0.15	84.10±0.17	82.65±0.35	82.63±0.15	83.95±0.07	83.40±0.17	84.40±0.57
S3-Fe									
-As1	82.77±0.23	82.30±0.17	82.17±0.15	82.53±0.06	83.35±0.21	82.70±0.10	82.75±0.49	82.90±0.10	80.40±0.57
-As2	171.50±0.40	170.67±0.23	170.30±0.17	170.10±0.01	172.35±0.49	172.17±0.23	170.80±0.01	171.77±0.23	170.25±0.21
-As3	90.50±0.26	91.33±0.25	91.43±0.12	91.43±0.06	90.65±0.49	91.57±0.12	90.20±0.19	90.63±0.06	88.70±0.57
Fe5-S1-Fe3	78.00±0.14	76.70±0.14	76.03±0.04	75.80±0.14	76.30±0.10	75.50±0.01	75.70±0.47	75.90±0.01	75.85±0.35
Fe3-As1-Fe1	100.65±0.07	101.40±0.14	101.65±0.07	101.75±.07	99.00±0.35	99.45±0.07	100.30±0.01	99.55±0.07	99.65±0.07
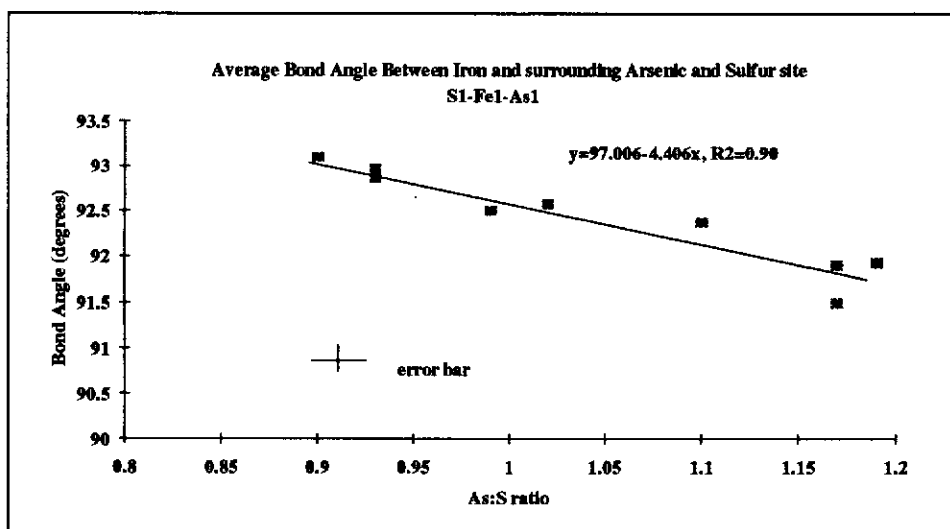
Figure 3.32 Bond angle between iron and surrounding arsenic and sulfur sites.
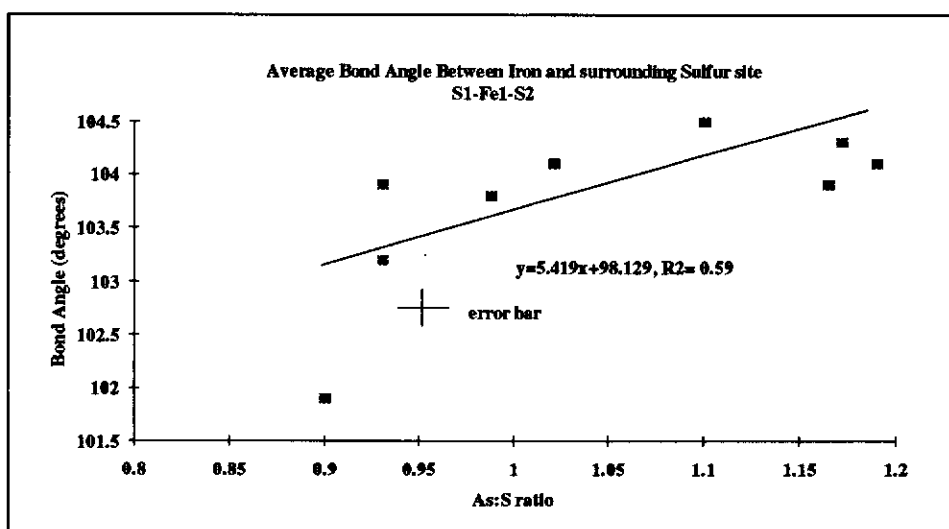
Figure 3.33 Bond angle between sulfur site and iron.
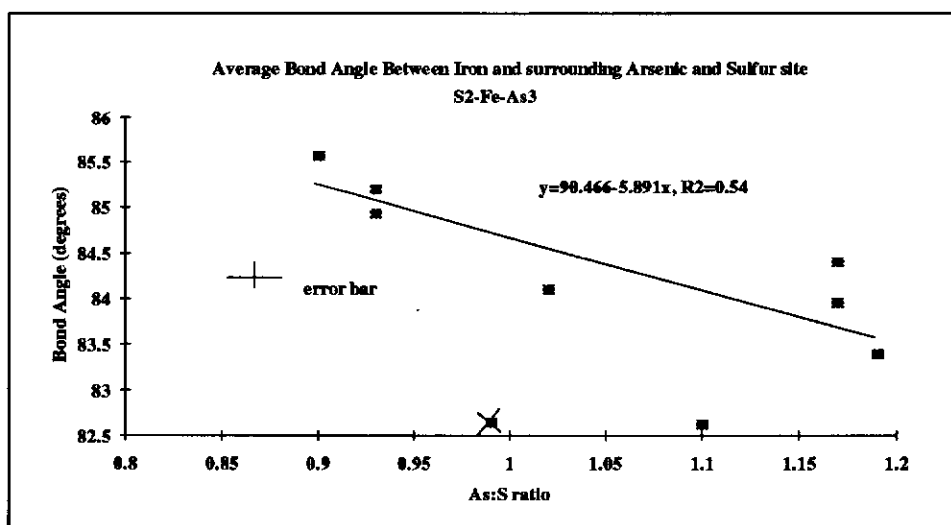
Figure 3.34 Bond angle between arsenic and sulfur sites to iron. Equation of line does not include the point marked with a cross which corresponds to the Mexican arsenopyrite.
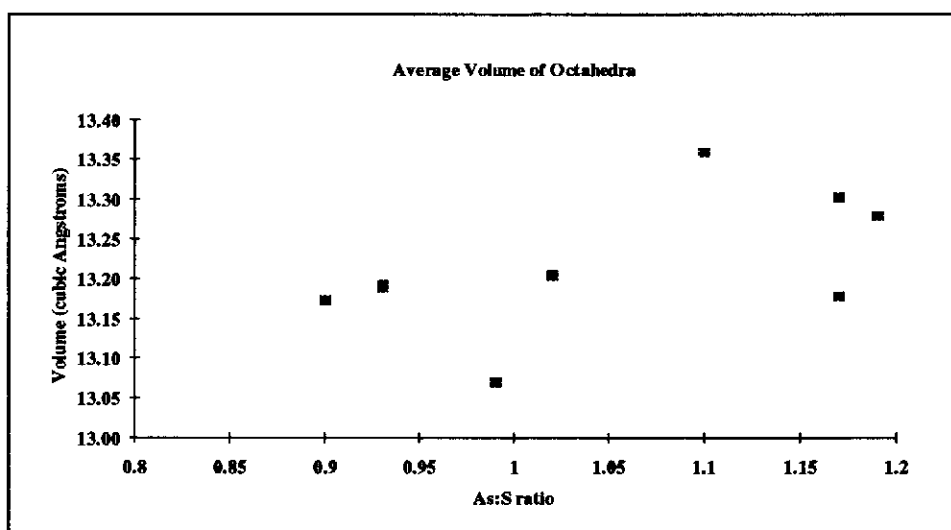
Figure 3.35 Average volume of octahedra in arsenopyrite structure.
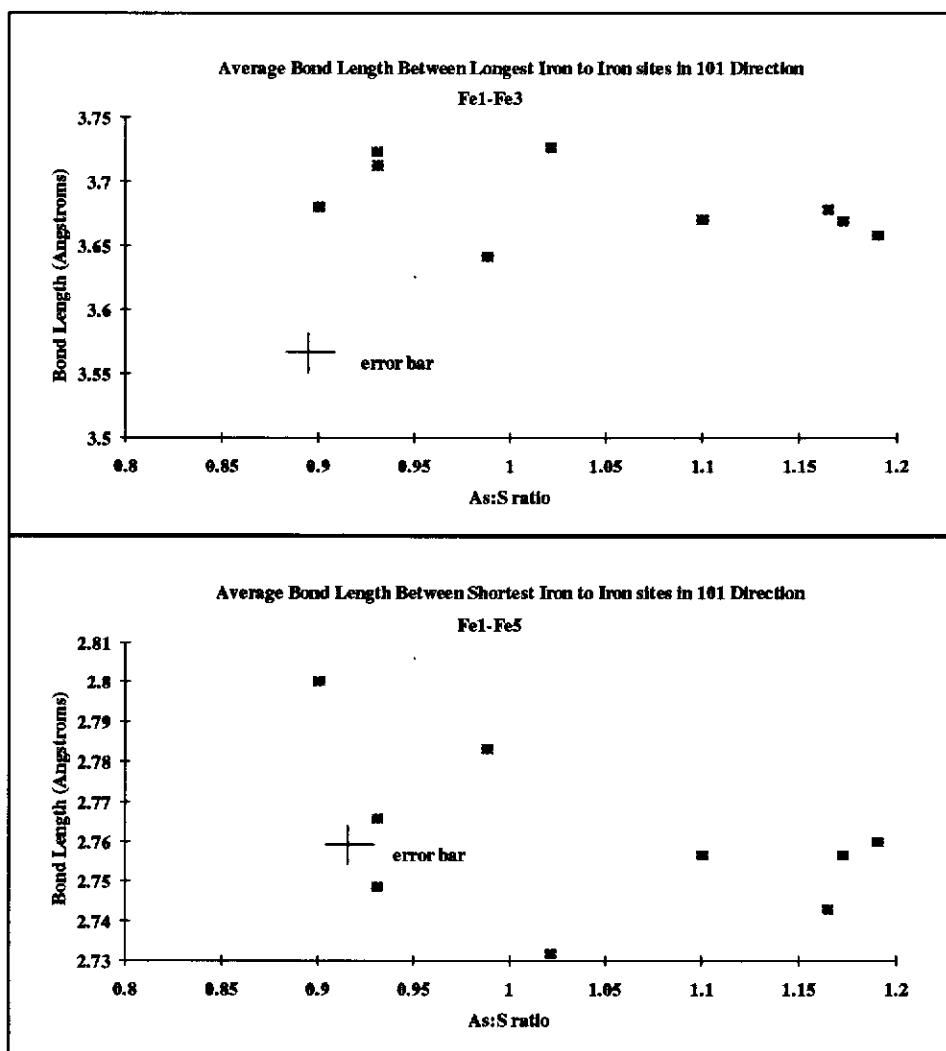
Figure 3.36 The relationship between the (a) long Fe1-Fe3 and short (b) Fe1-Fe5 distances are plotted respectively against variation in As:S ratio.

shortest distance in arsenopyrite. No obvious trend appeared to exist. The iron to iron angle with either arsenic or sulfur at the origin, showed a slight tendency for a decrease in angle with increase in arsenic content (Table 3.6, angles Fe5-S1-Fe1 and Fe3-As1-Fe1). The shift in these angles is a result of a shift in the S1 and As1 atoms positions rather than change in the Fe1 or Fe5 positions.

To determine what effect increased arsenic incorporation in the arsenopyrite structure had on the spaces between the octahedra, the distance across the arsenic and sulfur from one octahedron to the next was also calculated. These lengths are plotted against the As:S ratio in Figure 3.37. With an increase in arsenic content the distance between the arsenic and sulfur site increases slightly. These results indicate that the angle between the octahedra is enlarged. The average distance between As and S is normally 2.33Å while for As to As in löllingite it is 2.45Å. The incorporation of As into the S site has resulted in expansion between the octahedra. A plot of the volume of the gaps between the octahedra showed no significant changes.
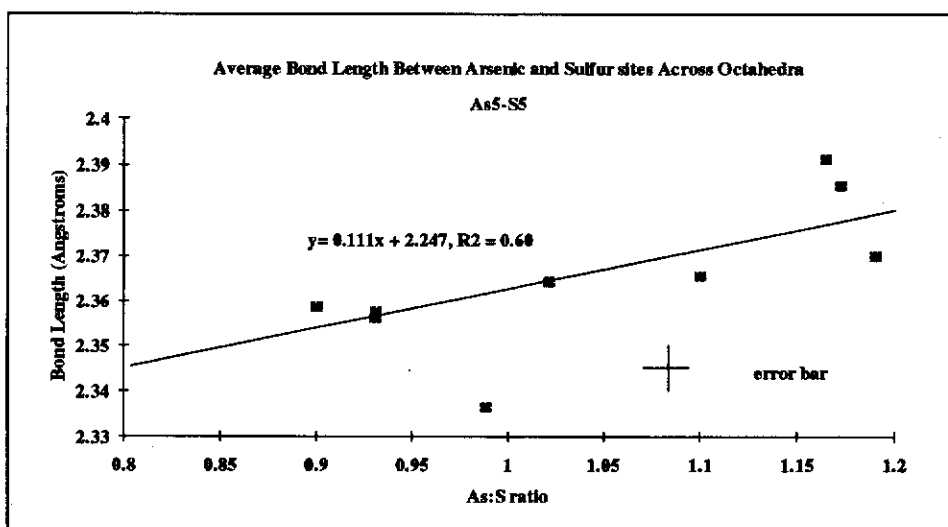
Figure 3.37 A plot of As:S ratio against the distance arsenic - sulfur from one octahedron to the next.

To confirm the slight decrease in the (101) and expansion in the (10-1) directions, the d_{202}-spacings and d_{20-2}-spacings were plotted against composition. Figures 3.38a and b show a decrease in the d_{202}-spacings and an increase in the d_{20-2}-

spacings with increasing arsenic content in the arsenopyrite structure respectively as expected.
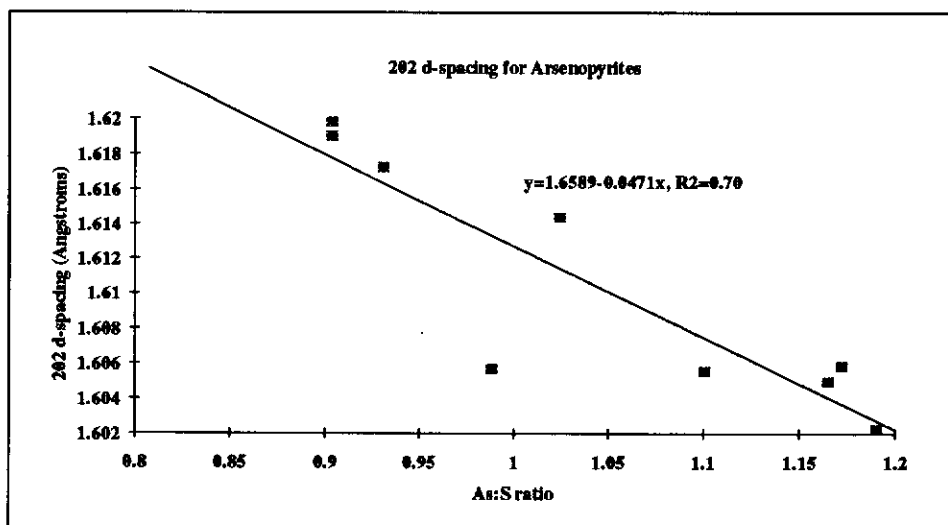
(a)
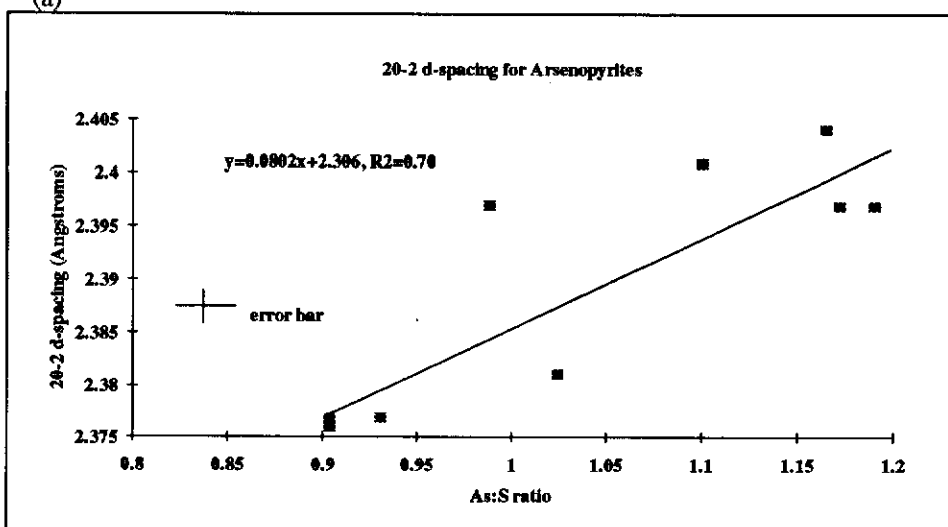
(b)

Figure 3.38 Plots of measured (a) d_{202}-spacings and (b) $d_{20\bar{2}}$-spacings against arsenic to sulfur ratio confirming contraction of unit cell in the 101 direction and expansion in the $10\bar{1}$ direction with increase in arsenic in arsenopyrite structure.

The results here indicate that the change in stoichiometry is accompanied by a change in unit cell volume, as first concluded by Morimoto and Clark (1961). The increase in unit cell volume with increase in arsenic replacing sulfur, is associated with a slight compression within the octahedra in the (101) direction of the monoclinic cell (with no observed change in octahedra volume), accompanied by an increase in space between octahedra in the $(10\bar{1})$ direction. The average bond lengths appear not to change with composition. Any other differences are too small to be detected. There

also appear to be differences which are not related to stoichiometry as exemplified by the Mexican sample. Some of the arsenopyrite grains analysed under TEM revealed strain or disorder in some structures and the slight differences observed may result from this. The presence of increased space between octahedra may allow the possibility of the existence of gold there as interstitial sites. However no obvious mechanism for gold substitution was found for favouring arsenic rich over sulfur rich arsenopyrites.

3.3.3.7 Twinning Mechanisms in Arsenopyrite and Effect on Stoichiometry

Changes in stoichiometry can occur by random substitution of arsenic or sulfur on each others' sites, by substitution in defects such as twin planes or antiphase domain boundaries, by chemical shears, or by regular substitution of löllingite or marcasite units in solid solution in arsenopyrite. No evidence of the latter two were observed. The presence of twinning and antiphase domains in arsenopyrite has been documented (Morimoto and Clark, 1961; Fuess et al., 1987). The presence of twinning may affect gold incorporation in the structure. Fuess et al. (1987) interpreted the occurrence of antiphase and twin domains on the basis of group-subgroup relationships. Morimoto and Clark (1961) observed correlation of twins with composition. Consequently it was decided to examine the effects that twinning and antiphase domains, had on the symmetry of the arsenopyrite since they may account for the variations in observation by various workers. It was also important to assess the effect of twinning on the arsenopyrite structure in order to interpret results on the atomic location of gold in the arsenopyrite structure which are discussed in Chapter 6.

The type of twinning and antiphase domains possible are shown in Figures 3.39 and 3.40. The orientation in relation to the monoclinic unit cell and the translation in relation to the unit cell are also given in each diagram. It is most probable that several of these twins and antiphase domains exist together as observed by Fuess et al. (1987).
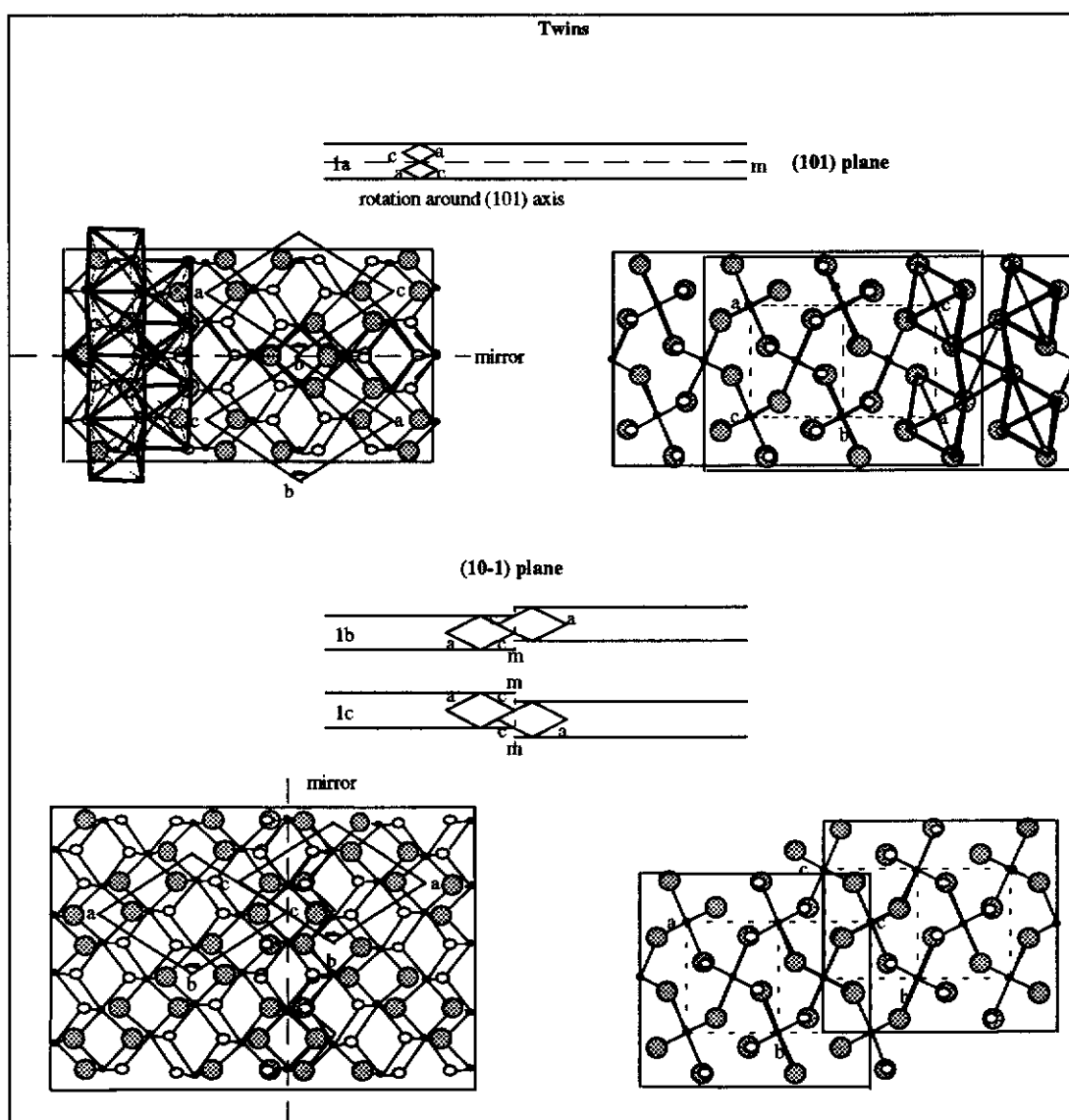
Figure 3.39 Projection of the arsenopyrite structure along the [010] and [101] zone axes showing various types of twin boundaries.
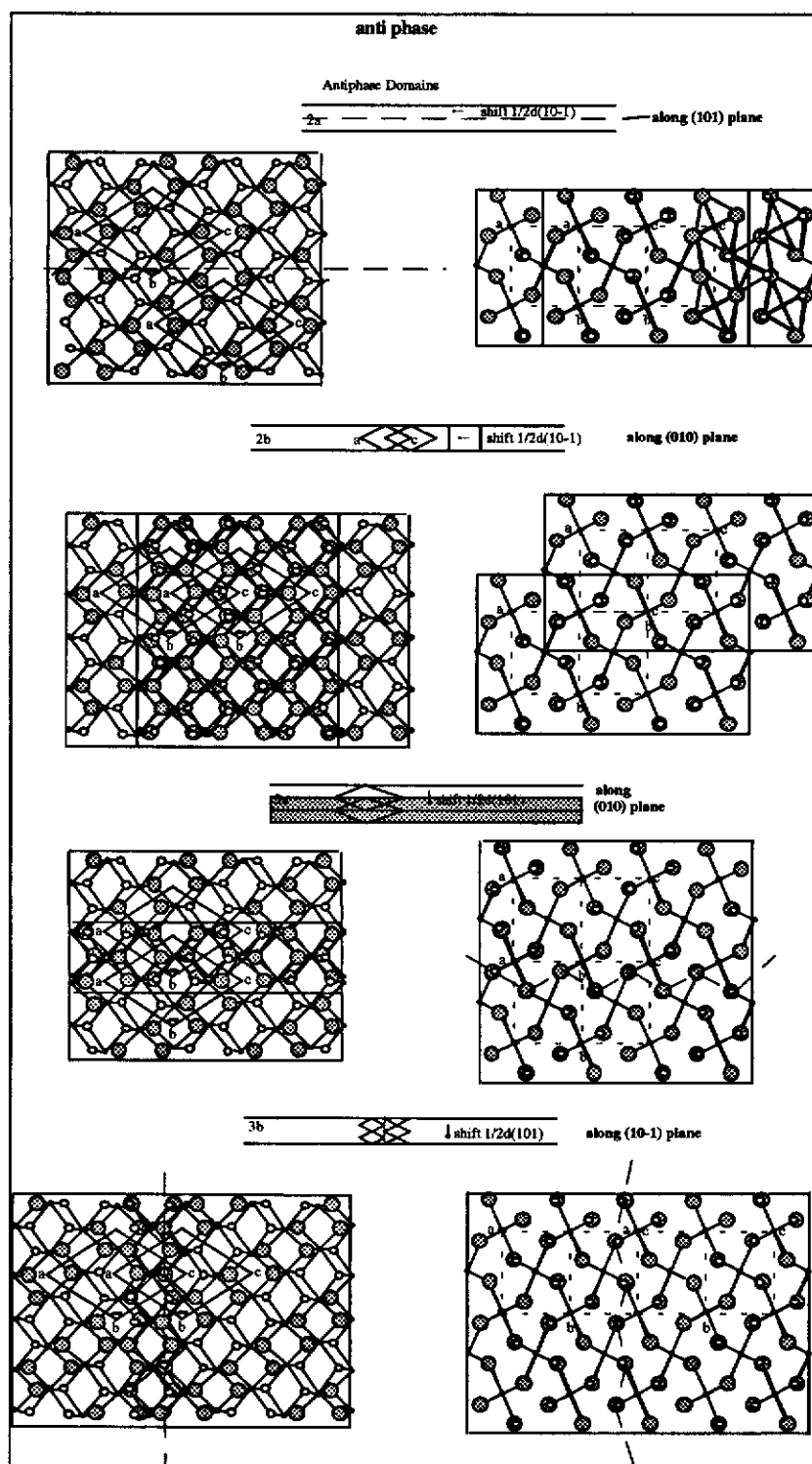
Figure 3.40 Projection along the [010] and [101] zone axes of the arsenopyrite structure showing antiphase domain boundaries.

Twins

Figure 3.39(1a) shows atomic models across a mirror twin plane in projection along the [010] zone and the [101] zone. In this twin an iron atom at the interface will have a different number of arsenic and sulfur neighbours than one in the ideal structure. In the ideal structure one iron is octahedrally coordinated by three arsenic and three sulfurs, whereas at the interface of this twin the iron atoms will be either coordinated with more sulfur atoms or more arsenic. At the twin interface the doubled iron indicates the position of the iron atoms as expected for each side of the twin interface. To make it energetically favourable the positions of the iron atoms in this interface will be slightly adjusted. The interchange of arsenic and sulfur on each others' site would affect the position of the site as well as other atoms surrounding it. It would be expected that the atoms at this interface would be slightly different from those in the ideal crystal. If this is the case the c glide and 2-fold screw axis would be distorted across this interface or possibly destroyed if multiple twins of this kind were present. In Figure 3.39(1a) the twin mirror plane appears to have no effect on the projection along the [101] zone axis. To accommodate for the differences in composition at the twin interface the octahedral unit would be slightly larger than the normal octahedra as a result of expansion in the (101) direction due to the increase in the number of arsenic or sulfur atoms. This would explain the decrease observed in bond angles S2-Fe-As3 and S1-Fe-As1 on the octahedra along the (101) direction (Section 3.3.3.6.2).

Alternatively a mirror twin plane along the $(\bar{1}\,01)$ plane can occur in which one unit cell is reversed with respect to another and displaced either partially on top or below a unit cell as shown in Figure 3.39(1b) and (1c). In obtaining this twin, iron atoms at the interface will also be octahedrally coordinated to a different number of arsenic and sulfur atoms. At the twin interface the positions of the atoms will most probably be distorted in relation to the ideal crystal, similar to the other mirror twin plane.

Antiphase Domains

Antiphase domains occur by translation by $\frac{1}{2}d(10\bar{1})$ along a (101) plane and along a (010) plane as shown in Figures 3.40(2a) and 3.40(2b). Alternatively, antiphase domains can also be obtained by translation of $\frac{1}{2}d(101)$ along either the (010) or $(10\bar{1})$ planes (Figure 3.40 (3a and 3b respectively)). Distortion observed in crystals projected along the [010] zone does not have any effect on the [101] zone axis. A combination of these antiphase domains may occur in which the bonding between the two crystals occurs diagonally along an axis plane such as the a or c axis. Fuess *et al.* (1987) reported such structures in their cobalt rich arsenopyrite.

Unfortunately, no crystals with obvious twins were observed in TEM carried out in this study which can conclusively demonstrate its effect on symmetry. The [101] zone CBED pattern will be affected by twinning and antiphase domains which cut diagonally across or perpendicularly to the incident electron beam. These effects will only influence the CBED pattern if the two sides of the crystal are thick enough. That is, the kinematic diffraction of the electron beam is affected by both crystals. The misfit of crystals observed in twins and antiphase domains would explain why CBED patterns were not clearly observed in the [010] zone and in some thick crystals in the [100] zone in the present study.

It is envisaged that some distortions in the arsenopyrite crystals can be due to displacement of the octahedra in the crystal caused by frequent twinning and antiphase boundaries. In high resolution arsenopyrite lattice images Cabri *et al.* (1989) observed misfits in the structure due to slight differences in a and c lengths. Twinning may provide sites of low energy for interstitial impurities such as gold. However, the fact that clear CBED patterns corresponding to the space group P2,/c were observed in all arsenopyrites examined in this study indicates that twinning and any other possible defects are not related to stoichiometry.

3.4 Summary and Conclusions

To provide information as to the possible environment for the retention of gold in solid solution in arsenopyrite, detailed chemical and structural analyses were carried out on natural arsenopyrite samples varying in compositions. EPMA of natural arsenopyrite with variation in stoichiometry showed no iron deficiency. It appeared that chemical composition has no effect on possible substitution of arsenic on iron sites. Samples analysed contained little gold except for the Sheba sample which contained high concentrations largely as inclusions and some possibly in solid solution. Evidence of the possible substitution of gold on iron sites from electron microprobe analyses could not be confirmed. Similarly, substitution of antimony on either arsenic or iron site was not conclusive.

The crystal structures of arsenopyrite of various compositions were investigated by X-ray diffraction and convergent electron diffraction studies and their structures refined using the Rietveld method. Structural analysis of stoichiometric arsenopyrite confirmed Buerger's (1936) hypothesis that the ideal arsenopyrite structure is monoclinic $P2_1/c$. For all stoichiometries the basic monoclinic $P2_1/c$ structure was always present and changes observed in the structures by single crystal studies are due to twinning (e.g. Fuess *et al.*, 1987). Cobalt or other impurities are not required to stabilise this structure as has been suggested for some arsenopyrite compositions in the literature. Low As:S ratio arsenopyrites were not triclinic as reported by Morimoto and Clark (1961). With an increase in the arsenic to sulfur ratio in arsenopyrite an increase in the unit cell volume was observed as first reported by Morimoto and Clark (1961). The change in unit cell volume was associated with a slight compression within the octahedra in the (101) direction of the monoclinic cell and an expansion of the octahedra in the (101) plane resulting in a slight opening of the voids between octahedra. Any other differences were too small to be detected. There also appear to be differences in structure which were not related to stoichiometry as exemplified by the Mexican sample and strain or disorder observed by TEM, for some of the arsenopyrite grains examined. Twinning and antiphase

domains provide mechanisms for arsenic and sulfur interchange, and possibly cause distortions in some of the arsenopyrite crystals due to displacement of the octahedra. The [101] zone appeared unaltered in all arsenopyrite compositions and provides the best direction for determining gold in the arsenopyrite structure by the electron channelling experiment (see Chapter 6). The structure analyses showed no obvious trends in which mechanisms for gold substitution in the arsenopyrite structure occurred. As arsenopyrite containing high gold concentrations in nature are associated with arsenopyrite containing high arsenic contents (Cook and Chryssoulis, 1990), the slight expansion of its structure with increasing arsenic content, may allow gold in interstitial sites. In addition, the presence of twinning may result in gold substitution in one of the atomic or interstitial sites.

Chapter 4

4.0 INCORPORATION OF GOLD IN ARSENOPYRITE

4.1 Introduction

The natural arsenopyrite available contained only relatively small concentrations of gold, and grains containing high concentrations of 'invisible gold' were particularly scarce. Furthermore, the distribution of gold in natural arsenopyrite samples was scattered and not suitable for gold mobility studies. Consequently, work was carried out to synthesise auriferous arsenopyrite containing high concentrations of gold since this would greatly enhance the effectiveness of a number of the analytical techniques to be used. Detailed analyses could then be carried out as to the form of the gold in the arsenopyrite structure. In addition, it was anticipated that the successful incorporation of gold into the arsenopyrite structure could provide information as to how gold is taken up in arsenopyrite.

In the first part of the study, several methods were attempted to synthesise arsenopyrite containing high concentrations of gold. Detailed compositional and structural analyses were then carried out on these synthetic arsenopyrites for comparison with the natural samples.

4.2 Materials and Methods

4.2.1 Synthesis of Auriferous Arsenopyrite

The three methods used in an attempt to synthesise auriferous arsenopyrite were dry synthesis, vapour transport and hydrothermal synthesis experiments.

4.2.1.1 Dry Synthesis

Several authors (Barton, 1969; Clark, 1960; Kretschmar and Scott, 1976) have utilised the dry synthesis technique, which is the most commonly used (outlined

by Kullerud, 1971) to make sulfide minerals, in the preparation of synthetic arsenopyrite.

Equimolar amounts of iron (99.99+% pure), arsenic (99.999+% pure) and sulfur (99.999% pure) were placed into nitrogen flushed vycor tubes (3mm I.D. x 5mm O.D. x 15 cm length) sealed at one end. A vycor space filler was place inside to reduce the space available to the gaseous arsenic and sulfur phases. The tubes were completely sealed under a vacuum of approximately 10^3 torr. The tubes were placed in a muffle furnace for a period of 7 to 14 days. The temperature of the furnace was monitored using a chromel-alumel thermocouple wire connected to a temperature readout display. The reaction followed was

$$Fe(s) + As(s) + S(s) \rightarrow FeAsS(s)$$
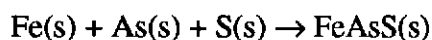
For experiments in which gold was added in an attempt to incorporate it into the arsenopyrite structure, gold wire (99.999% pure) was first dissolved and reprecipitiated as fine particles to provide a larger surface area for reaction with the arsenic, iron and sulfur. The procedure used was similar to that of Vogal's (1962) method for gravimetric analysis of gold. The fine particles (i.e. metallic gold Au^o) were added both to mixtures of arsenic, iron and sulfur and to ground synthesised arsenopyrite and sealed in evacuated vycor tubing.

A series of grinding experiments was also carried out in an attempt to incorporate gold into the arsenopyrite crystals via diffusion as well as to homogenise the chemical composition and to improve crystal size. Samples of synthetic arsenopyrite and starting materials (As, Fe and S powder), together with fine gold particles, were ground in a Spex mill for 2 days. These samples were resealed in vycor tubes and heated for up to 3 months.

4.2.1.2 Vapour Transport

Fushimi and Webster (1969) grew large crystals of arsenopyrite by an iodine vapour transport mechanism, and so attempts were made to grow auriferous

arsenopyrite crystals by the introduction of gold with the starting material. The iodine transport method generally follows the ideal reaction scheme

$$FeAsS +I_2 = FeI_3(g) + As_4S_4 (g)$$

Pyrite was required in the starting materials to raise the sulfur ratio in the gas phase. This compensates for excess arsenic which is distilled from the arsenopyrite breakdown following the ideal reaction

$$4FeAsS = 4Fe_{1-x}S(s) + As_4(g)$$

which also took place. The growth experiments for synthesising arsenopyrite by the vapour transport technique were undertaken using sealed, evacuated vycor tubes. The measured amounts of synthetic arsenopyrite and pyrite powder, with iodine, were loaded at the hot end of the tube which was then evacuated and sealed by a torch. The sealed vycor tubes were placed in a horizontal temperature gradient furnace. The temperature gradient ranges used in these experiments are shown in Figure 4.1. The larger temperature range was used to help increase gold transport.
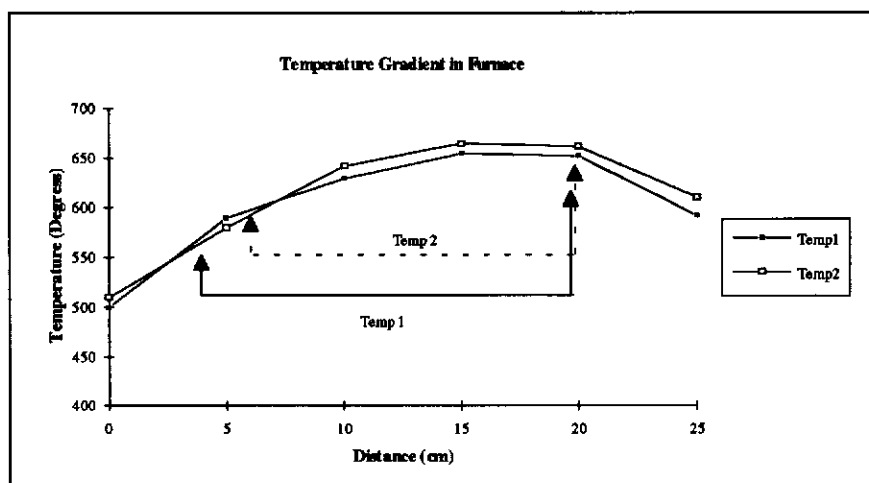
Figure 4.1 Temperature gradient in furnace used.

The hottest end was set at a temperature of 650°C while the cooler end was set at 590°C. Initially, experiments were carried out without any gold in order to obtain the best conditions for crystallisation of arsenopyrite. Once the conditions were

achieved, experiments were carried out with a small amount of gold placed with the various starting materials.

The volatilisation of gold follows the reaction

$$2Au(s) + 3I_2 = 2Au_2I_3(g)$$
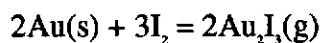
Ammonium chloride or gold chloride was also included in the starting materials to provide an increase in gold volatilisation. Under the conditions used the reaction is:

$$2Au(s) + 3Cl_2 = 2Au_2Cl_3(g)$$
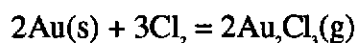
At the end of an experiment, samples were left to cool to room temperature. Samples were observed under an optical microscope through the unopened tube. In experiments where no transport occurred or where no silver crystals of arsenopyrite were observed, the samples were placed back in the furnace for a longer heating time.

4.2.1.3 Hydrothermal Synthesis

Many natural auriferous arsenopyrites are formed under hydrothermal conditions. Hence, hydrothermal incorporation of gold into arsenopyrite was examined.

For hydrothermal studies, standard high temperature and cold seal pressure vessels (pressure bombs) were used (Tem-Pres Model Hr-1b Hydrothermal research unit). An illustration of the apparatus used in these hydrothermal experiments is presented in Figure 4.2.

The pressure vessel consisted of a rod of high temperature alloy with an axial hole drilled in one end. The open end was closed by a threaded nut and a conical nipple, through which pressure was applied. The sample, sealed in a vycor tube or in gold tubing, was placed in the central cavity. A rod was placed in the space above the sample to minimise both the amount of pressure medium required and the convective heat transfer within it. Distilled water was used as the pressure medium. The pressures applied to the samples were controlled by a hydrostatic pressure gas-operated intensifier. The pressure vessels were heated externally in wire-wound tube furnaces with temperatures controlled automatically. The temperature was measured with a

chromel-alumel thermocouple in a small external well, while pressure was measured using a Bourdon gauge. Pressure was controlled to within ±50 bars and temperature to within ±5°C.

Auriferous arsenopyrite was synthesised following a similar method to Wu and Delbove (1989). Several modifications of composition and temperature were also tried. Starting materials consisted of either synthetic hematite or goethite, together with arsenic (99.999+% pure) and sulfur (99.999% pure), which were placed in sealed gold tubes of various dimensions. The use of iron oxides instead of pure iron in the starting materials prevented the preferential formation of pyrrhotite over arsenopyrite. Aqueous solutions or distilled water were added to the solid starting reactants for many of the experiments. The aqueous solutions used were either hydrochloric acid or gold chloride solutions. In some experiments no solution was added. The water used in these experiments was double distilled to remove all impurities, especially chlorine ions from solution. Gold chloride solutions were made by dissolving gold in aqua regia and heating until near dryness and then adding concentrated hydrochloric acid and heating again to near dryness. This was done to remove nitrate ions from solution. Hot double distilled water was then added and decanted into a volumetric flask and made up to the required volume.

The gold capsules were sealed and then placed in pressure bombs and heated to 300°, 400° or 500°C under pressures between 1 and 2 kbars. The gold capsules were carefully weighed before and after each experiment to check that no leakage had occurred.

The formation of arsenopyrite basically followed the reactions;

$Fe_2O_3(s) + 4As(s) + 2S(s) \rightarrow 2FeAsS(s) + As_2O_3(s)$
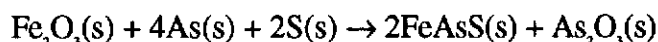
for hematite experiments and

$2FeOOH(s) + 4As(s) + 2S(s) \rightarrow 2FeAsS(s) + H_2O(aq) + As_2O_3(s)$
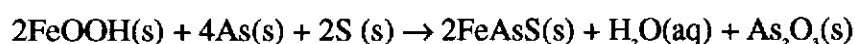
for goethite experiments.

However, in the lower temperature experiments, pyrrhotite, arsenic sulfide and arsenic were also present in the end products.

At the end of each experiment, the bombs were left to cool to about 200°C and then quenched in cold water with the experimental pressure maintained throughout the quenching process so as not to cause breakage of the gold capsules. The gold capsules were then opened and the contents transferred into a beaker. The products were first washed in hot 0.5M HCl to remove As_2O_3 and then washed several times in hot distilled water to remove any soluble impurities. The solutions were decanted after each wash. The synthetic arsenopyrite samples were washed in a cyanide solution to remove any gold which may have precipitated on the surface. Care was required as arsenopyrite left in cyanide solution for too long (e.g. ~6 hours) resulted in some dissolution of the arsenopyrite crystals. The products were then washed in ethanol and acetone and finally left to dry.

For samples from experiments at 400°C or lower, unreacted material was separated from arsenopyrite crystals by distillation, using a furnace with a low temperature gradient. Analyses of major d-spacings of XRD patterns from samples collected in this way showed there were no changes in the arsenopyrite. Samples were then placed in self sealing plastic vials flushed with nitrogen to prevent oxidation of crystals. Also present in some experiments were grains of auriferous and arsenic-containing pyrites which were also analysed in this study.

Experiments were also carried out with small grains of natural arsenopyrites being placed in gold tubes with various types of solutions and heated under pressure, in similar ways to the other experiments.

4.2.2 Analytical Techniques

4.2.2.1 Composition and Structure

The methods used for obtaining composition, trace gold analysis and structure of the synthetic samples were generally the same as outlined in Chapter 3. For trace

gold analyses by EPMA on the synthetic arsenopyrites, a beam current of 40 kV and 290 nA was used as the samples disintegrated with a higher current. The concentration of gold in the synthetic samples was usually above trace levels and was detectable using a much lower current. For X-ray diffraction studies, the synthetic arsenopyrites were lightly ground in acetone and smeared on a glass slide as the amount of sample were not sufficient for normal aluminium slide holders. Several XRD patterns were obtained and compared to reduce problems with preferred orientation.

The Philips EM430 Analytical Transmission electron microscope located at the EM centre, UWA, operating at 300 kV provides a point to point resolution of about 0.2-0.23 nanometres similar to that used by Cabri *et al.* (1989) and is ideal for distinguishing whether particulate gold is present. In order to determine whether certain features observed on the electron micrograph resulted from the presence of gold, selected area electron diffraction (SAED) patterns and convergent-beam electron diffraction (CBED) patterns were obtained. If gold was present as ultra fine grains, electron diffraction patterns would give a specific diffraction pattern corresponding to gold.

4.2.2.2 Gold Mössbauer

To provide extra information on the form of gold in the synthetic auriferous arsenopyrites, gold Mössbauer spectrometry was carried out.

For Mössbauer spectroscopy, γ-rays emitted during an isomeric transition of a nucleus in a radioactive source are absorbed by a nucleus of the same isotope, causing it to undergo a transition from its groundstate to the respective excited state. The decay of the radioactive isotope is accompanied by the emission of gamma-rays of various energies corresponding to decay of excited states of the stable isotope characterised by different nuclear spin quantum number.

In ^{197}Au, the only stable gold isotope, there is a transition suitable for Mössbauer work between the nuclear ground state and an excited state at 77 keV.

The γ-rays can be resonantly absorbed by [197]Au nuclei only if they do not lose recoil energy during emission or absorption. This requires the emitting and absorbing atoms to be embedded in a solid matrix. These recoil free fractions are obtained only at low temperatures because of the high energy of the [197]Au resonance and hence the measurements require cooling by liquid helium.

The information on the chemical state of the absorbing atoms is obtained from the hyperfine interactions of the nuclei with their electronic environment. The relevant interactions in gold compounds are the electric quadrupole interactions which measure deviations of the distribution of the electric charge around the nucleus from cubic symmetry. These interactions lead to splitting of the Mössbauer line into a doublet and a shift in the centre of gravity of the Mössbauer pattern, the isomer shift (which is proportional to the electron density at the site of the gold nuclei). Both the electric quadrupole interaction and the isomer shifts are influenced by the chemical bonding of the gold atom. By measuring both, one can distinguish between Au^I and Au^{III} and obtain information on the covalency of the bonds.

Mössbauer spectra were obtained for hydrothermally synthesised auriferous arsenopyrite from both goethite and hematite with arsenic and sulfur mixtures. The Mössbauer spectra were fitted assuming a Gaussian distribution of quadrupole splittings and of isomer shifts, with a correlation between these two parameters. The probability of finding an isomer shift (IS) is given by

$$P(IS) = \exp\{-(IS-IS_0)^2/2\sigma^2)\}$$

where IS_0 is the mean isomer shift and σ describes the width of the Gaussian distribution of isomer shifts. The quadrupole splitting QS is assumed to be linearly dependent on the isomer shift

$$QS = QS_0 + C (IS - IS_0)$$

where the correlation constant C is an adjustable parameter.

4.3 Results and Discussion

4.3.1 Dry Synthesis

In the first stage, the synthesis of arsenopyrite without gold was undertaken to make sure suitable arsenopyrite could be satisfactorily produced. Two different temperatures were used to obtain arsenopyrite with different stoichiometries (Clark, 1960; Kretschmar and Scott, 1976). To synthesise a high As:S ratio arsenopyrite, mixtures were heated to 600°C and for a low As:S ratio mixtures, were heated to 400 °C. It was hoped that the difference in stoichiometry produced at the different temperature would throw light on the potential for gold incorporation. The experiments carried out are shown in Table 4.1.

Table 4.1 - Dry Synthesis of Arsenopyrite with and without Gold Present							
	Starting Materials				Conditions		
Sample No.	Fe (grams)	As (grams)	S (grams)	Au (grams)	Temp (°C)	Period (days)	Major Products*
A1	1.3720	1.8404	0.7876	-	600	7	Asp,Pyrr
ASP1	1.3972	1.8808	0.7859				
A1/b	Ground A1 sample					30	
A3	1.336	1.976	0.688		635	7	Asp
A2	1.3720	1.8404	0.7876		400	7	Asp, Pyrr, As
ASP4	1.3906	1.8655	0.7842			14	
Addition of Gold							
A6-1	0.957 of Asp1 sample			0.1027	600	7	Asp,Au,Pyrr, As
A6-3	1.2167 of Asp1 sample				400		
A8	1.3769	1.8618	0.7898	0.1021	600	14	Asp,Au,Pyrr
A9	1.3465	1.9935	0.6877	0.1019	600		Asp,Au,Pyrr
A10	1.3917	1.8770	0.7946	0.103	400		Asp, Pyrr, As, Au
A23	0.6812	0.9176	0.3935	0.0417	660	2	Asp,pyrr,As,Au
A23x	Ground and pelletized A23				400	3 mths	Asp,pyrr,As,Au
A23y					500	3 mths	Asp,pyrr,As,Au
Grinding Expts - materials ground for two days prior to heating							
Ga1a	1.3972	1.8808	0.7859	0.04	600	3 mths	Asp,pyrr,Au
Ga1b					400		Asp,pyrr,As,Au
Ga2a	Ground Asp1 sample+Au				600		Asp,pyrr,Au
Ga2b	Ground Asp1 sample +Au				400		Asp,pyrr,Au
Ga5	Fe,O,As,S mixture		0.2363	0.0117	660	14	As,Au,pyrr,Asp
Gaa1	Reground Ga2				660	14	As,Au,pyrr,Asp

*As - arsenic, Au - gold, pyrr - pyrrhotite, Asp - arsenopyrite, py - pyrite

XRD analyses showed that the main phase produced from the high temperature experiments (600°C) was arsenopyrite with a minor phase of pyrrhotite. The addition of slightly greater amounts of arsenic in the starting materials reduced the presence of pyrrhotite. However, there was an increase in the amount of unreacted components and impurities. A slight increase in the temperature to 635°C resulted in only arsenopyrite. In the synthetic arsenopyrite the major peaks in the XRD pattern were similar to those observed by Morimoto and Clark (1961).

Heating at a lower temperature (400°C) resulted in arsenopyrite being the major phase in the centre of the reaction tube, with a moderate amount of pyrrhotite also being formed. However, crystals of euhedral arsenic were observed intergrown with some pyrrhotite, arsenopyrite and pyrite.

Slight changes in chemical composition in the starting material were also tried to see if the crystal size of the product could be improved and in an attempt to reduce impurities. However no improvements were observed. In most samples, the arsenopyrite appeared as silver-coloured aggregates 2 to 20 μm in size and anhedral to subhedral in form (Figure 4.3). The euhedral arsenopyrite grains had a rhombohedral habit. Pyrrhotite present in the samples was generally subhedral and ranged in size from 5 to 20 μm.

The arsenopyrite crystals were large enough to determine the composition using an electron microprobe. The composition of the arsenopyrite found in polished section mounts varied between $FeAs_{0.93}S_{1.07}$ and $FeAs_{1.06}S_{0.88}$. A similar correlation of As:S ratio with temperature was confirmed. The synthetic arsenopyrites made in the above experiments were used as starting materials in many of the following experiments.

The incorporation of gold into the structure of the synthetic arsenopyrite was then attempted. Fine particle gold (i.e. metallic Au^o) was added to both synthetic arsenopyrite sample (A6-1, A6-3) as well as equimolar amounts of Fe, As and S (A8,A9, A10). These mixtures were sealed inside evacuated vycor tubing separately using the same method as for dry synthesis. In an attempt to get as much gold as
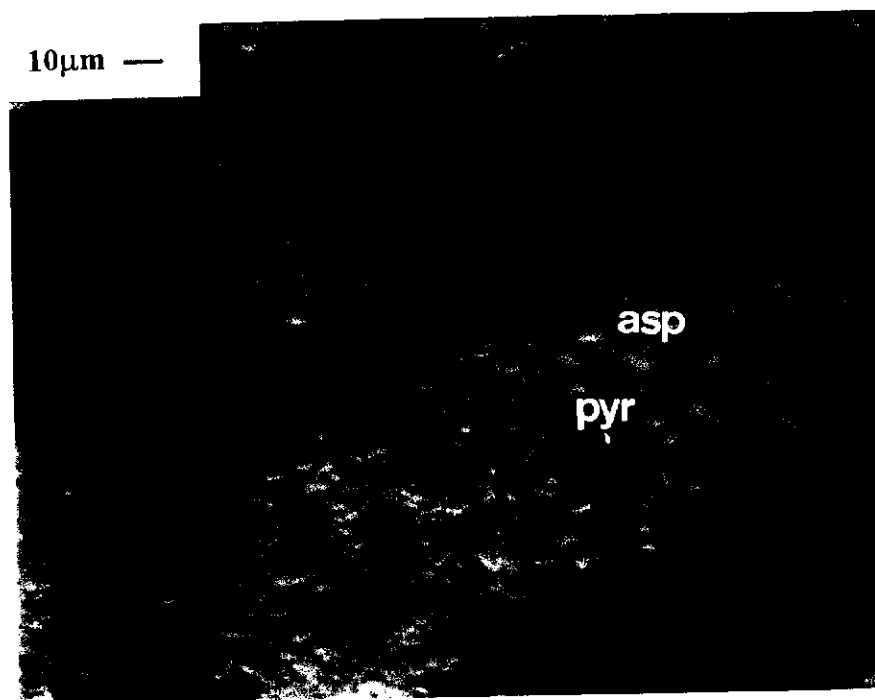
Figure 4.3 Synthetic arsenopyrite (Asp1) from Fe, As and S mixture heated at 600°C for 7 days. Sample also contains some pyrrhotite which was observed mainly in the centre of arsenopyrite grains.
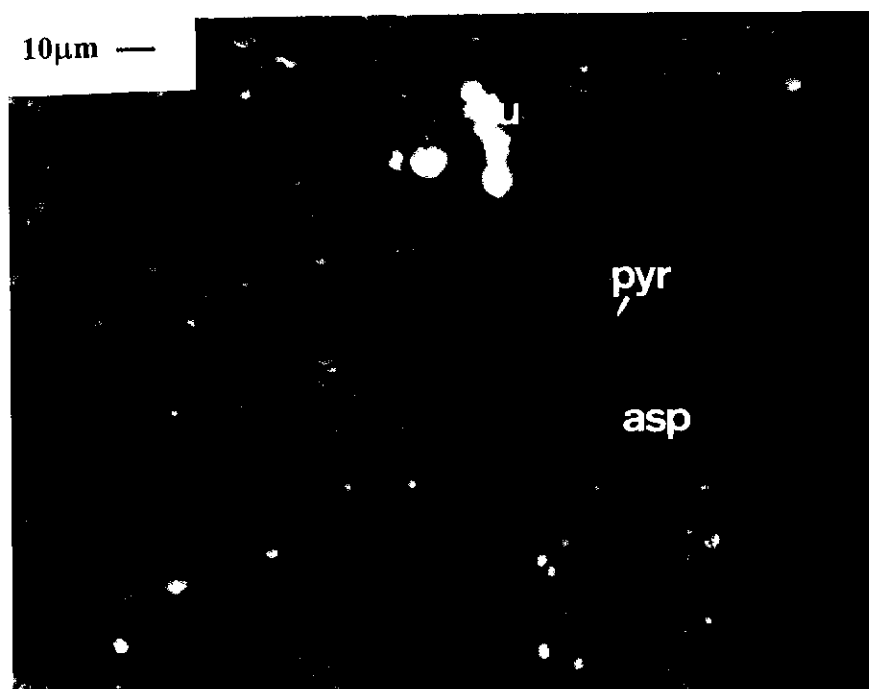
Figure 4.4 Synthetic arsenopyrite containing unreacted gold particles (A6-1) and pyrrhotite.

possible into the arsenopyrite produced, the amount of gold added to these samples was about 2.5 wt% of the whole material. This is above the maximum gold content (1.52 wt%) reported in the literature for natural arsenopyrite (Johan *et al.*, 1989; Marcoux *et al.*, 1989) and for synthetics of 1.7 wt % (Wu *et al.*, 1990). These samples were heated as outlined in Table 4.1. Measurement of d-spacings of arsenopyrite reflections in XRD powder patterns and optical examination showed that most of the previous synthesised arsenopyrite (A6-3) remained unchanged when heated with fine gold at 400°C. However, the sample heated at 600°C (A6-1) contained a higher concentration of pyrrhotite (Figure 4.4). Gold present appeared as round separate globules in both samples and showed no obvious difference to the initial form of the gold added to the starting materials.

Synthetic arsenopyrite formed from the starting materials (Fe, As and S powders, A8,A9) with gold, also produced a similar XRD trace to those samples without gold. Clark (1960) also found no difference in d-spacings of arsenopyrite synthesised in the presence and absence of gold. In these samples, SEM studies revealed (Figure 4.5a) euhedral aggregates of arsenopyrite (~60 μm in length) and the presence of gold grains. Gold also occurred as inclusions in some arsenopyrite grains (Figure 4.5b). No gold was detected by electron microprobe in the arsenopyrite grains using the trace gold analysis method.

A series of grinding experiments were carried out to help incorporate gold into the arsenopyrite crystals via diffusion as well as to homogenise the chemical composition and to improve crystal size. Polished section mounts of these samples showed grains of arsenopyrite ranging from 2-60 μm in size. Some pyrrhotite and arsenic were also present. In samples heated to 400°C, gold occurred as finely disseminated, unreacted grains amongst fine arsenopyrite grains. In samples heated to 600°C, (Ga2) coarse euhedral grains of arsenopyrite were formed and joined together by gold (Figure 4.6a) or the gold appeared as globules on anhedral pyrrhotite grain surfaces (Figure 4.6b). The gold associated with arsenopyrite tended to be angular, whereas gold associated with pyrrhotite was rounded. Energy dispersive analyses of
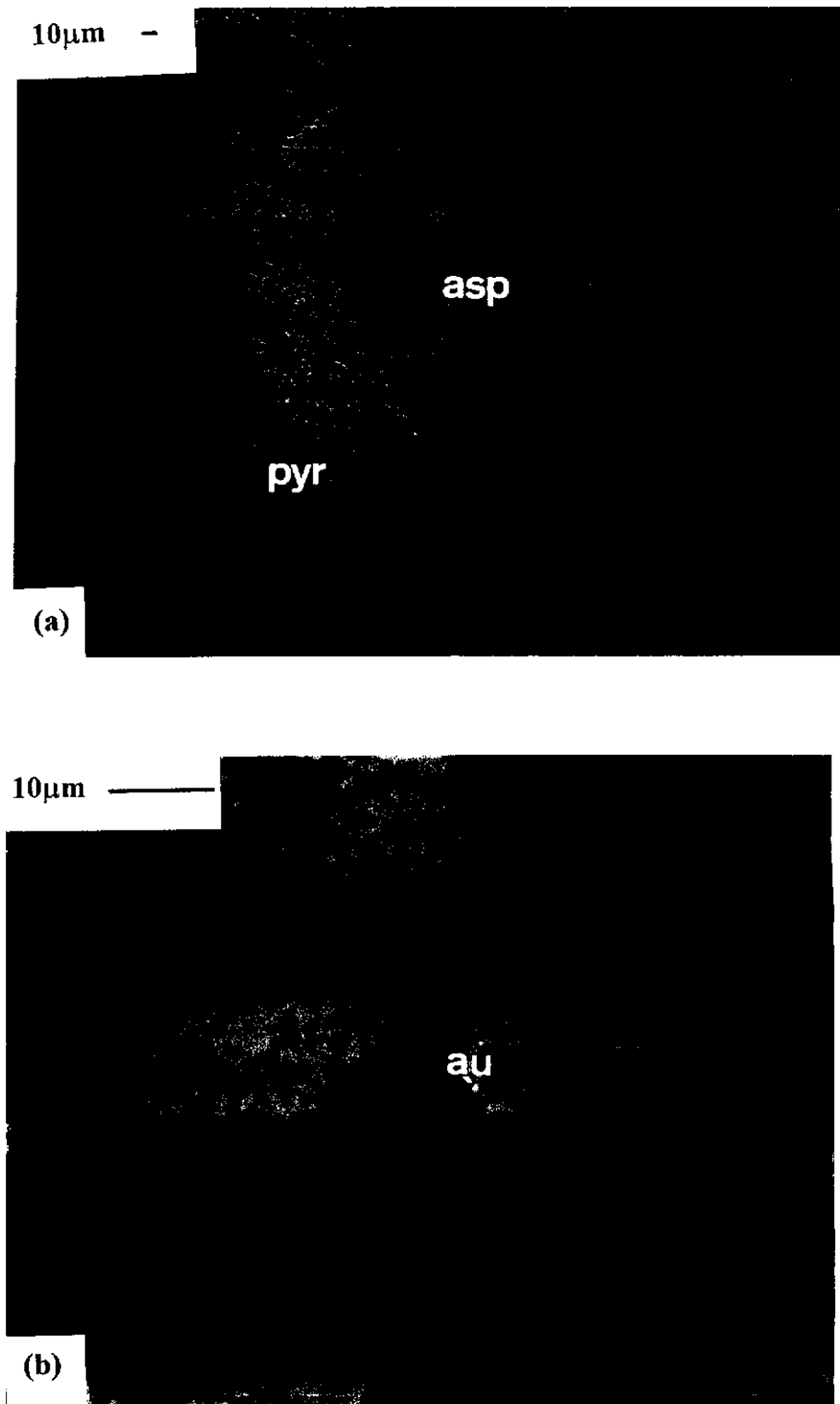
Figure 4.5 (a)Coarse grained aggregates of synthetic arsenopyrite and pyrrhotite (A8).
(b) Synthetic arsenopyrite and pyrrhotite containing inclusions of gold particles.
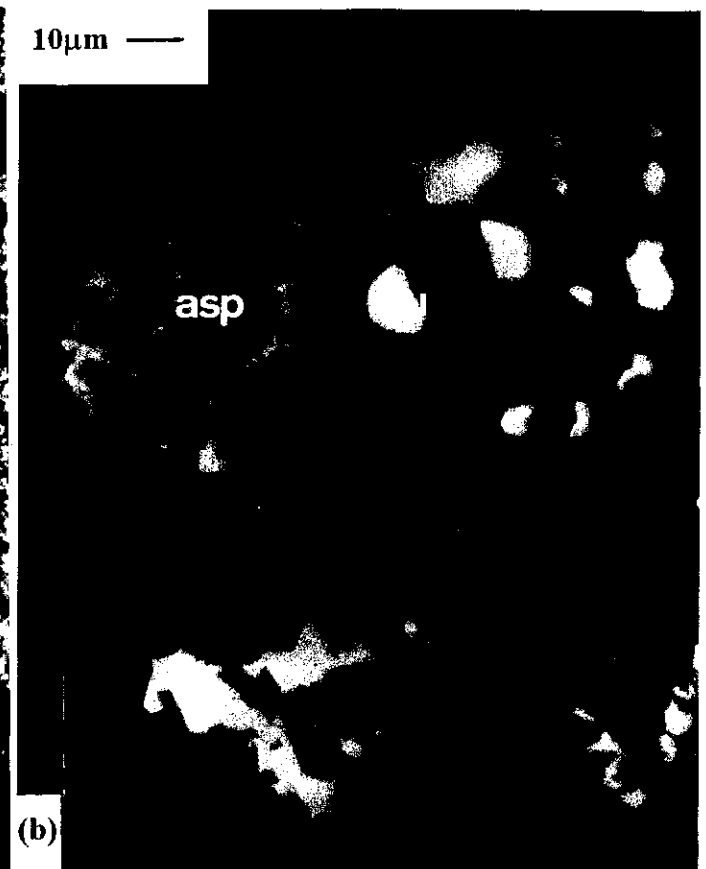
Figure 4.6 (a) Coarse euhedral arsenopyrite cemented together by gold (Ga2). (b) Rounded gold globules on pyrrhotite.
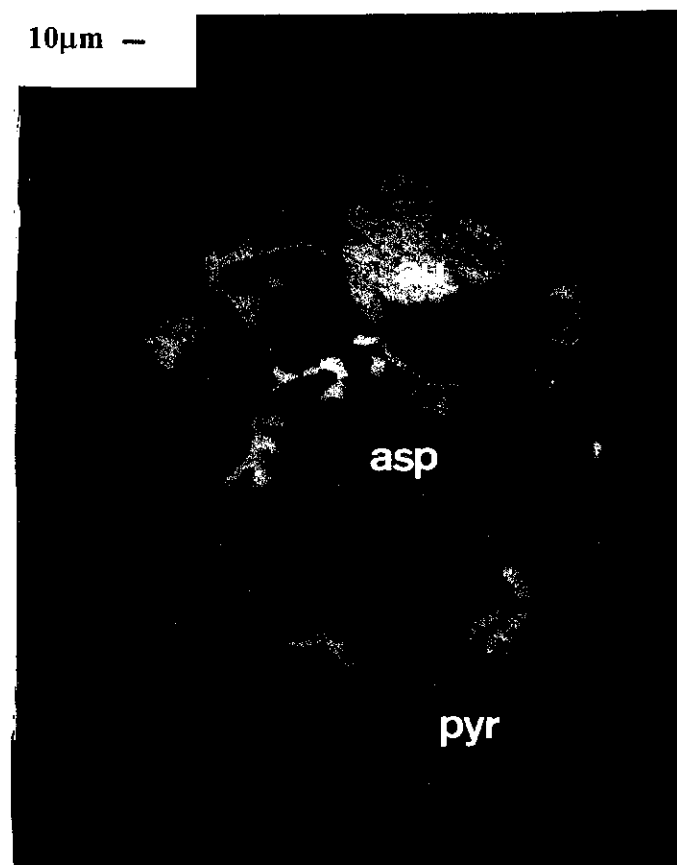
Figure 4.7 Arsenopyrite altered to pyrrhotite with a concentrated rim of gold (GAA1).

the arsenopyrite grains did not detect any gold. The sharp boundary between the gold and the arsenopyrite (and pyrrhotite) grains indicates that there was no diffusion of gold into the arsenopyrite grains. Close examination of the arsenopyrite showed no chemical zoning which would have indicated some interaction with gold. Figure 4.6 also suggests that gold enhances crystallisation of arsenopyrite and that the gold surface tension is affected by arsenopyrite. In addition, the shape of the gold indicates gold must have been mobile at 600°C. Regrinding some of the Ga2 sample and heating to 660°C, resulted in alteration of some arsenopyrite to pyrrhotite with gold appearing with arsenic metal as a eutectic texture (GAA1). Polished sections revealed an association of coarse grained arsenopyrite and pyrrhotite with gold coating the outside edges of the pyrrhotite grains (Figure 4.7) suggesting gold was expelled during the formation of pyrrhotite. Several experiments were also attempted similar to GAA1 where excess arsenic was added but resulted in similar findings as for the GAA1 sample.

Under the conditions used in the above experiments, gold appeared either as unreacted grains or showed some evidence of being mobile during the arsenopyrite crystallisation, recrystallisation or alteration of arsenopyrite to pyrrhotite. These results are consistent with phase diagrams of Au-S and Au-As systems which do not show any gold complexes between 300°C and 635°C (Okamoto and Massalski, 1985; Gather and Blachnik, 1976). Metallic gold was the most stable form between these temperatures. At temperatures above 630°C, gold is mobile in the presence of arsenic vapour pressure for certain As:Au ratios (Gather and Blachnik, 1976). This was confirmed in some of these experiments and this mobility possibly retards the growth of arsenopyrite (by reducing the arsenic vapour pressure) as was observed in samples Ga5 and Gaa1 heated to 660°C.

Another approach may have been to attempt to make auriferous arsenopyrite at temperatures below about 300°C where gold and sulfur compounds are present (Cardile et al., 1993). However, the kinetics would be too slow to make arsenopyrite at this temperature, although adding inert halide flux would increase the synthesis rate

(Scott, 1974). In addition, arsenopyrite formed at low temperatures has a low As:S ratio (Kretchsmar and Scott, 1976). Arsenopyrites reported in the literature which appear to have high gold contents are normally found to have high As:S ratios (Johan et al., 1989). Consequently, arsenopyrite formed at lower temperatures was unlikely to contain the high gold concentrations required for experiments in this study. Arsenic and sulfur phases are also stable at this temperature which would reduce arsenopyrite abundance. Hence low temperature experiments were not attempted.

The presence of unreacted metallic gold in most of the arsenopyrite products obtained suggests metallic gold is not readily soluble in arsenopyrite under the conditions used. While Clark (1960), and Wu and Delbove (1990) also reported that the use of dry synthesis methods did not result in metallic gold being incorporated in the arsenopyrite structure, they did not provide any conclusive evidence. Recently, Neumayr et al. (1993) have shown evidence of gold not being readily soluble in arsenopyrite at high temperatures in nature. The mobility of gold observed in some experiments is discussed in Chapter 7.

4.3.2 Vapour Transport Synthesis of Arsenopyrite

Attempts were made to incorporate gold into arsenopyrite by transporting the gold as a chloride or iodide complex. For incorporation of gold into the arsenopyrite structure, the starting composition of the experiment had to be optimised so that the gas composition was in equilibrium with the arsenopyrite and gold recrystallising simultaneously at the cool end of the tube.

In addition, gold volatilisation can be enhanced in the presence of other metals such as iron to form $AuFeCl_6$ (g) (Hager and Hill, 1970). That is, as the arsenopyrite and pyrite in the starting materials at the hot end of the tube decompose, some gold may be transported to the cooler end of the tube along with FeI_3 and As_2S_2. Without pyrite to buffer the sulfur concentration at the cool end of the tube the major phases obtained were löllingite and pyrrhotite (Av7c). Two temperature ranges were used. The experiments carried out are shown in Table 4.2. Synthetic arsenopyrites

(Asp1,A8, A9 and Asp4) prepared in earlier experiments were used as starting materials in the following experiments. Gold was placed with the starting materials in several experiments either as metallic gold (Au^0) or as gold chloride. The presence of pyrrhotite and arsenic crystals observed in the products indicated that the process of distillation of arsenic from arsenopyrite had not been totally suppressed by the addition of pyrite to the starting materials.

Table 4.2 - Iodine Vapour Transport Experiments						
	Starting Materials				Conditions		
	Synthetic arsenopyrite	Pyrite	Iodine	Gold (Au^0)	Temp Grad (°C)	Period (days)	Major Products
Av1	1g of Asp1	0.24g	0.18g	-	540-652	7	Asp,Pyrr
Av2	1g of Asp1	0.24g	0.18g	-	300-685	7	Asp,Pyrr,
Av3	1g of A8	0.24g	0.18g	0.0011g	540-652	6	As,Pyrr,Au
Av6	0.6374g of A9	0.2414g	0.1848g	0.006g	540-652	10	Asp,Pyrr,Au
Av7	0.7802g of A9	0.2449g	0.1853g	0.006g	540-652	12,10	Asp,Pyrr,Au
Av7c	0.7115 of Asp4	.0002g	0.017g	0.0238g	540-652	10	Pyrr,Lo, Au
Av8	0.3232g of Asp4	0.0825g	0.047g of NH_4Cl	0.004g	587-662	12,10	Asp,Pyrr,Au (hot end)
Av9	0.445g of Asp1	0.1496g	-	0.0735g of $AuCl_4$	587-662	12,10	Asp,Pyrr,Au
Av10	0.3173g of Asp4	0.0791g	0.0653g of I_2	0.0485g of $AuCl_4$	587-662	12,10	Lo,Asp,Pyrr,Au
Av11	0.3163g of Asp4	0.0838g	0.0565g of I_2, 0.0394g of NH_4Cl	0.0033g	587-662	12,10	Asp,Pyrr,Au (hot end)

Arsenopyrite appeared either as single acicular euhedral crystals (Figure 4.8a) or dendritic crystals (Figure 4.8b), growing from the vycor tube surface close to the cool end of the tube (Av1-7). Other products formed were anhedral to euhedral hexagonal platy crystals of pyrrhotite and amorphous reddish intermediate iodine compounds which precipitated on quenching. Crystals of arsenic metal were also present in most experiments. The gold transported appeared either as anhedral branch structures or precipitated as round globules on pyrrhotite grains. In several samples, (Av6, Av7) gold globules were present on arsenopyrite crystal surfaces (Figure 4.9). Polished sections showed irregular inclusions of gold in crystals of arsenopyrite and

10μm —

(a)

10μm —

(b)
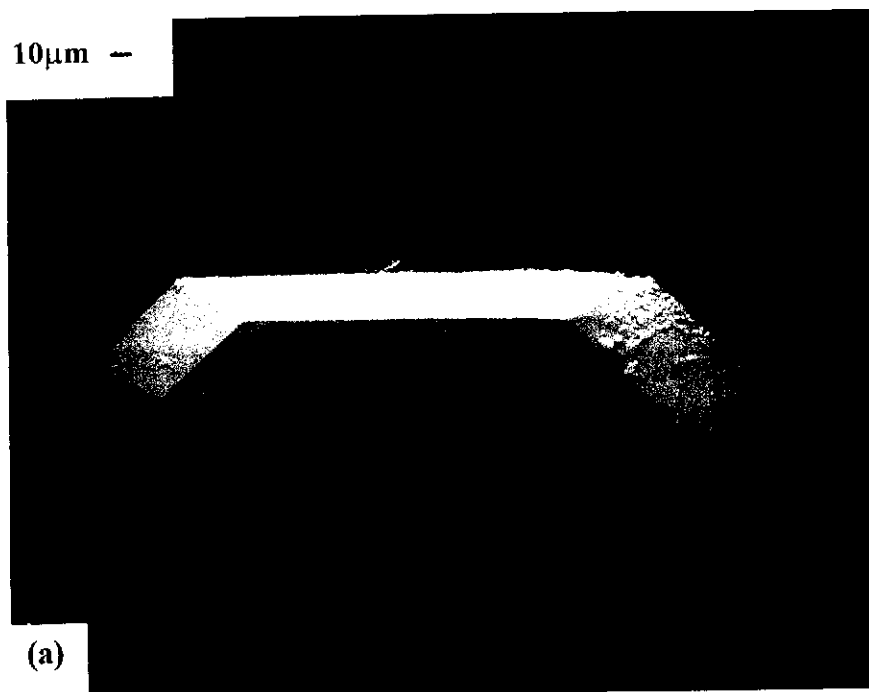
Figure 4.8 (a) Single acicular euhedral crystal of arsenopyrite recrystallised from iodine transport. (b) Acicular dendritic crystals of arsenopyrite. Iodine compounds are also deposited on some crystal faces.

Figure 4.9 Gold precipitated on arsenopyrite crystals which have recrystallised from iodine transport.
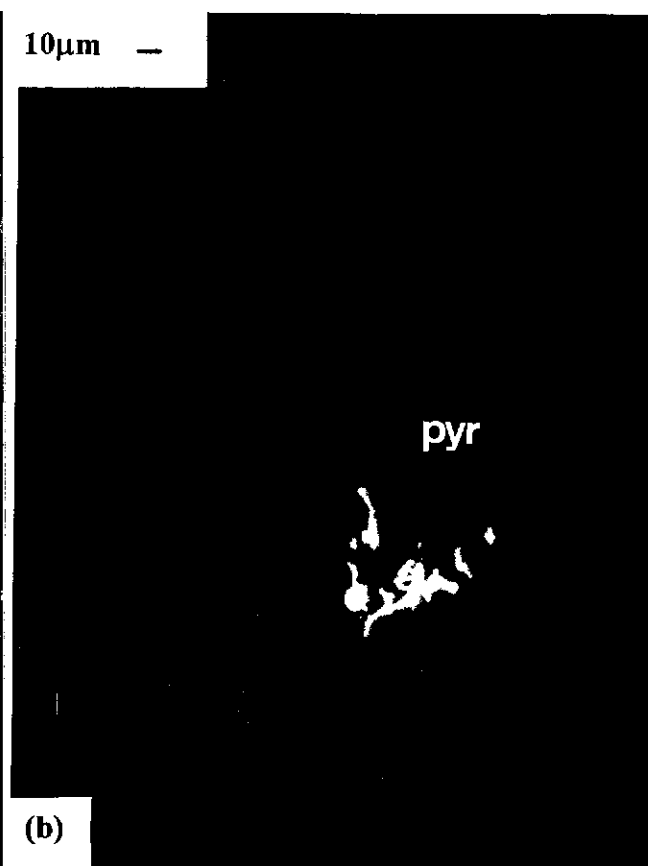
Figure 4.10 (a) Polished section of dendritic arsenopyrite crystals containing gold inclusions. (b) Close up of gold inclusions. The dark inclusions are pyrrhotite crystals.

löllingite (Figure 4.10a and b). The energy dispersive analyses of löllingite crystals (AV7c, Figure 4.11) indicated that they contained a small amount of sulfur. The presence of löllingite indicates that the pressure of the arsenic vapour must have been higher than for the arsenic sulfide gas. Experiments Av8, AV9 and Av11 resulted in little transport of the starting materials with them mostly recrystallising at the hot end, even when heated for a longer period of time. The use of ammonium chloride in these experiments did not provide a good transporting agent and resulted in arsenopyrite and pyrrhotite remaining in the hot end of the furnace. The gold present in these samples as irregular fine grains at the start of the experiment, recrystallised as octahedral crystals of pure gold (Figure 4.12a and b).

The results indicate that the gold appeared to have been transported at a different time to when the crystallisation of arsenopyrite occurred. Trace analyses of polished sections of several samples (AV7,AV9) did not detect any gold in the arsenopyrite crystals, indicating that the conditions used in these experiments were not suitable for gold incorporation in arsenopyrite.

4.3.3 Hydrothermal Synthesis in Gold Tubes

Synthesis experiments were initially carried out at 500°C and 2 kbars pressure under similar conditions to those outlined by Wu *et al.* (1989). Several modifications were carried out which provided some interesting results.

4.3.3.1 Arsenopyrite Synthesis from Mixtures of Fe_2O_3 +As+S

Arsenopyrite was synthesised from mixtures of hematite (Fe_2O_3), As and S with various aqueous solutions and under various temperature and pressure conditions in gold tubes as outlined in Table 4.3.

Examination of samples after heating (and washing the products), using both optical and scanning electron microscopes, showed that the products consisted mainly of arsenopyrite with varying amounts of pyrrhotite, and in some cases, gold inclusions and unreacted materials (arsenic, arsenic sulfur glass). In addition, several samples
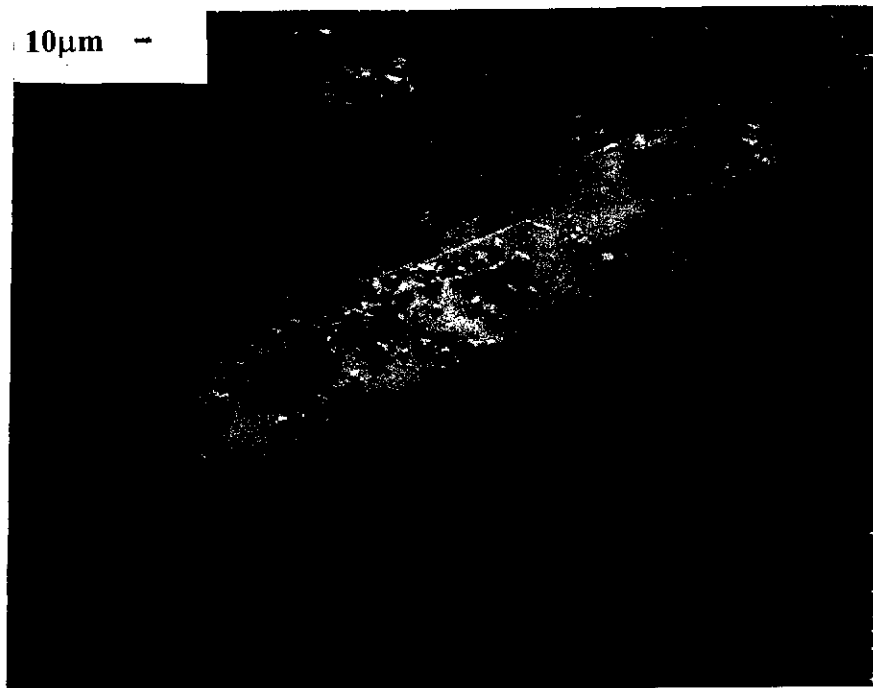
Figure 4.11 Scanning electron micrograph of a crystal of loellingite with striated faces due to rapid growth.
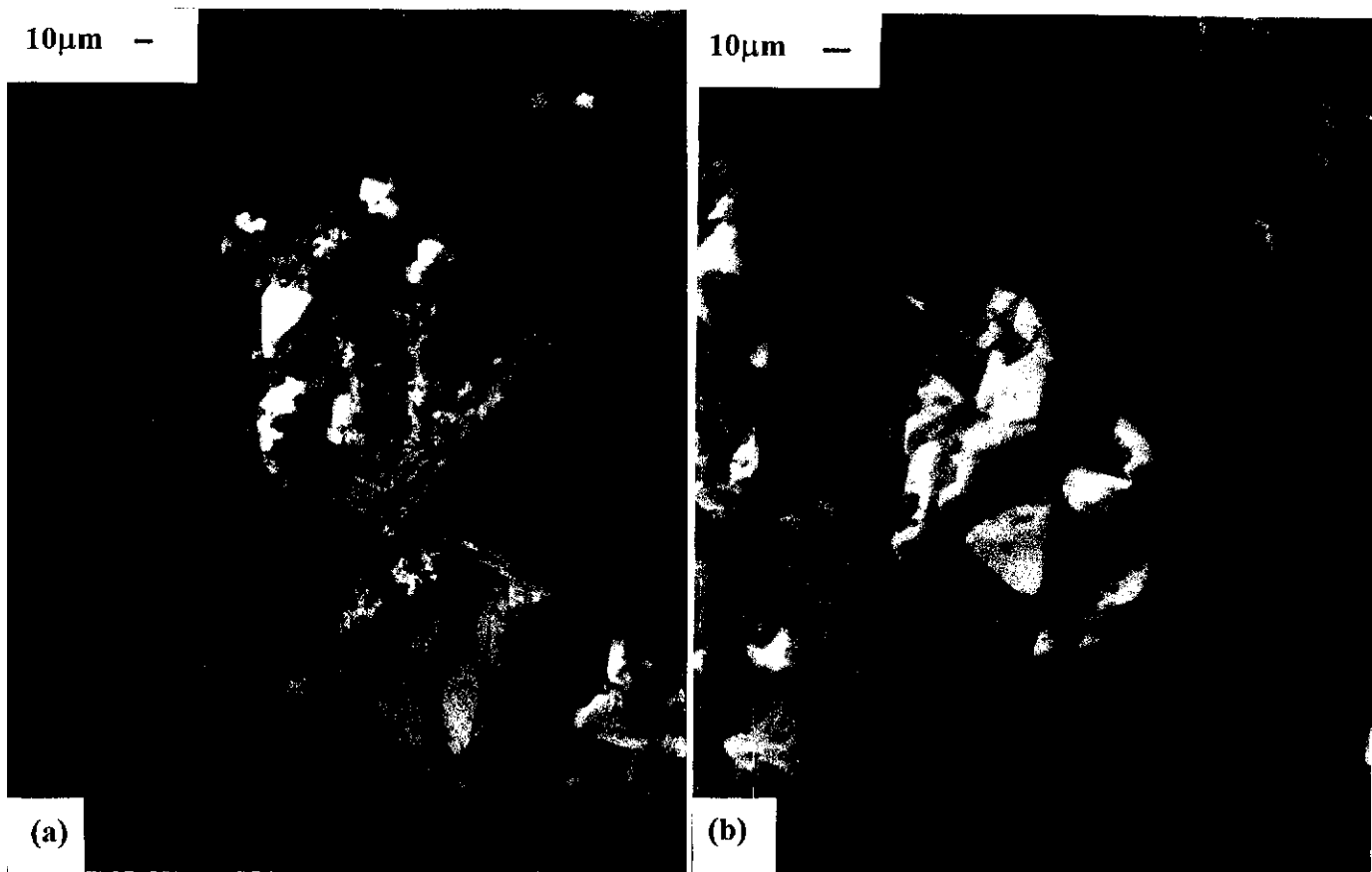
Figure 4.12 (a) Scanning electron micrograph of octahedral crystals of gold aggregated with striated arsenopyrite and platy pyrrhotite crystals. (b) Close up of octahedral gold crystals.

contained pyrite grains. The presence of arsenopyrite was confirmed by XRD patterns, electron microprobe analyses, and in some cases, by transmission electron microscopy.

Table 4.3 - Auriferous Arsenopyrite Experiments in Hematite , Arsenic and Sulfur Mixtures						
Sample	Conditions			Starting	Materials	major Products
	Press (kbars)	Temp (°C)	Period (days)	mixture* (g)	Solution (mls)	
Ap16b	2	500	17	0.2651	H₂O	0.27	Asp
Ap53			25	.1313		.2108	Asp
Ap14			20	0.203 +Au°	1.0M	0.416	Asp,Au
Ap33			6	0.1731of Ga2	HCl/H₂O	0.31	Asp
Ap11			7	0.1948		0.3792	Asp
Ap34			7	.21	1.6M	.3952	Asp
Ap35		537	2.5	0.1998	HCl/H₂O	0.4173	Asp
Ap40		500	10	.21	2M	.3952	Asp
Ap43			10	.25	HCl/H₂O	.4992	Asp
Ap70			7	.818		1.1318	Asp
Ap44			10	.1517	20000ppm	.4965	pyrr,Asp
Ap47	1		5	.2104	AuCl₃/H₂O	.55	pyrr,Asp
Ap48	2		15	.2087		.4847	pyrr,Asp
Ap49			8	.2062	2000ppm	.5852	Asp,pyrr
Ap13			14	0.1563	AuCl₃/H₂O	0.5043	Asp,pyrr
Ap16	1.8	495	17	2	pelletised	-	Asp,pyrr
Ap50	2	486	8	.201	AuCl₃/H₂O	.4551	Asp,pyrr
Ap41	1.5	405	52	.21	2M HCl/H₂O	.3952	Asp,py, pyrr,AsS
Ap56	2	400	7	.1945	2000ppm AuCl₃/H₂O	.5015	Asp,py, pyrr
Ap42			50		H₂O		Asp,pyrr, AsS
Ap58		300	50	.1233	2000ppm AuCl₃/H₂O	.5486	Asp,pyrr, AsS
Ap58b			50		H₂O		pyrr, AsS

*mixture - Fe₂O₃ 0.3545g, As 0.623g, S 0.128g

The acicular arsenopyrite grains ranged in size from 2μm to 50μm with an average grainsize being 10-20μm (Figure 4.13a). Large crystals of arsenopyrite, like those described by Wu and Delbove (1989), were never achieved. The crystals were mainly euhedral and grew as aggregates (Figure 4.13b and c). The faces of exposed crystals exhibited striations as a result of rapid growth under non-equilibrium conditions. Figure 4.13d shows a typical synthetic arsenopyrite formed at 500°C. The

Figure 4.13 Scanning electron micrographs of hydrothermally synthesised arsenopyrite from Fe$_2$O$_3$, As and S mixtures at 500°C and 2 kbars (a) Single crystals, (b) Aggregation of arsenopyrite crystals exhibiting striations on some crystal faces , (c) Polished section of aggregated arsenopyrite crystals containing ~1000ppm gold Dark grains are pyrrhotite; (d) Aggregated need-like crystals of arsenopyrite
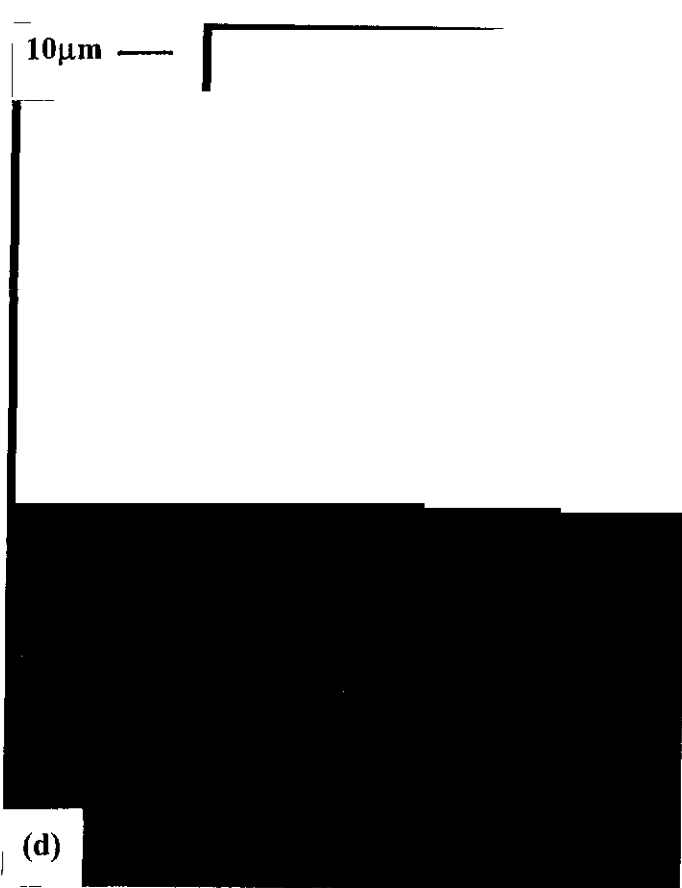
habits of all hydrothermally synthesised arsenopyrites were needle-like whereas arsenopyrites synthesised in the dry synthesis experiments were blocky rhombohedral in nature.

Attempts to grow arsenopyrite from starting materials in the absence of an aqueous solution resulted in the reaction of the starting materials with the gold tube. This problem has been observed by earlier workers (Clark, 1960; Kretschmar and Scott, 1976).

In experiments carried out at 300°C and 400°C, longer periods were generally required as the rate of reaction was much slower than at 500°C. Unfortunately, several experiments failed during the course of the experiment due to leakage of material past the sealed ends of gold tubes and also instrumental failure during electrical storms. Only the experiments which were successful are discussed. Despite the longer runs, particularly at 300°C, some of the starting materials remained unreacted in the presence of aqueous solutions of either distilled water or hydrochloric acid. The grainsize in the 400°C run ranged from 2-15μm in size (Figure 4.14a and b) whereas those experiments carried out at 300°C resulted in grainsizes less than 2μm. These grains were only confirmed to be arsenopyrite using a transmission electron microscope with an EDX. At 400°C, well crystallised pyrite grains were also observed along with arsenopyrite and pyrrhotite products. The pyrite grains were about 10μm in size and were blocky and euhedral in habit. The presence of pyrite was confirmed by transmission electron microscopic analyses (see Chapter 5).

The use of gold chloride solution with the starting materials resulted in some precipitation of gold. At 400°C, well crystallised arsenopyrite was produced in a shorter time than when distilled water or hydrochloric acid solutions were used (Figure 4.15a). In addition, several experiments resulted in the inclusion of gold within the arsenopyrite grains. The gold in the Ap56 run appears to be associated with the boundary of S-rich to As-rich arsenopyrite (Figure 4.15b). In experiments where 2 wt% Au chloride was used, the products consisted mainly of pyrrhotite, some gold
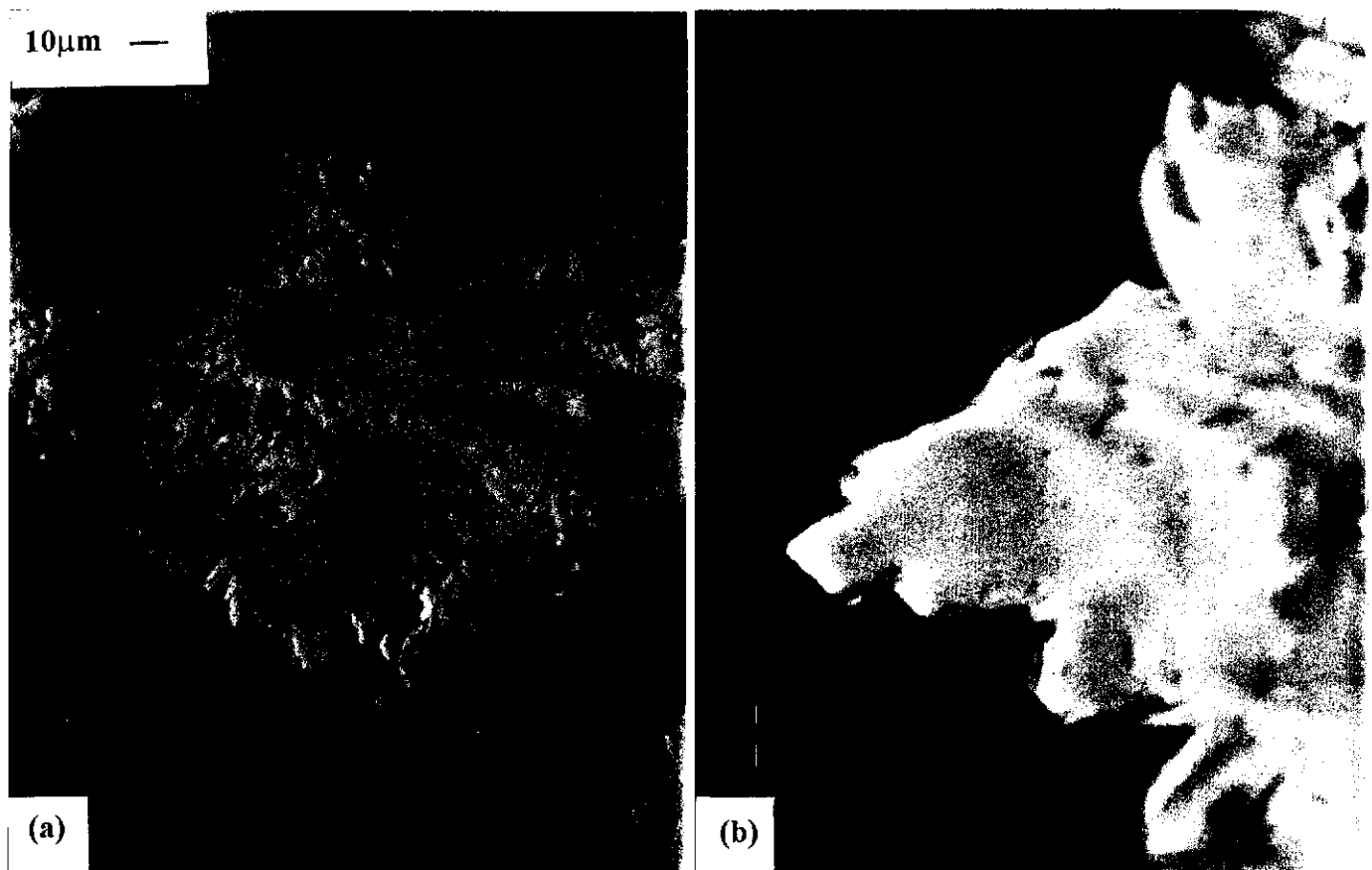
Figure 4.14 (a) Backscatter image of arsenopyrite crystals synthesised from Fe_2O_3, As and S mixtures at 400°C and 1.5 kbars in HCl/H_2O solution. (b) Close up of aggregated crystals of arsenopyrite.
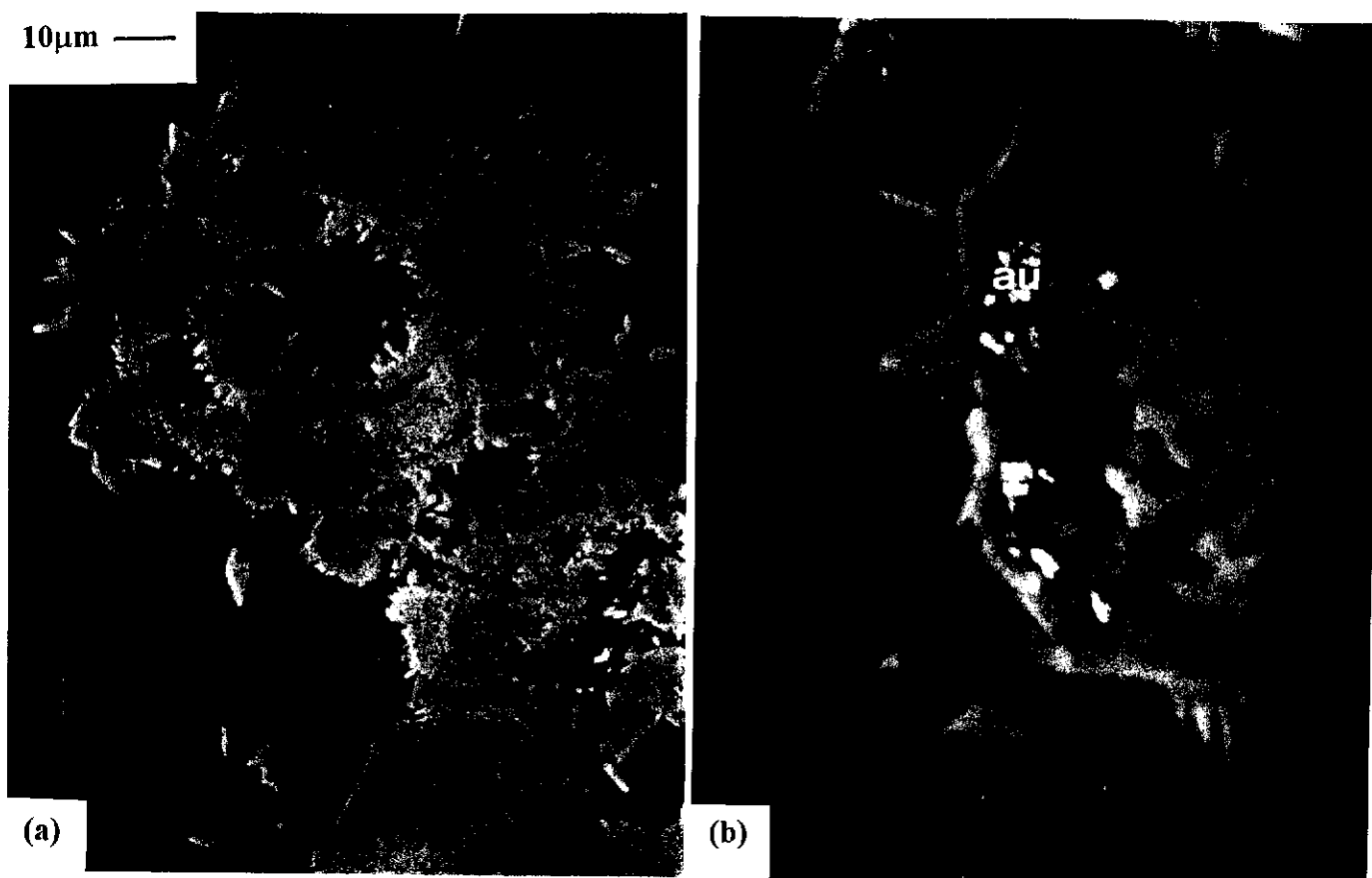
Figure 4.15 (a) Backscatter image of arsenopyrite crystals synthesised from Fe_2O_3, As and S mixtures at 400°C and 1.5 kbars in gold chloride solution (Ap56). (b) Gold inclusion in arsenopyrite crystals.

grains and fine arsenopyrite crystals. Figure 4.16 shows fine grained arsenopyrite within arsenic sulfide and pyrrhotite grains produced after heating to 300°C at 2 kbars.

4.3.3.2 Arsenopyrite Synthesis from Mixtures of FeOOH+As+S

In this synthesis method, goethite (FeOOH) was used instead of hematite in the starting material (Table 4.4). One advantage of using goethite instead of hematite was that no added aqueous solution was required to make crystals of auriferous arsenopyrite. The breakdown of goethite provided the aqueous solution. There was little reaction of the starting materials with the gold tubing. A higher content of gold was able to be incorporated in arsenopyrite using this method. Also, gold tubes could be packed with more starting materials, using less gold tubing and more easily sealed in the absence of aqueous solution in the starting material.

Table 4.4 - Auriferous Arsenopyrite Experiments in Goethite , Arsenic and Sulfur Mixtures							
Sample	Conditions			Starting	Materials		Major products
	Pressure (kbars)	Temp (°C)	Period (days)	mixture* (g)	Solution (mls)		
Ap52	2	500	20	0.7	-		Asp
Ap61			20	0.718			
Ap62			20	0.12+ 0.0018 As			
Ap63			20	0.0631+ 0.0031 S			Asp,pyrr
Ap71			7	0.8287			Asp
Ap51b			26	0.1135	2000ppm	0.2291	Asp,pyrr,
Ap54			25	0.151	AuCl$_3$/H$_2$O	0.4796	
Ap59			20	0.1709	HAuCl$_4$/H$_2$O	0.0044	
Ap60			22	.0889	2M	0.1473	
Ap64			20	.0702	HCl/H$_2$O	0.0372	
Ap72		300	10	0.4056	-		AsS,unrt

*mixture - FeOOH 0.3945g, As 0.623g, S 0.128g

The goethite used (FeOOH) has a larger surface area than the hematite (30m^3/gm and 15m^3/gm respectively). Although goethite breaks down at ~250-260°C it can absorb gold complexes on its surface (Schoonen et al., 1992) which increases the amount of gold in the arsenopyrite crystals formed.

The various experiments carried out are shown in Table 4.4. Generally, the same conditions of synthesis were used as for the hematite mixtures. These conditions resulted mainly in arsenopyrite except in experiments at 300°C where partially reacted mixtures of arsenic, sulfur and iron were present.

The crystals of arsenopyrite had euhedral needle-like habits, similar to those grown using hematite (Figure 4.17). When the As:S ratio of the starting materials (Ap62) was increased, no changes were observed in the crystal size or abundance of arsenopyrite (Figure 4.18). However, when the As:S ratio was decreased, smaller crystals of arsenopyrite were present, together with an increase in amount of pyrrhotite crystals (Figure 4.19). Synthesis of arsenopyrite crystals using 1M HCl/H_2O solution (Ap64) resulted in arsenopyrite crystals similar to those formed from FeOOH, As and S mixtures (Figure 4.20). Arsenopyrite crystals synthesised in gold chloride solutions resulted in gold inclusions (Figure 4.21) and an increase in pyrrhotite content. Figure 4.22 shows the mixture synthesised at 300°C containing mainly arsenic sulfur compounds and pyrrhotite.

4.3.4 Characterisation of Gold in Synthetic Arsenopyrite

All synthetic arsenopyrite samples were examined in detail using the scanning electron microscope in backscatter mode, at high contrast. These examinations revealed that gold inclusions were present in all samples except most of those synthesised hydrothermally in gold tubes. Even at a magnification of 40000 times, no inclusions could be observed in the latter. Trace gold analyses of the arsenopyrites synthesised using the dry synthesis and iodine transport methods indicated that no detectable gold occurred in the arsenopyrite crystals, except for the gold inclusions observed. However, for the hydrothermally synthesised samples, electron microprobe analyses using the trace analysis technique revealed the presence of high concentrations of gold not present as inclusions. TEM, image contrast and selected area diffraction of some of the samples rich in gold (Ap41 and Ap56), did not show any gold present as fine inclusions in the crystals examined. In the arsenopyrite
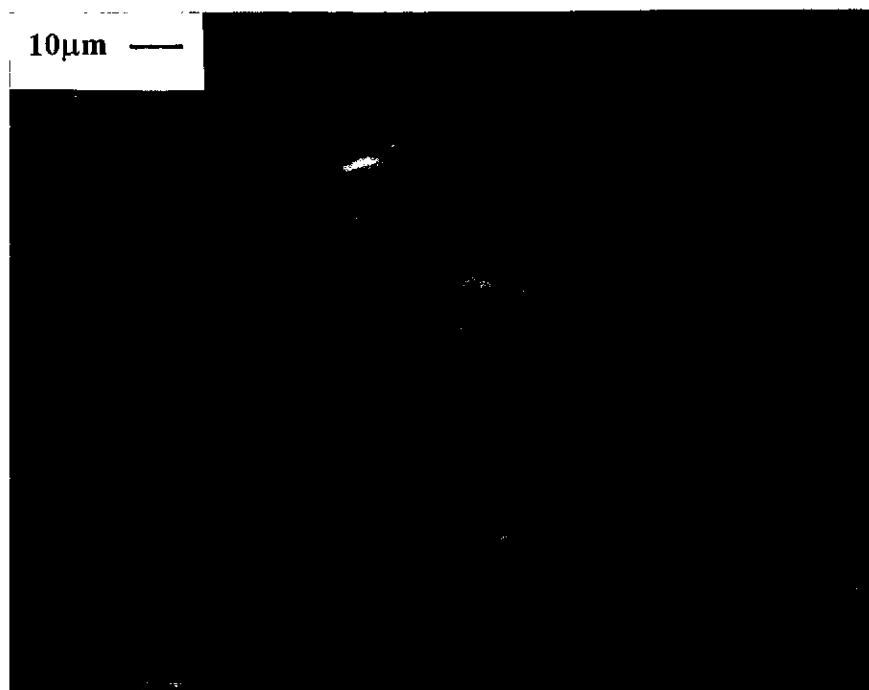
Figure 4.16 Backscatter image of arsenopyrite in a matrix of partially reacted material synthesised at 300°C (Ap58).
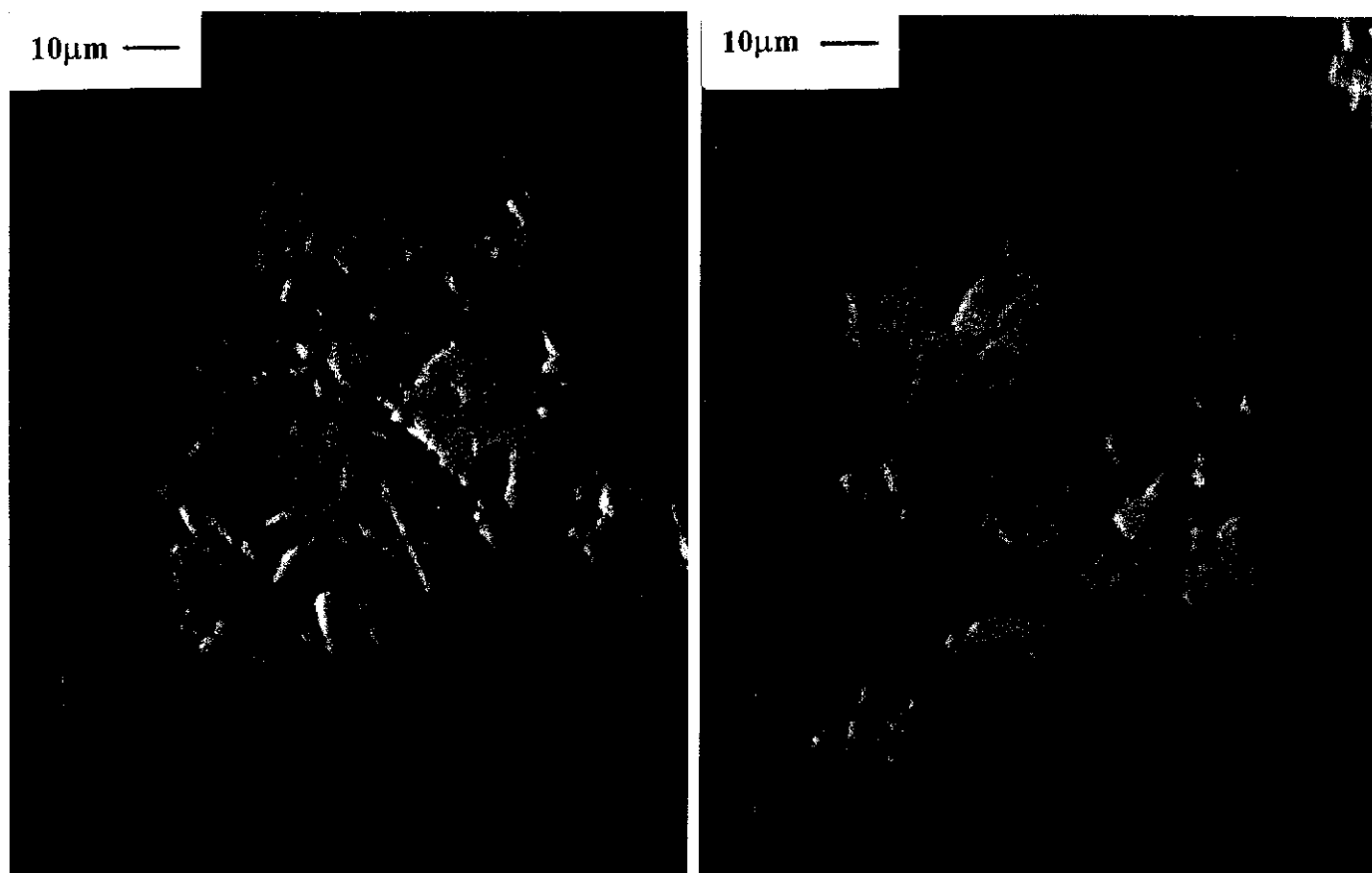
Figure 4.17 Backscatter images of typical arsenopyrite grains synthesised from FeOOH. As and S mixtures (AP52).
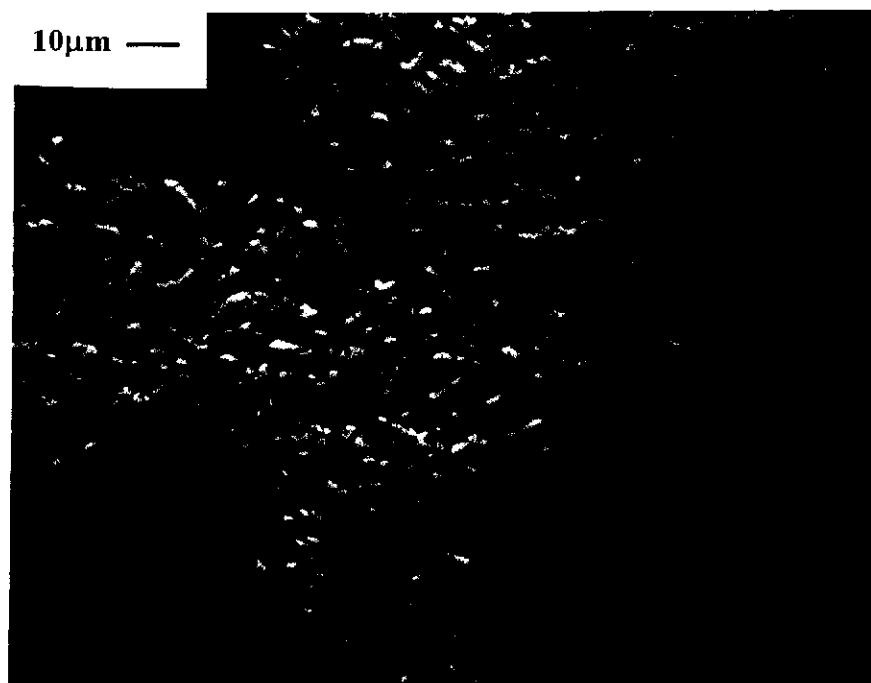
Figure 4.18 Backscatter image of arsenopyrite grains synthesised from a FeOOH, As and S mixture containing a higher As:S ratio (AP62).
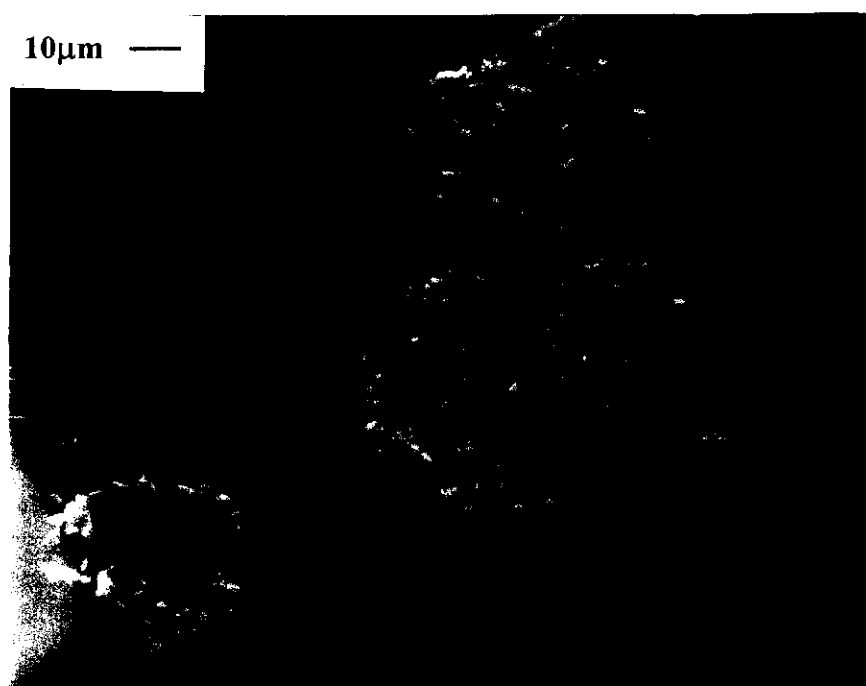
Figure 4.19 Backscatter image of arsenopyrite grains synthesised from a FeOOH, As and S mixtures containing a lower As:S ratio (AP63).
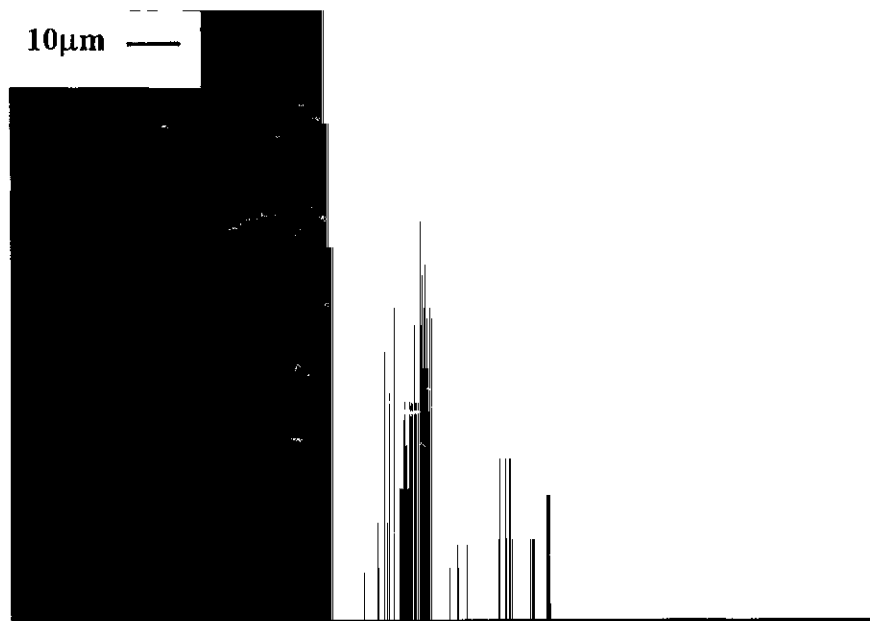
Figure 4 20 Backscatter image of arsenopyrite grains synthesised from a FeOOH, As and S mixture (AP64) in 1M HCl/H$_2$O solution.
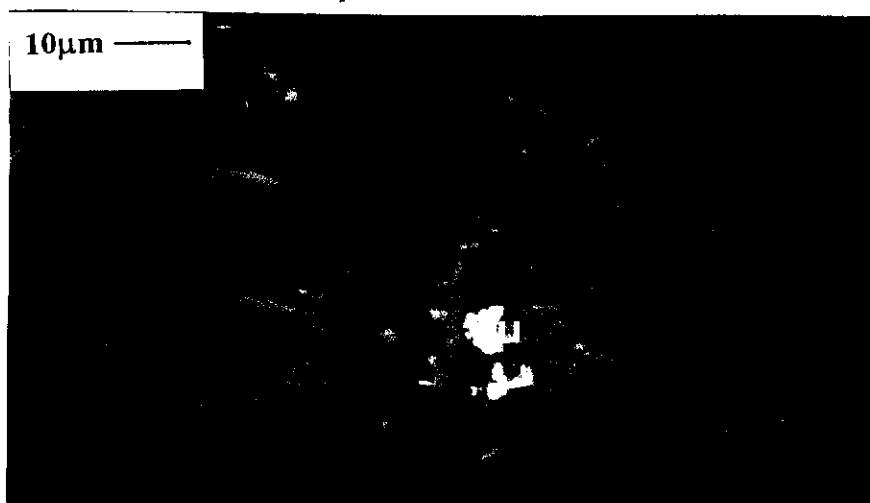
Figure 4.21 Backscatter image of arsenopyrite grains synthesised from a FeOOH, As and S mixture (AP64) in 2000 ppm AuCl/H$_2$O solution.
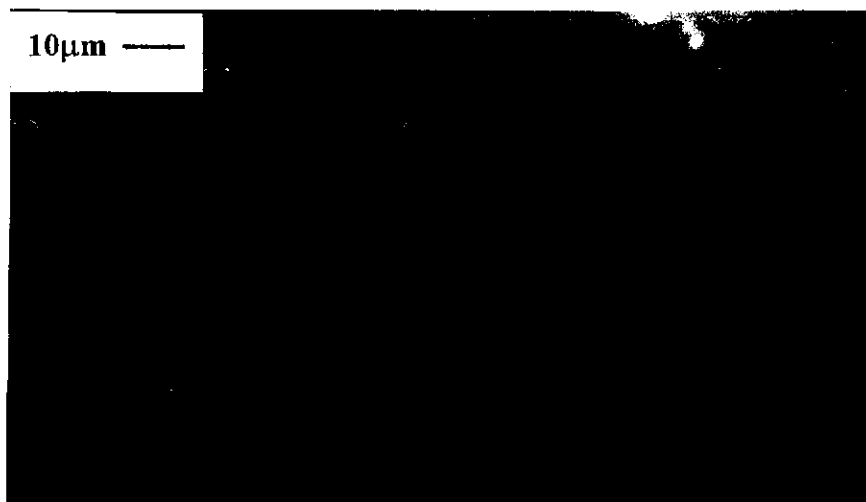
Figure 4.22 Backscatter image of arsenopyrite grains synthesised from a FeOOH, As and S mixture (AP72) at 300°C.

samples synthesised hydrothermally at 400°C, gold was easily detected by the energy dispersive analysis equipment mounted on both the SEM and TEM. However, gold was only detected in a few grains of arsenopyrite synthesised at 500°C.

4.3.4.1 Amount and Distribution of Gold in Hydrothermally Synthesised Arsenopyrite

The distributions of gold in several of the arsenopyrites synthesised are shown in Figures 4.23 to 4.31. Arsenopyrite synthesised from hematite, As and S mixtures in 1M hydrochloric acid solution (Figure 4.23) at 500°C, resulted in up to 0.6 wt% gold in arsenopyrite with most grains analysed ranging from 0 to 0.25 wt% gold. In 2M HCl solution the arsenopyrite synthesised contained up to 1.3 wt% gold with most ranging between 0 and 0.2 wt% of gold (Figure 4.24). Arsenopyrite synthesised in distilled water resulted in only a low amount of gold ($\leq$0.1 wt%). Arsenopyrite synthesis at 400°C in hydrochloric acid solution resulted in up to 2 wt% gold (Figure 4.25) with gold content distributed over the whole range. Wu and Delbove (1989) observed that more gold could be obtained in the synthetic arsenopyrite if hydrochloric acid solutions were used. They also found that increasing the hydrochloric acid concentration and reducing the temperature from 500°C to 400°C resulted in an increase in the amount of gold incorporated in arsenopyrite. The results obtained here are consistent with their results.

Arsenopyrite synthesised in gold chloride solution at 500°C resulted in up to 0.5 wt% gold in arsenopyrite (Figure 4.26) with most gold values between 0 and 0.3 wt%. Gold inclusions were also evident in some of the arsenopyrite grains. A higher percentage of gold was obtained in arsenopyrites synthesised in gold chloride solution at 400°C (Figure 4.27) than at 500°C. Gold inclusions were also observed at boundaries of zoned S-rich and As-rich arsenopyrite grains. Although the arsenopyrite synthesised in gold chloride solution at 400°C contained less gold compared with the arsenopyrite synthesised in hydrochloric acid solution at 400°C (period of 52 days), the first procedure resulted in a high gold content and higher percentage of
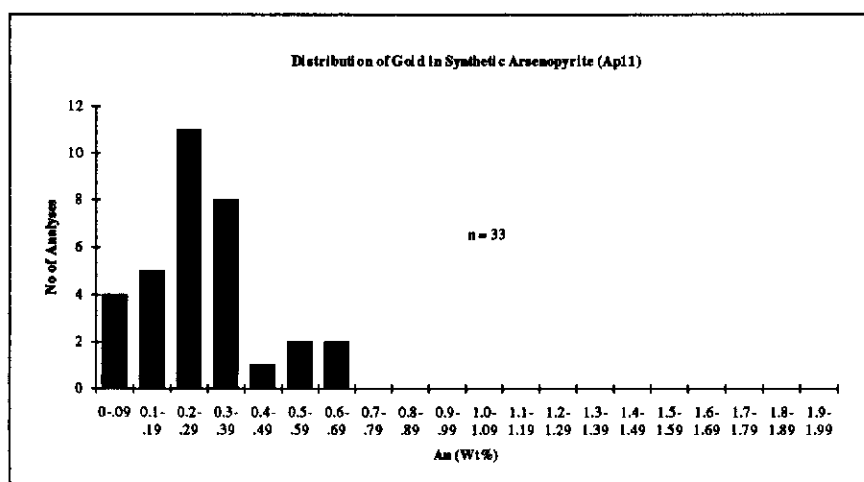
Figure 4.23 A histogram showing the distribution of gold concentration in synthetic arsenopyrite from Fe_2O_3, As and S in a 1M HCl/H_2O solution at 500°C and 2kbars.
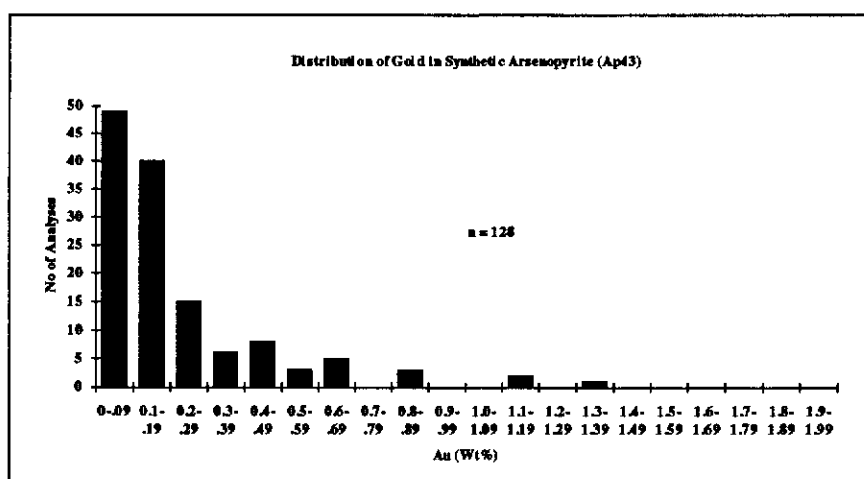
Figure 4.24 A histogram showing the distribution of gold concentration in synthetic arsenopyrite from Fe_2O_3, As and S in a 2M HCl/H_2O solution at 500°C and 2kbars.
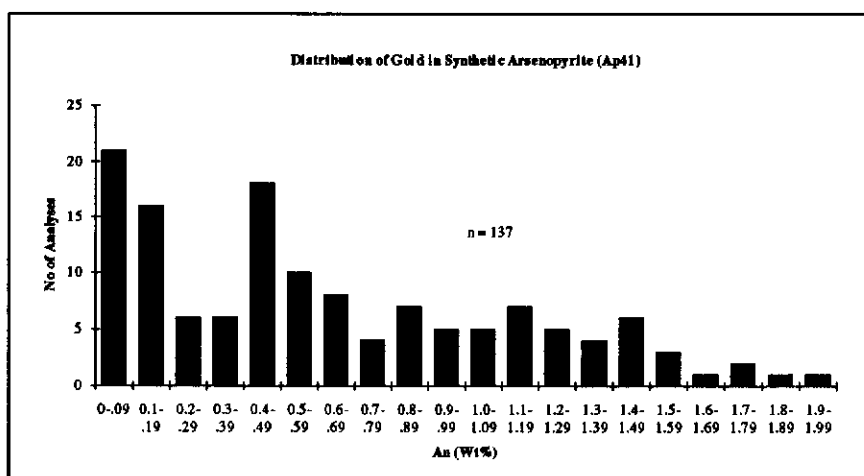
Figure 4.25 A histogram showing the distribution of gold concentration in synthetic arsenopyrite from Fe_2O_3, As and S in a 2M HCl/H_2O solution at 400°C and 1.5kbars.
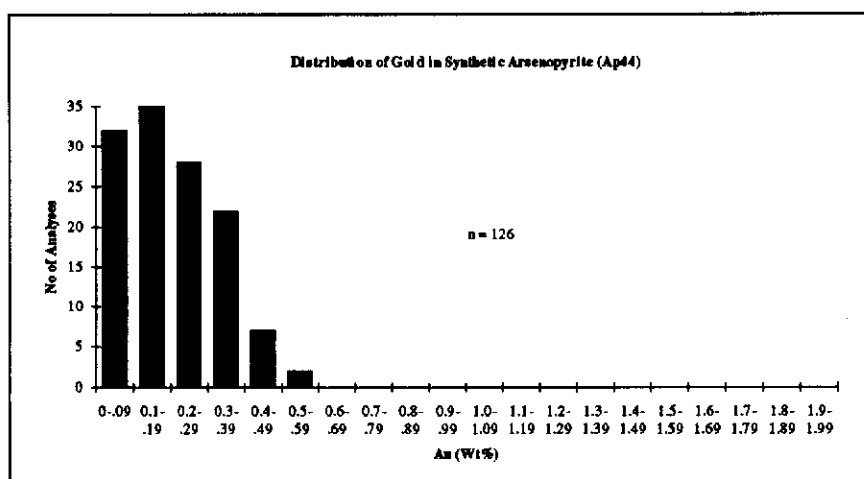
Figure 4.26 A histogram showing the distribution of gold concentration in synthetic arsenopyrite from Fe_2O_3, As and S in a 2000ppm $AuCl_3/H_2O$ solution at 500°C and 2kbars.
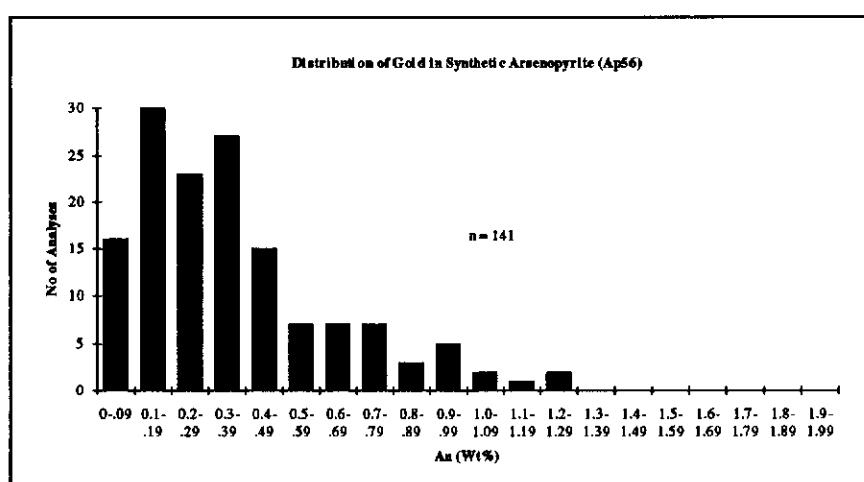
Figure 4.27 A histogram showing the distribution of gold concentration in synthetic arsenopyrite from Fe_2O_3, As and S in a 2000ppm $AuCl_3/H_2O$ solution at 400°C and 2kbars.

Distribution of Gold in Synthetic Arsenopyrite (Ap52)

n = 162

Au (Wt%)
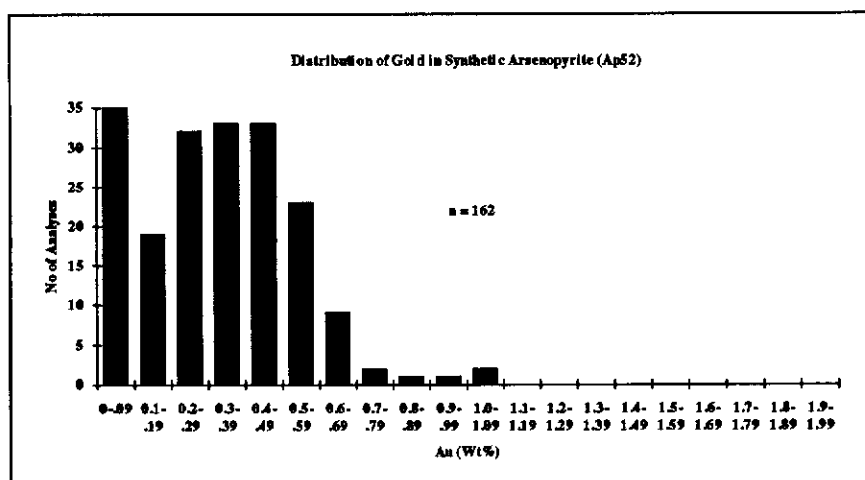
Figure 4.28 A histogram showing the distribution of gold concentration in synthetic arsenopyrite from FeOOH, As and S at 500°C and 2kbars.

Distribution of Gold in Synthetic Arsenopyrite (Ap64)

n = 51

Au (Wt%)
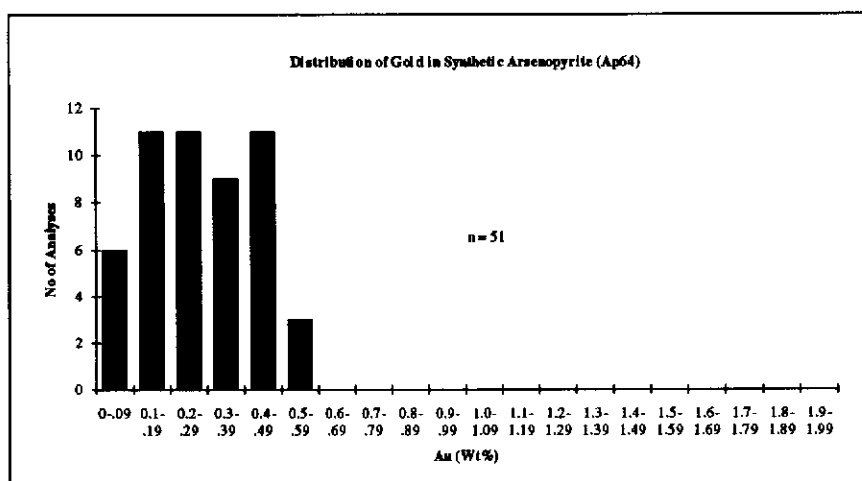
Figure 4.29 A histogram showing the distribution of gold concentration in synthetic arsenopyrite from FeOOH, As and S in a 1M HCl/H_2O solution at 500°C and 2kbars.
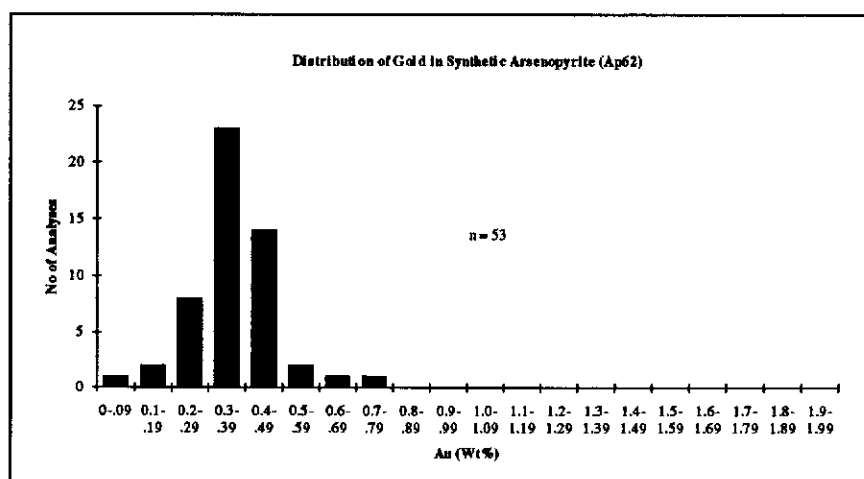
Figure 4.30 A histogram showing the distribution of gold concentration in synthetic arsenopyrite from FeOOH, As and S with an increased As:S ratio at 500°C and 2kbars.
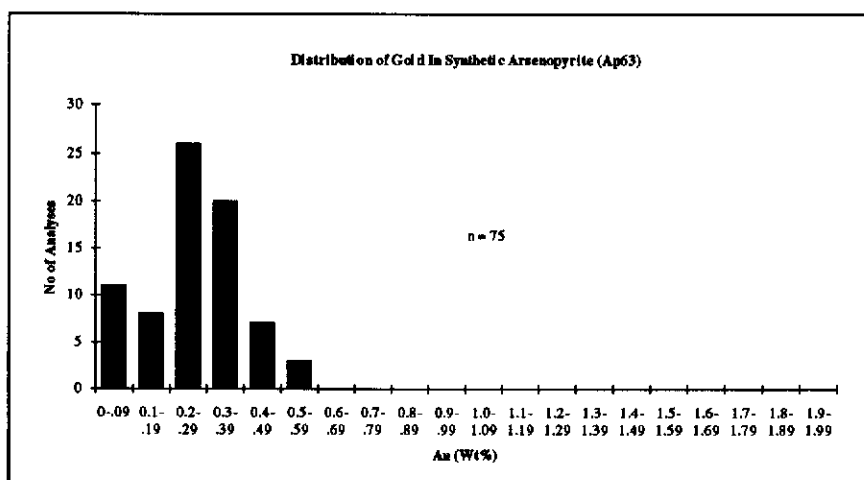
Figure 4.31 A histogram showing the distribution of gold concentration in synthetic arsenopyrite from FeOOH, As and S with a decreased As:S ratio at 500°C and 2kbars.

arsenopyrite in a shorter period of time (7 days). Thus, the presence of gold chloride may have enhanced crystal growth. The presence of gold grains and inclusions in the arsenopyrites synthesised indicate that the samples may have been supersaturated under the conditions used.

The use of goethite instead of hematite in the starting materials in the absence of aqueous solution, resulted in a higher gold content in the synthesised arsenopyrite (Figure 4.28) than was obtained in hydrochloric acid or gold chloride solutions at 500 °C. Arsenopyrite synthesised in the presence of hydrochloric acid with goethite, arsenic and sulfur, resulted in a greater number of grains containing evenly distributed gold between 0 and 0.5wt% (Figure 4.29). However, the gold content was lower than for those synthesised in hematite, arsenic and sulfur mixtures. This may be due to the reaction of hydrochloric acid with goethite occurring and being much faster than the reaction with hematite. The formation of ferric chloride would reduce the number of chloride ions available to take gold into solution. The reaction of chloride ions with iron in the iron oxides may account for the precipitation of gold in experiments carried out where gold chloride solution was used.

Several experiments were carried out in goethite mixtures, and in the absence of aqueous solution, where the arsenic to sulfur ratio was adjusted to determine if there was any effect on the amount of gold taken up by arsenopyrite. Figures 4.30 and 4.31 show the gold distribution in the arsenic and sulfur rich samples, respectively. For a higher As:S ratio in the starting materials, most grains contained greater than 0.2 wt% gold with an average of 0.35 wt% gold. For a lower As:S ratio in the starting materials, the amount of arsenopyrite present was reduced with pyrrhotite (and pyrite) also being present. The gold content in arsenopyrite is slightly less than in the other samples synthesised with goethite mixtures with an average of 0.2 wt %. No gold was detected in the pyrrhotite samples.

The high gold content observed in arsenopyrite synthesised from FeOOH, As and S mixtures indicates that gold is transported as either a sulfide complex or possibly as an arsenic sulfide complex. Under the acidic conditions and high oxidation

potentials in the system, arsenic most probably exists in solution as the acid $H_3AsO_3^0$. Therefore, the gold would be transported as a sulfide complex (possibly as $Au(HS)^0$, Seward, 1991). In contrast to Wu and Delbove (1989) findings, chloride solutions are not required for high gold concentrations in arsenopyrite.

4.3.4.2 Chemical Composition of Synthetic Arsenopyrite

Table 4.5 shows the average iron, arsenic, sulfur and gold compositions of the various synthetic auriferous arsenopyrites produced together with their standard deviations.

Table 4.5 Synthetic Arsenopyrite samples (average, sd)				
	Fe (At frac)	As (At frac)	S (At frac)	Au (At frac)
Synthesis at 500°C, 2k Bars, from hematite + As + S mixtures				
Ap11	0.334±0.004	0.337±0.02	0.328±0.02	0.001±0.0004
Ap43	0.331±0.007	0.356±0.03	0.311±0.03	0.001±0.001
Ap48	0.334±0.007	0.316±0.02	0.349±0.02	0.0004±0.0002
Ap44	0.336±0.006	0.328±0.04	0.335±0.05	0.0008±0.0003
Synthesis at 400°C, 2k Bars, from hematite + As + S mixtures				
Ap41	0.328±0.01	0.322±0.02	0.350±0.02	0.003±0.001
Ap56	0.331±0.005	0.328±0.02	0.340±0.02	0.001±0.001
Synthesis at 500°C, 2k Bars, from goethite + As + S mixtures				
Ap52	0.328±0.009	0.352±0.01	0.318±0.02	0.0014±0.0005
Ap62	0.334±0.006	0.356±0.007	0.309±0.01	0.0013±0.0003
Ap63	0.335±0.01	0.339±0.01	0.325±0.02	0.0012±0.0004
Ap64	0.332±0.01	0.346±0.02	0.321±0.03	0.0009±0.0004

The arsenic and sulfur contents varied, as indicated by the high standard deviation values. The iron values also appeared to vary (±0.01at. frac.) compared with those obtained for natural arsenopyrite samples (±0.002 at. frac.). The small size (~15-60μ m) and aggregated nature of the synthetic crystals made it difficult to distinguish different chemical zones at high image contrast in a backscattered image from the SEM. Where boundaries occurred they were diffuse. In many cases, the chemical composition obtained by the electron microprobe represented a compositional average. Figures 4.32a to g show the arsenic to sulfur ratio versus gold content. The arsenic to sulfur ratio varied from 0.8 to 1.2 with a high percentage ratioes below one, as indicated by the average sulfur values in Table 4.6. Generally, an increase in As:S
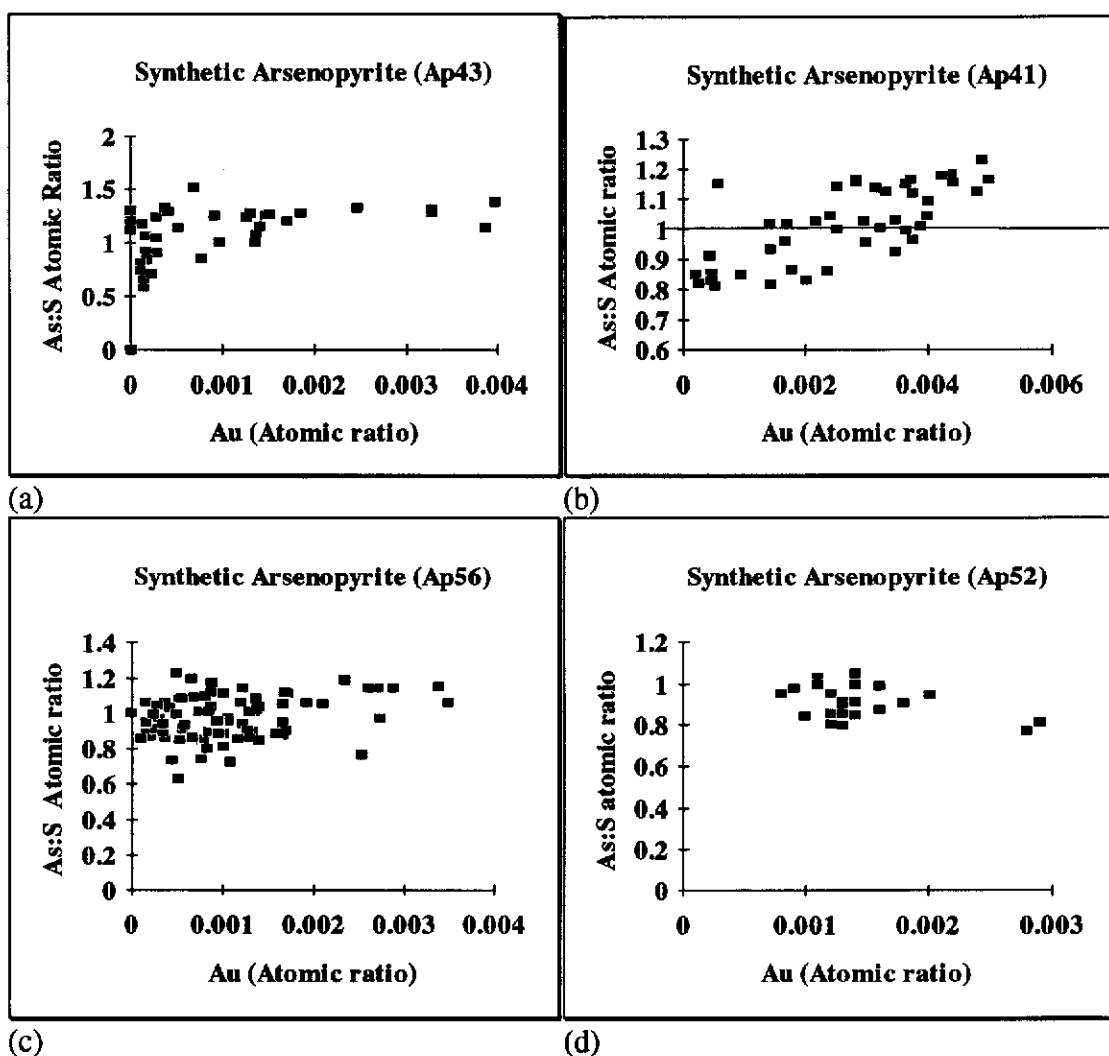
Figure 4.32 As:S ratio of synthetic arsenopyrites versus gold content from Haematite, Arsenic and sulfur mixtures . (a)500°C in 2M HCl, 2 kbars; (b) 400°C in 2M HCl, 1.5 kbars; (c) 400°C in AuCl, 2 kbars; and (d) from Goethite, Arsenic and sulfur mixture at 500°C , 2 kbars.
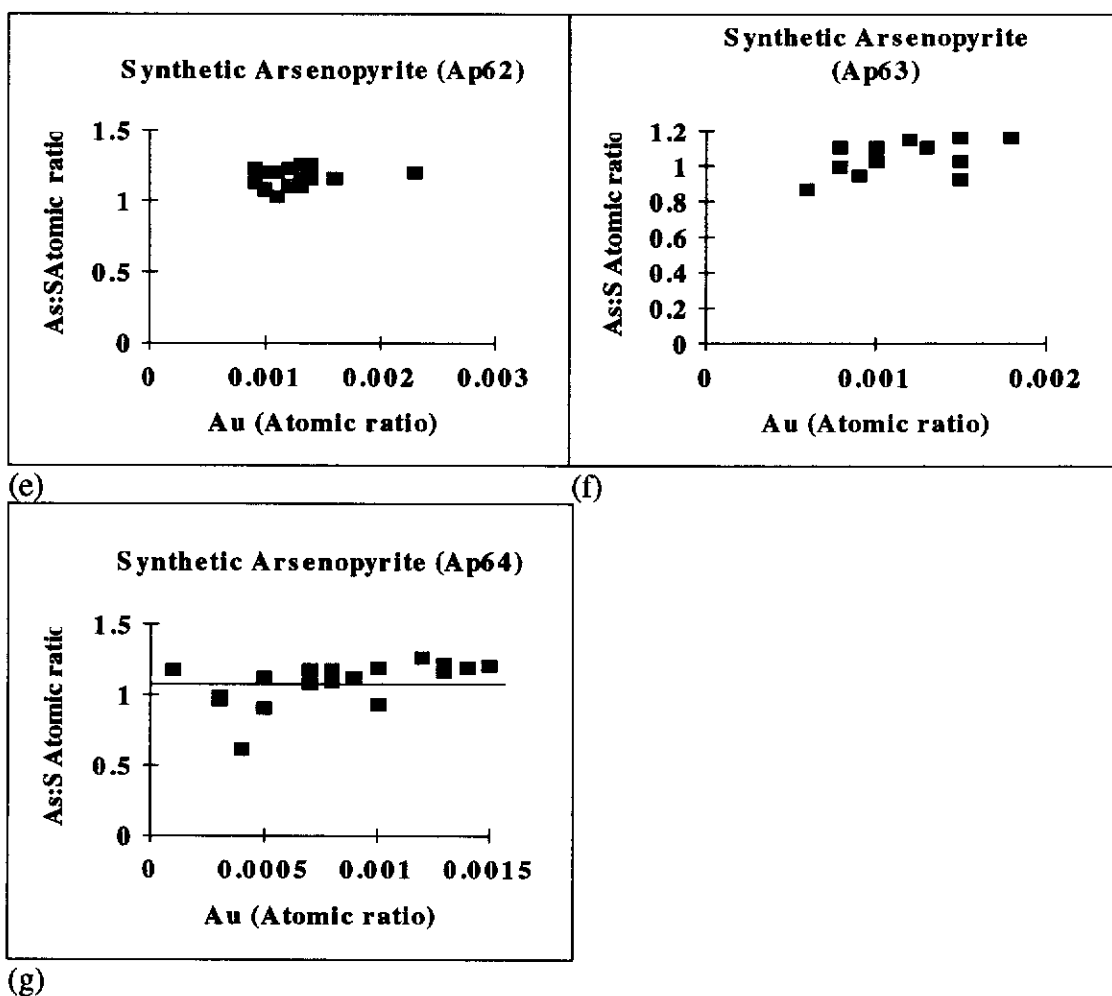
Figure 4.32 As:S ratio of synthetic arsenopyrites versus gold content from Goethite, Arsenic and sulfur mixtures (500°C, 2kBars). (e) excess arsenic; (f) excess sulfur; and (g) in HCl.

ratio resulted in an increase in gold content for arsenopyrites synthesised in the presence of chloride solutions (Figures 4.32a, b, c and g). The gold was more homogeneous and independent of the As:S ratio value for arsenopyrites synthesised from goethite mixtures (Figures 4.32d to f). It is possible that the form of the gold species in solution has an influence on the distribution of gold in the arsenopyrite structure. This is discussed in section 4.3.4.4.

In view of the variation in iron values observed in these synthetic arsenopyrite samples, the distribution of arsenic, sulfur and gold among structural sites was calculated in order to see whether gold could be associated with the iron site, using the rules devised by Johan *et al.* (1989). When (As/S)<1 the excess sulfur is attributed to the arsenic site and the excess arsenic thus formed was transferred to the iron sites. For (As/S)>1 the sulfur sites were first filled by arsenic and the excess of arsenic is attributed to iron sites. Figures 4.33a, b, c and d show the excess arsenic and combined excess arsenic and gold versus the iron content for various arsenopyrite samples. Many of the points fall into the range of the error bars shown in the graphs which makes it inconclusive as to whether gold can be attributed to the iron sites. The presence of excess arsenic correlates well with iron content and some outlier points appear iron deficient. This would appear to indicate that some arsenic is associated with the iron site. However, the good correlation and perfect straight line observed when gold is taken into account, is a consequence of the normalisation procedure. For this relationship to be of value the assumption has to be made that all sites in arsenopyrite are filled and that no sites are vacant (i.e. Fe:As:S site ratio is 1:1:1). The negative values indicate excess iron and may be attributed to site vacancies in the arsenopyrite structure or experimental error. In addition, no correlation was observed with the calculated excess arsenic and gold as was found by Johan *et al.* (1989) in their analyses of natural arsenopyrites. Therefore using the electron microprobe, it is uncertain as to whether gold is on the iron site.
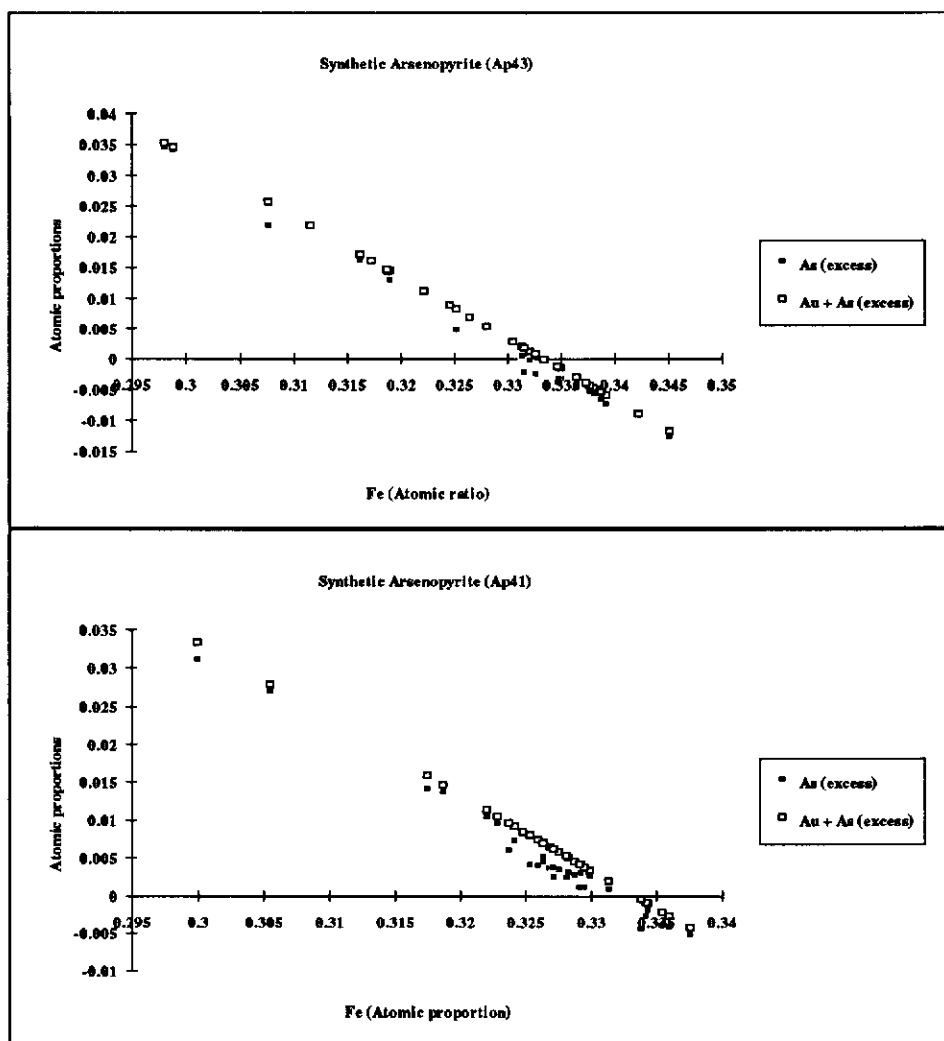
Figure 4.33 Excess arsenic and combined excess arsenic and gold versus iron content. (a)500°C in 2M HCl, 2 kbars; (b) 400°C in 2M HCl, 1.5 kbars.
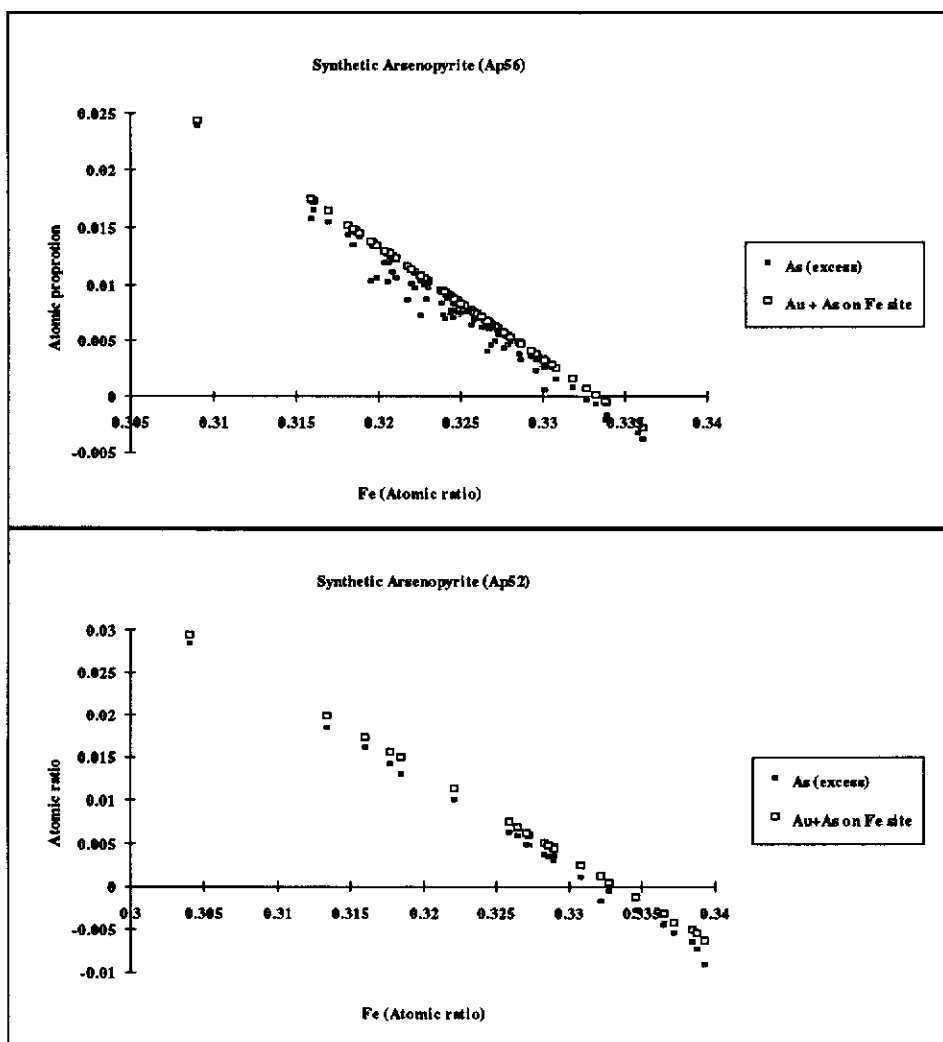
Figure 4.33 Excess arsenic and combined excess arsenic and gold versus iron content.
(c) 400°C in AuCl, 2 kbars; and (d) 500°C , 2 kbars.

4.3.4.3 Gold Mössbauer Studies on Synthetic Arsenopyrite

The [197]Au Mössbauer spectra of two synthetic arsenopyrites, one synthesised from a mixture of hematite, arsenic and sulfur mixture (AP41) and the other from goethite, arsenic and sulfur (AP52) are shown in Figures 4.34a and b respectively. In both spectra there are two distinct peaks, one at a positive velocity of ~3.5 mm/s and a smaller peak at a negative velocity. Both spectra are very similar to the spectrum obtained by Wu *et al.* (1990) for a synthetic arsenopyrite sample. The small peak probably represents metallic gold although bulk metallic gold has an isomer shift of - 1.23 mm/s, while in these two samples they are -1.15±0.04 mm/s and -1.42±0.09 mm/s respectively. The appearance of this peak may be attributed to very small gold inclusions either not removed when the sample was washed or fine inclusions within the arsenopyrite grains. Alternatively this small peak may represent one of two components of a quadrupole doublet whose second component hides below the main dip at about +3.5 mm/s. This, however, cannot be proven at this stage (Wagner, *pers. comm*).

The large asymmetrical peak at +3.5 mm/s corresponds to combined gold in arsenopyrite samples as has been observed in many natural and synthetic arsenopyrites analysed by Wagner (Friedl *et al.*, 1992). The isomer shift for arsenopyrites normally falls into the range of +3.2 to +3.7 mm/s. The asymmetry fit was reproduced by superimposing several quadrupole doublets with different quadrupole splittings and isomer shifts. The main purpose of these Mössbauer studies was to confirm whether the gold was bonded and did not exist as fine submicron inclusions. The results confirm that most of the gold in the arsenopyrites synthesised using either hematite or goethite, with arsenic and sulfur mixtures, was in solid solution. The question as to where the gold is situated in the arsenopyrite structure will be discussed in Chapter 6.

4.3.4.4 Discussion on Gold Uptake in Arsenopyrite

Interpretation of possible mechanisms of gold substitution in arsenopyrite and the precipitation observed in several experiments was hindered by the absence of
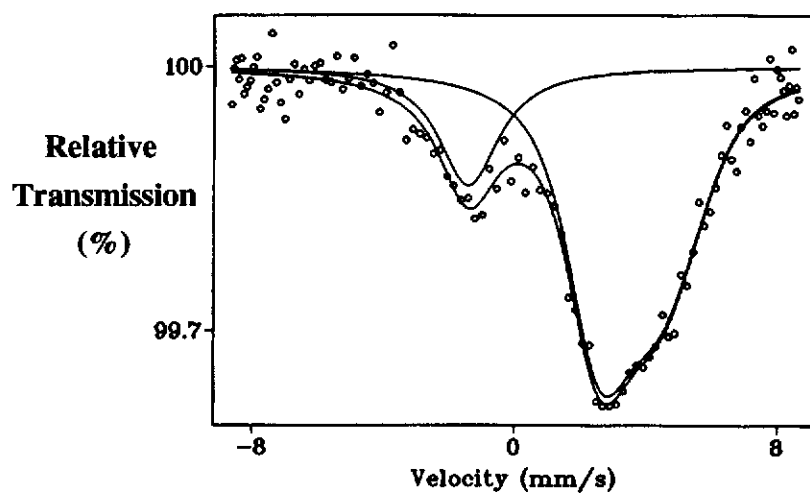
(a)
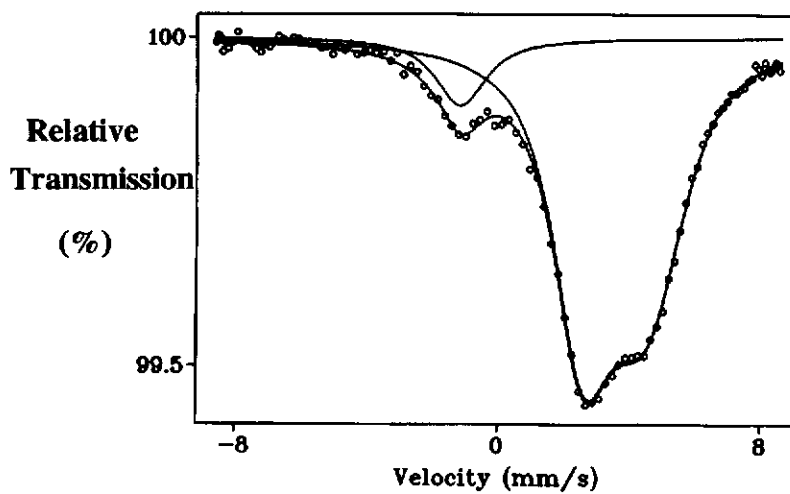
(b)

Figure 4.34 [197]Au Mössbauer spectrum of synthetic auriferous arsenopyrite from (a) Fe_2O_3, As and S mixtures and (b) FeOOH, As and S mixtures.

information on arsenic, sulfur, iron and gold species in solution under the conditions used. It was not possible in the current studies to monitor the reaction processes during the experiments and information can only be provided from observations of the starting and final products. Most experimental work on hydrothermal chemical species has been carried out on systems from room temperature to 350°C for gold sulfide species (Seward, 1991) and only gold chloride species have been investigated to higher temperatures (500°C) (Henley, 1975). However, thermodynamic calculations and experimental data obtained at low temperatures can, to a limited extent, be extrapolated to higher temperatures to give possible mechanisms (Heinrich and Eadington, 1986). Variations observed in the compositions of the synthetic arsenopyrites examined, showed that none of the systems was ever in equilibrium.

The amount of oxygen can be calculated from the fact that the oxygen fugacity in the system will be that from the oxygen obtained from the breakdown of Fe_2O_3 (and FeOOH) and the formation of arsenopyrite and arsenolite (As_2O_3). The fO_2 was calculated from the reaction scheme

$$2As(s) + 3/2O_2 \text{ (g)} = As_2O_3 \text{ (s)}$$
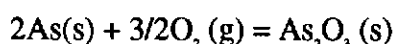
and the general thermodynamic equation

$$\Delta G^\circ_{r,T} = -RT \ln K_r$$

where $\Delta G^\circ_{r,T}$ is the estimated free energy of the above reaction at the temperature (T K) and K_r is the equilibrium constant of the above chemical equation.

Calculations of the oxygen fugacity under conditions carried out in the synthesis of arsenopyrite indicated that the oxygen fugacity in terms of log fO_2 was around -36 and -38 for 400°C and 500°C respectively. Under these high oxygen potentials and low pH conditions the form of arsenic is most probably H_3AsO_4, as was shown in area predominance diagrams calculated by Heinrich and Eadington (1986). Therefore, it is possible that arsenic does not participate directly in the transport of gold. High gold concentrations in arsenopyrites have been associated with high

arsenic to sulfur ratios in auriferous arsenopyrite synthesised in this study and by other workers (Johan *et al.*, 1989; Marcoux *et al.*, 1989; Wu *et al.*, 1989). Hence, it would appear that arsenic plays a stronger role at the growing surface of arsenopyrite crystals, rather than an influence on gold in solution. This has been observed mainly in synthetic arsenopyrite samples where hydrochloric acid solutions were used in the starting materials.

In auriferous arsenopyrite synthesised in the chloride system, the gold would most probably be transported as the Au(I) dichloro complex ($AuCl_2^-$) (Henley *et al.*, 1975; Seward, 1982). The incorporation of gold is probably by adsorption on the growing arsenopyrite crystal face. Initially, sulfur rich arsenopyrite is formed because under the condition of temperature used (400-500°C), the sulfur rich arsenopyrite is stable (Kretschmar and Scott, 1976). As the solution becomes depleted of available sulfur, more arsenic is incorporated into the growing arsenopyrite crystals. In the process more $AuCl_2^-$ species are adsorbed on the growing crystal face, due to gold attraction to arsenic. The $AuCl_2^-$ adsorbed on the surface may be reduce to metallic Au^0 with the removal of Cl^- anions or the gold may be bonded by electronic charge transfer, replacing iron on the iron site or placed in point defects in the arsenopyrite structure.

The high concentrations of gold obtained in synthetic arsenopyrite from the goethite, arsenic and sulfur hydrothermal heated mixtures, indicates that gold is transported as a sulfide complex. In arsenopyrite synthesised from these mixtures with no added solution or where gold chloride solutions have been used in the starting materials in this study, the As:S ratio appears independent of gold concentration in the crystals. In these systems, gold was transported as $Au(SH)^0$ or possibly as $Au(SH)_2^-$. The adsorption of these species on the growing crystal face possibly results in both the gold and sulfur from the complex being attached to the arsenopyrite lattice resulting in high gold content over a range of As:S ratios. Renders and Seward (1989a,b) and Cardile *et al.* (1993) have shown that the absorption of $Au(HS)^0$ on to

colloidal As_2S_3 resulted in $Au(I)$ linearly coordinated to two sulfur atoms and not present as a metallic Au precipitiate.

From the above work, it is possible that the form of the gold species (i.e. $AuCl^2$ or $Au(SH)^0$ or possibly as $Au(SH)^2$) in solution has an influence on the distribution of gold in the arsenopyrite structure, as was observed in comparison of the two methods of synthesis of auriferous arsenopyrite (Figures 4.32a to g). It may also have an effect on the form of gold associated with the arsenopyrite structure (i.e. Au^0 or Au-X). However, [197]Au Mössbauer data shows that Au is mostly bonded in both conditions with and without hydrochloric acid in the starting materials.

The stoichiometry of arsenopyrite formed is largely dependent on temperature (i.e. low temperature a low As:S ratio), however the effect of others factors (e.g. pH or Cl) may affect the selectivity of excess arsenic or sulfur in its structure. In addition, the availablity of arsenic and sulfur in the system will also affect the arsenopyrites composition.

4.3.5 Structure of Synthetic Auriferous Arsenopyrite

The structures of several synthetic auriferous arsenopyrite samples obtained hydrothermally were characterised and refined by XRD and CBED analysis. This information was compared with structural information for natural arsenopyrites.

4.3.5.1 Comparison of Synthetic Auriferous Arsenopyrite with Natural Arsenopyrites

In the first instance, arsenopyrite synthesised by various methods and in which gold could not be successfully incorporated into the arsenopyrite structures, was compared with synthetic auriferous arsenopyrite from hydrothermal experiments. The XRD powder patterns of auriferous arsenopyrite hydrothermally synthesised from either mixtures of hematite, arsenic and sulfur or goethite, arsenic and sulfur were then compared with XRD powder patterns of natural arsenopyrite samples.

Figure 4.35a shows a typical XRD pattern of synthetic arsenopyrite made from arsenic, iron and sulfur mixture sealed in vycor tubes. Fine gold which was also added to the sample was not incorporated into the arsenopyrite but appeared as distorted globules amongst the grains of synthetic arsenopyrite and pyrrhotite. Figures 4.35b, c and d show XRD patterns from synthetic auriferous arsenopyrite obtained by hydrothermal synthesis at 500°C or 400°C. All XRD patterns are indexed according to the monoclinic $P2_1/c$ setting. The second and third patterns are from arsenopyrite hydrothermally synthesed from hematite mixtures, whereas the fourth pattern is from a synthetic arsenopyrite from a goethite mixture.

In all cases, the synthetic arsenopyrite samples had XRD powder patterns that were generally similar to each other. Some arsenopyrite samples were not completely free of impurities as reflections of trace pyrite and pyrrhotite were present in their XRD patterns. The XRD patterns are very similar to those of synthetic arsenopyrite samples reported by Morimoto and Clark (1961). The major peaks in the synthetic arsenopyrite show no tendency to split, as was observed in some natural arsenopyrites. The synthetic arsenopyrite XRD patterns are similar to the arsenic rich natural arsenopyrites. In addition, the peaks tend to be broader than the natural arsenopyrite sample which indicates some disorder or inhomogeneity. In the synthetic samples, the (-121) reflection is much further away from the 210, 012 reflections. The (100) and ($\bar{1}$10)(110) and (021)(0$\bar{2}$1) reflection intensities are also reduced. The cell constants in all the synthetic arsenopyrite samples (a=5.80, b=5.72, c= 5.79Å, β = 113.2°) were much larger than for the natural arsenopyrite samples (Figure 3.30 and Appendix D) due to compositional differences. However, it would appear that some differences may be due to rapid crystallisation rather then just composition differences alone. All the synthetic samples exhibited some variations in chemical composition, as was observed in EPMA determined compositions. Measurements of the 131 d-spacing following the method of Morimoto and Clark (1961) gave an average arsenic concentration similar to the average chemical composition.

Figure 4.35 (a) Typical XRD pattern of synthetic arsenopyrite made from arsenic, iron and sulfur mixture sealed in vycor tubes. (b) Typical XRD powder pattern of hydrothermal synthetic auriferous arsenopyrite.
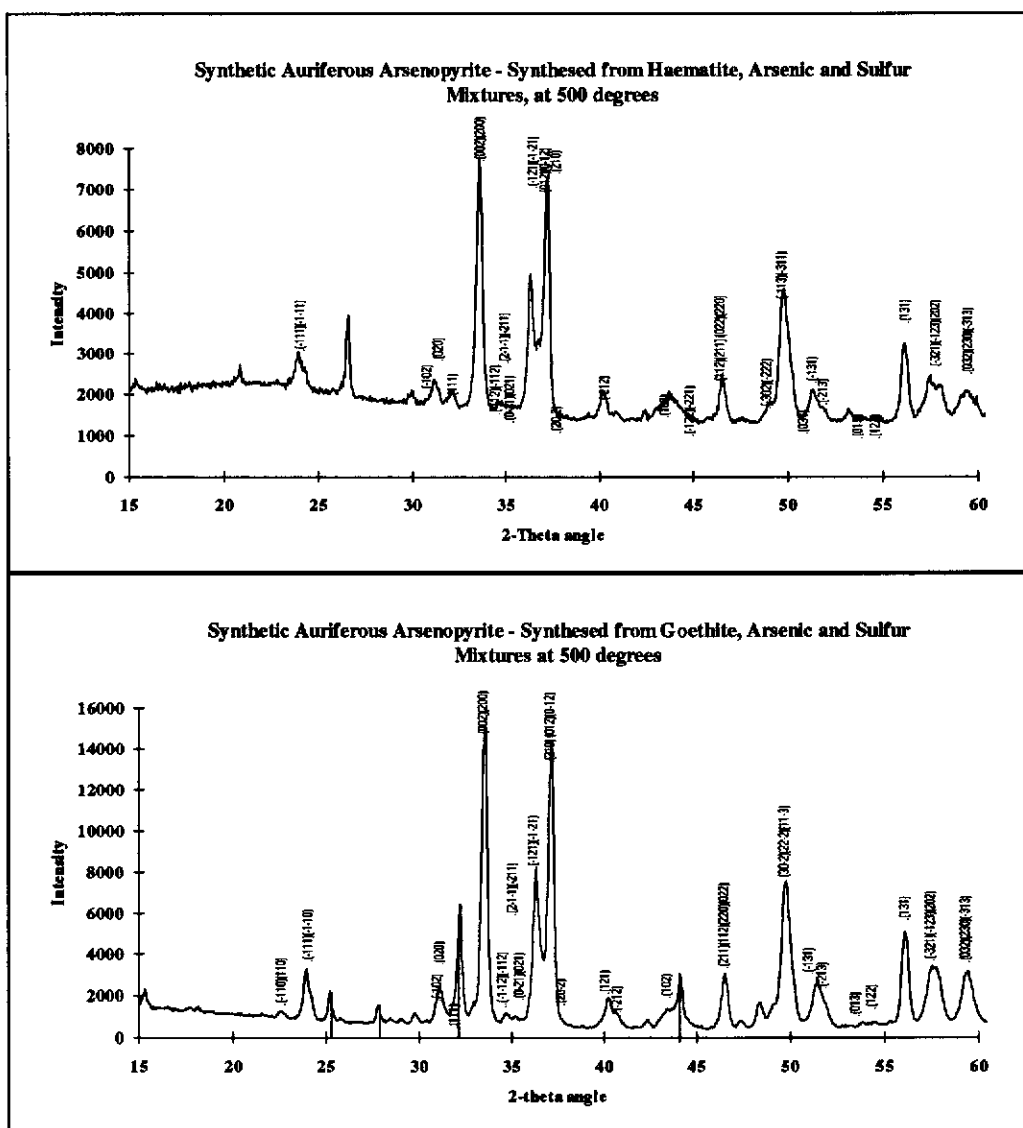
Figure 4.35 Typical XRD powder pattern of hydrothermal synthetic auriferous arsenopyrite from (c) hematite, arsenic and sulfur mixtures and (d) goethite, arsenic and sulfur mixtures.

4.3.5.2 Examination of Synthetic Arsenopyrite by CBED

In view of the differences observed between the XRD powder patterns of synthetic arsenopyrite and the natural arsenopyrite samples, synthetic arsenopyrites were examined by CBED for structural differences. Crystals of synthetic arsenopyrite were tilted to major zone axes similar to the method followed for the natural arsenopyrite samples. The [101] and [100] zone axes were readily obtained, although in thick crystals clear CBED patterns were not easily distinguishable. The CBED patterns were similar for all synthetic samples examined. SAED patterns of long slender crystals showed that the elongated direction in the crystals corresponded to the a-axis direction which is common in arsenopyrite crystals (Figure 4.36).

[101] Zone Axis

Figure 4.37a and b show [101] zone axes for the synthetic auriferous arsenopyrite samples. A mirror line can be observed through the whole pattern along the (10$\bar{1}$) direction in both patterns. GM lines are also evident corresponding to a 2-fold screw axis along b and a glide along c, in agreement with the P2$_1$/c monoclinic symmetry, as with all the natural samples in some CBED patterns (Figure 4.37a). However, in many patterns the GM lines corresponding to the 2-fold screw axis in the b* direction are missing or appear considerably distorted (Figure 4.37b). The measurements of the d spacings were slightly larger than those in the JCPDS files, however, they agreed well with those measured from XRD patterns. In all [101] patterns, the dynamic absences can be readily seen along the ($\bar{1}$ 01)* direction with a mirror line in the first Laue zone corresponding to the glide plane.

[100] zone axis

Figure 4.38 shows a typical [100] axis found in synthetic arsenopyrite samples. The forbidden reflections (dark bars or GM lines) occur in the b* direction and a mirror line runs perpendicular to this direction in the FOLZ. In the c* direction, the GM lines are not easily identifiable. The d spacing along c* is similar to that which
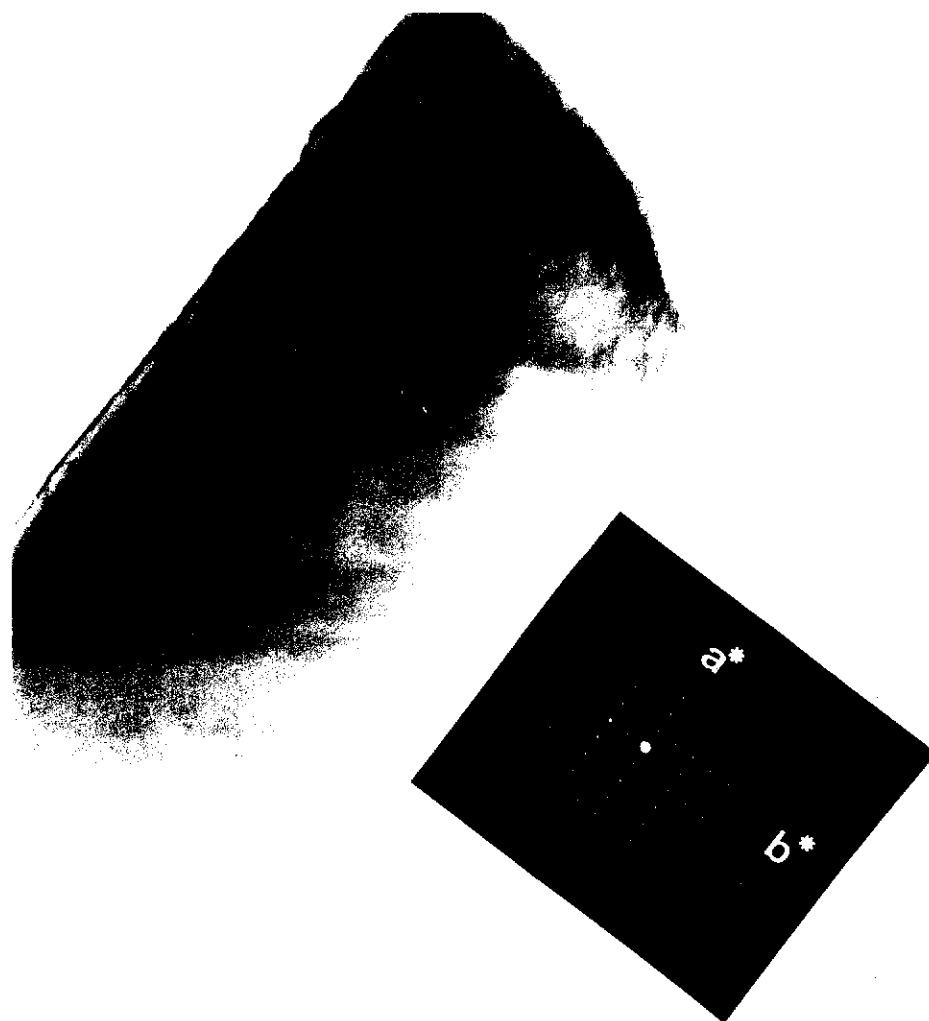
Figure 4.36 Electron micrograph of synthetic arsenopyrite and selected area electron diffraction pattern showing orientation of crystal. All synthetic crystals were elongated in the a direction.
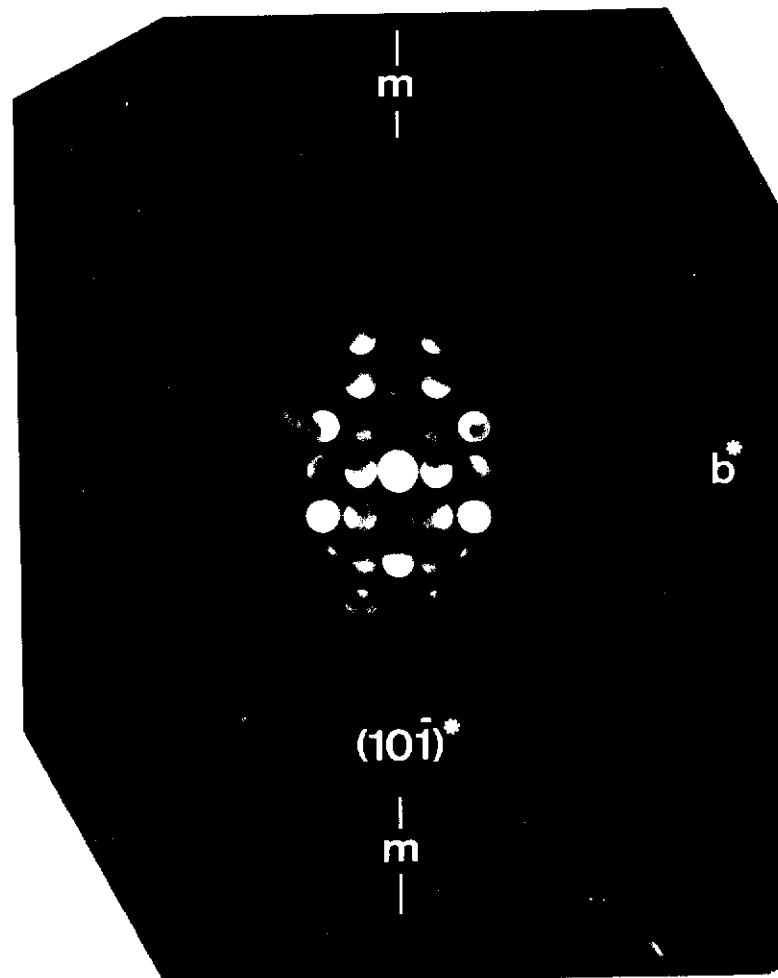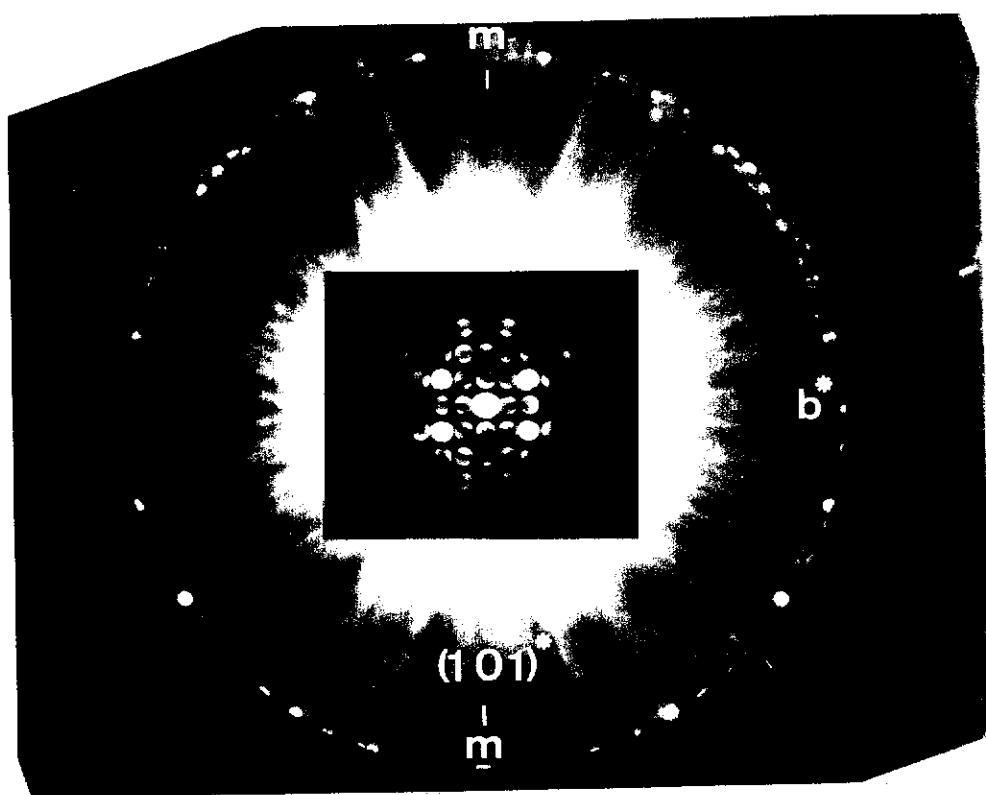
Figure 4.37 Convergent beam electron diffraction pattern of (a) complete [101] zone axes pattern and (b) distorted b* axis pattern for the synthetic auriferous arsenopyrite samples.
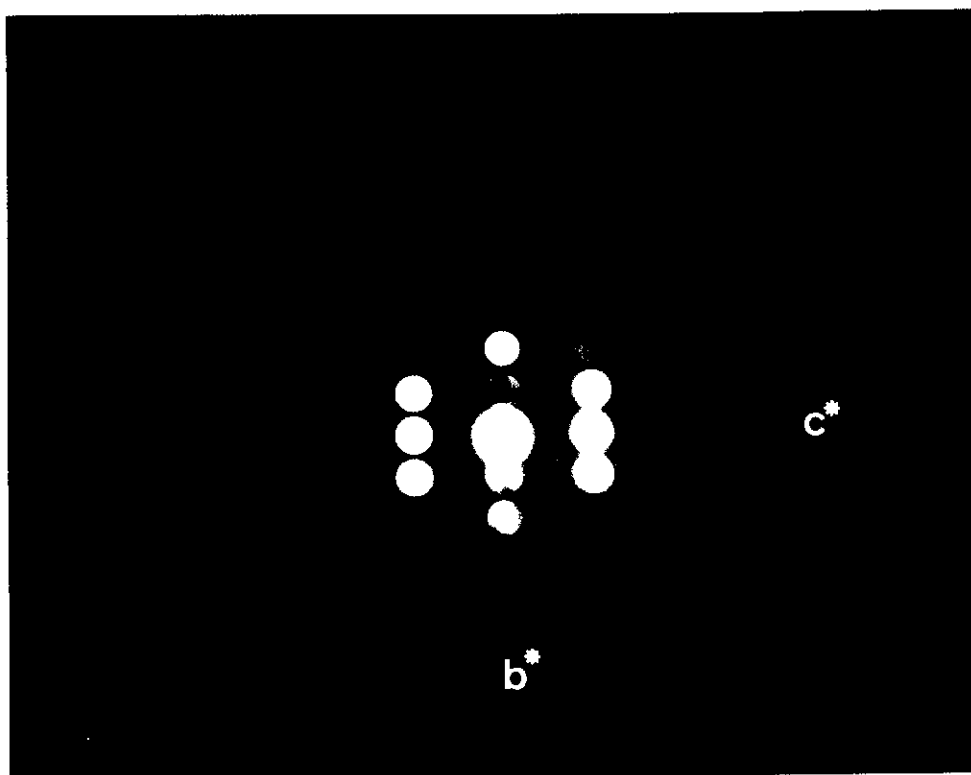
Figure 4.38 A typical [100] axis found in synthetic arsenopyrite sample.

would be expected for the a* and the way to distinguish the two is by the presence of the GM lines along every second disc in the ZOLZ, corresponding to the c glide in the c* direction. The pattern however contains some features similar to the [100] zone found in the natural samples. The width of GM lines and other features within the discs is a function of thickness of the crystal (Steeds and Vincent, 1983). The crystal is much thinner in the c direction than in the b direction. Similar types of patterns were observed in natural samples and information in the c direction was obtained by finding an edge of the crystal which was thicker. However, in the synthetic samples this was not always possible.

In comparison, the natural and synthetic samples have similar structures as seen by similar features in their CBED patterns. That for the synthetic sample contains more disorder than the natural sample, which makes it harder to obtain good CBED patterns. The rapid crystallisation of the synthetic sample is a cause of these problems and the large variation in composition may also cause more distortions.

4.3.5.3 Rietveld Refinement of Synthetic Auriferous Arsenopyrite

The structures of auriferous arsenopyrite hydrothermally synthesised from mixtures of (a) hematite, arsenic and sulfur and (b) goethite, arsenic and sulfur were then refined by the Rietveld method on several XRD powder patterns in the space group $P2_1/c$. The starting structural parameters used were those of Fuess et al. (1987) and translated to the $P2_1/c$ space group. The refinement converged for both types of samples to Bragg R factors around 4.00 with profile fits about 10.0 or less. The agreement was not as good as that obtained for the natural arsenopyrite samples. This is most probably a result of disorder and variations in composition of crystals.

Table 4.6a shows the final refined parameters obtained from the Rietveld refinement. The unit cell constants are similar for both synthetic auriferous arsenopyrites and are larger than those obtained for natural samples. The site occupancy variation is larger, which indicates considerable interchange of arsenic and sulfur. The observed, calculated and difference patterns for one synthetic auriferous

Table 4.6a - Unit Cell Dimension (based on space group $P2_1/c$) of Synthetic Auriferous Arsenopyrites

SAMPLE	Ap41	Apm	Ap40	Ap71
Starting materials	Fe_3O_4+As+S	Fe_3O_4+As+S	Fe_3O_4+As+S	FeOOH + As +S
	2m HCl Soln	2m HCl Soln	2m HCl Soln	-
Conditions	2 Kbars, 400°C	2 Kbars, 500°C	2 Kbars, 500°C	2 Kbars, 500°C
Unit cell Dimensions				
a	5.7905±0.002	5.7988±0.002	5.7936±0.0004	5.7957±0.002
b	5.7225±0.002	5.7215±0.0008	5.7131±0.0004	5.7186±0.001
c	5.8224±0.002	5.804±0.001	5.7935±0.0005	5.797±0.002
Beta	112.969±0.002	113.095±0.009	113.199±0.005	113.3303±0.01
Volume	177.6	177.1	176.383	176.4
Sites Occupancies				
As	not determined	0.82	0.81	0.76354
S		1.180	1.19	1.236
Atomic Coordinates				
Fe				
x		0.277±0.001	0.275±0.001	0.26735±0.002
y		-0.007±0.002	-0.009±0.001	0.01609±0.002
z		0.2818±0.001	0.282±0.001	0.28433±0.002
As				
x		-0.15572±0.001	-0.165±0.001	-0.14821±0.002
y		-0.1363±0.001	-0.133±0.001	-0.13018±0.002
z		0.132±0.001	0.124±0.001	0.13907±0.002
S				
x		0.333±0.002	0.329±0.001	0.34098±0.003
y		-0.123±0.002	-0.131±0.001	-0.13655±0.002
z		0.661±0.002	0.666±0.001	0.67994±0.003

SAMPLE	Ap41	Apm	Ap40	Ap71
WHH	not determined	1.744	0.897	1.89777
		-0.0329	-0.414	-0.6263
		0.03874	0.130	0.17489
Peak		0.847	0.651	0.4
shape				
expected		7.270	6.330	3.05
RP		11.950	7.620	12.24
RWP		14.950	9.750	18.92
GOF		4.250	2.370	38.49
Bragg R		5.370	4.120	5.53
Durbin-Watson				
UW			0.628	0.133
W			0.806	0.106

Table 4.6b - Profile and Agreement Indices for Synthetic Auriferous Arsenopyrite refined by Rietveld Method

arsenopyrite are shown in Figure 4.39. The high isotropic temperature factors, besides resulting from accumulated errors from the Rietveld refinement, are possibly associated with variation in stoichiometry and disorder of the atomic sites.

4.3.5.4 Bond Lengths and Angles

The calculated bond lengths and angles are shown in Table 4.7. There are some variations in the bond lengths and angles between different synthetic samples. These are most probably associated with the non-perfect model fit obtained from the XRD powder patterns. The iron to arsenic bond lengths are generally similar to those obtained for natural arsenopyrite samples, although one of the bond lengths for the arsenopyrite synthesised from goethite , arsenic and sulfur mixture is lower, possibility corresponding to the sulfur on the arsenic site (2.25Å). The iron to sulfur bond lengths are larger and may be associated with some arsenic replacing sulfur on the sulfur site producing a larger bond length. The bond angles are generally the same except the As1-Fe-As3 and S1-Fe-S2 are slightly less. The S1-Fe to As1, As2 and As3 angles are also slightly different.

4.3.5.5 Conclusions on Synthetic Auriferous Arsenopyrite Structure

The synthetic arsenopyrite structures were much more structurally disordered than were the natural arsenopyrites as seen from the broad peaks in the XRD powder patterns and the distortion observed in some of the CBED patterns. The presence of the c-glide plane and the reduction of symmetry along the distorted b axis indicates that faults occur along the b axis, which do not significantly affect the glide in the structure. The faults have occurred due to rapid growth in the b direction of the arsenopyrite crystals. From the twins and antiphase domains described in Chapter 3, the reduction in symmetry may be interpreted as a result of multiple displacement occurring along different (010) planes with the displacement vector of $\frac{1}{2}d(101)$ or $\frac{1}{2}d(10\bar{1})$. The displacement plane would occur along octahedra as illustrated in Figure 4.40. By shifting the octahedra, the ordering of the arsenic and sulfur atoms
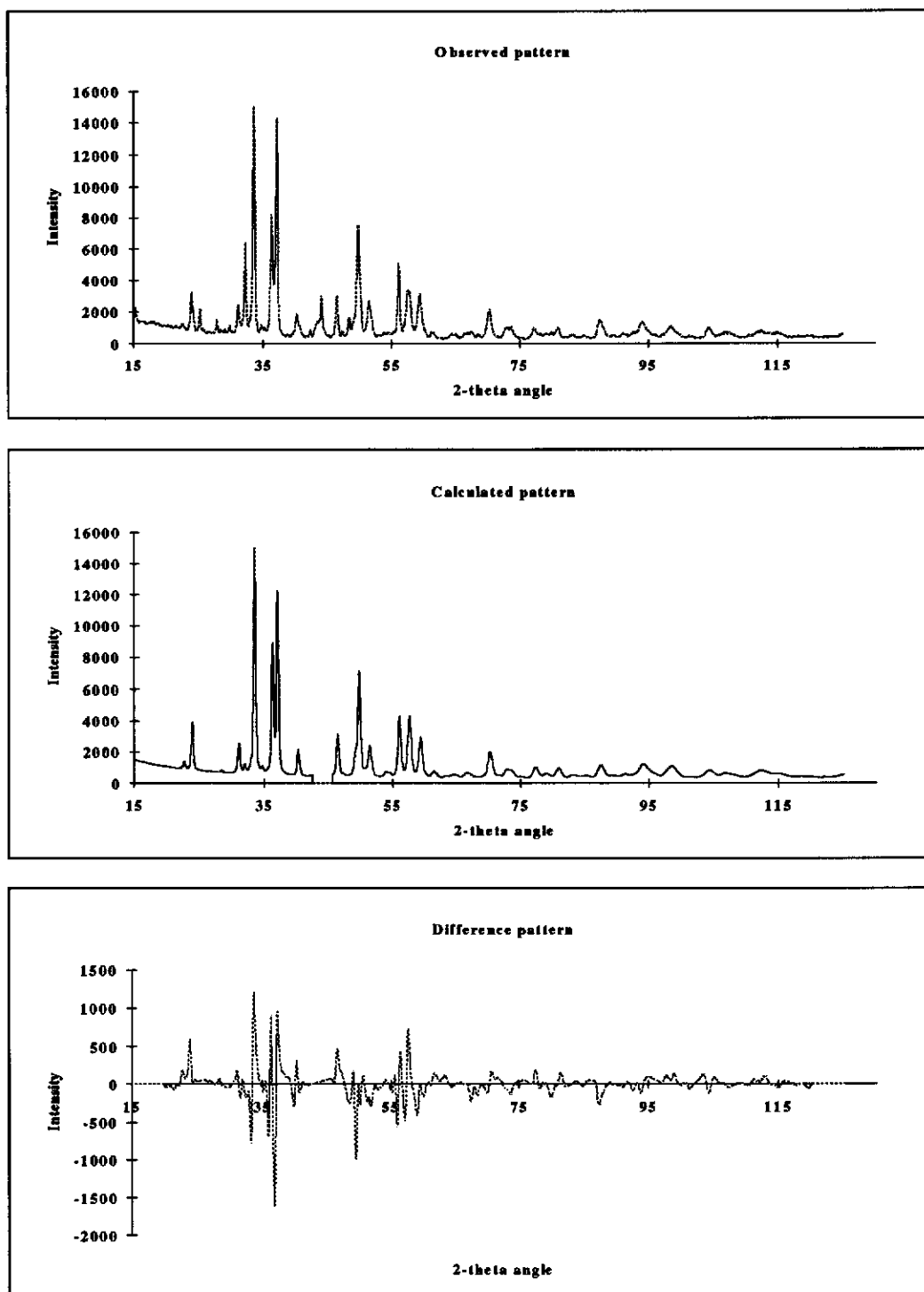
Figure 4.39 X-ray Diffraction patterns of (a) observed, (b) calculated and (c) difference of observed and calculated patterns of a synthetic auriferous arsenopyrite.

Table 4.7a Bond Lengths of Synthetic Auriferous Arsenopyrite

SAMPLE	Ap41	Apm	Ap40	Ap71
Bond lengths				
Fe1-As1		2.434±0.004	2.45±0.005	2.4093±0.002
Fe1-As2	not determined	2.347±0.004	2.36±0.005	2.2458±0.002
Fe1-As3		2.367±0.004	2.33±0.005	2.3729±0.002
Fe1-S1		2.197±0.005	2.23±0.006	2.2334±0.021
Fe1-S2		2.280±0.005	2.22±0.006	2.3327±0.021
Fe1-S3		2.292±0.005	2.23±0.006	2.3497±0.021
As5-S5			3.09±	
Fe1-Fe3		3.575±0.054	3.56±0.052	3.5431±0.106
Fe1-Fe5			2.87±0.052	

Table 4.7b - Bond Angles of Synthetic Auriferous Arsenopyrite

SAMPLE	Ap41	Apm	Ap40	Ap71
Bond angles				
As1-Fe				
-As2		90±0.4	90.8±0.7	92.6±1.2
-As3		83.7±0.4	83.8±0.30	84.4±1.1
S1-Fe				
-S2	not determined	101.8±1.0	103.5±0.40	102.8±0.8
-S3		92.6±0.9	93.7±0.02	88.6±0.7
As2-Fe				
-As3		84.8±0.4	85.4±0.3	87.5±1.2
S2-Fe				
-S3		95.5±0.9	96.2±0.02	92.8±0.8
S1-Fe				
-As1		89.5±0.9	89.9±0.3	88.6±0.7
-As2		89.9±0.9	89.9±0.02	94.4±0.8
-As3		171.5±1.6	167.75±0.04	172.7±1.4
S2-Fe				
-As1		168.5±1.6	163.2±0.04	166.7±1.4
-As2		91.9±0.9	92.1±0.02	93.7±0.8
-As3		85.1±0.8	84.0±0.02	84±0.7
S3-Fe				
-As1		82±0.8	82.5±0.02	80.4±0.7
-As2		171.5±1.6	174.0±0.04	172.3±1.4
-As3		91.7±0.9	92.2±0.02	88.6±0.7
Fe5-S1				
-Fe1			79.1±0.2	
Fe3-As1				
-Fe1			94.9±0.2	
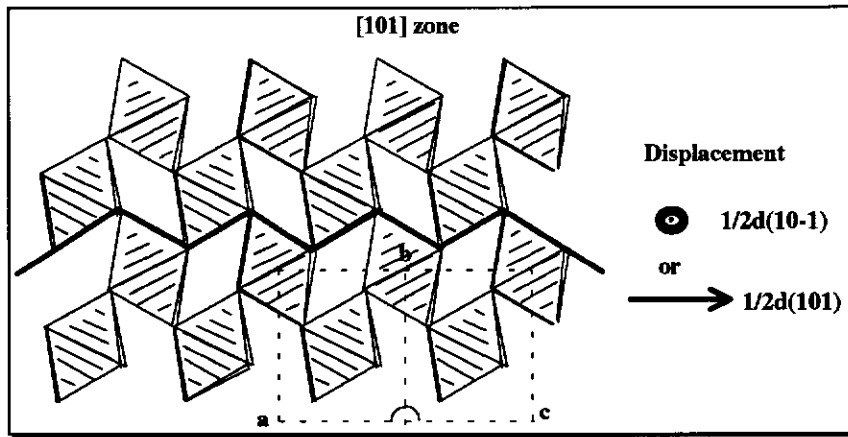
Figure 4.40 Displacement of octahedra along the (010) plane either by ½d(101) or ½d(10-1) along dark line.
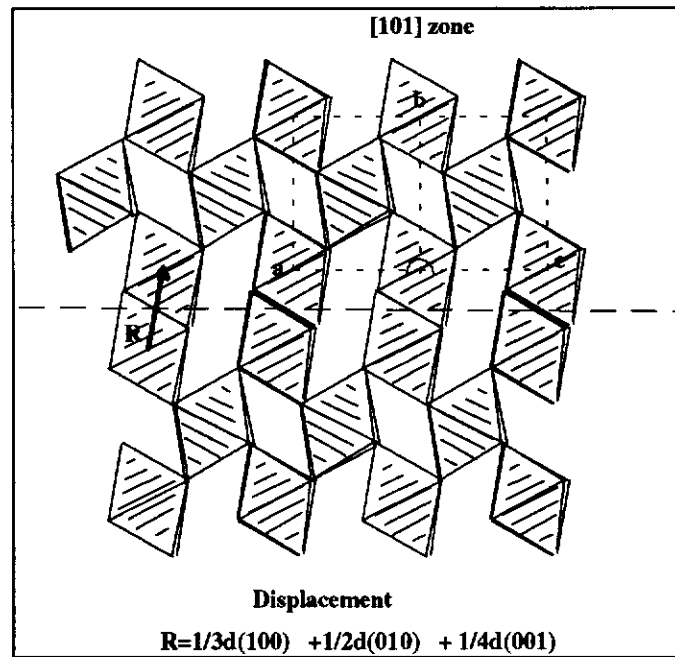
Figure 4.41 Displacement of octahedra by 1/3d(100) + 1/2d(010) + 1/2d(001).

along the displacement plane is changed, resulting in shifts in positions of atoms. The As1-Fe-As3 and S1-Fe-S2 angles are slightly smaller than natural samples which coincide with observed distortion in the (010) plane. Alternatively, a displacement fault as shown in Figure 4.41 could occur, similar to that observed in structures of MnO_2 compounds (Wadsley, 1955). In order to destroy the 2-fold screw axis, the $P2_1/c$ structure has to be sheared along the ($10\bar{1}$) plane with the octahedral column in the [101] direction maintained so as to preserve the glide plane. This results in the column octahedra along the [101] direction sharing edges with other octahedra as shown in the Figure. As a result, larger gaps are present between some octahedra in which an impurity atom such as gold may be positioned there.

4.3.6 Diffusion of Gold into Natural Arsenopyrite

In addition to the previous methods, attempts were also made to incorporate gold into arsenopyrite by either diffusion or dissolution and reprecipitation reactions. Natural or synthetic arsenopyrite samples were placed in gold tubes and heated at high temperatures and pressures, some with aqueous solutions and some in the absence of aqueous solution and simply pelletised. Table 4.8 shows the various experimental conditions used.

Dry Experiments

Clark (1960) observed that gold could diffuse through arsenopyrite at 660°C under 2k bars of pressure. The first dry experiments attempted simulated these conditions.

Polished sections of a (AD1) natural arsenic rich arsenopyrite heated under similar conditions to those outlined by Clark (1960), showed slight decomposition to pyrrhotite on the edges of the arsenopyrite grains. No gold was observed in the pyrrhotite formed. Three separate samples were then made, one consisting of several natural stoichiometric grains of arsenopyrite (AD2a) together with synthetic arsenic rich arsenopyrite, another consisting of only synthetic arsenopyrite (AD2b) and the

	Conditions			Starting Materials in	Gold Tube
Sample	Press (kbars)	Temp (°C)	Period (days)	Mixture* (g)	Soln (mls)
Dry experiments					
AD2a	1	695	1	0.5	-
b			1	A5 0.5	
c			1	Gb 0.5	
AD1	2	660	1	Ch 0.5	
AD7	1	660	4hrs	Ch 0.2018	
Ap22	2	500	7	A4 0.4321+Au 0.025	
Ap66	2		20	syn asp 0.25+Au 0.022	
Ap67	2		10	syn asp + Au 0.2	
Ap69a	1.2	400	10	Ch 0.0987	
Aqueous experiments					
AD3	1	705	4hrs	Gb 0.0393	2mHCl/H_2O 0.0872
AD4	1	660	4hrs	Ch 0.2282	2mHCl/H_2O 0.0332
AD6	1	660	4hrs	Ch 0.1743	H_2O 0.054
AD5	1	500	4hrs	Ch 0.2358	2mHCl/H_2O open
Ap20	2		7	A5 0.3217	2mHCl/H_2O 0.3467
Ap65	2		20	Ch 0.0072	H_2O
Ap68	2		10	Ch 0.2	$HAuCl_3$ +HCl/H_2O
Ap55	2	400	7	Ch 0.0192	2000ppm $AuCl_3$/H_2O 0.219
Ap69b	1.2		10	Ch 0.0669	H_2O 0.0653
Ap69c	1.2		10	Ch 0.0551	2mHCl/H_2O 0.0703
Ap69d	1.2		10	Ch 0.0433	2mHCl/H_2O 0.0198

Table 4.8 - Experiments on Diffusion of Gold into Arsenopyrite

*mixture - Ch China arsenopyrite, Gb Greenbushes arsenopyrite, A4 A5 syn asp synthetic arsenopyrite from Table 4.1

last consisting only of natural stoichiometric grains of arsenopyrite (AD2c). After heating, a polished section of the sample containing natural arsenopyrite alone revealed little alteration had taken place. In the sample containing only synthetic arsenopyrite, the gold tubing had burst resulting in the arsenopyrite breaking down in the presence of distilled water surrounding the gold tube (in the pressure bomb). The resulting product was hematite with gold grains of various sizes diffused through the hematite matrix as shown in Figure 4.42a. In the sample consisting of synthetic arsenopyrite and natural arsenopyrite, the synthetic arsenopyrite and pyrrhotite recrystallised onto several of the natural arsenopyrite grains. A close scan of a polished section of these grains, revealed the presence of fine grained gold less than one micrometre in diameter, within the recrystallised layer (Figure 4.42b). The recrystallised layer showed no particular orientation with the natural arsenopyrite and appeared at various locations around the grains.

Electron probe analyses of points tranversed from the natural arsenopyrite across the recrystallised layer are shown in Figures 4.43a and b. An increase in iron is observed in the recrystallised area compared with the unreacted natural arsenopyrite composition. The arsenic content has generally increased with a decrease in sulfur. However, in some parts this is reversed, having a chemical composition approaching that of pyrrhotite. Some of the arsenic-rich regions are associated with the presence of gold (Figure 4.43c). Synthetic arsenopyrite pelletised with fine gold grains and sealed in a gold tube and heated to 500°C under 2k bars of pressure (Ap22), resulted in little observed alteration (Figure 4.44).

The results can be explained by Clark's (1960) phase diagram (Figure 4.45). The conditions of experiments in this study are shown by a 'X' in Figure 4.45. Samples heated under the conditions to the left of the curve generally remained unchanged (Ap22, Ap33) except for sample Ap67 which showed evidence of gold being attacked and undergoing some alteration during the experiment (Figure 4.46). This may be because the synthetic arsenopyrite used in the starting material contained free arsenic which most probably attacked the gold.
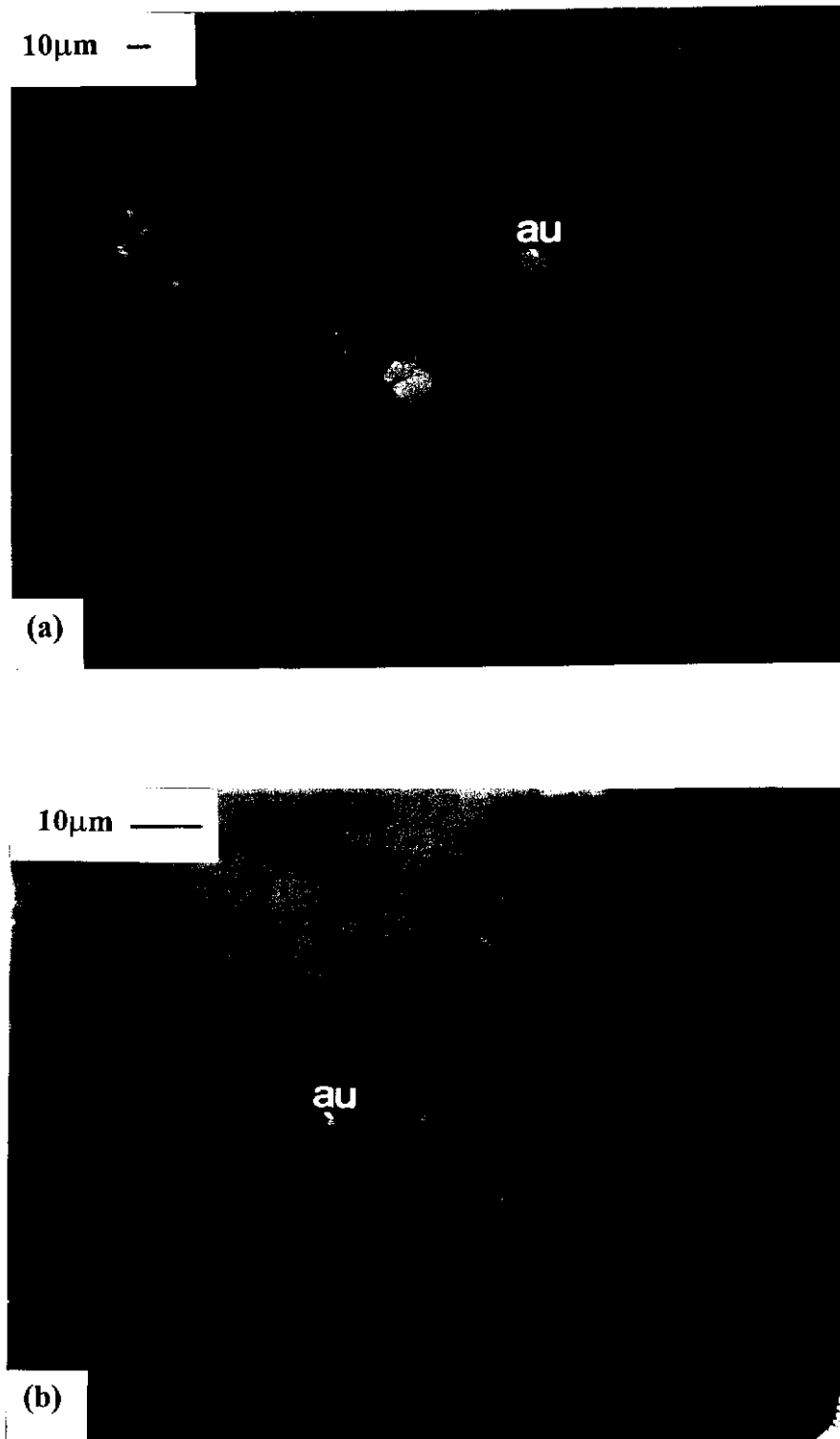
Figure 4.42 (a) Evidence of gold mobility during the breakdown of synthetic arsenopyrite to iron oxide. (b) Unaltered arsenopyrite and recrystallised area containing fine gold particles.
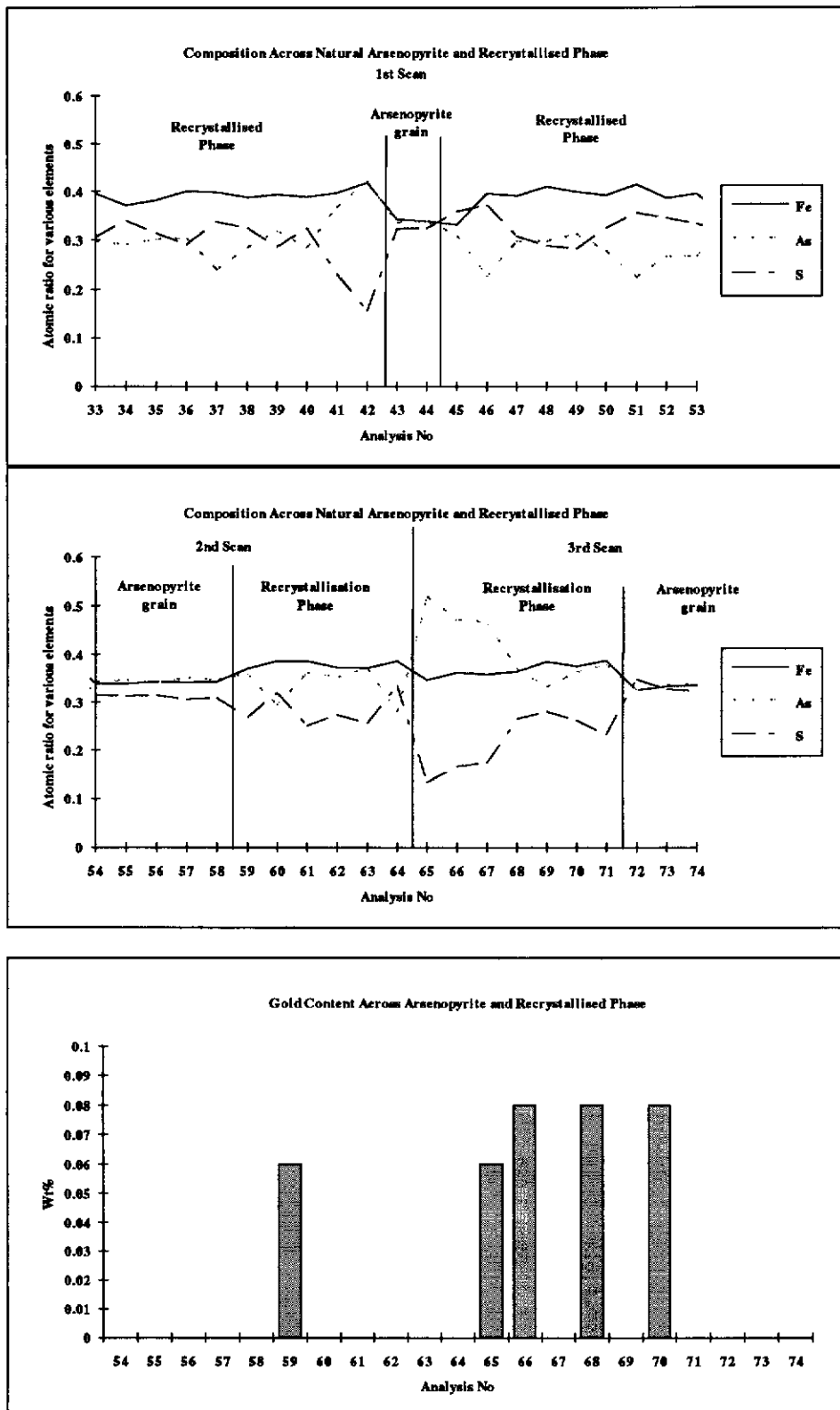
Figure 4.43 (a) and (b) Results of electron microprobe analyses across Unaltered Greenbushes arsenopyrite and recrystallised area. (c) Trace gold analyses over points in (b).
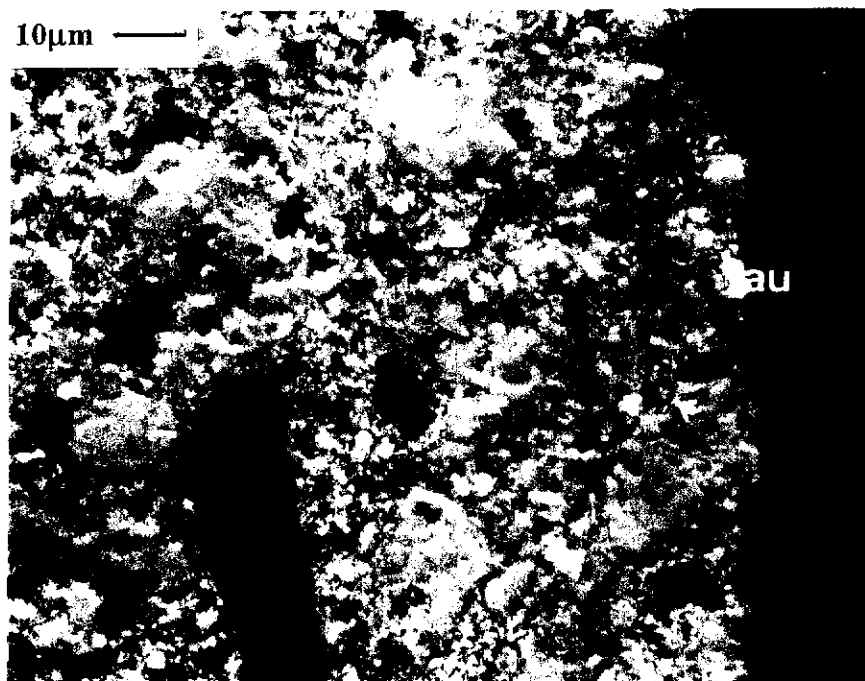
Figure 4.44 Backscattered image of disseminated gold grains amongst unreacted pelletised arsenopyrite (Ap22).
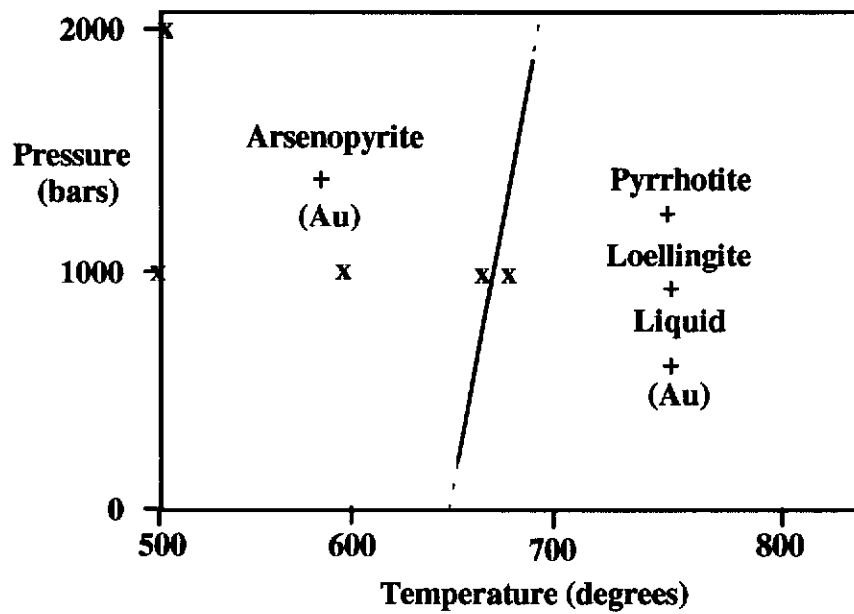
Figure 4.45 Temperature versus pressure diagram for of the As-Fe-S-Au system (after Clark, 1960). The crosses indicate conditions used in experiments carried out in this study.
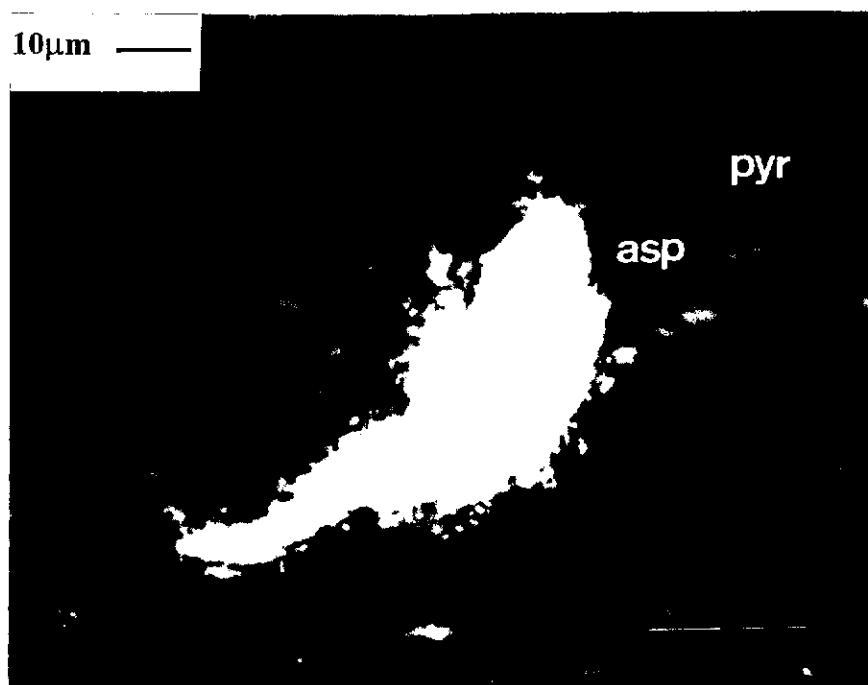
Figure 4.46 Backscattered image of partially mobilised gold from the partial decomposition of pelletised arsenopyrite to pyrrhotite (Ap67).

Clark (1960) reported diffusion of gold into arsenopyrite taking place over a period of 4 hours. It appears from the above experiments that little alteration took place in the natural arsenopyrite samples and only the synthetic sample altered. This infers that the natural arsenopyrite grains are more stable. For diffusion of gold through arsenopyrite to occur, the arsenopyrite must first cross the arsenopyrite=löllingite+pyrrhotite+liquid boundary to the right and then reverse to the left, i.e. gold only diffuses when arsenopyrite is altered or mobilised in some way. Thus, gold is not readily diffused through arsenopyrite.

Aqueous Experiments

In view of the observed mobility of gold in sample AD2b, experiments (AD3-7) were carried out in which natural arsenopyrite and aqueous solutions of either HCl or water (Table 4.7) were added and sealed in gold tubes. Samples were heated at either 705°C (above the phase stability temperature of arsenopyrite at 702°C, (Clark, 1960)), 660°C or 500°C. Over the 4 hour time period for these experiments, only the sample heated to 705°C resulted in any reaction. In this particular sample, both pyrrhotite and arsenic crystals were present on the inside and outside of the gold sealed tubing (i.e. the gold tube had been penetrated).

Similar experiments (Ap20, Ap65; Ap69a,b and c) were tried at temperatures at either 500°C or 400°C, for longer periods (7 to 20 days) of time, in solutions of either double distilled water or 1M HCl solution. In the presence of distilled water, arsenopyrite partially broke down along a crystallographically orientated direction (Figure 4.47a) forming pyrrhotite. Some round gold grains were also observed amongst the pyrrhotite product. Arsenic from the partial breakdown of arsenopyrite was found deposited on the inside of the gold tubing. In some parts, gold was deposited on arsenopyrite surfaces where a channel resulted from the partial dissolution of arsenopyrite (Figure 4.47b). It appears that the dissolution of some of the arsenopyrite resulted in precipitation of gold. In other parts of the grains, regular step channelling along fractures had also occurred (Figure 4.47c). Pelletised synthetic

(a)
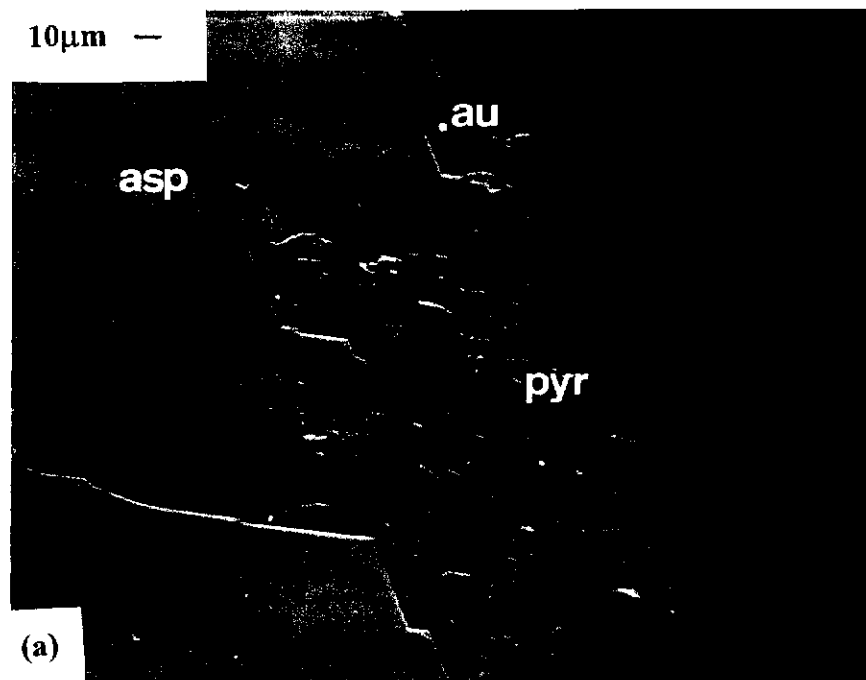
Figure 4.47 Backscattered image of natural arsenopyrite breaking down along a crystallographically orientated direction (a) forming pyrrhotite under the conditions of 500°C and 2kbars in water. Some round gold grains were also observed amongst the pyrrhotite product. (b) Precipitation of gold on the side of arsenopyrite Some dissolution of the arsenopyrite has taken place (c) Regular dissolution channels

(b)

(c)
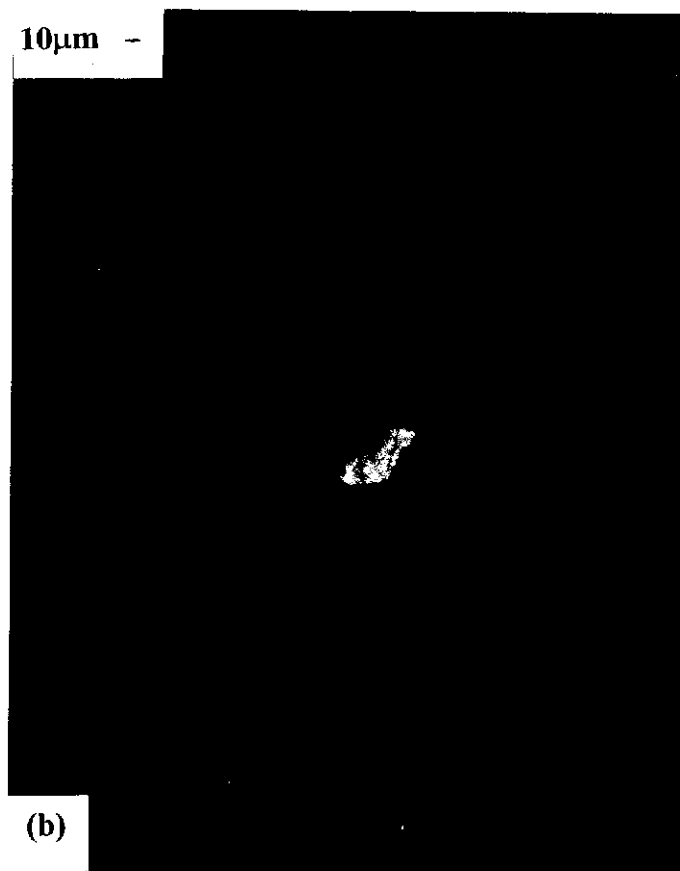
arsenopyrite (Ap20) in the presence of 1M HCl/H$_2$O solution and heated to 500°C under 2 kbars of pressure, resulted in reprecipitation and diffusion of gold into the synthetic arsenopyrite (Figure 4.48).

The use of a 2000 ppm gold chloride solution in the presence of natural or synthetic arsenopyrite exhibited total disintegration of the grains with the precipitation of gold, arsenic and coarse pyrrhotite (Ap66, Ap68) (Ap55) at 500°C and 2 kbars of pressure (Figure 4.49). At 400°C and 2 kbars, examination of the surface of the arsenopyrite grains after 7 days showed gold precipitated on the surface around some of the grains (Figure 4.50a). A polished section of these grains showed extensive irregular fracturing in some grains. Dissolution channels were observed throughout some grains. Some of these dissolution channels appeared to have followed along the fractured grain boundaries. There was no apparent orientation of dissolution as was observed in natural arsenopyrites heated in water (Ap65). In most of these channels, gold was either deposited at the end of the channels which appeared to stop within the grain or was deposited during the channelling process (Figure 4.50b).

From the results above, it appears that aqueous solutions reduce the temperature at which arsenopyrite decomposes. In these experiments, it was difficult to maintain a closed system, as the reaction of arsenic with the gold tube in which the sample was contained, resulted in arsenic deficient phases. This appeared to prevent recrystallisation of arsenopyrite.

4.3.5.1 Discussion on Arsenopyrite Dissolution and Precipitation of Gold

In the presence of aqueous solutions, natural arsenopyrite appeared to decompose leaving either some residual pyrrhotite or resulting in total dissolution along channels. Gold precipitated either along channels or on the arsenopyrite surface. Two mechanisms are possible for the precipitation of gold on and in arsenopyrite grains. One is the process of adsorption of gold complexes in solution onto the sulfide surface and subsequent reduction of the gold complex to metallic gold. The reduction of gold on some sulfide surfaces has been documented in laboratory experiments (e.g..
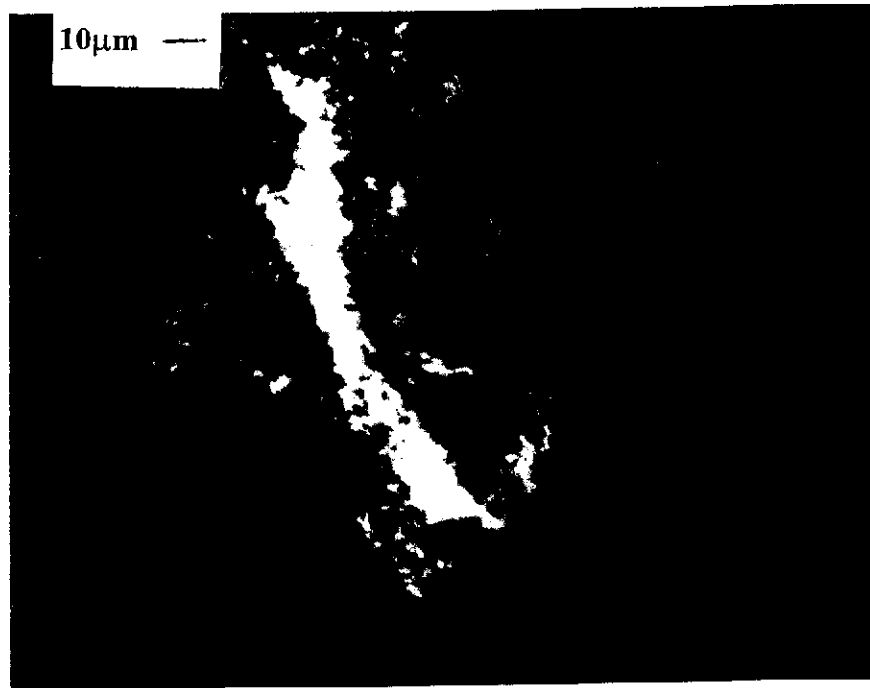
Figure 4.48 Mobilisation of gold through synthetic arsenopyrite (Ap22).
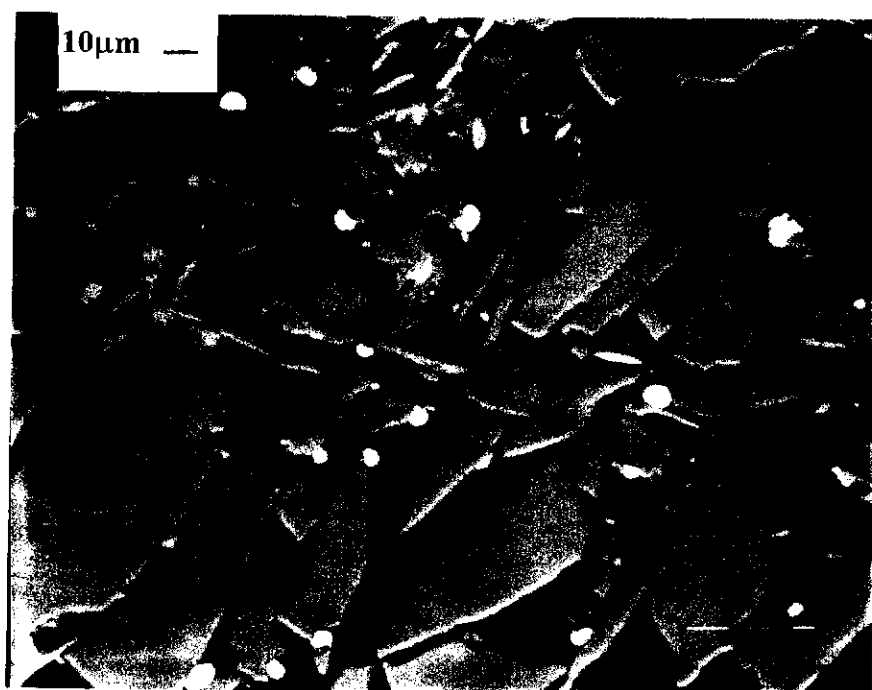
Figure 4.49 Total breakdown of natural arsenopyrite to pyrrhotite with globules of gold (Ap66, Ap68).
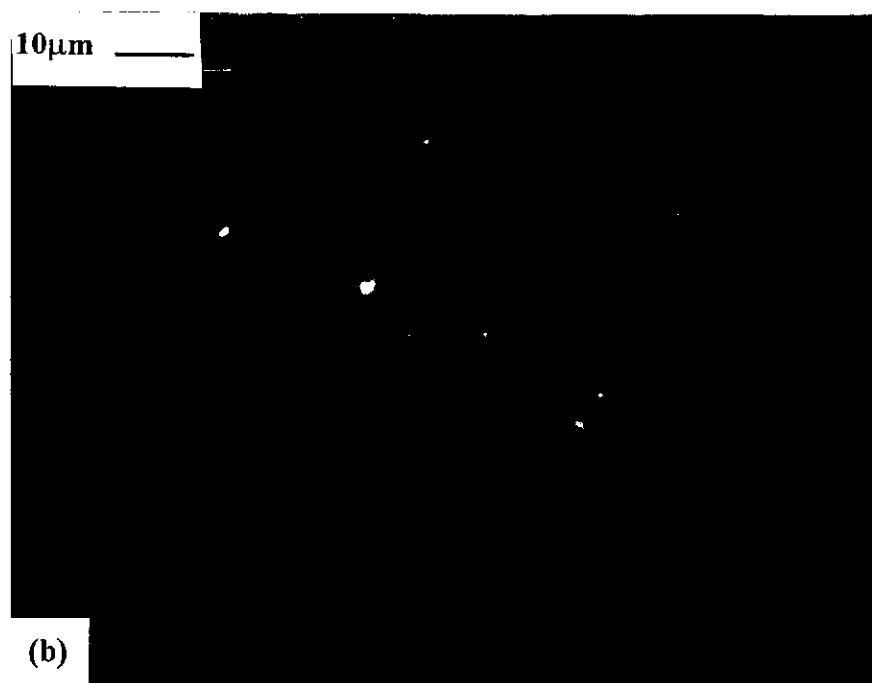
Figure 4.50 (a) Precipitation of gold on natural arsenopyrite from samples in the presence of 2000ppm AuCl$_2$ solution heated to 400°C and 2 kbars (b) Precipitation of gold in dissolution channels.

Jean and Bancroft, 1985) as well as in natural systems (e.g. Knipe *et al.*, 1992). Evidence supporting the importance of the reduced sulfur-donor ligand for adsorption with sulfides has been presented by Jean and Bancroft (1985, 1986). In the first stage, physical adsorption of the gold species occurs by weak van der Waals forces. The attractive force is provided by the instantaneous dipole moments of the absorbed atom and electrons of the nearest surface atoms but with no charge transfer. Renders and Seward (1989) have studied the adsorption of gold from aqueous sulfide solution onto colloidal arsenic and antimony sulfides. They suggested that the neutral monohydrosulfidogold (I) complex, $AuHS^{\circ}$, can be absorbed from acid solutions onto the charged sulfide surface to form the triatomic surface complex [S---Au(I)-SH] in which the gold remains in the +1 oxidation state. [197]Au Mössbauer data support this conclusion (Cardile *et al.*, 1993). The second stage involves a reduction-driven chemical adsorption where the physically adsorbed precursor overcomes the surface energy barrier through electronic or vibrational processes (Knipe *et al.*, 1992). Adsorbed atoms may diffuse across the sulfide surface until they reach 'high-energy' sites where clusters will occur (Bancroft and Hyland, 1990).

The other possibility, is a process of dissolution of arsenopyrite followed by precipitation of gold from solution. This appeared to be the more probable as observed in Figure 4.47. One important part of the mechanism concerns the source of electrons necessary to reduce gold. To determine the importance of a reduction sorption mechanism for Au sorption onto arsenopyrite, it is necessary to evaluate the redox potential of the gold solution versus the redox potential of the arsenopyrite surfaces. The difference between these two redox potentials provides the driving force for reductive sorption.

The precipitation of gold most probably follows the reactions

$$Au(HS)^{\circ} + e- = Au^{\circ} + HS^{-} \qquad \text{...(4.1)}$$
$$Au(HS)^{-}_{2} + e- \rightarrow Au^{\circ} + 2HS^{-} \qquad \text{...(4.2)}$$

or

$$AuCl^{-}_{2} + e- = Au^{\circ} + 2Cl^{-} \text{ .} \qquad \text{...(4.3)}$$

The gold deposited on the grain boundaries and in the cracks of arsenopyrite (Figure 4.43) can be explained by the minor dissolution of some arsenopyrite according to the reaction

$$4FeAsS + 3O_2 + 4nCl^- + 8H^+ + 6H_2O \rightarrow 4FeCl_n^{2+} + 4H_2S^0 + 4H_3AsO_3^+ + 4e\text{-} \quad .....(4.4)$$

a process which would act as a local redox trap for gold precipitation (Heinrich and Eadington, 1986). Gold precipitation requires a reduction from oxidised complexes to native metal and the reactions of (4.3) and (4.4) would explain conditions in which chloride ions were present. In the case where no chloride was present, instead of iron chloride species being formed, pyrrhotite is precipitated as was observed in Figure 4.40a.

4.4 Summary and Conclusions

The main aim of this work was to obtain arsenopyrite containing solid solution gold. However, of the various methods attempted to incorporate gold into the structure of arsenopyrite, only samples synthesised from mixtures of iron oxides, arsenic and sulfur under hydrothermal conditions were successful. Gold was only taken up in the arsenopyrite structure where gold was in solution. The results support the idea that for gold to be taken up in arsenopyrite (and pyrite) it must be taken up by gold adsorption during growth of host mineral (Cabri et al., 1989; Chryssoulis and Cabri, 1990; Schoonen et al., 1992) and not by solid state diffusion which result in metallic gold inclusions. Metallic gold (Au⁰) appears to be insoluble in sulfides as was observed from the sharp boundaries between crystallised arsenopyrite and gold in the dry synthesis work. The presence of metallic gold reduced the breakdown temperature of arsenopyrite to pyrrhotite and loellingite, as reported by Clark (1960). Arsenopyrite hydrothermally synthesised at 400°C in hydrochloric acid solution resulted in up to 2 wt% gold contained in its structure.

The form of the gold species in solution had an influence on the distribution of gold in the arsenopyrite structure. High gold concentrations in arsenopyrites prepared

in the presence of hydrochloric acid were associated with high arsenic to sulfur ratios in the auriferous arsenopyrite synthesised. In arsenopyrite synthesised without added solution, particularly goethite containing mixtures, the As:S ratio appeared independent of gold concentration in the crystals. [197]Au Mössbauer spectra of synthetic auriferous arsenopyrites, prepared in different starting mixtures showed that the gold was in solid solution. Composition by EPMA showed a possible slight iron deficiency in some auriferous arsenopyrite grains analysed, however the errors in the analyses were too high to be conclusive. While gold concentration in arsenopyrites was increased with chloride activity in the aqueous solutions, high gold concentrations were also obtained in chloride free conditions. These results provide good argument for significant dissolution of gold in chloride free complexes in nature. The high concentrations of gold observed in synthetic arsenopyrites varying over a range of As:S stoichiometries emphasises that composition alone is not a major factor in gold uptake.

Structural analyses of various synthetic auriferous arsenopyrite crystals showed that there were similarities with natural arsenopyrite samples. However, the unit cell dimensions were larger and some crystals exhibit loss in symmetry. Rapid crystallisation along the b axis caused some disorder, resulting in many crystals exhibiting displacement faults. The presence of these faults may contribute to high concentrations of gold in its structure. The displacement results in the reordering of the arsenic and sulfur atoms along the displacement plane. The location of gold in the arsenopyite structure is discussed in Chapter 6.

While the dry synthesis approach did not succeed in incorporating gold in solid solution in arsenopyrite these experiments provide information on the mobility of gold as discussed in Chapter 7

Chapter 5

5.0 COMPOSITION AND STRUCTURE OF NATURAL AND SYNTHETIC PYRITE

Auriferous pyrite, like arsenopyrite is also an important mineral in many gold ore deposits. In the course of the present studies, the presence of pyrite in a number of the arsenopyrite samples studied prompted the investigation of pyrite and its relationship with gold in terms of its structure and composition. In the arsenopyrites synthesised at 400°C, the presence of small amounts of arsenian pyrites was also confirmed, mostly by TEM studies. The data on both natural and synthetic pyrites are discussed and compared in the following section.

5.1 Compositions

The average compositions and their standard deviations for natural pyrites found in several of the arsenopyrite samples analysed are shown in Table 5.1. The arsenic content in the grains analysed appeared to vary from grain to grain, even within the one sample. A high percentage of the pyrite grains had little arsenic present. The measured iron content varied between 0.330 and 0.335. Values below 0.33 may arise as a result of vacancies in the pyrite structure or substitution of arsenic on iron sites, as has been proposed by Johan *et al.* (1989) and Marcoux *et al.* (1989) for arsenopyrite. The deviation of pyrite from FeS_2 to $FeS_{1.93}$ has been reported by Finklea *et al.* (1976).

Most of the synthetic pyrite grains analysed contained some arsenic. This is most probably associated with the high arsenic content in the starting materials used to make synthetic arsenopyrites. Several pyrites contained very high arsenic contents which suggested the possibility of an error in their analyses. However, examination of several arsenian pyrite grains, which structures were confirmed to be pyrite under the TEM, revealed arsenic contents between 5 to 10wt%. Figure 5.1 shows the

Table 5.1 - Composition of pyrites (Atomic frac, sd)			
	Fe	As	S
Sheba	0.330±0.001	0.002±0.002	0.668±0.002
Coolgardie	0.333±0.001	0.001±0.001	0.666±0.002
Paddington	0.336±0.002	0.001±0.001	0.663±0.002
Pine Creek	0.333±0.003	0.001±0.002	0.666±0.003
Utah	0.333±0.004	0.003±0.007	0.662±0.005
Le Chatelet	0.334±0.003	0.03±0.01	0.65±0.02
	Sb 0.0002±0.0002		

Table 5.2 Structural parameters of some pyrites						
Unit Cell Dimension (based on space group Pa3)						
SAMPLE	Le Chatelet	Sheba	Pine Creek	Utah	Victory	Synthetic
Unit cell Dimensions						
a (Å)	5.417	5.420	5.416	5.420	5.417	5.42
Volume (Å^3)	158.96	159.22	158.84	159.21	158.92	159.21
Sites Occupancies						
As	0.01	-	0.03	-	-	nd
S	1.99	-	1.97	-	-	nd
Atomic Coordinates						
Fe	fixed 0,0,0					
S x,y,z	0.385	0.383	0.387	0.382	0.385	.37
Isotropic temperature factors						
Fe	fixed			0.26		
S				0.33		
Profile						
Shape	0.74	0.88	0.49	0.88	0.50	.88
WHH						
	0.03	0.08	-0.02	0.10	0.05	-.0.04
	-0.02	-0.10	0.03	-0.10	-0.07	0.11
	0.03	0.06	0.04	0.06	0.05	0.04
RP	8.49	4.97	6.07	7.25	8.99	10.3
RWP	12.65	6.72	8.57	9.80	12.43	13.35
GOF	11.83	4.23	6.76	9.77	8.42	17.50
Bragg R	2.39	2.60	2.78	2.84	2.21	6.18

Relationship of Gold content versus As:S ratio in Synthetic Pyrite Samples

$y = 251.37x + 0.0153, R2 = 0.87$
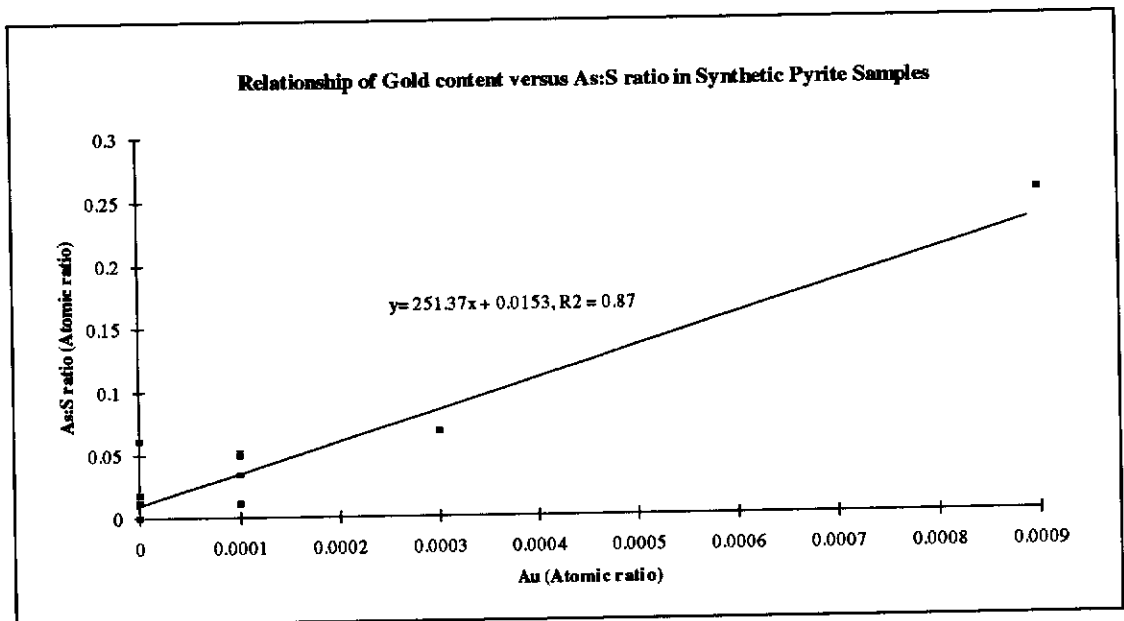
Figure 5.1 The relationship between As:S ratio and gold content for synthetic pyrite crystals.

relationship between the As:S ratio and gold content. Although the number of data points are small, the strong correlation observed here has also been found in many natural auriferous arsenian pyrite grains examined in the literature (Cook and Chryssoulis, 1990; Marion *et al.* 1991; Fleet *et al.* 1993).

5.2 Structure of Pyrite

Both natural and synthetic pyrite samples were analysed by XRD and CBED patterns for deviations in structure.

5.2.1 Rietveld Refinement

The structure of pyrite was refined using the Rietveld method on XRD patterns from powdered samples. Several of the data were during the refinement of arsenopyrite described in the previous section. The starting values for the refinement were those obtained by Bayliss (1977). The final values obtained are shown in Table 5.2. Generally, there appeared to be no correlation of stoichiometry with the refined parameters. The concentration of pyrite in several samples mixed with arsenopyrite was small and therefore the data for these is not so reliable. The presence of arsenic in pyrite did not appear to effect the unit cell dimensions in samples which contained sufficient concentrations of arsenic. The amount present was probably not sufficient to cause much variation in structural dimensions. Clark (1960) also observed no difference in unit cell dimensions in the synthetic sample which he analysed.

5.2.2 Structure Determination by Convergent Beam Electron Diffraction

Figures 5.2a to d show CBED patterns of [001] and [011] zone axes for natural and synthetic pyrite samples. The measurements of d-spacings agree with values obtained from XRD analyses as shown in Table 5.3. For the [001] pattern, 2mm symmetry was observed in the whole pattern. In the ZOLZ reflections GM lines were observed in (h00) for h odd reflections corresponding to the a-glide. A mirror plane is observed in the reflections perpendicular to the glide. In [011] patterns, GM lines were observed in (0kl) for k odd and (h00) for h odd reflections with a whole
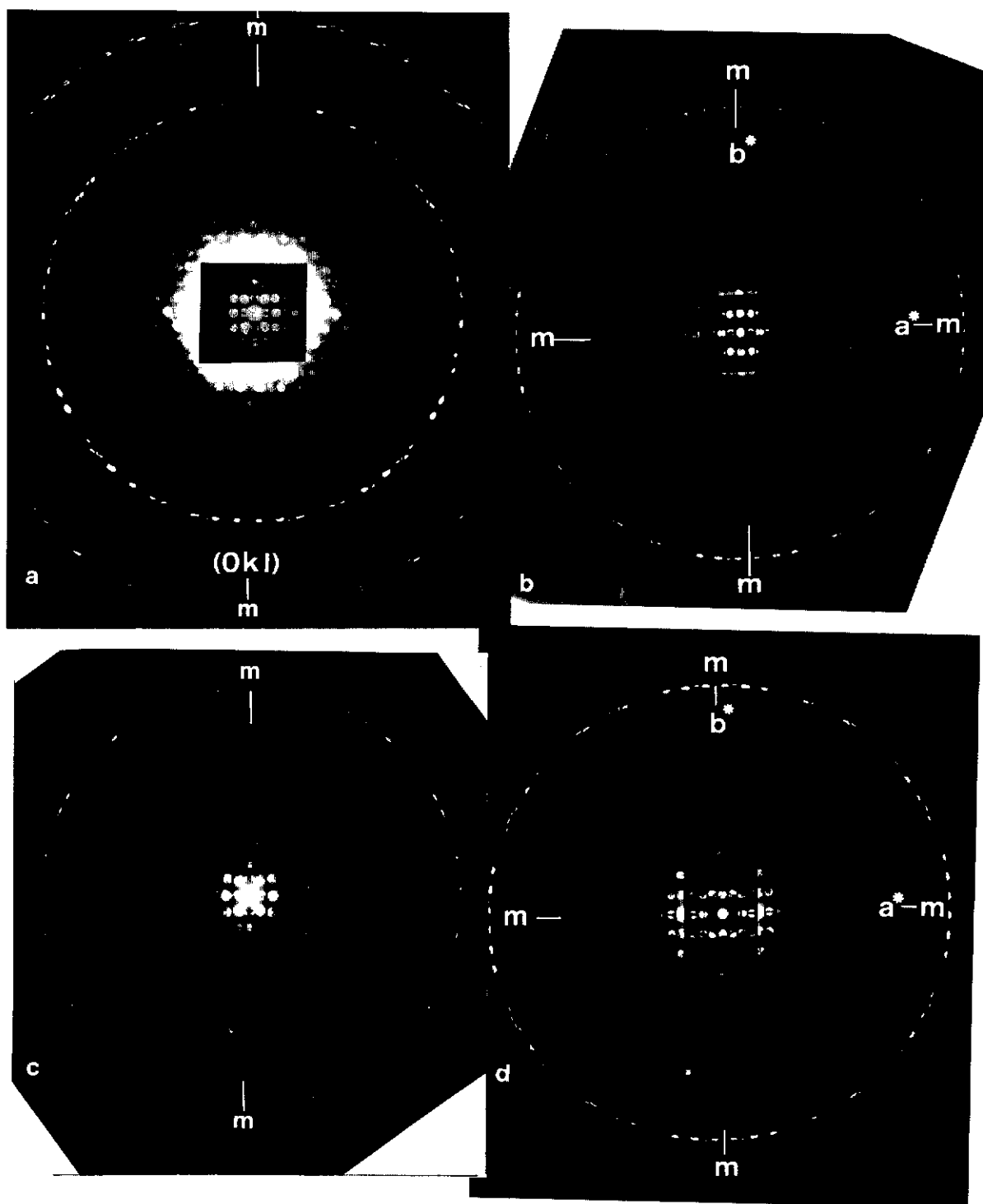
Figure 5.2 CBED patterns of [001] and [011] zone axes for a natural (a and b) and synthetic pyrite samples (c and d).

Table 5.3 Measured d-spacings of some major pyrite reflections							
Reflections	JCPDS	Le Chatelet	Sheba	Pine Creek	Utah	Synthetic	Victory
(111)	3.128	3.128	3.127	3.127	3.130	3.129	3.133
(002)	2.7088	2.713	2.708	2.708	2.711	2.710	2.713
(022)	1.9155	1.915	1.915	1.915	1.917	1.916	1.918

Table 5.4 Measured d-spacings from CBED and SAED patterns for pyrite					
	Photo No	(02-2)	(200)	(020)	Ratio
Le Chatelet	6769	1.898	2.730		0.70
	6755	1.920	2.704		0.71
	6778		2.729	2.723	1.00
	6776		2.674	2.713	0.99
	6760		2.750	2.698	1.02
Synthetic	4307	1.905	2.687		0.71
	4556	1.915	2.691		0.71
	4312	1.954	2.779		0.70
	4552	1.915	2.703		0.71
	4562		2.709	2.721	1.00
	4563		2.706	2.730	0.99

pattern with mirror symmetry in the direction of the (0kl) reflections. In this projection, a 2-fold screw axis was observed in the a* direction perpendicular to a glide in the other direction. The same patterns were observed in both synthetic and natural samples. In some studies GM lines have been observed in the HOLZ reflections for pyrite (Tanaka *et al.*, 1988) corresponding to vertical glide planes in the direction of the incident beam. Fine lines were observed in the HOLZ for some [001] CBED patterns.

The labelling of the zones is arbitrary for the following reasons. The a, b and c axes are all the same as expected for the cubic structure. The projection of CBED patterns along the [100] and [010] zones would be the same as in Figure 5.2 except that the GM lines for (0k0) and (h00) odd reflections would correspond to glide planes. This was confirmed in some patterns taken to two orthogonal axes. It was not possible in most cases to observe the three major zone axes in one crystal, due to the limitations of the tilt and rotate goniometer on the stage used in the TEM. Similarly, CBED patterns observed along the [011], [101] and [110] zones would all show mirror symmetry in the whole pattern with GM lines in both directions corresponding to glides along the a, b and c directions respectively, with two fold screw axes perpendicular to the glide and incident beam direction. The space group Pa3 has systematic absences of hk0 and h00 with h odd, 0kl and 0k0 with k odd and h0l and 00l with l odd. Some of these absences were confirmed in the previous discussion. Two types of pyrite, one isotropic and the other anisotropic have been observed (Smith, 1942). The isotropic pyrite has a cubic structure with space group Pa3 (Finklea *et al.*, 1976) and the anisotropic pyrite is pseudocubic (Bayliss, 1977). The latter has been interpreted, like cobaltite, as a sextuplet of interpenetrating twin-related orthorhombic (space group $Pca2_1$) domains about a $\overline{3}$ twin axis [111] (Bayliss, 1989). For the space group $Pca2_1$, the forbidden reflections 010 and 011 in the space group Pa3 would be present. However these were not observed.

The crystals examined showed no variation from the Pa3 structure for both natural and synthetic pyrites. The presence of impurities (e.g. Sb and As) in some of

the pyrites may suggest that these should adopt the ordering scheme of the cobaltite subgroup (Pca2$_1$) through twinning (Bayliss, 1989). If this is the case, then twinning possibly occurs at a macroscopic scale, rather than a microscopic scale, for these types of pyrites. No distortions were observed in any CBED patterns indicating little, if any, disorder in the structure which would also correspond to deviations in the cubic structure. Measurements of d-spacing of CBED and SAED patterns showed no real change in unit cell dimensions with chemical composition obtained from EDX under TEM (Table 5.4).

Figures 5.3a and b show the projections of the pyrite structure along the [001] and [011] directions respectively. The pyrite structure is essentially the NaCl structure, where iron replaces Na and two sulfur atoms replace Cl. The iron atoms are octahedrally coordinated to six sulfur atoms. The octahedra share only corners as shown in Figure 5.3.

5.3 Conclusions on Pyrite Structure

For both natural and synthetic pyrites examined, the structure appeared not to deviate from cubic pyrite with the space group Pa3. Twinning was not observed in CBED patterns. No deviations in the structure were observed between natural and synthetic pyrites along the [001] and [011] zones, which would hinder interpretation of data for the electron channelling experiments carried out in determining gold in the pyrite structure (see Chapter 6).

The presence of isotropic or anisotropic pyrite may not be controlled by chemical composition and the presence of one or the other may be controlled by temperature, as suggested by Bayliss (1977). Fleet et al. (1989) reported {100} planar faults in both arsenic poor and arsenian pyrites, hence their presence is probably not related to arsenic content. Chang and Zang (1991) observed an increase in unit cell dimensions in the pyrite structure associated with gold ores. However, subsequent examination of some of their material (Victory sample listed in the Tables) has shown the presence of some gold inclusions. Therefore, their relationship of gold

The crystals examined showed no variation from the Pa3 structure for both natural and synthetic pyrites. The presence of impurities (e.g. Sb and As) in some of the pyrites may suggest that these should adopt the ordering scheme of the cobaltite subgroup (Pca2₁) through twinning (Bayliss, 1989). If this is the case, then twinning possibly occurs at a macroscopic scale, rather than a microscopic scale, for these types of pyrites. No distortions were observed in any CBED patterns indicating little, if any, disorder in the structure which would also correspond to deviations in the cubic structure. Measurements of d-spacing of CBED and SAED patterns showed no real change in unit cell dimensions with chemical composition obtained from EDX under TEM (Table 5.4).

Figures 5.3a and b show the projections of the pyrite structure along the [001] and [011] directions respectively. The pyrite structure is essentially the NaCl structure, where iron replaces Na and two sulfur atoms replace Cl. The iron atoms are octahedrally coordinated to six sulfur atoms. The octahedra share only corners as shown in Figure 5.3.

5.3 Conclusions on Pyrite Structure

For both natural and synthetic pyrites examined, the structure appeared not to deviate from cubic pyrite with the space group Pa3. Twinning was not observed in CBED patterns. No deviations in the structure were observed between natural and synthetic pyrites along the [001] and [011] zones, which would hinder interpretation of data for the electron channelling experiments carried out in determining gold in the pyrite structure (see Chapter 6).

The presence of isotropic or anisotropic pyrite may not be controlled by chemical composition and the presence of one or the other may be controlled by temperature, as suggested by Bayliss (1977). Fleet *et al.* (1989) reported {100} planar faults in both arsenic poor and arsenian pyrites, hence their presence is probably not related to arsenic content. Chang and Zang (1991) observed an increase in unit cell dimensions in the pyrite structure associated with gold ores. However,

Figure 5.3 The [011] and [100] zone projections of the ideal structure of pyrite as octahedra model as well as an atoms model.

subsequent examination of some of their material (Victory sample listed in the Tables) has shown the presence of some gold inclusions. Therefore, their relationship of gold to structure appears irrelevent. In this study, measured SAED patterns of both non-auriferous and auriferous pyrite showed no change in cell dimensions. In addition, the high arsenic content appeared not to affect the dimensions.

Chapter 6

6.0 LOCATION AND FORM OF GOLD IN PYRITE AND ARSENOPYRITE STRUCTURE

6.1 Introduction

To provide direct evidence of structurally incorporated gold, the following studies were undertaken to determine the location of gold within synthetic auriferous arsenian pyrite and arsenopyrite structures using the technique known as ALCHEMI (Atomic Location by CHannelling Enhanced MIcroanalysis) (Taftø and Spence, 1982a,b).

From the detailed structural analyses of pyrite and arsenopyrite described in the earlier sections, several crystallographic directions which produced separation in projection of the different sites as well as strong channelling effects between the host cations and anions were sought. In pyrite, the partitioning of both arsenic and gold impurities on to either iron or sulfur host sites was examined because of the likely association of these elements in the structure. In arsenopyrite partitioning of the gold impurity on to either the iron, arsenic or sulfur host sites was assessed. For the channelling experiments only one synthetic sample of arsenopyrite containing pyrite contained sufficient gold to be detectable by an EDX detector mounted on the TEM. The natural Sheba arsenopyrite sample also contained sufficient detectable gold in some grains and was examined. In general, for channelling experiments no specific attention is paid to the selection of a zone axis or a particular orientation (Turner *et al.*, 1991). However, to aid in the interpretation of the results, particularly for arsenopyrite, it was necessary to find crystallographic orientations which were not affected by twinning or structural distortion. It was noted in Chapter 4 that CBED patterns showed some distortions in the GM lines along the b axis. Therefore the channelling effects and gold substitution in both well formed and disordered CBED patterns were analysed.

6.2 Materials and Methods

6.2.1 Atomic Location by Channelling Enhanced Microanalysis Technique (ALCHEMI)

Conventional X-ray microanalysis in the transmission electron microscope assumes that all atomic species in a crystalline phase experience an equal flux of electrons averaged through the crystal thickness. Both theoretical calculations and experimental measurements (Hashimoto et al., 1962; Duncumb, 1962; Hall, 1966; Hutchings et al., 1978) indicate that anomalous increases in characteristic X-ray production (by as much as a factor of three), can result when thin crystalline foils are oriented in strongly diffracting conditions.

electron current density distribution
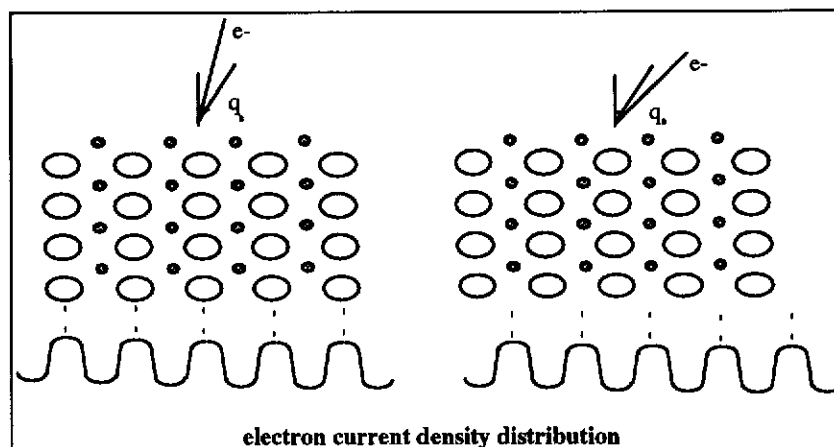
Figure 6.1 Schematic representation of the orientation dependence of the electron current distribution (a) With the incidence angle θ less than the Bragg angle θ₍ᵦ₎, the current maxima coincide with the planes of atoms with the highest projected potential (b) With a larger incidence angle the current maxima lie on another set of planes.

Borrmann (1941) first observed that the absorption of an X-ray beam depended on its crystallographic direction. The mechanism has since been studied by many workers. The Borrman effect was first interpreted by von Laue (1949). The first experimental study of the orientation dependence of the emission product was carried out by Knowles (1956), who used an incident neutron beam to excite X-ray emission. Cowley (1964) suggested that these effects may contain useful structural information and provided an analysis of the depth dependence of the dynamical two-beam electron

wavefield. The variation of X-ray emission with the direction of an exciting electron beam was first studied by Duncumb (1962) and a thorough analysis of this effect including an assessment of its (unwanted) influence on X-ray microanalysis, has been given by Cherns et al. (1973). A detailed analysis of the structural information in diffuse inelastic electron scattering has been given by Gjonnes and Hoier (1971), while a technique for locating atom positions based on the X-ray Borrman effect has been described and used by Batterman (1969). This work has since been developed by several workers (Cowan et al., 1980). The essential idea is that the incident radiation establishes a standing wave across the crystal with the period of the lattice whose maxima coincide with the atoms for certain incident beam directions (Figure 6.1). These standing waves, known as Bloch waves (Kittel, 1986), are sets of plane waves propagating through the crystal from the top surface with their wave front normal to the surface. The probability of finding an electron at any point, or the local current density in a macroscopic sense, is given by the square of the amplitude of the Bloch wave at the point. The form of these Bloch waves can be calculated and modelled (Self, 1992). At these orientations, in addition to an enhanced absorption of the primary beam (Hashimoto et al., 1962) due to inelastic excitation processes that are highly localised at atomic sites, a corresponding higher emission product would also be observed. That is, the characteristic X-ray emission excited by the electron beam is detected and this is proportional to the magnitude of the electron wave field. By changing the direction of the incident electron beam to other orientations, the standing wave intensities would be a minimum on these crystallographic sites with a concomitant reduction in absorption and emission products.

6.2.1.1 Determination of Site Occupancy

The ALCHEMI technique for determining the site distribution of impurity elements in a host crystal was first described by Taftø and Spence (1982a,b) and Spence and Taftø (1982,1983). The technique has found application in many mineral, oxide and ceramic systems. Krishnan (1988) and Smyth and McCormick (1988) have

extensively reviewed the formulation, development and applications of the channelling analysis technique. More recently, Buseck and Self (1992) have also reviewed channelling techniques.

In general, this technique can distinguish neighbours in the periodic table; involves no adjustable parameters, external standards or special specimen preparations, is applicable to trace element concentrations (0.2-0.3wt%), is very accurate (3-10% error in site occupancy determinations depending on the formulation used) and can be routinely applied at very high spatial resolutions (10-40nm). Three crucial assumptions are made: the inelastic scattering events are assumed to be highly localised; the impurities/additions are assumed to be distributed uniformly with depth in the specimen and impurity elements are located on unique crystallographic sites.

6.2.1.2 Types of Channelling

There are two types of channelling conditions and these are either planar or axial channelling. An axial or planar channelling direction for the incident beam can be chosen in which Bragg scattering from only one set of parallel crystal planes occurs. These planes are selected to separate the sites of interest into alternating non-equivalent planes.

6.2.1.2.1 Planar Channelling

A planar channelling condition is one in which the crystal potential is averaged in two orthogonal directions normal to the excited systematic row. Experimentally, this corresponds to the case when single rows of spots are seen in the transmitted electron diffraction pattern. That is, crystals can be resolved into alternating layers of parallel non-identical planes, with each plane containing one or more specific crystallographic site.

6.2.1.2.2 Axial Channelling

Many crystals structures do not have an orientation for which the various atom species lie in alternative planes and so only axial channelling can be used. In low

order zone axis orientations, the atoms do not line up in planes but instead line up in columns. There are generally a large number of diffracted reflections at zone axis orientations and so the current variation is greater for axial orientations than for planar diffraction (Pennycook and Narayan, 1985; Rossouw and Maslen, 1987). For axial channelling the electron beam current falls on columns of high electrostatic potential for orientations inside the Bragg angles of the first order reflections. Using zone axis conditions, much stronger channelling is observed (Pennycook and Narayan, 1985; Otten and Buseck, 1983; Rossouw et al., 1989, 1988) as may be expected from the nature of the 2-D standing wave patterns produced at axial orientations. Such conditions often result in variations of X-ray emission from different host species even when the projected positions of the species do not vary greatly (Rossouw and Maslen, 1987; Rossouw et al., 1988). Even if sites overlap in projection, the rapid z-modulation of the fast electron wavefunction, due to HOLZ components in the diffracted beams, can enable different sites to be distinguished (Lynch and Rossouw, 1987).

6.2.1.3 Delocalisation Effects

One problem with electron channelling experiments, particularly using the ratio method, is the assumption that the impurity species samples the same electron flux as the host species on a particular site. Because atoms are not stationary at one point in a crystal, the combination of thermal vibrations and the electron-interaction range effectively delocalises the atom position in a structure. Phenomena related to these effects are collectively known as localisation effects.

A number of studies have demonstrated failure of this localisation approximation (Pennycook and Narayan, 1985; Otten and Buseck, 1987; Rossouw and Maslen, 1987; Rossouw et al., 1989). Various methods to correct for delocalisation have been suggested, but none is of general applicability (Pennycook and Narayan, 1985; von Hugo et al., 1988; Pennycook, 1988; Rossouw et al., 1988; Spence et al., 1988). If the sum of the thermal vibration amplitude and the impact

parameter is greater than the interplanar spacing, channelling effects will not be observed (Self and Buseck, 1983). If the elements in a structure have widely differing delocalisations, channelling experiments will not work (Buseck and Self, 1992).

There are two methods for analysing ALCHEMI data. The first original method developed by Spence and Taftø (1982), involves the ratio of the normalised X-ray count rates. The second is a refinement of the first and is a statistical method (Rossouw et al., 1989) involving standard multivariate analysis. Both these methods were used and are discussed below.

6.2.1.4 Ratio Method

For the ratio method a crystallographic orientation is chosen which separates two or more sites. If $N_A^{(1,2)}$, $N_B^{(1,2)}$ and $N_X^{(1,2)}$ are the six X-ray counts from host atom on reference sites A and B, and X is the impurity distributed on one or both host sites, then the relationships between the X-ray counts and the two beam orientations, channelling (1) and nonchannelling (2) can be described as follows:

$$N_B^{(1)} = P_B m_B I_B^{(1)} \tag{6.1}$$

$$N_A^{(1)} = P_A m_A I_A^{(1)} \tag{6.2}$$

$$N_X^{(1)} = P_X m_X C_X I_B^{(1)} + P_X m_X (1-C_X) I_A^{(1)} \tag{6.3}$$

$$N_B^{(2)} = P_B m_B I_B^{(2)} \tag{6.4}$$

$$N_A^{(2)} = P_A m_A I_A^{(2)} \tag{6.5}$$

$$N_X^{(2)} = P_X m_X I_c^{(2)} \tag{6.6}$$

where $I_A^{(1,2)}$ and $I_B^{(1,2)}$ are the thickness averaged electron intensities on the A and B sites for the incident beam directions (1) and (2), m_A, m_B and m_X are the number of sites per unit cell for the A, B and X species, while P_A, P_B and P_X are factors which take into account differences in fluorescent yield and other scaling factors. C_X is the fraction of species X on the B site. Then using equations (6.1) to (6.6) the fraction of species X on the B site is obtained from

$$C_X = [1-(N_X^{(2)}/N_A^{(2)})/(N_X^{(1)}/N_A^{(1)})]x[(N_X^{(2)}/N_B^{(2)})/(N_X^{(1)}/N_B^{(1)})$$
$$-(N_X^{(2)}/N_A^{(2)})/(N_X^{(1)}/N_A^{(1)})]^{-1} \tag{6.7}$$

In the equation, only measured intensities are used. Knowledge of k-factors, specimen thickness, or even absolute elemental concentration are not required. This is a modification of Spence and Taftø's (1982) method as the final equation derived differs in that only one channelling orientation is used instead of two. Otten and Buseck's (1987) method outlined above was used so that results could be obtained for each diffraction condition while not masking localisation effects.

6.2.1.5 Multivariate Statistical Analysis Method

Rossouw *et al.* (1989) and Turner *et al.* (1990) have developed an improved approach for the analysis of ALCHEMI data which combines data from several experiments. Their method involves standard multivariate analysis to obtain the best fit, and uncertainties in the fit, of impurity counts as a linear combination of the counts from the host species. The method provides values for the fractional partitioning of an impurity species between host sites and the concentration of the counts from the host species. This technique was initially developed for the case of a single impurity which could partition over several host atom sites (Rossouw *et al.*, 1989). However it has now been extended to the case of multiple substitutional impurities and multiple host atom sites (Turner *et al.*, 1990).

In this method the assumption is made that for each substitutional impurity species p (p=1,.....,P), the counts N_p may be written as a linear combination of the host atom count N_i (i=1,.....,I) for each of the spectra s (s=1,.....,m):

$$N_p^s = \sum_i \alpha_{ip} N_i^s$$

The coefficients α_{ip} and their errors are determined by multivariate analysis. For m separate EDX spectra and $v = I.P$ fitted parameters α_{ip}, the criterion $v < m$ must be satisfied, to give m- v degrees of freedom. The coefficients α_{ip} are obtained by the χ^2 minimisation technique, i.e. by minimising the quantity

$$\chi^2 \ = \ \sum_s \left| \frac{\sum_i \alpha_{ip} N_i^s \ - \ N_p^s}{\sigma_s} \right|^2$$

In the first instance the standard deviation in the spectrum s is estimated by adding statistical noise in quadrature, and then obtaining a final value from

$$\sigma^2 = \frac{\sum_s \left| \sum_i \alpha_{ip} N_i^s - N_p^s \right|^2}{s}$$

recomputing, $\chi^2 \approx m$ - v (the number of degrees of freedom).

The concentration C_p of impurity atom p and the fraction f of p atoms which reside on the host sites i are obtained from the α_{ip} coefficients, to give

$$C_p = \sum_i \frac{\alpha_{ip} n_i / k_{ip}}{(1 + \sum_q \alpha_{iq} n_i / k_{iq})}$$

where n_i is the number of host atoms of type i per unit cell and k_{ip} is the k-factor ratio k_i / k_p for atoms i and impurity p. The fractional partition f_{ip} is then

$$f_{ip} = \frac{1}{C_p} \frac{\alpha_{ip} n_i / k_{ip}}{(1 + \sum_q \alpha_{iq} / k_{iq})}$$

The uncertainties in C_p and f_{ip} are determined from partial derivatives to give

$$\delta C_p^2 = \sum_i \left[\frac{\delta \alpha_{ip} n_i / k_{ip}}{(1 + \sum_q \alpha_{iq} / k_{iq})^2} \right]^2$$

$$\delta f_{ip}^2 = \left[\frac{\delta \alpha_{ip} n_i / k_{ip}}{C_p (1 + \sum_q \alpha_{iq} / k_{iq})^2} \right]^2 + \left[\frac{\delta C_p \alpha_{ip} n_i / k_i}{C_p^2 (1 + \alpha_{iq} / k_{iq})} \right]^2$$

6.2.2 Sample Preparation

Samples were prepared in the same way for TEM studies as those described in Chapter 3. However, in addition to using copper grids, crushed samples were

dispersed on carbon coated beryllium grids to reduce background radiation within the EDX spectra obtained.

6.2.3 Energy Dispersive Analysis -Calibration of As,Fe,S and Au

For analytical electron microscopy, relative concentrations of atomic species in thin film samples were measured using energy dispersive X-ray spectroscopy and the Cliff-Lorimer "k-factor" analysis (Goldstein, 1979). For thin samples, the intensities of the emitted characteristic X-rays were directly proportional to the elemental concentrations in the irradiated sample volume. Thus the effects of absorption and fluorescence were neglected.

A k-factor was obtained using the equation described by Cliff and Lorimer (1972) as follows:

$$k = k_{AFe} = C_A/C_{Fe} \cdot I_{Fe}/I_A$$

where I_{Fe} and I_A are the measured intensities from the same point for iron and another element A (which is either As, S or Au) and the compositions C_A and C_{Fe} are known from the standard.

A sample of natural arsenopyrite characterised by Kretschmar and Scott (1976) known as ASP200, was crushed and dispersed on a carbon grid. Using the lithium-drifted silicon (EDAX™ Pv9900) energy dispersive X-ray detector mounted on the 430 TEM, the spectra of arsenopyrite were recorded for different orientations on several grains. Prior to collecting the data, the orientation of the crystal was observed so that the point where the analysis was chosen did not fall on a zone axis or major kikichi lines where some channelling may occur and give incorrect intensities. Potential errors in k-factor measurements have been reported as a result of channelling or due to absorption (Eades et al., 1990). The integrated intensities of the As Lα, As Kα, Fe Kα and S Kα were obtained after the background was removed using EDAX™ software. From the known composition of ASP200 the k-factors were obtained and processed following the method of Turner and White (1992). The ratios

of Fe Kα to As Lα, As Kα, and S Kα obtained were plotted in ascending order (Figures 6.2a to c). These plots showed that a plateau was observed with points dropping off on one side and increasing on the other side. The values on either side of the plateau were discarded and attributed to absorption and channelling orientations.

On the assumption that the extreme points are due to systematic errors, a search was made for a sub-set of n data points which had a spread consistent with random errors about their mean. The resulting k-factor would have a standard deviation equal to $<\delta k>/\sqrt{n}$, where $<\delta k>$ is the average error in the individual estimates. This was achieved by calculating a series of running averages $<k_j>$ over j points (j=5,7,9,...n) and the corresponding standard deviations σ_j. For each j, the average k-factor which had the minimum deviation, σ_{min}, was compared with $<\delta k_j>/\sqrt{j}$. The most acceptable estimate of k was that for which these two measures of error were equal (Turner and White, 1992). The values obtained are shown in Tables 6.1a to 6.1c. From the tables the consistent set of n estimates of k_{AsKFeK}, k_{AsLFeK} and k_{SKFeK} was n= 5. Therefore the best k-factor values were $k_{AsKFe} = 1.294 \pm 0.003$, $k_{AsLFeK} = 2.09 \pm 0.01$, and $k_{SKFeK} = 1.711 \pm 0.008$. The errors appeared to be much higher for the low energy elements of S K (2.30 keV) and As L (1.85 keV) which may be attributed to localisation effects or absorption.

To determine the k-factor for iron and gold, a mixture of gold and iron powder was placed in a test tube and heated with a torch to over 1000°C. The sample was then crushed and reheated to produce a homogeneous sample. The sample was made into a polished section and its composition determined using an electron microprobe. A selected area was then scraped off and dispersed on a carbon coated copper grid and analysed under the TEM in the same way as the arsenopyrite sample. The gold L peak at 9.71 keV was measured, as the gold M peak (2.00 keV) is masked by the sulfur peak at 2.30 keV in the arsenopyrite samples analysed. The k-factor was determined in the same way as for As, S and Fe. A plot of the k-factors obtained is shown in Figure 6.2d. The best estimate from Table 6.1d for k_{AuFe} was 1.009 ± 0.008 for n= 5. Qualitative chemical analyses were collected for all observations.
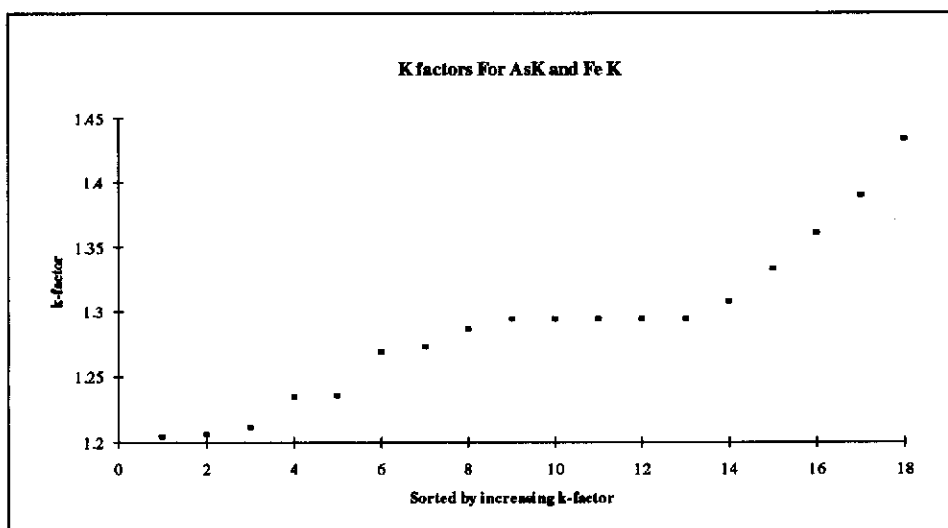
Figure 6.2a Experimental values of k_{AsKFe} in order of increasing k.
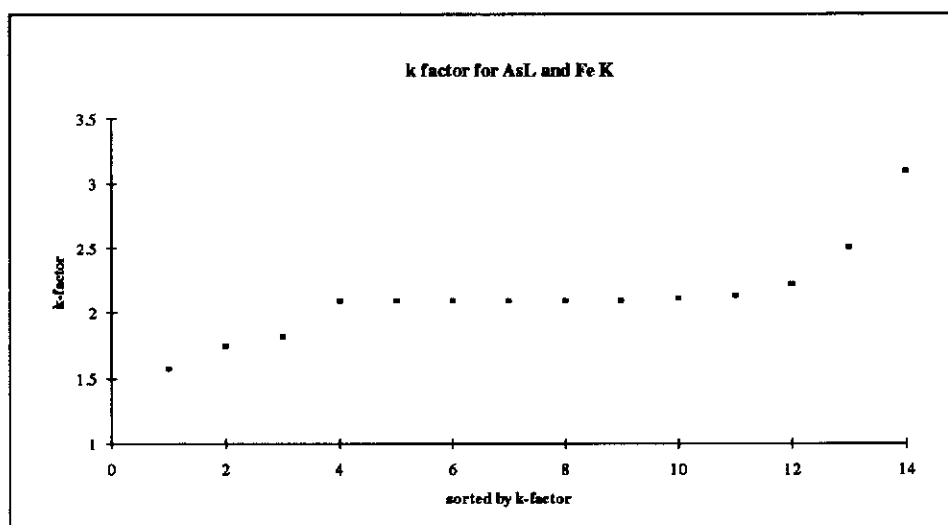
Figure 6.2b Experimental values of k_{AsLFe} in order of increasing k.
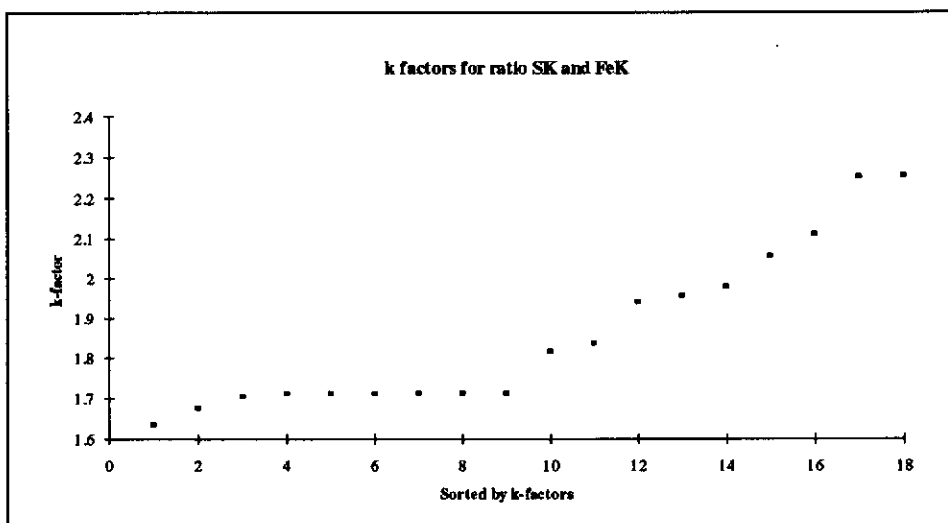
Figure 6.2c Experimental values of k_{SFe} in order of increasing k.
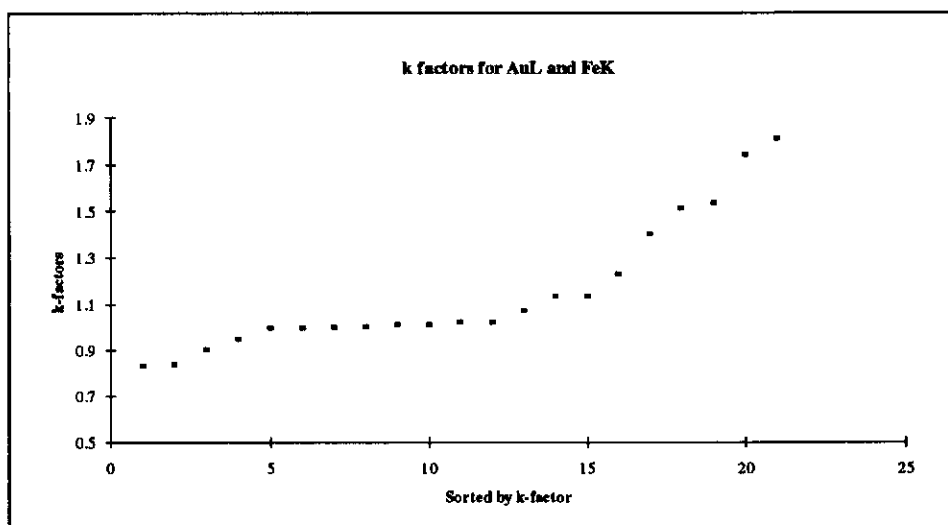
Figure 6.2d Experimental values of k_{AuFe} in order of increasing k.

Table 6.1a - Selection of Optimum k-factor for As K and FeK			
j	σjmin	$<\delta kj>/\sqrt{j}$	$<kj>$
5	0.2%	0.2%	1.294
7	0.6%	0.2%	1.295
9	1.2%	0.2%	1.289

Table 6.1b - Selection of Optimum k-factor for AsL and FeK			
j	σjmin	$<\delta kj>/\sqrt{j}$	$<kj>$
3	0.9%	0.3%	2.092
5	0.8%	0.2%	2.090
7	4.2%	0.2%	2.109
9	14.1%	0.2%	2.048

Table 6.1c - Selection of Optimum k-factor for SK and FeK			
j	σjmin	$<\delta kj>/\sqrt{j}$	$<kj>$
3	0.5%	0.5%	1.710
5	0.4%	0.5%	1.711
7	0.3%	0.4%	1.711
9	2.7%	0.4%	1.699

Table 6.1d - Selection of Optimum k-factor for AuL and FeK			
j	σjmin	$<\delta kj>/\sqrt{j}$	$<kj>$
5	0.8%	0.8%	1.009
7	0.9	0.7%	1.008
9	2.2%	0.6%	1.001

6.2.4 Strategies and Problems in Collecting Data

For suitable zone axes, data were collected by systematically obtaining an EDX spectrum on the zone axis and then collecting three or four analyses along two orthogonal systematic rows followed by an interdisposed systematic row. Finally the crystal was tilted well away from the zone axis and a 'non-channelling' pattern collected. During this procedure, spectrum analyses were recollected periodically at the zone axis and the elemental ratios calculated and checked with the original spectrum to ensure no changes had occurred during the experiment.

The main problems were firstly locating a pyrite or arsenopyrite crystal with sufficient detectable gold or arsenic and secondly finding a zone axis which provided strong channelling effects. Also, grains were not homogeneous in composition and so data from each crystal could not be correlated together as has been successfully done in some channelling experiments (Turner *et al.*, 1990), but had to be correlated separately. Consequently, the number of data points for each experiment was small. For determining channelling in pyrite the relative intensities of the iron and sulfur X-ray counts were observed. For the arsenopyrites the relative intensity of the Fe K and As K X-ray counts was monitored.

Suitable zone axes were chosen to minimise problems likely to be associated with twinning. For arsenopyrite, clear [101] zone patterns could be obtained and were used in most experiments, however, several minor zone axes were also used. An extensive search was made to find grains containing at least 0.5 wt% concentration of gold in order to determine channelling effects. The $K\alpha$ peak intensities of As, Fe and S and the $L\alpha$ of Au were recorded for channelling and non-channelling orientations for 200 seconds. Between five and ten spectra were collected for each mineral as the sample decomposed over time.

6.3 Results and Discussion

6.3.1 Channelling in Pyrite

As a preliminary to the location of any gold present, the strength of the channelling effect for iron and sulfur sites was first examined. Since very few crystals contained detectable gold the location of arsenic was also examined, because of its presumed association with gold in the structure. To determine the best direction, electron channelling was attempted along the [001] and [011] axes of the pyrite structure described in Chapter 5. The projected crystal structures of these two orientations are shown in Figures 5.4a and b. In these orientations the iron and sulfur sites are separate with both being columned into the page. Figure 6.3 shows an EDX spectrum of arsenian pyrite showing the channelling effect for two orientations, one for an 'off' zone and the other for the 'on' [011] zone orientation. This spectrum shows marked differences in peak intensities for iron and sulfur. With an increase in iron intensity for the direct zone orientation the sulfur and arsenic decreases indicating arsenic is on the sulfur site. To assess the extent of channelling between Fe and S sites, plots of the ratio of Fe K counts against S K counts are shown in Figures 6.4a, 6.5a, 6.6a and 6.7a for all pyrite zones analysed. The Fe K/S K ratio would remain the same for both 'on' zone (marked with a 'Z') and 'off' zone data if there was no effective relative change in the thickness-averaged electron fluxes for Fe and S for different orientations. Channelling effects were stronger for the [011] zones (~60%) than for the [001] zone (~20%). This was because the [011] zone was an axial orientation which has stronger channelling effects than the [001] which was more of a planar orientation.

Plots of the ratio of the host Fe K and S K counts against impurity As K or As L counts are shown in Figures 6.4(b and c), 6.5(b and c), 6.6(b and c) and 6.7(b and c) for various natural and synthetic pyrite crystals for the two zone axes examined. These disparate energy levels were chosen to assess the level of any delocalisation and/or absorption effects. The effect of channelling between the sulfur and iron sites
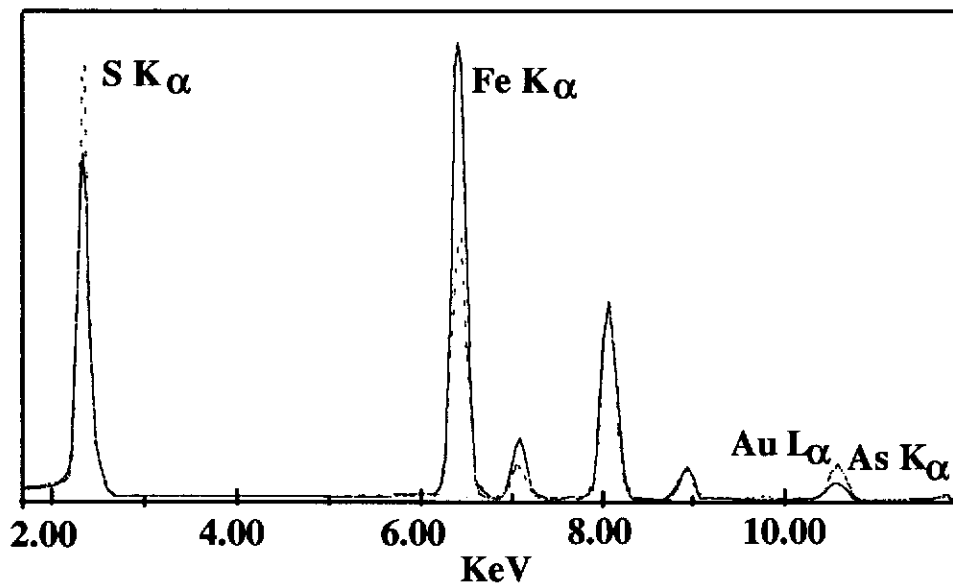
Figure 6.3 An EDX spectrum of arsenian pyrite showing the channelling effect for two orientations, one for an 'off' zone and the other for the 'on' [011] zone orientation. This spectrum shows marked differences in peak intensities for iron and sulfur. With an increase in iron intensity for the direct zone orientation the sulfur and arsenic decreases indicating arsenic is on the sulfur site.

Solid line - 'on zone, channelling
Dotted line - 'off' zone, non-channelling
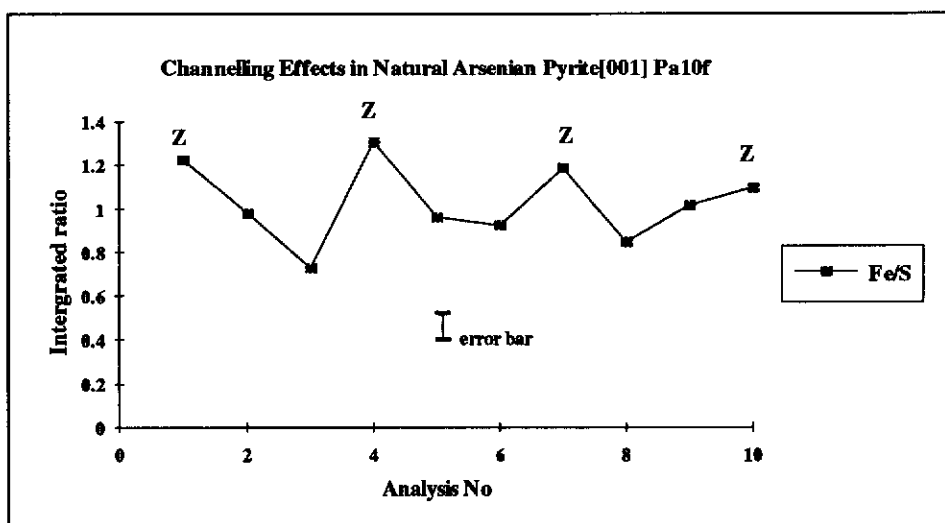
(a)
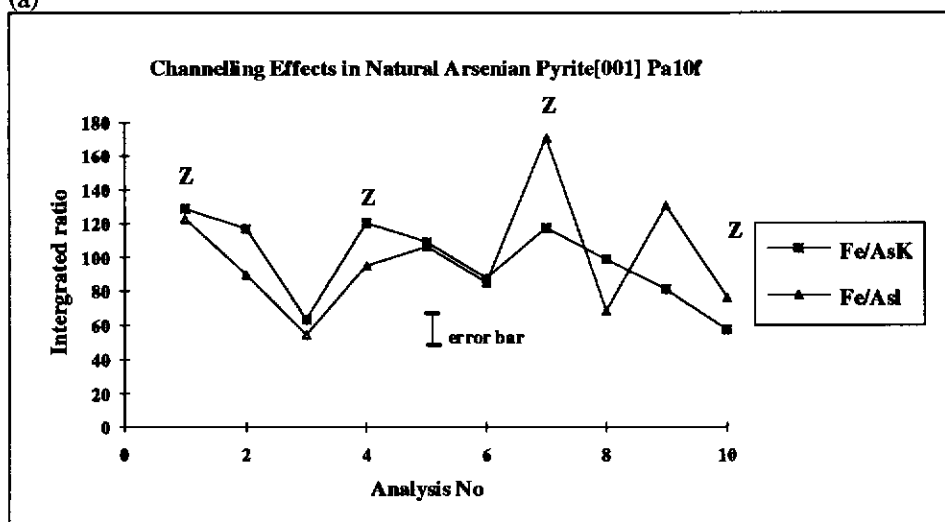
(b)
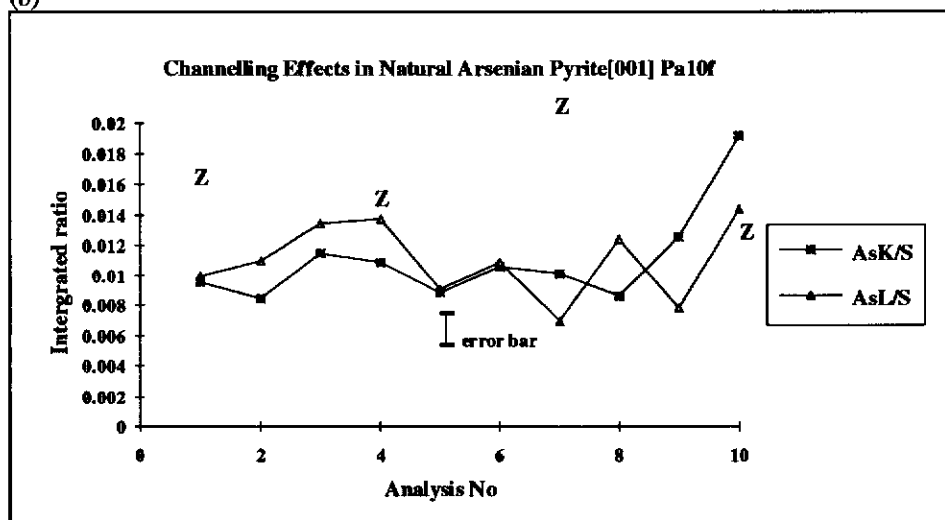
(c)

Figure 6.4 (a), A plot of Fe K/S K ratio showing the extent of channelling between Fe and S sites, (b) Plots of FeK/As ratio for both AsK and AsL showing the extent of channelling between As and Fe sites, (c) Plots of AsK and AsL to SK ratio showing the extent of channelling between As and S sites (Pa10f - [001]). (Z- 'on' zone or channelling direction)
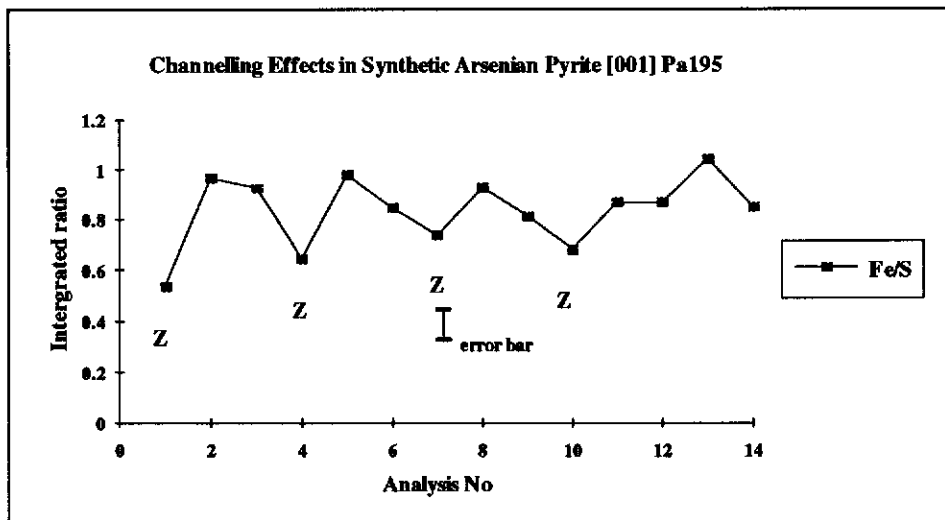
(a)
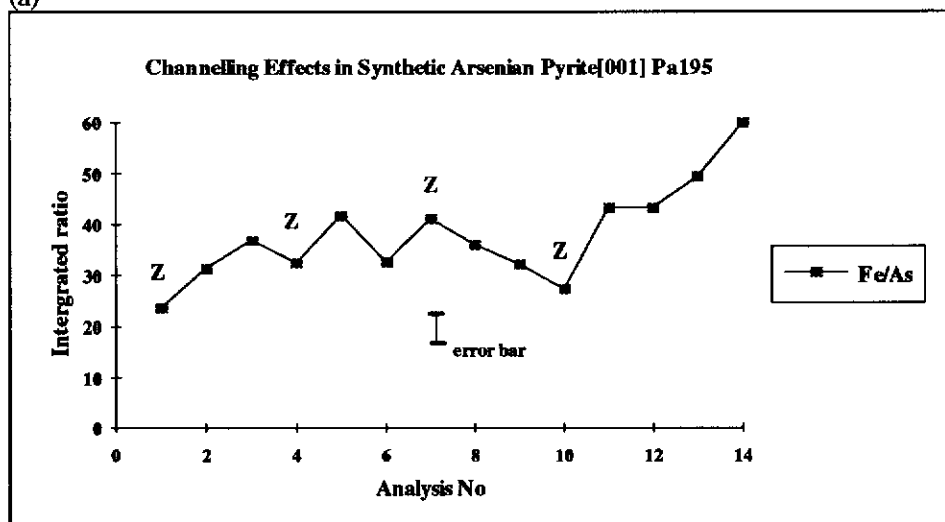
(b)
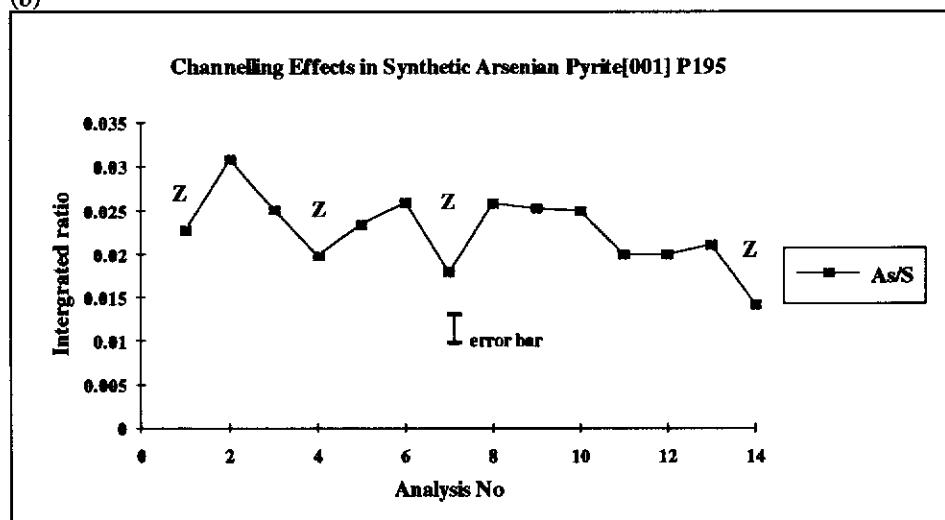
(c)

Figure 6.5 (a), A plot of Fe K/S K ratio showing the extent of channelling between Fe and S sites, (b) A plot of FeK/AsK ratio showing the extent of channelling between As and Fe sites, (c) A plot of AsK/SK ratio showing the extent of channelling between As and S sites (P195 - [001]). (Z- 'on' zone or channelling direction).
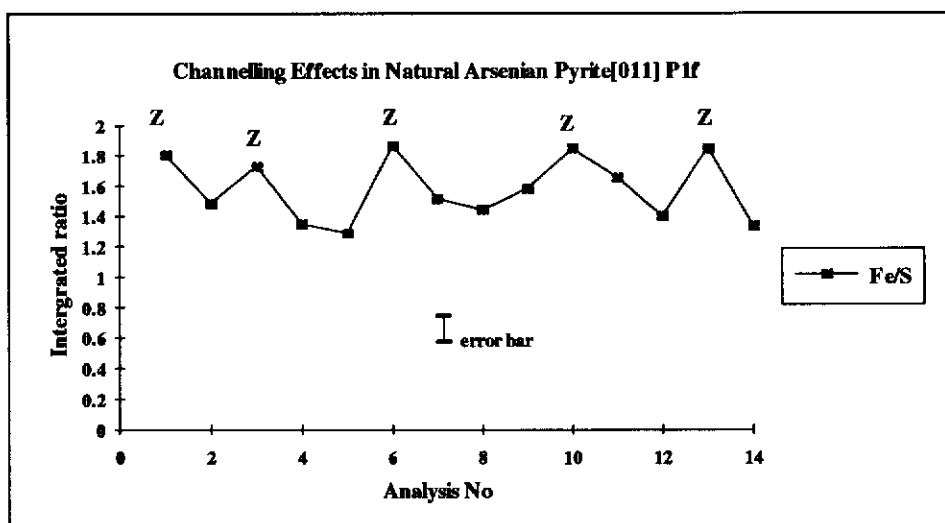
(a)
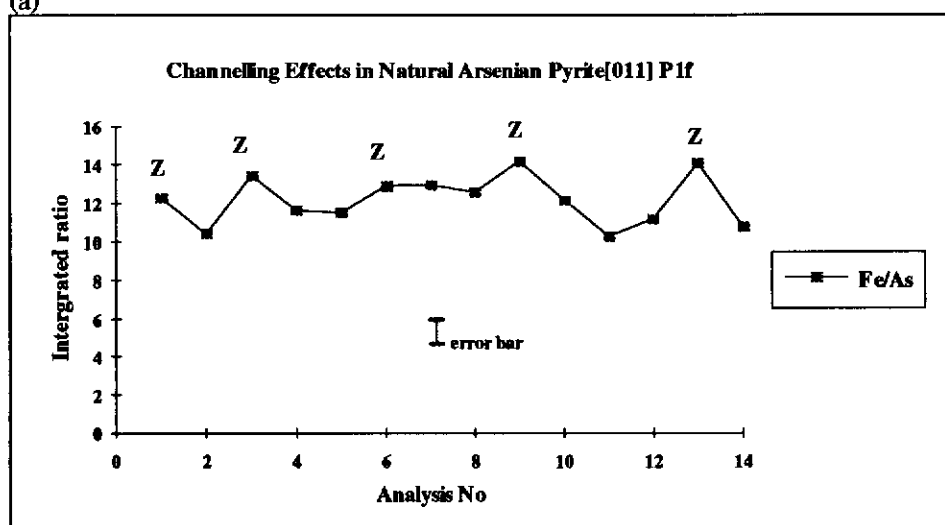
(b)
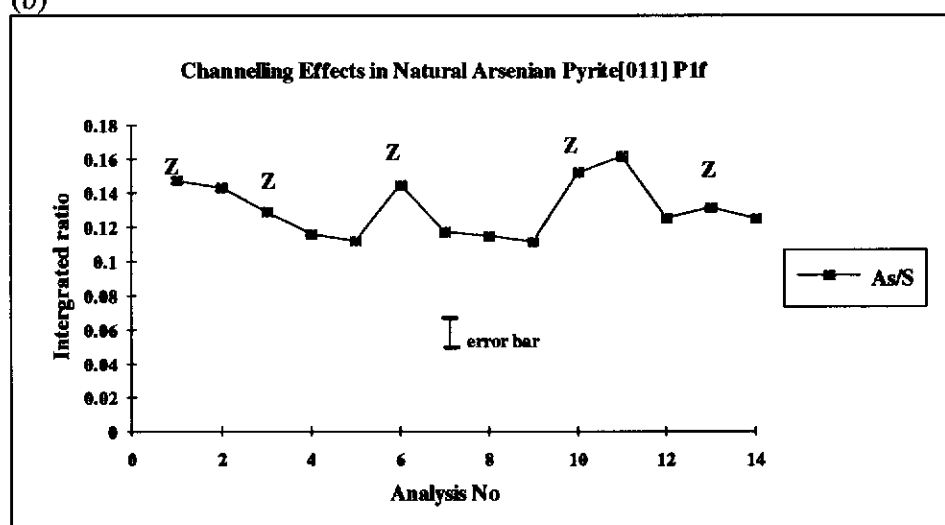
(c)

Figure 6.6 (a), A plot of Fe K/S K ratio showing the extent of channelling between Fe and S sites, (b) A plot of FeK/AsK ratio showing the extent of channelling between As and Fe sites, (c) A plot of AsK/SK ratio showing the extent of channelling between As and S sites (P1f - [011]). (Z- 'on' zone or channelling direction).
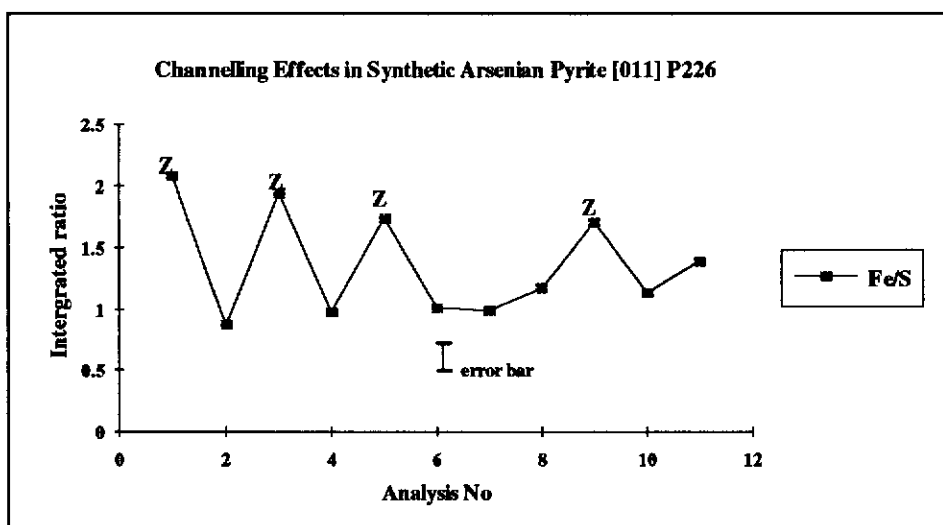
(a)
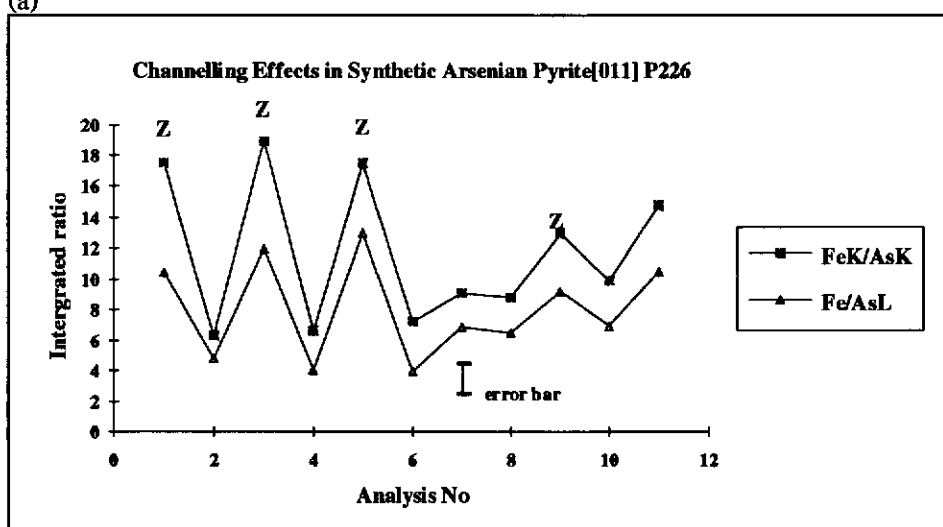
(b)

Figure 6.7 (a), A plot of Fe K/S K ratio showing the extent of channelling between Fe and S sites, (b) Plots of FeK/As ratio for both AsK and AsL showing the extent of channelling between As and Fe sites, (P226 - [011]). (Z- 'on' zone or channelling direction)

Channelling Effects in Synthetic Arsenian Pyrite [011] P226

(c)

Channelling Effects in Synthetic Arsenian Pyrite[011] P226
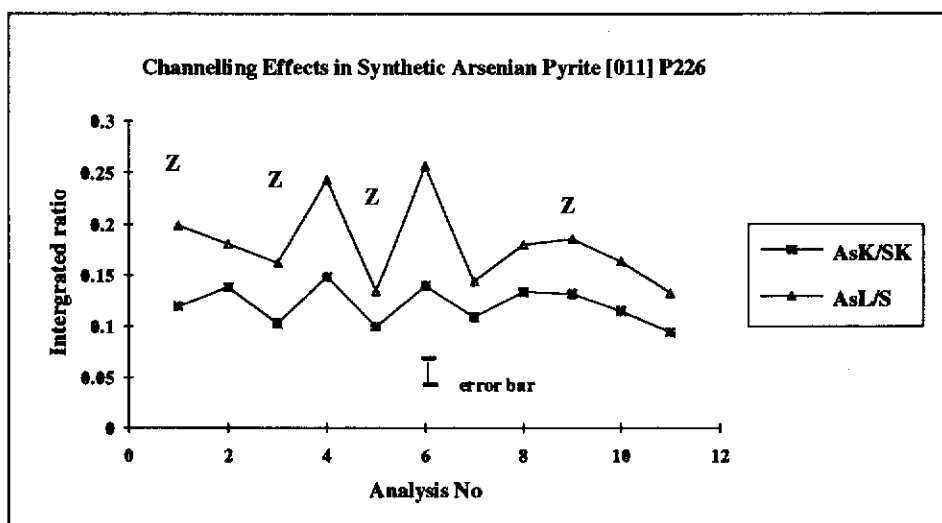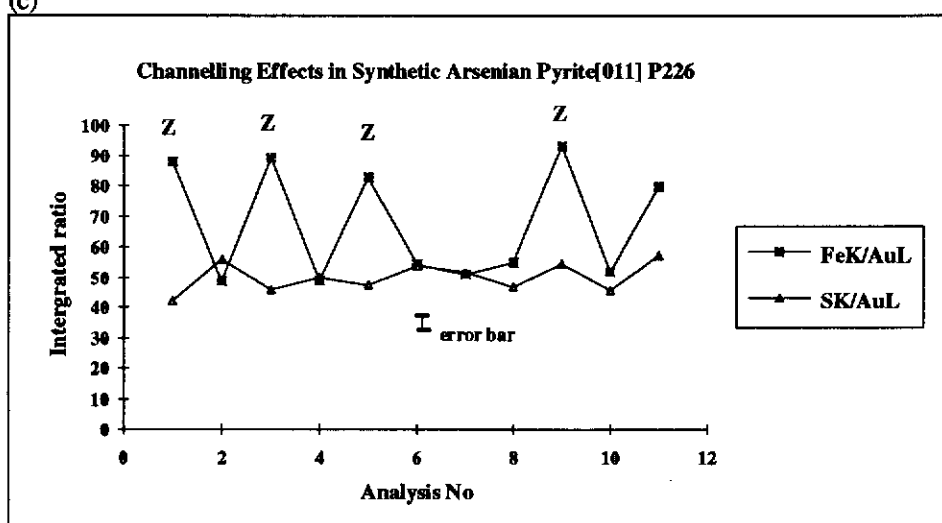
(d)

Figure 6.7 (c) Plots of AsK and AsL to SK ratio showing the extent of channelling between As and S sites. (d) Plots of Fe K and SK against Au L showing the extent of channelling between Au and the Fe or S sites (P226 - [011]). (Z- 'on' zone or channelling direction)

relative to the arsenic impurity can also be seen. For the arsenic impurity to be associated with one of the two sites in pyrite the ratio of Fe to As or As to S counts would remain the same for both channelling and non-channelling orientations.

For [001] zone data, (Figure 6.4 and 6.5) several crystals revealed variations in both the iron and sulfur data with arsenic, suggesting that both sites contain arsenic. The counting errors indicated that the slight change in As/S ratio was insignificant. A plot of the As L counts against Fe K and S K showed a similar trend as the As K counts data indicating no real problems associated with delocalisation effects and absorption. The As L energy resides next to the S K energy

For the [011] zone data (Figures 6.6 and 6.7) the arsenic impurity appears to follow the sulfur counts fairly well. There are some slight deviations which may account for some arsenic partitioning on the iron sites as well as most on the sulfur sites. Alternatively, the deviations may be attributed to delocalisation effects as the arsenic K peak at 10.45 keV has a higher energy than does the sulfur K peak at 2.30 keV. However, plotting the ratios of As L counts (1.30 keV) against Fe K and S K counts show similar relationships to the As K counts and so delocalisation and also absorption in this case, were not major problems.

Auriferous pyrites have been reported to contain up to 1400 ppm of gold in solid solution (Shui, 1991) which is below the detection limit of EDX (~0.4 wt%). Several crystals were located which had gold contents above the detection limit. However, very few crystals of pyrite contained sufficient gold to distinguish channelling effects and so data was limited to one crystal. A plot of the ratio of S K counts against Au L counts shows no change, indicating a strong association of gold to the sulfur sites. (Figure 6.7d). The ratio of Fe K counts to Au L counts deviate from linearity indicating that little, if any, gold is substituted on the iron site.

6.3.1.1 Analysis of Site Occupancy

Ratio Method

For the ratio method of analysis an internal standard was needed to calculate the site occupancies (Taftø and Spence, 1982a,b). The iron atoms only occur on the iron site and so these were used as the internal standard. As a measure of the channelling effects the following formula can be used (Taftø and Spence, 1982a,b):

$$R(Fe/X) = [N_{Fe}/N_x]_{ch}/[N_{Fe}/N_x]_{non-ch}$$

where N_{Fe} and N_x are the X-ray counts from Fe and the element X (X=S, As or Au) respectively. That is the channelling effects are expressed by the ratio of Fe/S for an 'on' zone channelling spectrum (ch) over that of the off zone (non-ch) spectrum for a set of analyses on and around the zone axis for all pyrites analysed. Calculated R(Fe/X) values were generally close to 1.0 for direct 'on' zone orientations. Some variation occurred for ratios with arsenic X-ray counts.

Figure 6.8a shows the calculated occupancies for As on S sites against the channelling effect [(Fe/S)$_{ch}$/(Fe/S)$_{non-ch}$]. There is a spread of data partially due to results representing a distribution of partially channelling and non-channelling orientations. Generally, there is a spread of data points for data collected on [001] zone axes whereas for the [011], data are close to 1.0 for As on S sites. The use of As L instead of the As K line data produced values in excess of one. These data points, as well as all data points larger than 1.0 or smaller than 0.0, are due to the localisation effect (Otten and Buseck, 1987). The degree of channelling (ratio R(Fe/S)) can be seen to have varied from one crystal to another even for similar zone axes. This is most probably related to the thickness of the crystals analysed. The thicker the crystal the larger the channelling effects (Rossouw and Maslen, 1987). The data conclusively show arsenic to be associated with the sulfur site in pyrite and that pyrite can give strong channelling.

The detectable gold presence in the pyrite P226 crystal showed a strong association of gold on the sulfur site (Figure 6.8b) since most of the points are
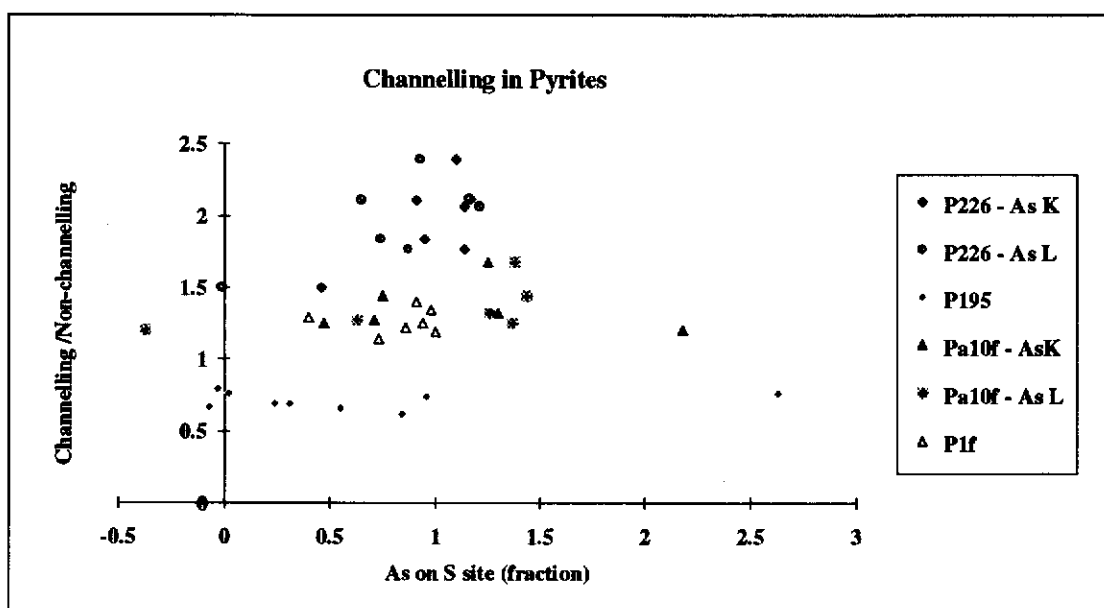
Channelling in Pyrites

Figure 6.8a shows the calculated occupancies for As on S sites against the channelling effect [(Fe/S)$_{ch}$/(Fe/S)$_{non-ch}$]. There is a spread of data partially due to results representing a distribution of partially channelling and non-channelling orientations. Generally there is a spread of data points for data collected on [001] zone axes (Pa195 and P10f).

Channelling in Pyrite (P226)
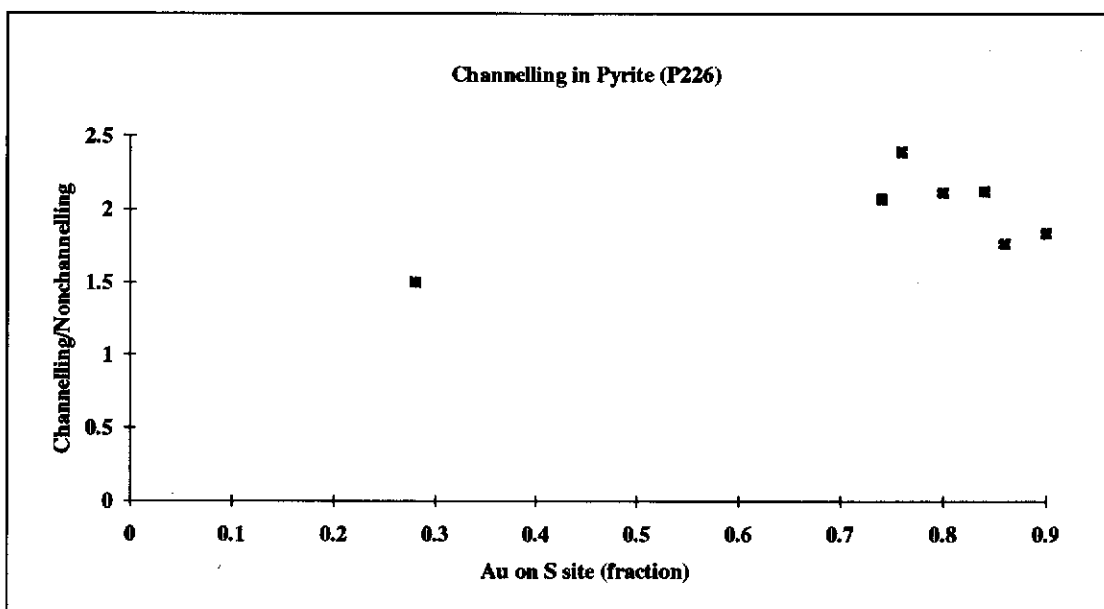
Figure 6.8b shows the calculated occupancies for Au on S sites against the channelling effect [(Fe/S)$_{ch}$/(Fe/S)$_{non-ch}$].

clustered around 0.8. The deviation from 1.0 may indicate some gold associated with sites other than sulfur.

Statistical Method

The channelling data for pyrites were then analysed using the multivariate technique. Figures 6.9 to 6.12 show the fit of N_A to $\alpha_{SAs}N_s$ together with Tables 6.2 to 6.5(a and b) of measured parameters for the various pyrites. Table 6.5a and b for the auriferous pyrite, also contain the fit of N_{Au} to $\alpha_{FeAu}N_{Fe}$ and $\alpha_{SAs}N_s$ and its associated measured parameters. As indicated by the fitted parameters (α_p), all the arsenic impurity was found on the sulfur sites. No arsenic partitioned on the iron site, as indicated by a high error associated with the fit as well as in some cases, a negative α_{FeAs} compensating for the non-perfect fit for N_A to $\alpha_{SAs}N_s$. The arsenic content generally appeared higher than that found in natural pyrite. The [001] zone results provided lower arsenic contents than the [011] zone results. The maximum reported in the literature is approximately 10 wt % arsenic (Fleet *et al.*, 1993) whereas some of the present samples appeared to contain ~15 wt %. The synthetic arsenian pyrites were synthesised under high arsenic conditions and their higher arsenic content is indicated by their chemical analyses described in Chapter 5. Another possible reason for a high arsenic content is that a true non channelling orientation may not have been analysed during the experiments, particularly for the [011] zones, due to time limits associated with sample degradation. Non-channelling orientations can be difficult to select (Eades *et al.*, 1990). The use of the As L counts gave fitted parameters similar to those using As K counts, however, the calculated atomic concentration was higher. This may result from the difficulties experienced in obtaining good atomic k-factors for the As L to Fe K ratio in the calibration where a higher error was observed than for the As K to Fe K atomic k-factor i.e. the atomic factor may be inaccurate. A difference between As K and As L against S K counts could also possibly be due to delocalisation of the As L emission which will have a different electron flux than will the As K emission near and on the zone axis orientations.
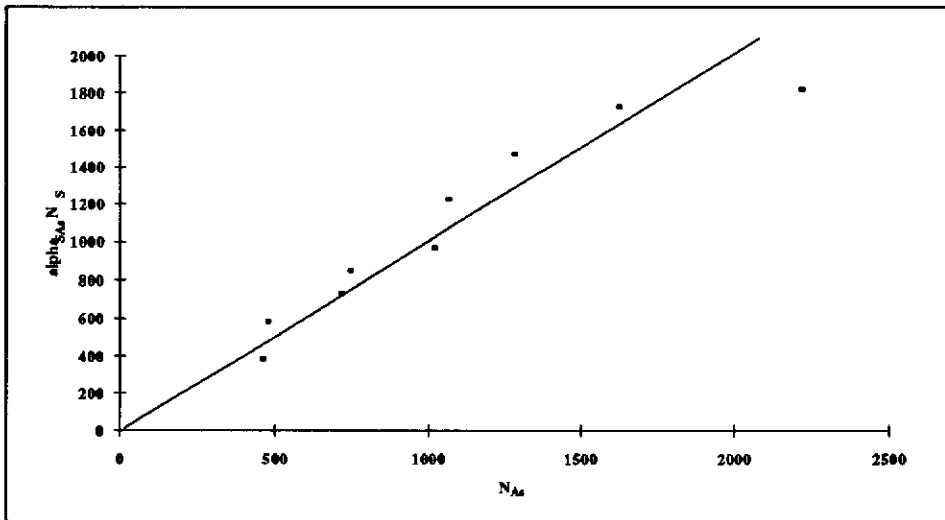
Figure 6.9 The linear fit between $\alpha_{SAs}N_s$ and N_{As} for pyrite(Pa10f - [001]).
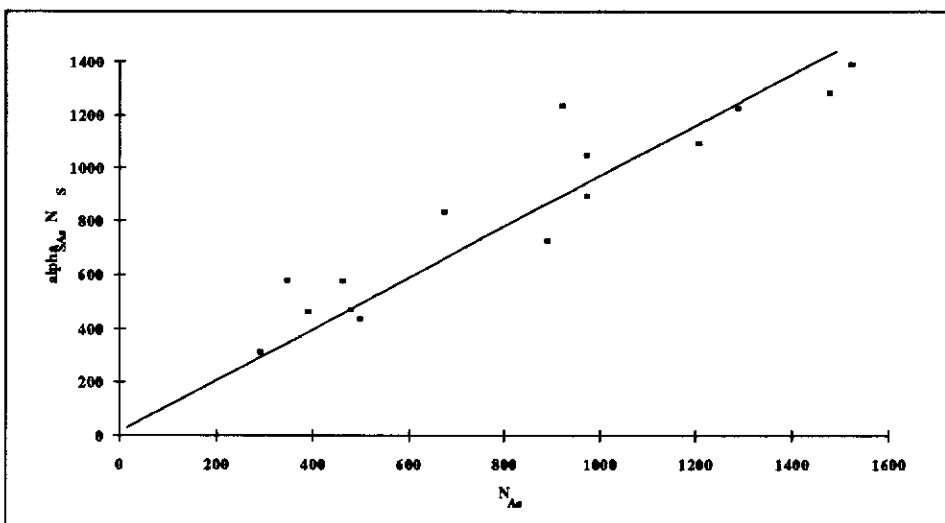
Figure 6.10 The linear fit between $\alpha_{SAs}N_s$ and N_{As} for pyrite(P195 - [001]).
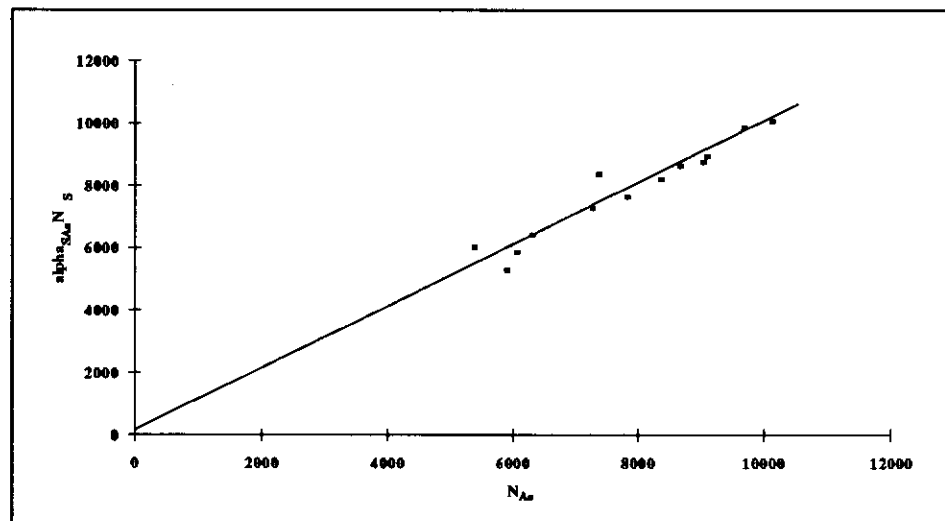
Figure 6.11 The linear fit between $\alpha_{SAs}N_s$ and N_{As} for pyrite (P1f - [011]).
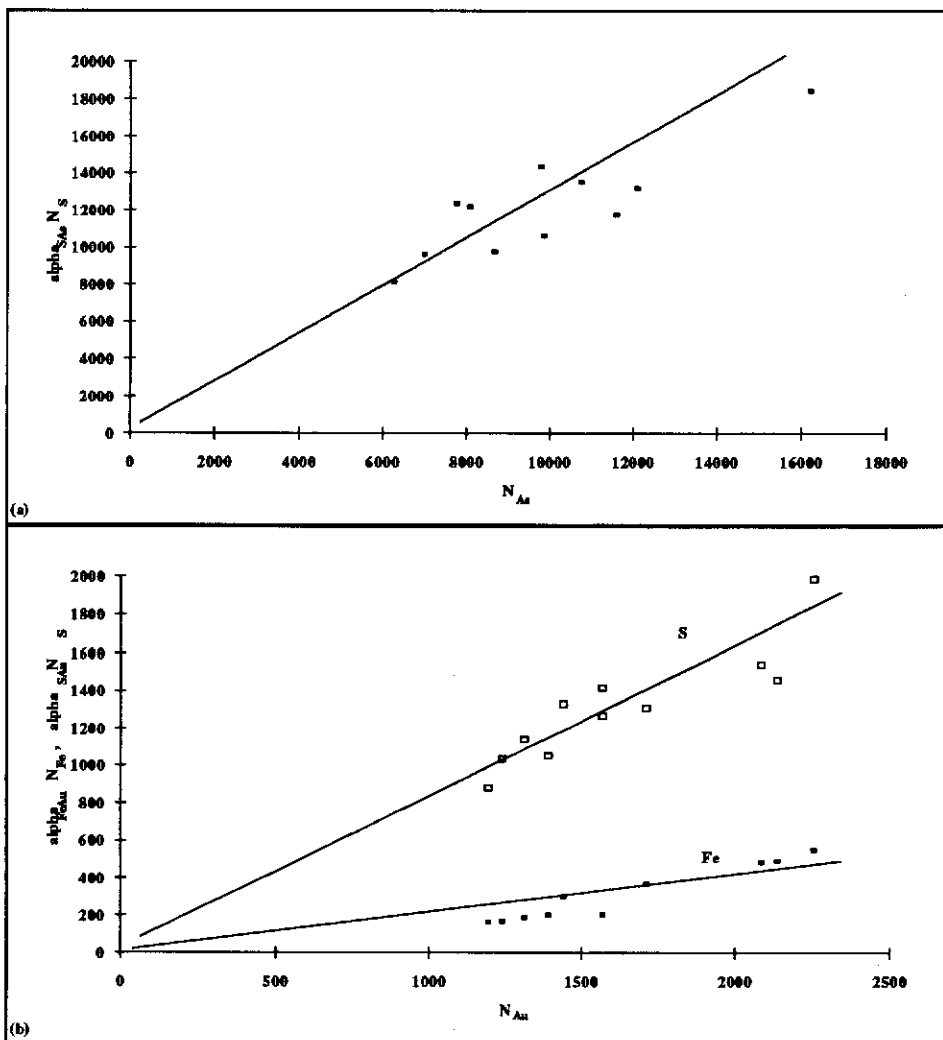
Figure 6.12 The linear fit between $\alpha_{SAs}N_s$ and N_{As} (a) and $\alpha_{FeAs}N_{Au}$ and $\alpha_{SAs}N_s$ to N_{Au} (b) for pyrite (P226 - [011]).
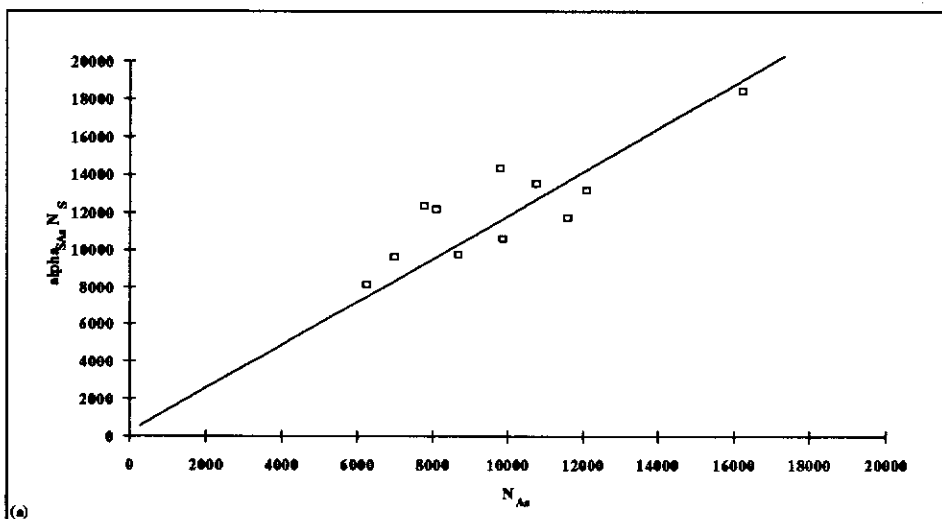
Figure 6.12c The linear fit between $\alpha_{SAs}N_s$ and N_{As} using As L line for pyrite (P226 - [011]).

Table 6.2 - Measured Parameters for Site Occupancies of As substituted in FeS$_2$(PA10f)					
Alpha values for this Crystal (α_{ip})			Distribution of Impurities on Hosts		Total Atomic Concentration (%)
		Fe	S	f$_{Fe}$	f$_S$	
p						
As:		0.003 +/- 0.009	0.076 +/- 0.01	0.2+/-0.7	0.8 +/- 0.6	1.4 +/-2

Table 6.3 - Measured Parameters for Site Occupancies of As substituted in FeS$_2$(P195)					
Alpha values for this Crystal (α_{ip})			Distribution of Impurities on Hosts		Total Atomic Concentration (%)
	i	Fe	S	f$_{Fe}$	f$_S$	
p						
As:		0.01 +/- 0.01	0.014 +/- 0.009	0.3+/-0.2	0.7 +/- 0.2	10 +/-4

Table 6.4 - Measured Parameters for Site Occupancies of As substituted in FeS$_2$(P1f)					
Alpha values for this Crystal (α_{ip})			Distribution of Impurities on Hosts		Total Atomic Concentration (%)
	i	Fe	S	f$_{Fe}$	f$_S$	
p						
As:		0.01 +/- 0.02	0.13 +/- 0.04	-	0.93 +/- 0.1	18.8 +/- 06

Table 6.5a - Measured Parameters for Site Occupancies of As and Au substituted in FeS$_2$ (P226)					
Alpha values for this Crystal (α_{ip})			Distribution of Impurities on Hosts		Total Atomic Concentration (%)
	i	Fe	S	f$_{Fe}$	f$_S$	
p						
AsK:		-0.01 +/- 0.02	0.14 +/- 0.03	-	1.0 +/- 0.1	18 +/- 4
Au:		0.003 +/- 0.001	0.016 +/- 0.002	0.15 +/- 0.05	0.85 +/- 0.05	0.4 +/- 0.05

Table 6.5b - Measured Parameters for Site Occupancies of As and Au substituted in FeS$_2$ (P226)					
Alpha values for this Crystal (α_{ip})			Distribution of Impurities on Hosts		Total Atomic Concentration (%)
	i	Fe	S	f$_{Fe}$	f$_S$	
p						
AsL:		-0.03 +/- 0.06	0.40 +/- 0.07	-	1.1 +/- 0.2	36 +/- 9
Au:		0.002 +/- 0.001	0.011 +/- 0.001	0.17 +/- 0.06	0.83 +/- 0.6	0.01 +/- 0.002

The previous results demonstrate that for the auriferous pyrite crystal, most of the gold was associated with the sulfur sites. A small correlation for gold with the iron site occurs, however, the error associated with the alpha value is too high.

From the Tables the formula for each pyrite can be written as:

Pa10f	$[Fe][S_{1.96}As_{0.04+/-0.06}]$	[001] zone
P195	$[Fe][S_{1.7}As_{0.3+/-0.07}]$	[001] zone
P1f	$[Fe][S_{1.44}As_{0.56+/-0.02}]$	[011] zone
P226	$[Fe_{0.9982}Au_{0.0018+/-0.0009}][S_{1.49}As_{0.5+/-0.2}Au_{0.010+/-0.002}]$	[011] zone

An EDX spectrum taken under kinematical diffraction conditions for the auriferous pyrite (P226) gave a composition of

$$[Fe_{0.999}Au_{0.001}][S_{1.870}As_{0.200}Au_{0.010}]$$

Gold values are in good agreement, however, arsenic is still high and this may be due to the fact that a real non-channelling orientation was not recorded for the [011] zone data.

6.3.2 Channelling in Arsenopyrite

Electron channelling experiments in arsenopyrite were much more difficult than for pyrite. Gold was more abundant in the arsenopyrite crystals than in the pyrite crystals. However, finding crystallographic orientations which gave effective channelling was a problem. One of the major problems was to locate zone axes which were not disordered through twinning or stacking faults in the synthetic crystals examined. The [101] zone axis of arsenopyrite was the most stable under the electron beam as well as being readily obtainable. Also the symmetry elements (GM lines) could be observed in the diffraction disks which provided accurate information and confirmed the orientation of the crystal structure being examined. A projection of the [101] zone axis was shown in Figure 3.18. In projection, the iron sites are distinguishable from the combined arsenic and sulfur sites. For the ideal arsenopyrite structure the arsenic and sulfur alternate in columns into the page. All the arsenopyrite crystals examined were non-stoichiometric. Because of this, data for arsenic and sulfur were combined in the ALCHEMI analysis. It is possible that arsenic atoms may be substituted on the iron site. However, the amount of arsenic is too small to cause
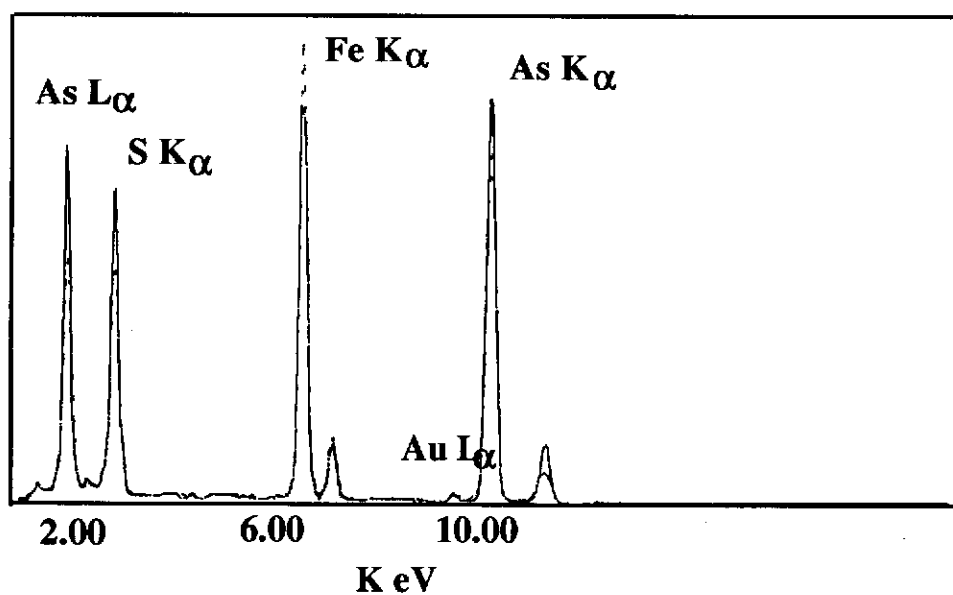
Figure 6.13 An EDX spectrum of channelling in arsenopyrite along the [101] zone. With an increase in iron intensity for the direct zone orientation the sulfur and arsenic decreases.

Dotted line - 'on zone, channelling
Solid line - 'off zone, non-channelling
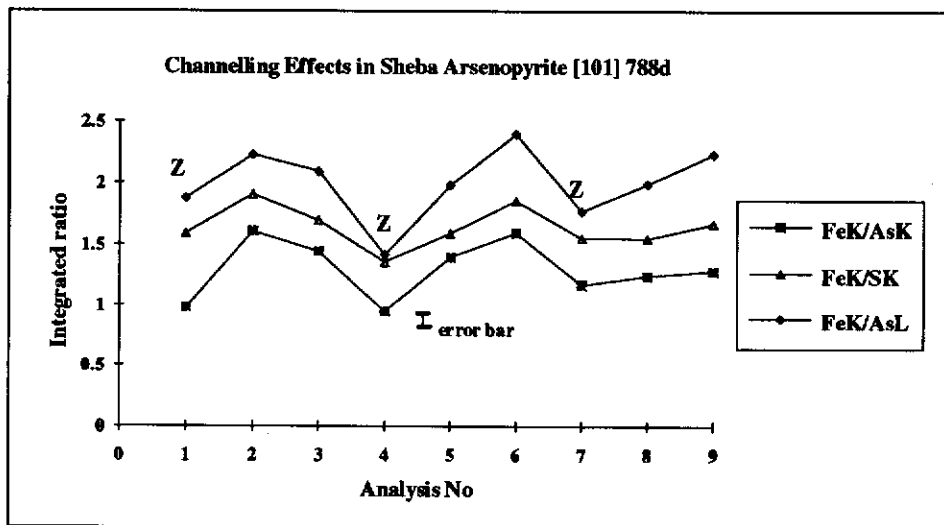
(a)
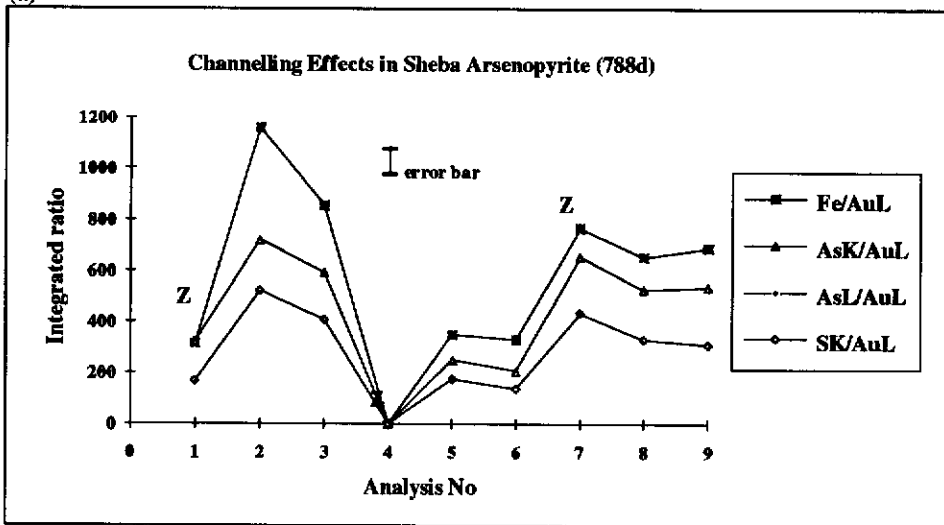
(b)

Figure 6.14 (a) Plots of the ratio of FeK to As K, As L and S K showing the extent of channelling between Fe and and the other sites, (b) Plots of the ratio of FeK, As K, As L and S K to AuL showing the extent of channelling between Au and the arsenopyrite sites for the [101] zone axis of Natural arsenopyrite (Sheba sample- 788d). (Z- 'on' zone or channelling direction)

Channelling in Synthetic Auriferous Arsenopyrite

Integrated Ratio

2.1
1.9
1.7
1.5
1.3
1.1
0.9

Z   Z   Z

Fe-K/As-K
Fe-K/S-K

Counting Error
Fe-K/As-K +/- 0.01
Fe-K/S-K +/- 0.02

0   1   2   3   4   5   6

No of Analysis

(a)

Channelling in Synthetic Auriferous Arsenopyrite

integrated ratio

68
58
48
38
28
18
8

Z   Z   Z

Fe-K/Au-L
As-K/Au-L
S-K/Au-L

Counting errors
Fe-K/Au-L +/- 0.5
As-K/Au-L +/- 0.4
S-K/Au-L +/- 0.2

0   1   2   3   4   5   6

No of Analysis
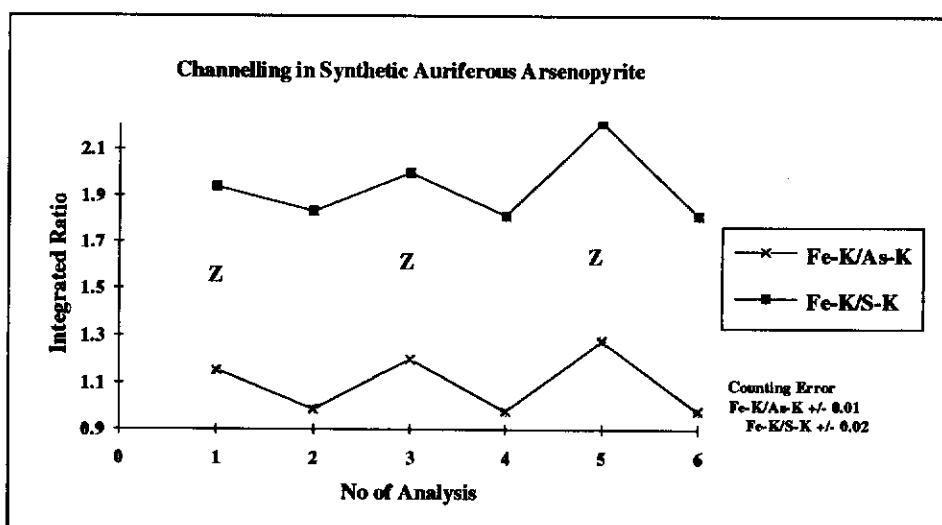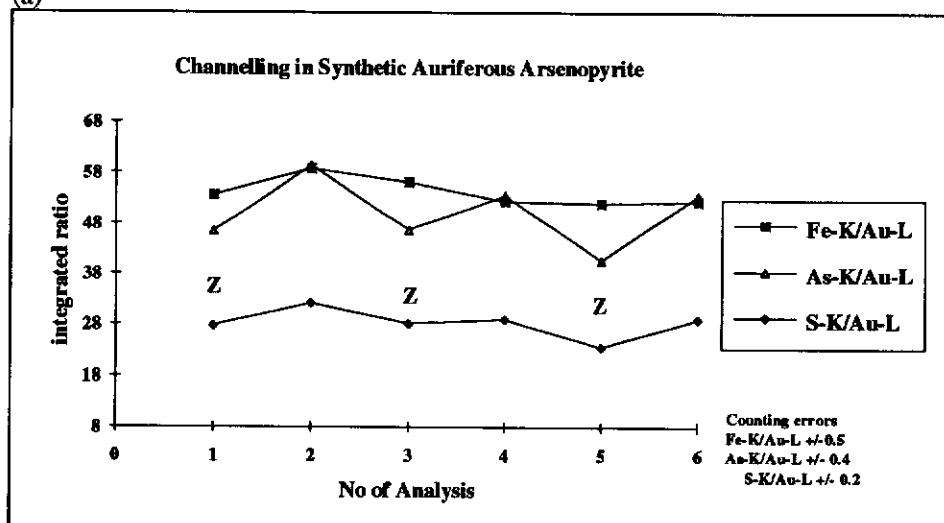
(b)

Figure 6.15 (a) Plots of the ratio of FeK to As K and S K showing the extent of channelling between Fe and and the other sites, (b) Plots of the ratio of FeK, As K, As L and S K to AuL showing the extent of channelling between Au and the arsenopyrite sites for the [101] zone axis of synthetic auriferous arsenopyrite (Ap41 sample - NB226). (Z- 'on' zone or channelling direction)

(a)

Channelling in Synthetic Auriferous Arsenopyrite

Integrated Ratio

2.5

2

1.5

1

0.5

Z   Z   Z   Z

0   2   4   6   8   10   12   14   16

No of Analysis

Fe-K/As-K
Fe-K/S-K

Counting Error
Fe-K/As-K +/- 0.01
Fe-K/S-K +/- 0.02

(b)

Channelling in Synthetic Auriferous Arsenopyrite

integrated ratio

68

58

48

38

28

18

8

Z   Z   Z   Z

0   2   4   6   8   10   12   14   16

No of Analysis

Fe-K/Au-L
As-K/Au-L
S-K/Au-L

Counting errors
Fe-K/Au-L +/-0.5
As-K/Au-L +/- 0.4
S-K/Au-L +/- 0.2
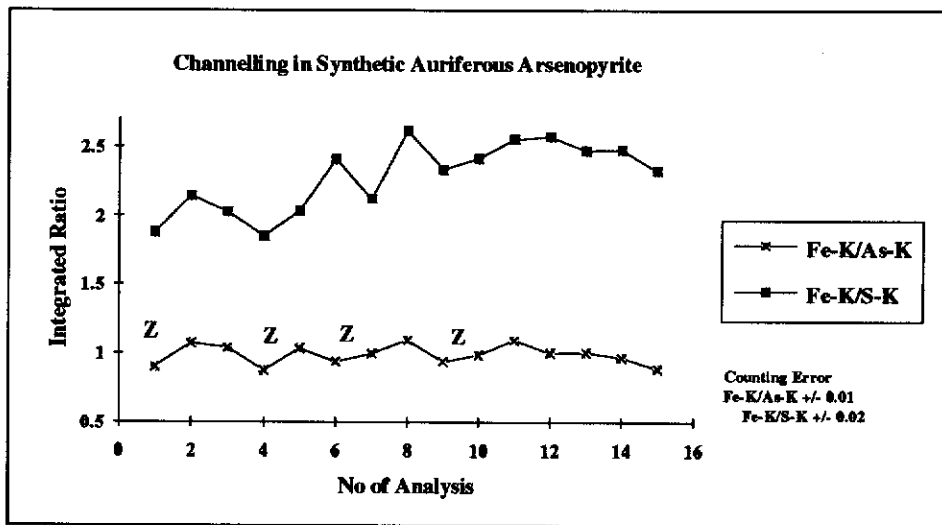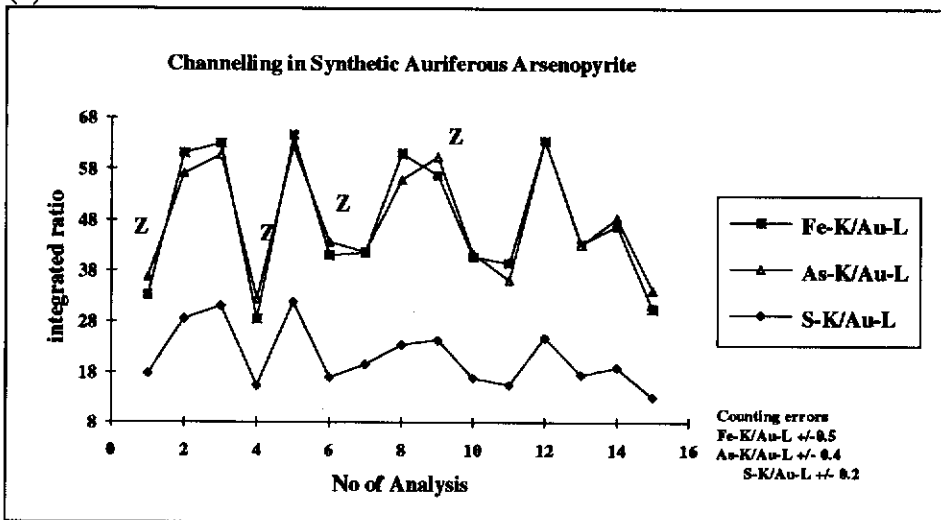
Figure 6.16 (a) Plots of the ratio of FeK to As K and S K showing the extent of channelling between Fe and and the other sites, (b) Plots of the ratio of FeK, As K, As L and S K to AuL showing the extent of channelling between Au and the arsenopyrite sites for the [101] zone axis of synthetic auriferous arsenopyrite (Ap41 sample - A16). (Z- 'on' zone or channelling direction)
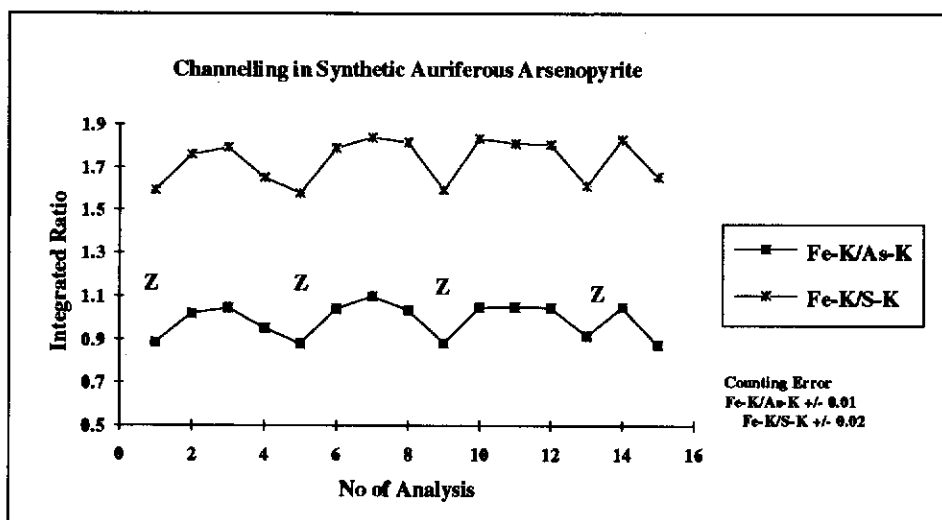
(a)
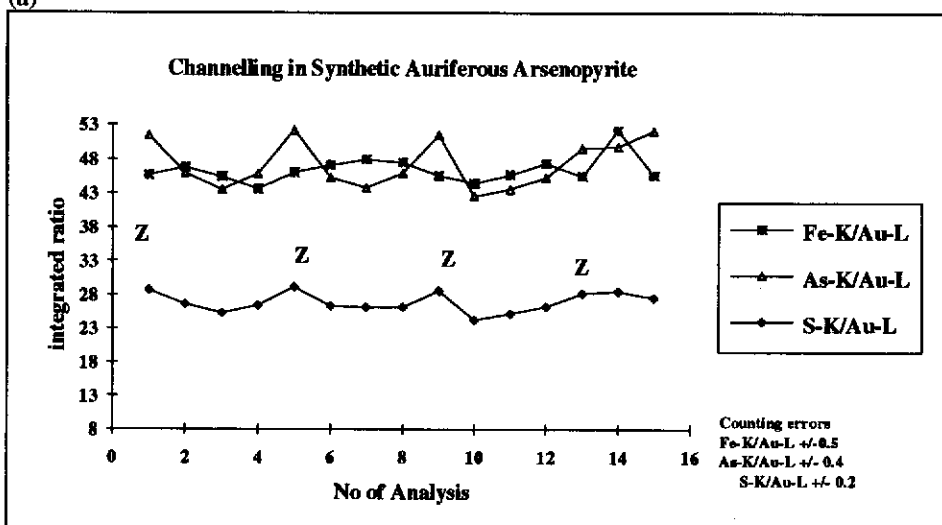
(b)

Figure 6.17 (a) Plots of the ratio of FeK to As K and S K showing the extent of channelling between Fe and and the other sites, (b) Plots of the ratio of FeK, As K, As L and S K to AuL showing the extent of channelling between Au and the arsenopyrite sites for a minor zone axis of synthetic auriferous arsenopyrite (Ap41 sample - a36). (Z- 'on' zone or channelling direction)
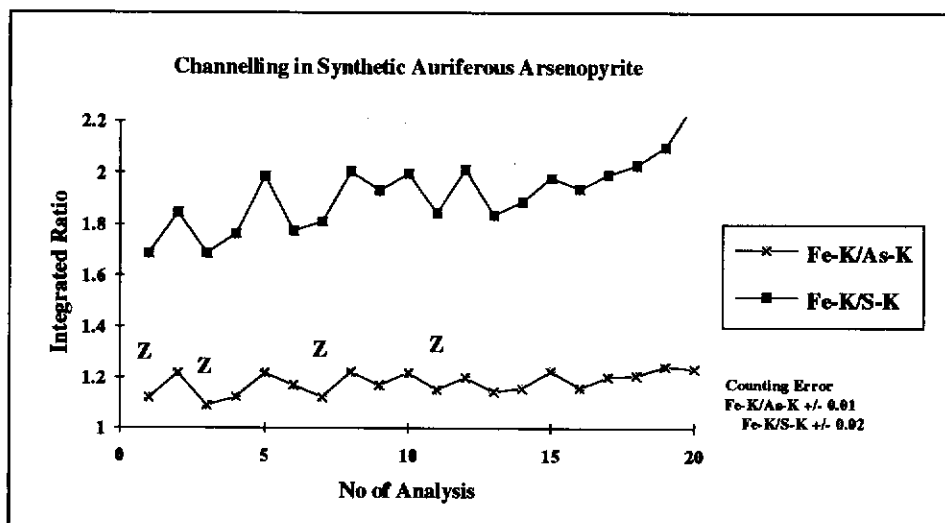
(a)
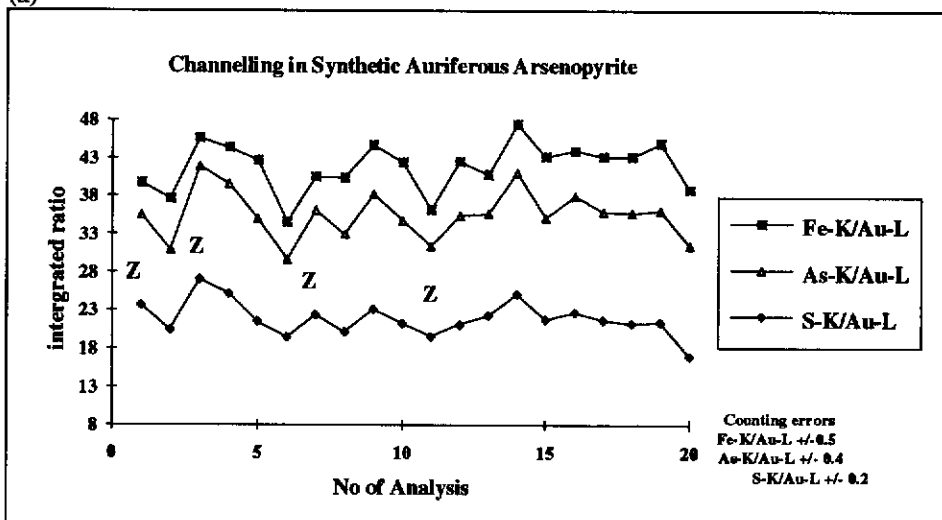
(b)

Figure 6.18 (a) Plots of the ratio of FeK to As K and S K showing the extent of channelling between Fe and and the other sites, (b) Plots of the ratio of FeK, As K, As L and S K to AuL showing the extent of channelling between Au and the arsenopyrite sites for a minor zone axis of synthetic auriferous arsenopyrite (Ap41 sample - a156). (Z- 'on' zone or channelling direction)

probably reflects the presence of fine gold inclusions. For the B226 and A36 data points, the 'off' zone data do not vary from the 'on zone' data which possibly indicates some gold on the iron sites.

Several channelling and nonchannelling data points were also collected over longer periods of time to improve counting statistics on some crystals, however no difference in result to those outlined above occurred.

6.3.2.1 Analysis of Site Occupancy

Ratio Method

Using the ratio method, calculations of site occupancy of gold on either iron or combined arsenic and sulfur sites from channelling and non-channelling data generally resulted in meaningless values which were in excess of 1.0 or less than 0.0. This occurred for all data collected except for data collected from one crystal orientated along the [101] and one oriented along a minor zone.

Figure 6.19 shows the calculated occupancy of gold on the iron sites against the channelling effect expressed by the ratio $(Fe/As+S)_{ch}/(Fe/As+S)_{non-c}$ for the B226 and A36 data, which showed some gold associated with the iron sites. The minor zone axis shows a cluster of points close to 1.0, which indicates that gold is mostly associated with the iron site. The [101] zone data shows more of a spread of data points possibly corresponding to some gold on both iron and arsenic - sulfur combined sites. Unfortunately, not many points were available for the B226 sample due to a reduction in channelling effects after 7 analyses. The points greater than 1.0 are due to localisation effects.

Statistical Method

For most of the channelling data, no correlation on either the iron or combined As+S sites were observed, as confirmed with the ratio method. The results of multivariate analyses for the partitioning of gold between the iron sites and the combined arsenic and sulfur sites in the arsenopyrite structure are shown in Tables
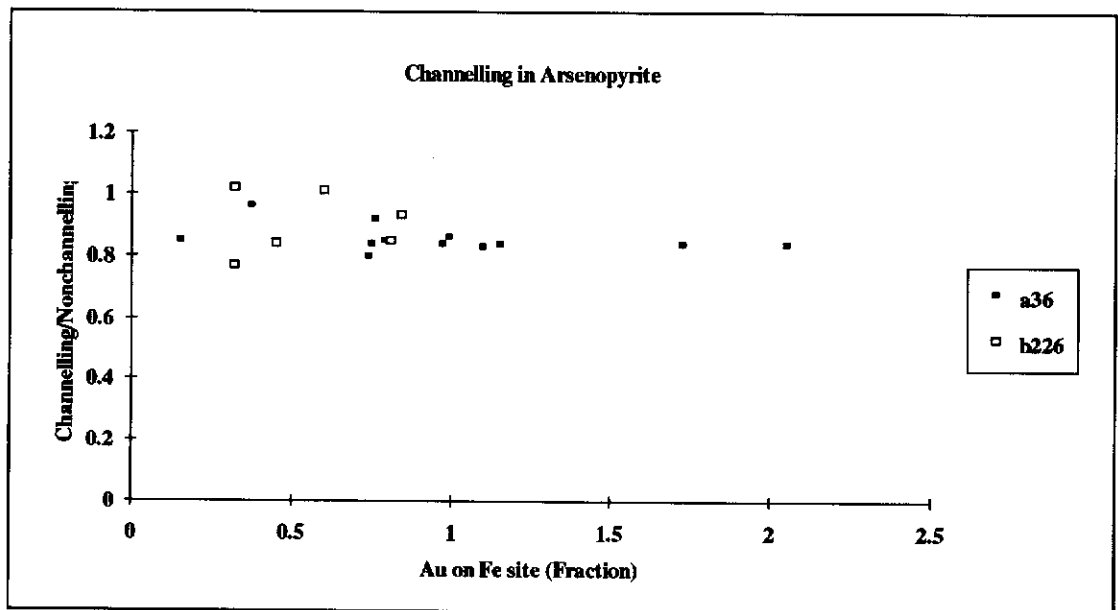
Figure 6.19 The calculated occupancy of gold on the iron sites against the channelling effect expressed by the ratio Fe/As+S)$_{ch}$/(Fe/As+S)$_{non-c}$ for the B226 and A36 data.

6.6a,b and c. For two sets of data which showed correlation in the ratio method (B226 and A36), a slight correlation was observed for the partitioning of gold onto the iron site. However, the errors associated with the alpha values were too high to be conclusive. Part of the reason for this is the lack of points available for the statistical analysis. No correlation exists for the combined arsenic and sulfur data. Thus the results indicated a high percentage of the gold was present either as fine inclusions or located in lattice defects or interstitial sites.

Examination of CBED patterns indicated that the results which showed some possible substitution of gold on the iron site were from crystals with well formed GM lines (i.e. all symmetry elements) whereas those which showed no possible correlation with either iron or the combined arsenic and sulfur sites, were associated with CBED patterns which contained distortions in the GM lines.

6.3.3 Possible Sites for Interstitial Gold in Arsenopyrite

The possible location of gold in interstitial sites in arsenopyrite structure is in the gaps between the iron centred octahedra (see Figures 4.40 and 4.41, in Chapter 4). The average bond lengths for gold, arsenic and sulfur reported in the literature are:

Au-S   2.290Å

Au-As   2.386Å

These are slightly larger than those for the two possible calculated interstitial sites listed in Table 6.7 below. However, with some interchange of arsenic and sulfur on each others site or some vacant sites, this may well be possible. To accomodate gold in these positions some iron, arsenic or sulfur sites must be vacant or the sites be modified by twinning or other defects.

Table 6.6a - Measured Parameters for Site Occupancy of Au in FeAsS
Well formed CBED patterns

Alpha values for this Crystal (α_{ip})			Distribution of Impurity on Hosts		Total Atomic Concentration (%)
		Fe	As +S	f_{Fe}	f_{As+S}	
788e		0.005 ± 0.2	0.02 ± 0.2	0.2 ± 8	0.8 ± 8	2 ± 3
b226:		$0.03 +/- 0.02$	$0.02 +/- 0.03$	$0.7 +/- 0.3$	$0.3 +/- 0.3$	$3.1 +/- 0.2$

Table 6.6b - Measured Parameters for Site Occupancy of Au in FeAsS
Slightly distorted CBED patterns

Alpha values for this Crystal (α_{ip})			Distribution of Impurity on Hosts		Total Atomic Concentration (%)
		Fe	As +S	f_{Fe}	f_{As+S}	At (%)
a16		-0.01 ± 0.1	0.02 ± 0.09	-	-	-
a246		0.1 ± 0.3	-0.06 ± 0.2	2 ± 6	-0.8 ± 6	5 ± 3

Table 6.6c - Measured Parameters for Site Occupancy of Au in FeAsS
Minor zone axes

Alpha values for this Crystal (α_{ip})			Distribution of Impurity on Hosts		Total Atomic Concentration (%)
		Fe	As +S	f_{Fe}	f_{As+S}	
a36		0.02 ± 0.01	0.004 ± 0.006	0.8 ± 0.3	0.2 ± 0.3	2 ± 1
a156		0.02 ± 0.08	0.002 ± 0.06	0.9 ± 2	0.08 ± 2	2 ± 9

Table 6.7 - Distance between possible gold interstitial sites and its closest surrounding arsenic, sulfur and iron atoms

	Sheba (low As:S ratio)	Panasqugira (high As:S ratio)	Synthetic Auriferous (Ap40)
Atom	Distance from Gold Atoms (Angstroms)*		
Au1 at atomic coordinates 0.97,-0.055,0.53			
As^i	2.183	2.171	2.124
As^{ii}	2.118	2.10	2.064
As^{iii}	2.917	2.935	2.115
As^{iv}	2.085	2.097	2.961
S^i	2.029	2.050	2.116
S^{ii}	2.029	2.040	2.111
Fe^i	2.085	2.095	
Au2 at atomic coordinates 0.53,0.44,0.47			
S^i	1.971	1.934	1.876
S^{ii}	1.959	1.962	1.878
S^{iii}	3.059	3.077	3.072
S^{iv}	2.173	2.184	2.221
As^i	2.071	2.075	2.09
As^{ii}	2.027	2.030	2.042

* calculated from structural refinement data in Ch3 and Ch4.

6.4 Summary and Conclusions

Pyrite

Griffin et al. (1991) suggested that interelement correlation which they observed in arsenic rich pyrite from the North Arm epithermal Ag-Au deposit, was consistent with a physical mixture of pyrite, arsenopyrite and sulfosalt phase rather than atomic substitution of arsenic for sulfur. However, they found no direct evidence for the existence of inclusions of arsenopyrite and sulfosalts in their study. The present study has conclusively confirmed the presence of arsenic on sulfur sites in both natural and synthetic pyrite containing various concentrations of arsenic. The sulfur is normally present as the disulfide ion $[S_2]^{2-}$ (pyrite can be written as $[Fe]^{2+}[S_2]^{2-}$), and incorporation of arsenic would presumably give $[AsS]^{3-}$. Cook and Chryssoulis (1990)

suggested that such an imbalance could be met by trivalent cations such as gold replacing the divalent iron. However, the present results indicate that gold occurs on the sulfur sites. The arsenic charge imbalance could be met by occasional sulfur vacancies, or by some Fe^{3+} replacing Fe^{2+}. Slight sulfur deficiencies have been reported by Finklea et al. (1976) and should be associated with a reduction in sulfur vapour pressure. Not all arsenic-rich pyrites contain gold (Cook and Chryssoulis, 1990; Fleet *et al.*, 1993), so the substitution mechanism must be at least partially independent of gold content. Gold on the sulfur sites may be present as Au^-, Au^0 or Au^+ most probably combined as an anion pair of the form $[AuAs]^{2-}$. Alternatively, with the presence of gold on the sulfur sites, anion pairs such as $[AuS]^-$ could possibly exist. The presence of $[AsS]^{3-}$ pairs would be required to balance the charge of the Fe^{2+} ions.

Arsenopyrite

The ALCHEMI results for arsenopyrite show some correlation of gold with the iron sites. However, a high percentage of gold is not on either the iron or the arsenic-sulfur combined sites as shown by analyses by both the ratio and statistical methods. Gold Mössbauer studies carried out on the synthetic auriferous arsenopyrites indicated that most gold was chemically bonded (Chapter 4). This implies that much of the gold is on interstitial sites or in defects in the structure and not present as fine inclusions. Image contrast and selected area diffraction showed no gold present as fine inclusions in the crystals observed. The best results obtained for the [101] zone arsenopyrite crystal experiments came from crystals that were less distorted. In [101] zone data, extensive distortions in the b-axis resulted in gold present in defects of the arsenopyrite structure. One of the reasons for the errors being so high in the statistical analyses was that the number of data points available was small as a result of the sample not being stable for long periods of time under the electron beam. White and Turner (1992) have used the ALCHEMI statistical method to verify the partitioning of impurities over the calcium and zirconium sites into defects in the zirconolite ($CaZrTi_2O_7$) structure. They compared a 'perfect' crystal

(confirmed by HRTEM studies), which gave good partitioning of impurities on the Ca and Zr sites, with crystals containing extensive defects which failed to partition impurities on the Ca and Zr sites. Similarly, gold may be partitioned into defects in arsenopyrite.

Relevance to natural samples

'Invisible' gold is often associated with chemically zoned arsenic-rich regions in natural arsenopyrite and pyrite grains (Cook and Chryssoulis, 1990), which reflect non-equilibrium conditions and rapid crystallisation. Crystals which are rapidly crystallised will probably be less well ordered. It is possible that during rapid crystallisation, gold atoms are trapped on interstitial sites or point defects, particularly in arsenopyrites. In well crystallised arsenopyrite, some gold may be taken up on the iron sites. The difference in the form of gold in both pyrite and arsenopyrite related to the differences in crystal structure. Because arsenopyrite frequently exhibits faults of various finds, it is more readily able to accommodate gold in dislocations in its structure than pyrite. Mössbauer data obtained by several authors on pyrites have shown that the gold absorption peak corresponding to the combined gold does not have the same peak position as for gold combined in arsenopyrite. This suggests the gold bonding environments are different between pyrite and arsenopyrite. The ALCHEMI results are consistent with these findings.

Chapter 7

7.0 THERMAL BEHAVIOUR OF ARSENOPYRITE AND ITS RELATIONSHIP TO GOLD MOBILITY

7.1 Introduction

The mobilisation of gold in arsenopyrite during thermal treatment will undoubtedly depend on the mechanism involved in the decomposition of the arsenopyrite structure. Consequently in the first instance, the thermal behaviour of the arsenopyrite samples was examined. The effect of arsenopyrite stoichiometry and ambient conditions was then analysed and the relationship to gold agglomeration considered. The decomposition products of the arsenopyrites and the gold agglomeration process were examined under the TEM.

7.2 Materials and Methods

Several techniques were used to gain information on the structural breakdown of the arsenopyrites under thermal treatment and the accompanying mobilisation and agglomeration of gold within the structure.

7.2.1 Simultaneous Thermogravimetry/Differential Thermal Analysis (TG-DTA)

TG-DTA were carried out on the 63μm sized fractions of concentrated arsenopyrite with different arsenic and sulfur stoichiometries. A Stanton Redcroft Model 781 Simultaneous TG-DTA was used in these studies. Between 7 and 10 mg of sample were placed in vycor crucibles and counter-balanced in the instrument. A heating rate of 20°C/min from room temperature to 900°C was used in an oxygen-scrubbed nitrogen atmosphere. Several experiments were also carried out in an oxygen environment. Data was collected by a computer interfaced to the instrument.

Several experiments were carried out at different heating rates to determine their effect on arsenopyrite breakdown and gold agglomeration. The flow rate of nitrogen was also adjusted and the effects monitored. Polished sections of heated samples were made and examined under optical and scanning electron microscopes for phase changes. In cases where gold was present, its morphology was observed. In several experiments, heating was stopped before or after a major thermal event (e.g. an endothermic peak) and the product examined as above.

In addition, TG-DTA was carried out on pure arsenic or mixtures of arsenic and sulfur, combined with gold in open vycor crucibles with flowing nitrogen, to ascertain the effects on gold mobility. The gold present after the heating run was then examined at high magnification under a SEM.

7.2.2 Electron Beam Heating

In order to visually observe the gold agglomeration process, a novel approach was developed where auriferous arsenopyrite was broken down to pyrrhotite by heating the grain using the TEM electron beam.

A video camera was set up and focused on the screen of the TEM. The largest condenser aperture was chosen so as to provide as much heat as possible. The largest spot size was then chosen and carefully set up so as not to destroy the grain before the experiment commenced. The electron beam was first set up so as to illuminate the whole screen without destroying the grain. The focus was adjusted on the TEM and the video camera was checked, and at the appropriate time was set to record. The electron beam was then slowly focused until the grain started to decompose. After each experiment an X-ray spectrum was obtained of the dark globules to confirm that they were gold. Crystallographic data from CBED and SAED patterns of the grain were obtained before and after heating and compared. Chemical compositions were obtained from EDX analysis.

7.2.3 Muffle Furnace Experiments involving Arsenopyrite, Arsenic, Sulfur and Gold Mobility

The effect of arsenopyrite breakdown on gold mobility was examined by heating in a muffle furnace. Several experiments were carried out in which arsenopyrite grains (~63μm) and gold of varying quantities were placed together and sealed in an evacuated vycor tube. Different samples were heated for 10 days at temperatures of 340, 400 and 500°C respectively. Another series was heated to 600, 636 and 650°C respectively for 12 hours. The heating of the vycor tubes was carried out in a muffle furnace with a calibrated temperature gauge and chromel-alumel thermocouple (furnace accuracy ±10°C). After each experiment, samples were quenched and examined under optical and scanning electron microscopes for changes in the appearance of the gold.

7.3 Results and Discussion

7.3.1 Effect of Stoichiometry of Arsenopyrite on its Thermal Behaviour

Figure 7.1 shows a TG-DTA graph of the decomposition of the Greenbushes arsenopyrite which has the composition FeAsS. The decomposition appeared to start at around 470°C but ceased when the temperature approached 550°C. The analyses of the other arsenopyrites with different stoichiometries gave similar results to that observed for the Greenbushes arsenopyrite. However, the position of the main endothermic peak varied. In all samples, a weight loss was observed at 470°C with a small endothermic peak. In each case, a major endothermic peak occurred between 650°C and 750°C with a large loss of weight. In addition, some samples had a small endothermic peak on the left side of the major endothermic peak which may be due to slight differences in chemical composition.

Figure 7.2 shows a plot of the temperatures at which the major endothermic peak appeared against the arsenic content for all arsenopyrite samples examined. Several experimental runs were made for each arsenopyrite and are shown in the

TG-DTA Curve of Greenbushes Arsenopyrite
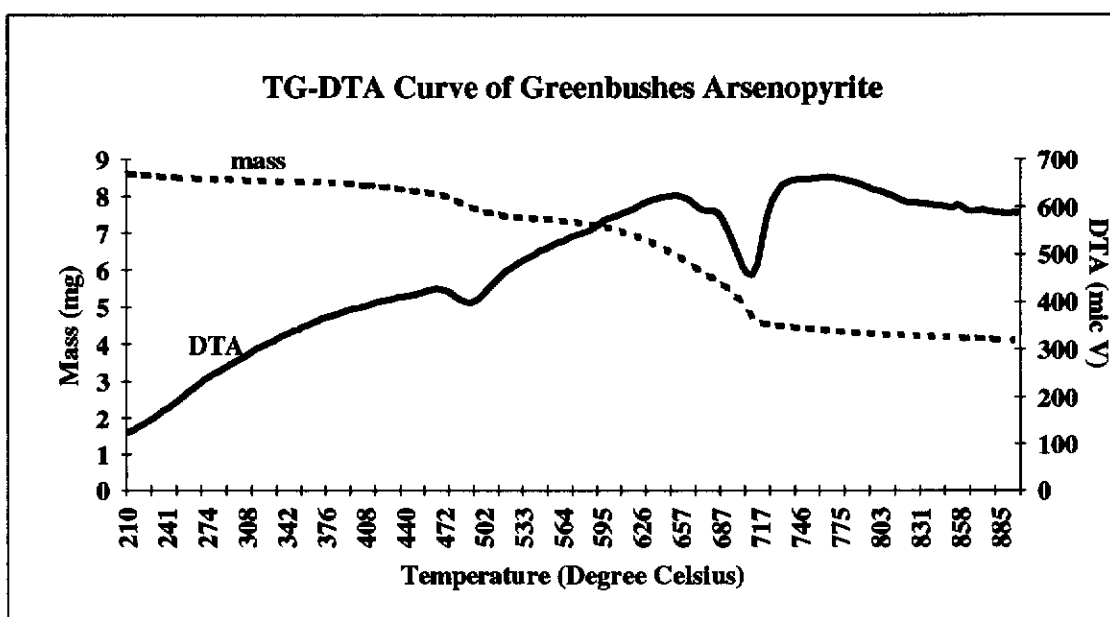
Figure 7.1 Differential thermal and gravimetric analyses of Greenbushes arsenopyrite. (heating rate 20°C/min,nitrogen atmosphere)

Differential Thermal gravimetric Analyses
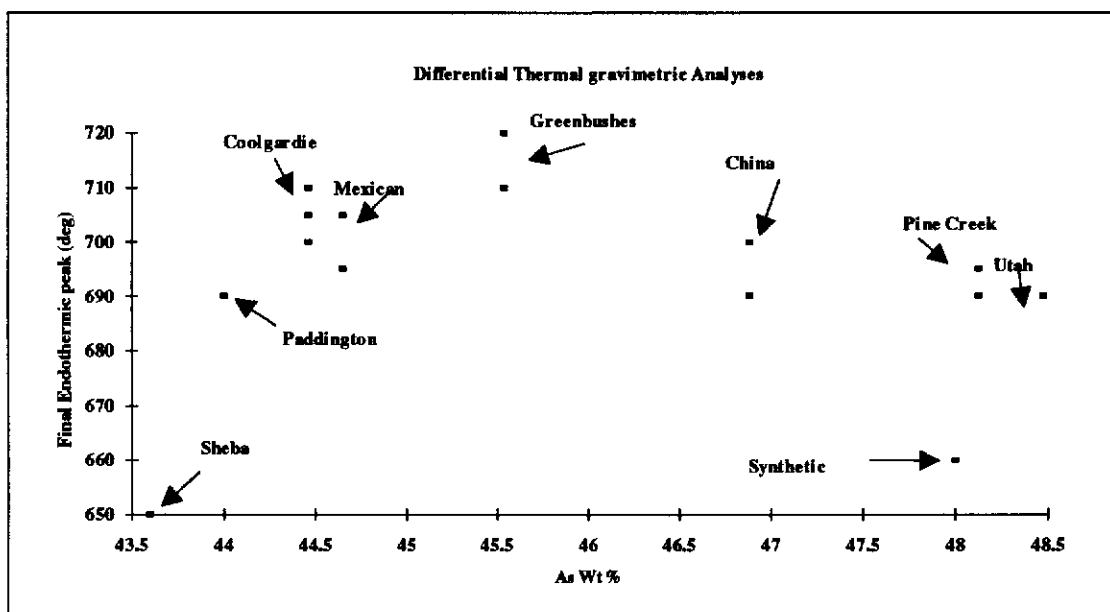
Figure 7.2 A plot of the temperatures at which the major endothermic peak appeared against the arsenic content for all arsenopyrites samples examined.

graph. With increasing arsenic content, until the arsenopyrite approaches stoichiometry, the temperature at which the endothermic peak was at its minimum point increased. For arsenopyrites containing more arsenic than the stoichiometric amount, this temperature decreased with increasing arsenic content. This trend suggests that as the arsenopyrite approaches stoichiometric composition (i.e. FeAsS, with As content ≈ 45 wt%) the arsenopyrite structure is more stable and requires more heat energy to decompose the arsenopyrite lattice. The auriferous arsenopyrite samples, the Sheba S-rich sample and the synthetic arsenopyrite have minimums at 660°C. The synthetic sample had a chemical composition which varied from 40 to 47 wt% arsenic and so did not fit into any particular category. Both the synthetic and Sheba samples contained high concentrations of gold and the low decomposition temperature may reflect its presence. The presence of gold was observed in earlier experiments (see Chapter 4) to reduce the decomposition temperature of arsenopyrite as also observed by Clark (1960). The presence of impurities as inclusions or within the arsenopyrite structure also appeared to reduce the temperature of decomposition. This was particularly true for pyrite or pyrrhotite which were present in small quantities in some of the earlier samples which were not screened. These impurities resulted in a small exothermic peak being observed in the TG-DTA graph at around 450°C followed by an endothermic peak for the decomposition of arsenopyrite (Figure 7.3). The amount of arsenic being evolved at any given time was also affected by the rate of heating and arsenopyrite grain size.

To investigate the significance of the differences in decomposition temperature observed for arsenopyrites with varying composition, arsenopyrite samples were heated for long periods of time below their melting point. Apart from a slight decomposition of arsenopyrite to equilibrate with the evacuated space present in the sealed vycor tube, little alteration occurred to the bulk of the arsenopyrite. Measurement of d-spacings in XRD patterns of samples both before and after heating revealed no high or low temperature transformation in either natural or synthetic auriferous samples. Similarly, Clark (1960) showed that arsenopyrite would not
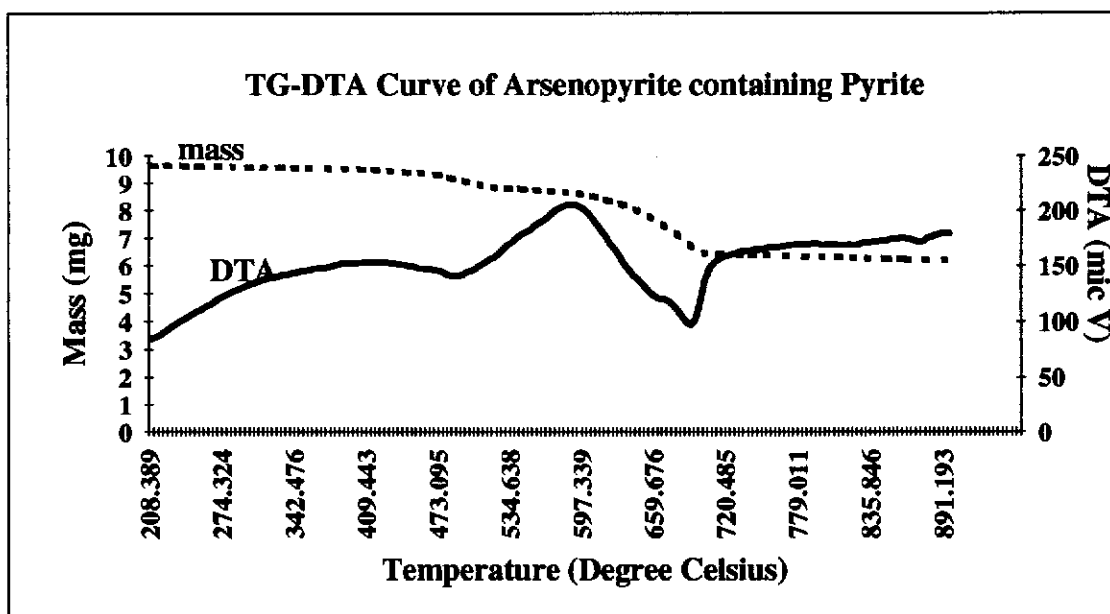
Figure 7.3 Differential thermal and gravimetric analyses of arsenopyrite containing pyrite impurity (heating rate 20°C/min,nitrogen atmosphere).

readily transform to a new physical and chemical polymorph even after months of heating at near melting temperatures. Differences in the free energy of formation of arsenopyrite of different compositions must therefore be very small. However the temperatures at which breakdown (under low ambient partial pressures) is observed, are slightly different between the different stoichiometries.

The decomposition products of arsenopyrite on heating varied depending to a large extent on the conditions under which the heating occurred. A partial heating of arsenopyrite to 570°C resulted in the pyrrhotite formed containing some arsenic ($Fe_{0.48}S_{0.52}As_{0.0003}$) and some residual arsenopyrite. No obvious arsenic mineral phase (e.g. löllingite) was detected in the pyrrhotite. A complete run to 900°C resulted in no arsenic being present and the formation of a pyrrhotite of composition ($Fe_{0.89}S$).

Detailed electron microprobe analyses of one low As:S ratio arsenopyrite and one high As:S ratio arsenopyrite after heating to 900°C were then carried out. The chemical composition of the resultant pyrrhotite for both samples was $Fe_{0.89}S$. Arsenic was not detected in either of these samples. Examination of polished sections of these grains also showed an iron phase present in detached rims around some grains. The rim was found to be hematite which may have formed after the experiment as no exothermic reaction corresponding to iron metal reacting with oxygen was observed in the TG-DTA scan.

The decomposition of arsenopyrite roughly follows the simplified endothermic reaction given in equation 2.5 (Chapter 2). The reaction for the breakdown of the two arsenopyrites described above at 900°C can be written as equations (7.1) and (7.2) assuming no loss of sulfur:

Sheba (Low As:S ratio)
$$FeAs_{0.91}S_{1.03} \rightarrow 1.03Fe_{0.89}S + 0.08Fe_{(excess)} + 0.91As \quad ....(7.1)$$

Utah (High As:S ratio)
$$FeAs_{1.06}S_{0.88} \rightarrow 0.88Fe_{0.89}S + 0.22Fe_{(excess)} + 0.97As \quad ....(7.2)$$
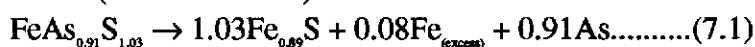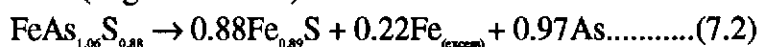
The average total arsenic for Sheba and Utah arsenopyrites were 43 and 48 wt% respectively. The total weight losses for Sheba and Utah arsenopyrites were 56 and 63 wt% respectively. The weight losses in the As-rich arsenopyrites corresponded to total removal of As with some S released, whereas for the S-rich samples the weight losses corresponded to removal of arsenic and more sulfur. The stoichiometry of arsenopyrite affects the final decomposition temperature, however the resulting pyrrhotite product (under the conditions of temperature and sulfur pressure) was always the same. The pyrrhotite formed was always deficient in iron. Excess iron was always present and formed an iron phase in an inert roast. The amount of this phase was governed by the stoichiometry of the arsenopyrite (i.e. As:S ratio) as well as the amount of sulfur removed.

In pyrrhotite, the iron atoms are known to be mobile in the pyrrhotite lattice through iron vacancies (Bennett and Graham, 1977). The excess iron formed from the decomposition of arsenopyrite possibly diffuses and reacts with oxidising or reducing gases at the surface of the grains. This would explain the lack of löllingite (or any iron arsenic phase) found in arsenopyrite decomposed to pyrrhotite in open systems.

The amounts of the above product species as well as their compositions varied according to the composition of the initial arsenopyrite phase and period of heating. The composition of pyrrhotite formed is temperature dependent as well as being a function of sulfur activity (Toulmin and Barton, 1964).

7.3.1.1 Mechanism of Arsenopyrite Breakdown

Several arsenopyrites from different localities were partially heated using an electron beam with a large aperture and spot size under the TEM. An example of arsenopyrite partially altered to pyrrhotite is shown in Figure 7.4. Lattice fringes can be seen in the photo corresponding to layers of iron and sulfur atoms in the pyrrhotite product. Convergent beam electron diffraction patterns confirmed the 2/m point group symmetry and [101] orientation of arsenopyrite. Selected area diffraction patterns of the pyrrhotite product showed a direct crystallographic relationship with
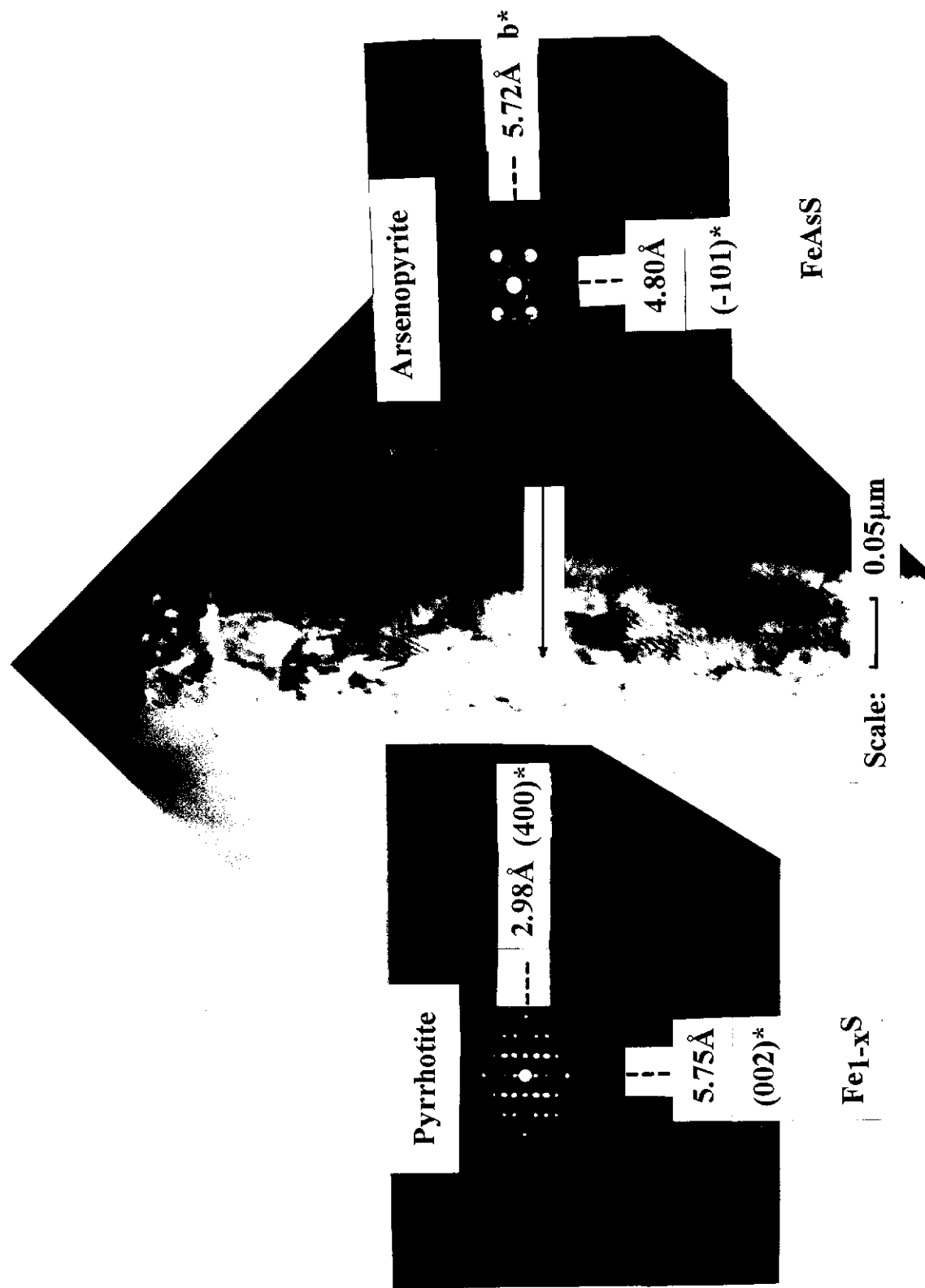
Figure 7.4 An electron micrograph of a topotactic breakdown of arsenopyrite to pyrrhotite (direction of arrow in photo). A convergent beam electron diffraction pattern showing the symmetry of arsenopyrite is on the right side. The selected area diffraction pattern (left side) confirm the orientation relationship between pyrrhotite and arsenopyrite. Lattice fringes can be seen in the photo corresponding to layers of iron and sulfur atoms in the pyrrhotite product(near arrow head in photo).

arsenopyrite. The b* axis of arsenopyrite converts to the c* axis of the pyrrhotite formed. Also the/(10$\bar{1}$)* of arsenopyrite is orientated with the a* axis of the pyrrhotite. The measured d-spacings of the SAED patterns as well as EDX spectra analysed confirmed the presence of pyrrhotite and its orientation. This orientated breakdown was not continuous over the whole arsenopyrite crystal face and was broken in a number of places. Globules of arsenic were also present and appeared to have little sulfur or iron present. The electron diffracted spots for arsenopyrite, which represent lattice planes in real space, have slightly larger d-spacings than those of pyrrhotite as can be seen in the SAED pattern in Figure 7.4. These results showed that the initial breakdown of arsenopyrite is topotactic along its b axis. This observation constitutes the first documented evidence of this ordered breakdown. Subsequent heating of the pyrrhotite caused recrystallisation to a composition stable at local conditions (i.e. S_2 activity and temperature). With continued heating the pyrrhotite continued to recrystallise with loss of sulfur until an iron phase was present. Grains of arsenopyrite heated in other orientations resulted in no observed ordered breakdown. The recrystallisation of pyrrhotite formed complex domain structures which varied in orientation (Figure 7.5).

7.3.1.1.1 Reconstructive Transformation

The orientation of arsenopyrite structure and pyrrhotite products are shown in Figure 7.6. Models of both arsenopyrite and pyrrhotite structures were made and examined for displacement transformations and obvious structural similarities for the orientated breakdown observed. The growth of products by planar shear defects along certain crystallographic directions rather than by bulk diffusional mechanisms through solids, has been observed in the partial reduction of rutile and hematite systems (Hayes, 1992). The rutile structure can be related to the arsenopyrite structure (Buerger, 1936; Fuess et al., 1987) and so a slightly modified mechanism may occur. However, no obvious direct transformation could be proposed. It is envisaged that
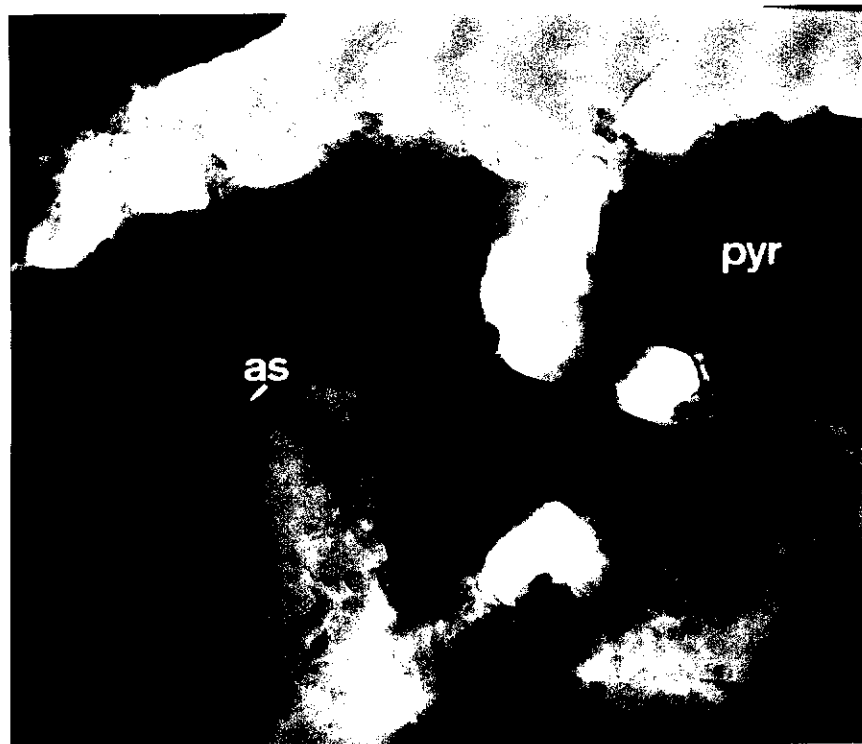
Figure 7.5 Transmission electron micrograph of complex domain structures in pyrrhotite after arsenopyrite. Globules of arsenic are also present.
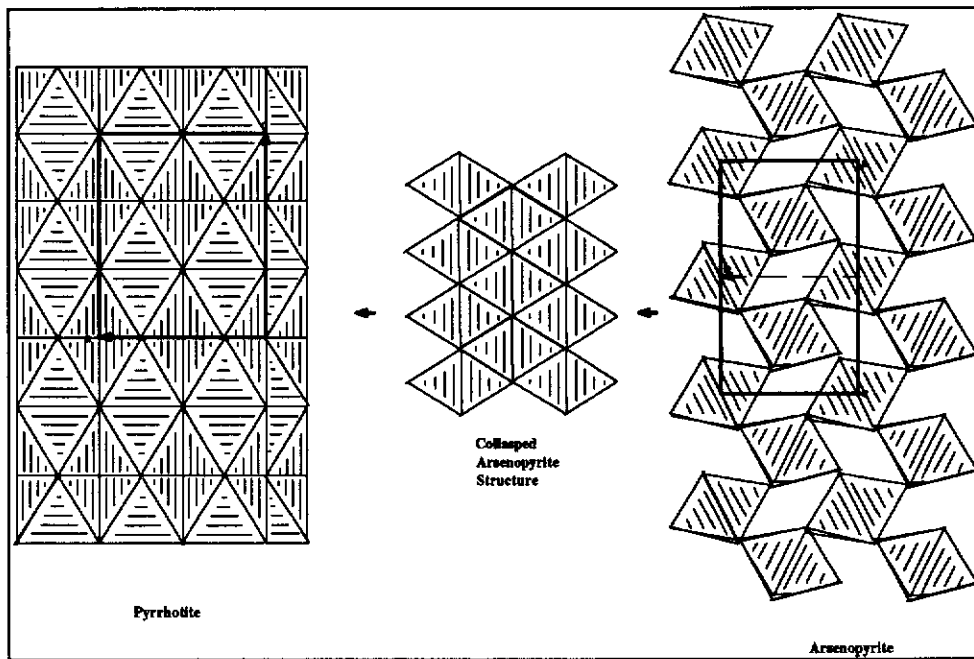
Figure 7.6 Comparison of arsenopyrite orientation with the pyrrhotite structure.

either a transitional phase is present and/or that the transformation involved is a reconstruction process.

In the ideal arsenopyrite structure, the iron atoms are octahedrally coordinated with three arsenic and three sulfur on opposite triangular faces. Strings of edge shared octahedra along the (101) direction are joined together by corners with the next string of octahedra as shown in Figure 7.6. On heating arsenopyrite grains, the binding energy of arsenic in the arsenopyrite lattice is lower than that of sulfur and results in the preferential removal of arsenic over sulfur along channels in the arsenopyrite structure. With the arsenic sites vacant the octahedra collapse in the (101) plane and then are further condensed in the ($10\bar{1}$) direction, resulting in strings of octahedra sharing triangular faces. This leads to faceting of the arsenopyrite surface i.e. complex planes and geometries are replaced by close-packed planes of lower energy in the form of the pyrrhotite structure.

The existence of an oriented interface of arsenopyrite altering to pyrrhotite was probably because of the low surface energy associated with the common structural plane. A similar oriented breakdown has been reported by Francis *et al.* (1976) for the segregation of pentlandite and pyrrhotite from a monosulfide solid solution of Fe-Ni-S system.

The formation of pyrrhotite probably starts at different rates and at many separate centres. When these ordered structures grow towards one another they may result in twins or antiphase domains. The thickness is restricted by the buildup of stresses in the pyrrhotite due to the differences in molar volume with the original arsenopyrite. The pyrrhotite continues to recrystallise in an attempt to become stable under the changing conditions of temperature and vapour pressure.

7.3.2 Agglomeration of Gold in Arsenopyrite

7.3.2.1 Observation of Mobile Gold during Arsenopyrite Alteration

To date, evidence for the exsolution and agglomeration of gold in arsenopyrite on thermal treatment has been essentially indirect and based entirely on analyses carried out on materials before and after heating. Figure 7.7 shows a series of electron micrographs of a synthetic auriferous arsenopyrite grain decomposing under the heat produced by the electron beam. It was previously demonstrated (Chapter 6) that gold in the synthetic auriferous arsenopyrite was in solid solution. By heating the grains with the electron beam, arsenopyrite recrystallised to pyrrhotite with arsenic being expelled. The gold was mostly insoluble in the pyrrhotite lattice and therefore exsolved out and was clearly seen to combine with other gold to form droplets at the boundary of the pyrrhotite formed. The temperature in the TEM during beam heating could not be determined but the process of decomposition would be expected to follow the same process as shown in Figure 7.1. A video of this gold agglomeration process similar to the frames shown in Figure 7.7 was also obtained and is available from the author.

Figure 7.8a shows an EDX spectrum of the synthetic arsenopyrite shown in Figure 7.7a which contained approximately 0.7 wt% gold. An EDX spectrum of the same grain after heating (Figure 7.8b), shows a reduction in the iron peak intensity relative to the sulfur peak. The EDS analyses indicated some arsenic present amongst the altered product and this appeared closely associated with the gold. Other round 'blobs' of material were also found and an EDX spectrum of these indicated a high concentration of arsenic whereas the pyrrhotite matrix contained little (Figure 7.9). There was also a difference in Fe:S ratio intensities. The pyrrhotite recrystallised during heating and changed in composition until all the sulfur was removed leaving an iron phase with the gold reabsorbed.

Although other workers have postulated and observed what appeared to be gold agglomeration after heating samples (e.g. Graham *et al.*, 1989), the present
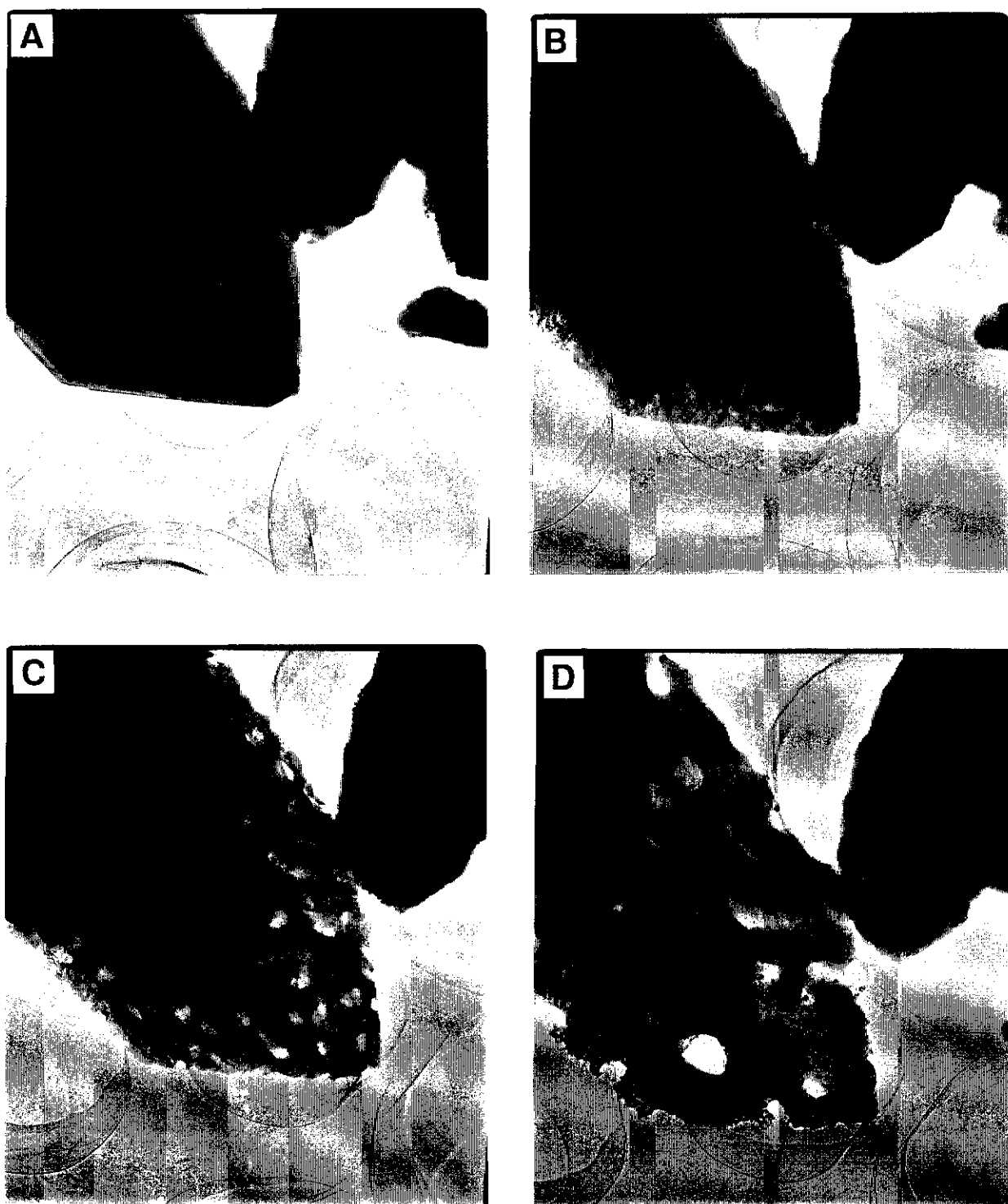
·5 µm

Figure 7.7 A series of electron micrographs of a beam heated auriferous arsenopyrite grain altering to pyrrhotite with the agglomeration of gold (After Aylmore and Graham, 1992).
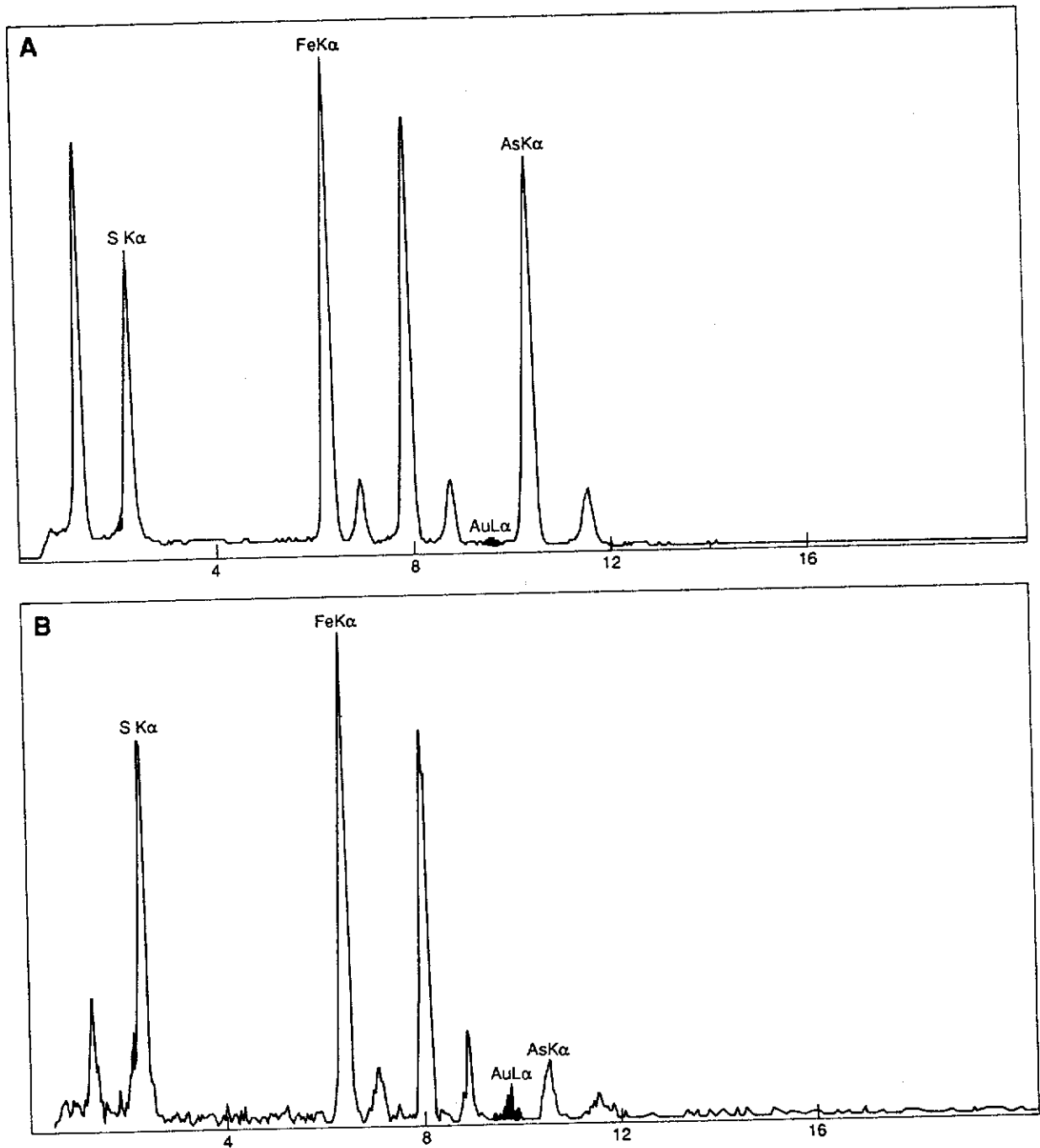
Figure 7.8 Energy dispersive spectrum of arsenopyrite (a) before heating, containing detectable gold and (b) a spectrum of an aggregated gold grain.
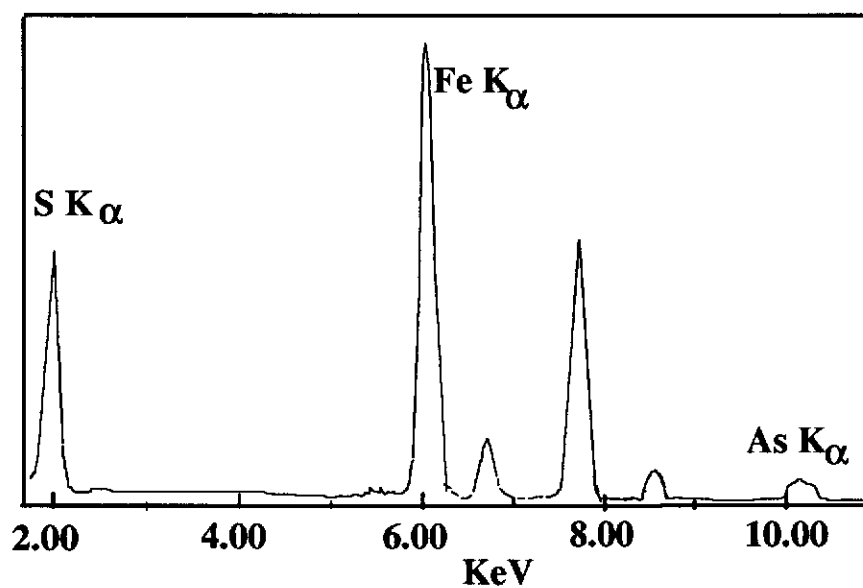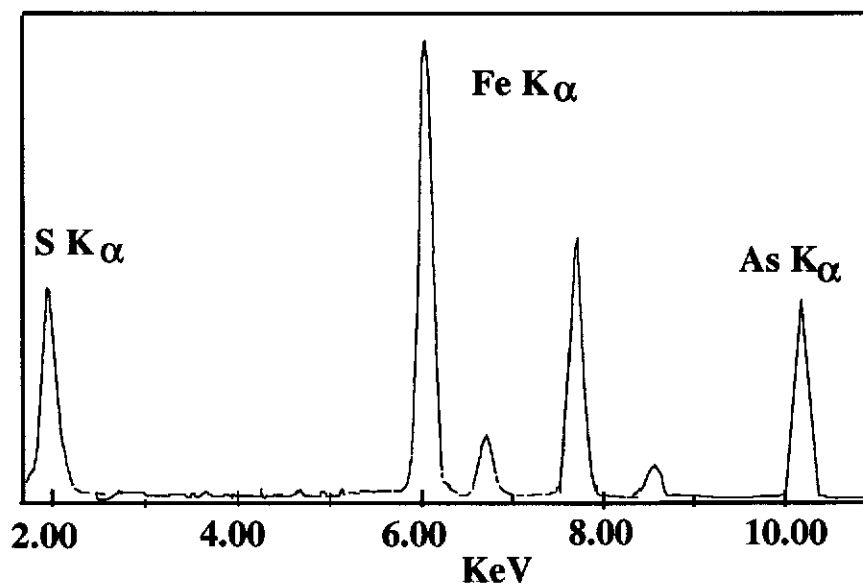
Figure 7.9 Energy dispersive spectrum of (a) arsenic 'blobs' and (b) the pyrrhotite matrix from thermally altered arsenopyrite.

results are the first in which the actual process of gold exsolving and agglomerating has been clearly demonstrated. This process was observed in both the Sheba and synthetic auriferous arsenopyrite samples.

7.3.2.2 Effect of Temperature on Gold Mobilisation in Auriferous Arsenopyrites

The temperature at which gold becomes mobile was examined for both synthetic and natural auriferous arsenopyrite samples. Heating of two auriferous arsenopyrites in sealed evacuated tubes at temperatures below 470°C in a muffle furnace, resulted in no observed changes in the arsenopyrites. Figure 7.10 shows a partially heated grain of Sheba arsenopyrite to 570°C. Electron microprobe analyses indicated that the unaltered part contained 0.5 wt% Au. A scan of a polished section after heating showed no evidence of coalesced gold. A full heating to 700°C resulted in only pyrrhotite being formed and round fine gold grains distributed throughout many of the grains as shown in Figure 7.11. With increasing temperature the pyrrhotite appeared to be coarser.

Heating of synthetic auriferous arsenopyrite (Figure 7.12a) resulted in similar observations. No gold was observed until 600°C was reached. Figure 7.12b show a grain of synthetic auriferous arsenopyrite heated over 600°C altering to pyrrhotite containing agglomerated gold. A partial breakdown in arsenopyrite up to the main endothermic peak resulted in no observed agglomeration of gold. The lack of observed gold in the samples heated below the main decomposition temperature suggests that either the gold was still locked up in the pyrrhotite structure or that any gold that had exsolved from the breakdown of the arsenopyrite structure was very small in size. As pyrrhotite can contain very little gold in solid solution (Cook and Chryssoulis, 1990) the gold was most probably very fine. Since the synthetic sample was abundant in solid solution gold the latter possibility is the most likely. In addition, experiments carried out in Chapter 4 showed no gold in either arsenopyrite or pyrrhotite formed from solid state reactions.
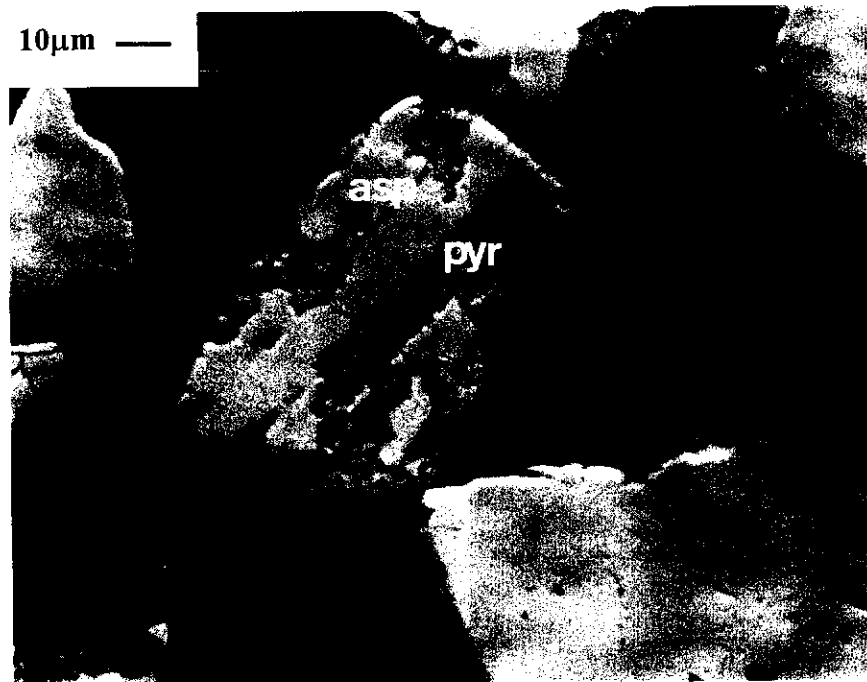
Figure 7.10 Partial Roast of Sheba arsenopyrite at 570°C. The unreacted arsenopyrite contains 0.5 wt% 'invisible' gold.
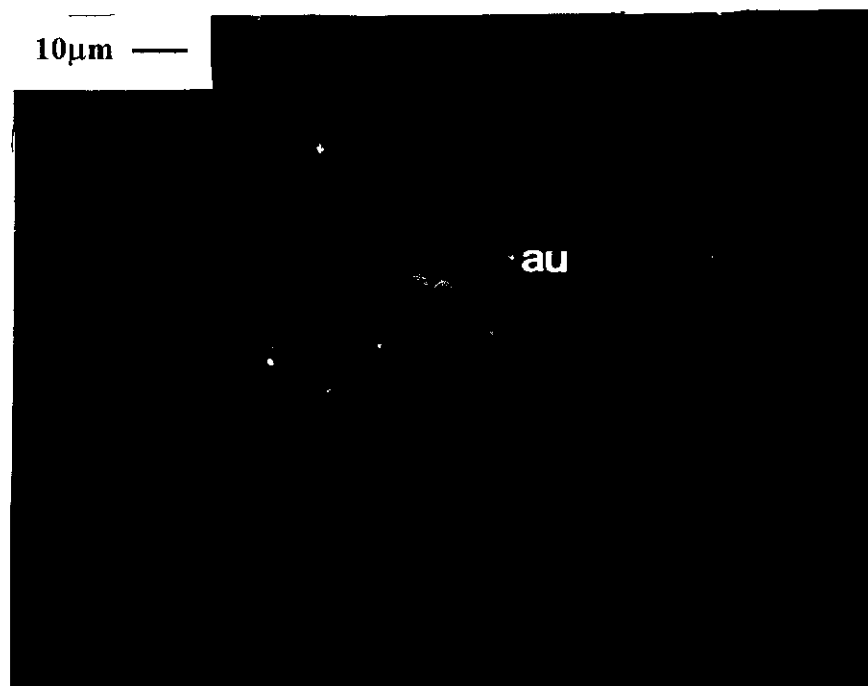
Figure 7.11 A complete roast of Sheba arsenopyrite to pyrrhotite containing aggregated gold.

10μm —

(a)

10μm —

·au

(b)
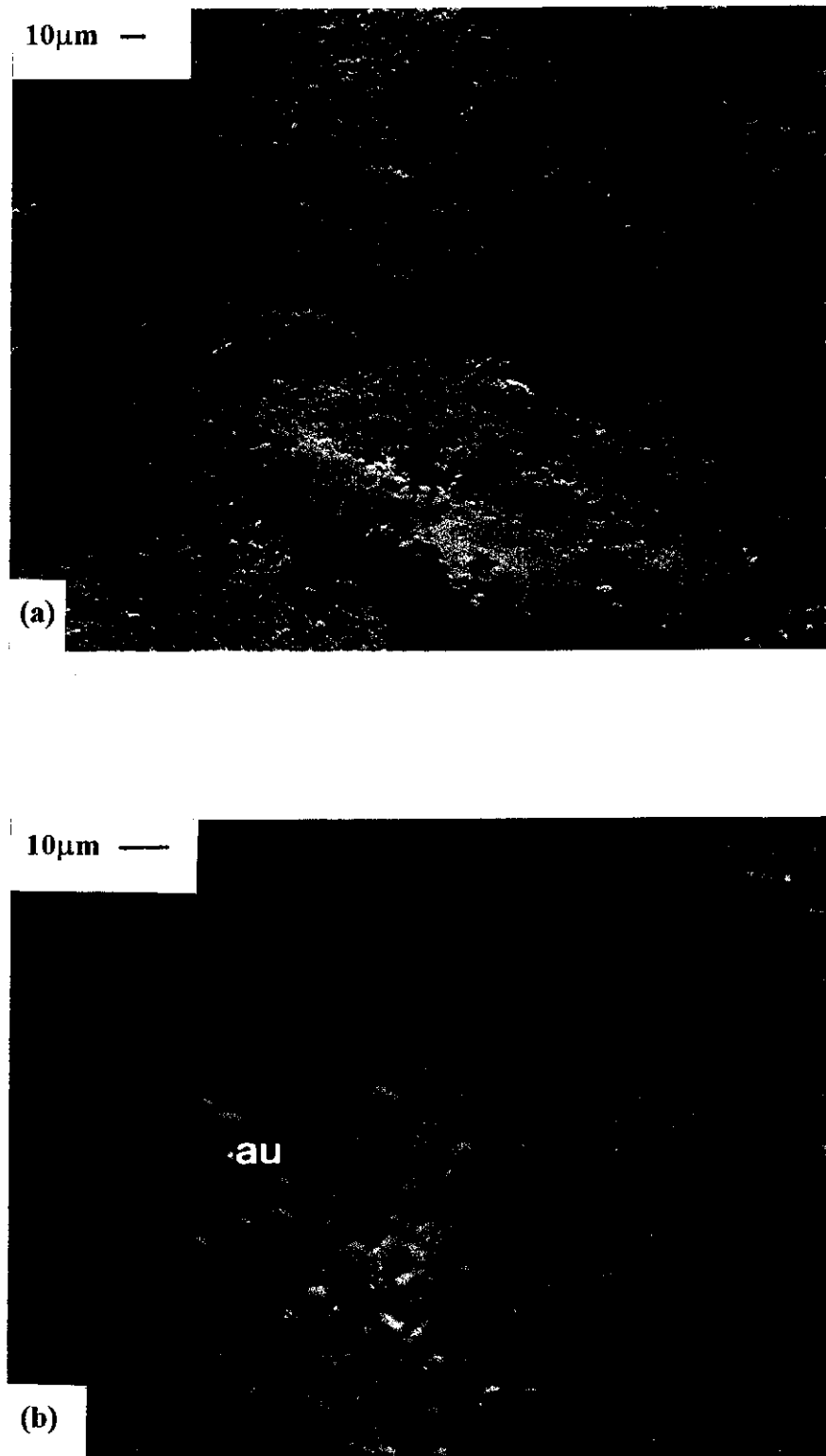
Figure 7.12 Scanning electron micrograph of (a) partially altered grains of synthetic auriferous arsenopyrite heated below 600°C and (b) pyrrhotite containing conglomerating gold after synthetic auriferous arsenopyrite heated over 600°C.

Figures 7.13a and b show the EPMA analyses of Sheba arsenopyrite grains partially altered to pyrrhotite for several scans across different grains. No löllingite composition was observed. The pyrrhotite composition varied slightly. Little arsenic is associated with the pyrrhotite phase. Both Clark (1960) and Barton (1969) observed little arsenic soluble in pyrrhotite. Gold detected in the pyrrhotite product varied from 0 to 0.45 wt%. There appeared to be no relationship between where gold was and the position within the grains, which indicated that gold was not carried along the alteration interface of the grains during heating as proposed by Swash and Ellis (1986). In the presence of nitrogen at a fast heating rate of 50°C/min, arsenopyrite altered to pyrrhotite at around 600°C, whereas at a slower heating rate of 5°C/min it started to breakdown at approximately 470°C. Gold was only observed to have agglomerated at the higher temperature. That is, the rate of removal of arsenic from the altering arsenopyrite increased the gold agglomeration process.

Because the breakdown of arsenopyrite is endothermic, arsenic is only evolved when arsenopyrite is heated to ~470°C. Consequently, a high arsenic vapour pressure was present to react with the gold only when the temperature was high enough to drive more arsenic off.

7.3.2.3 Effect of Ambient Gas Composition on Gold Agglomeration in Arsenopyrites

Heating auriferous arsenopyrite samples in the muffle furnace at 612°C in air resulted in arsenopyrite altering to hematite pseudomorphs (Figure 7.14a and b). Examination of polished sections of this material showed no gold agglomeration. However, analyses of some of the altered hematite under the TEM revealed fine gold grains (<1μm) (Figure 7.15). The presence of oxygen increased the rate at which arsenic was removed from the arsenopyrite structure (Chakraborti and Lynch, 1983). However, the consumption of arsenic by oxygen (to form As_2O_3) appeared to reduce the size of the gold agglomerated.
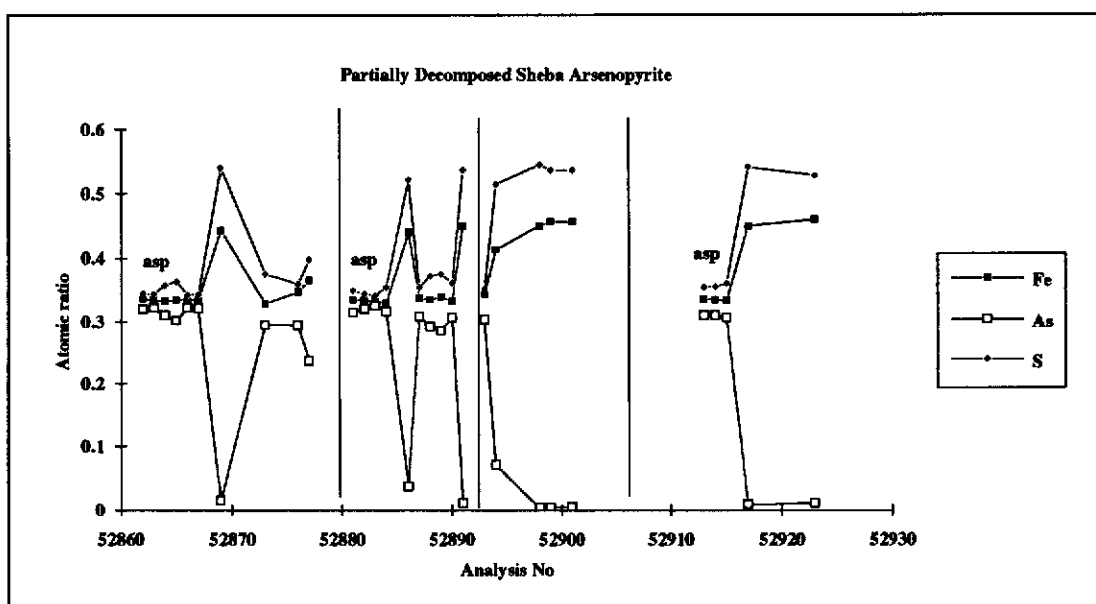
asp- arsenopyrite grain
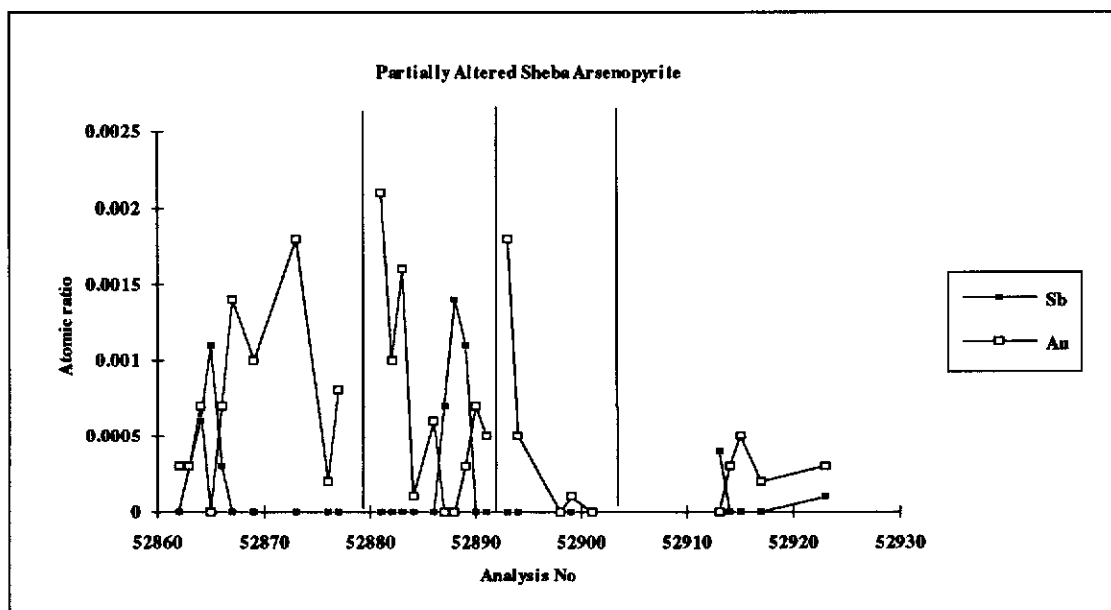
Figures 7.13a and b EPMA analyses of Sheba arsenopyrite grains altering to pyrrhotite.

5μm —

(a)

10μm ———

(b)
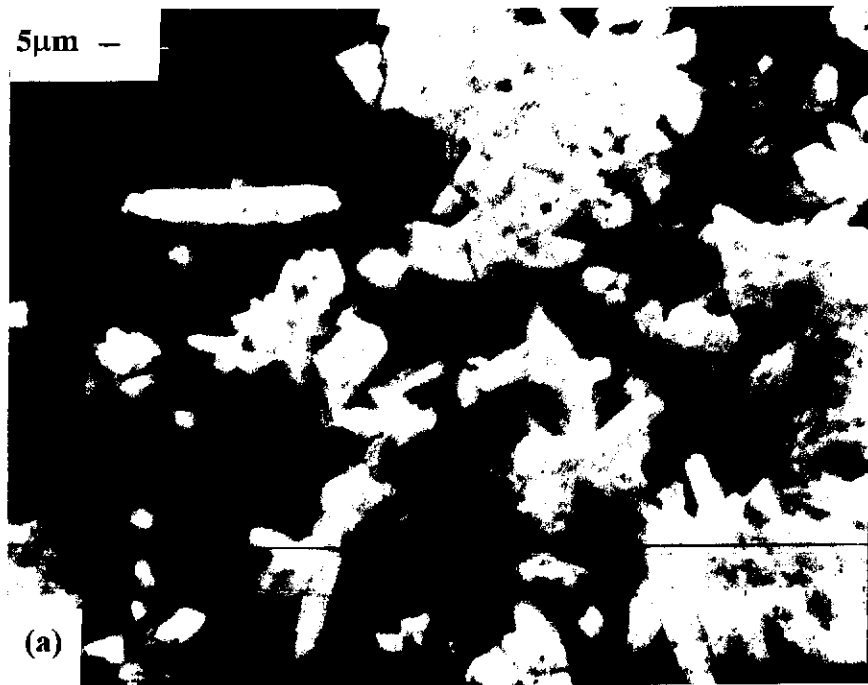
Figure 7.14 (a) and (b) Scanning electron micrograph of haematite pseudomorphs after heating auriferous arsenopyrite to 612°C. No gold grains were visible.
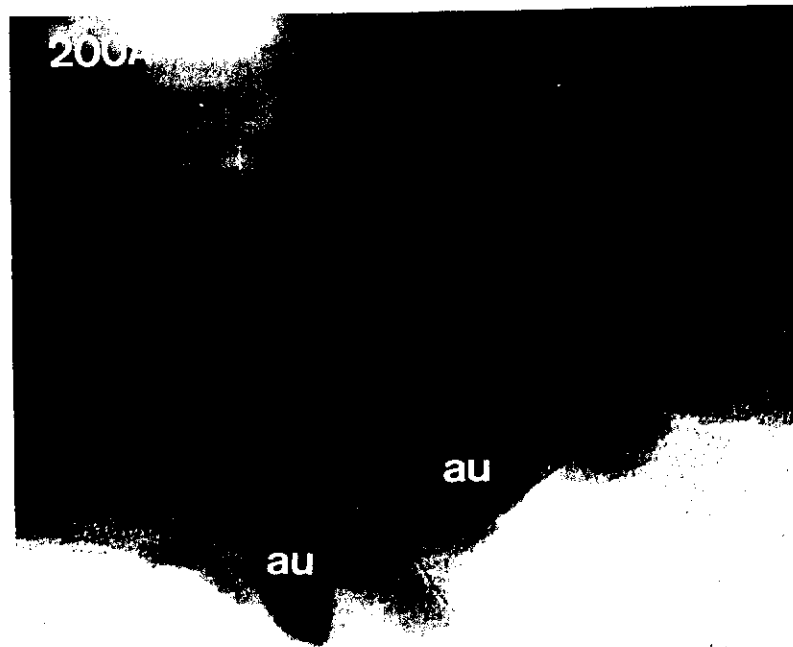
Figure 7.15 Transmission electron micrograph showing the presence of fine gold particles in haematite pseudomorphs after auriferous arsenopyrite heated at 612°C in air.

Heating auriferous arsenopyrite samples at different heating rates was then examined to observe what effect it had on the gold agglomeration process. Figures 7.16a and b show differential thermal and gravimetric analyses of synthetic auriferous arsenopyrite at heating rates of 5°C/min and 50°C/min in air respectively. Heating a sample in a TG-DTA from room temperature through to 700°C at a slow heating rate of 5°C/min also resulted in no large agglomeration of gold (Figure 7.17a). On the other hand, increasing the heating rate to 50°C/min resulted in a large agglomerated gold grain (~20μm) on the edge of some aggregates of hematite pseudomorphs (Figure7.17b). No gold was observed in the hematite pseudomorphs. Therefore, the rate and the residence time of arsenic vapour within the altering arsenopyrite grain had an effect on the size of the gold agglomeration.

7.3.2.4 Mobility of Coarse Gold during Arsenopyrite Alteration

Several heating experiments of auriferous arsenopyrite have shown large concentrations of gold agglomerating. However, the amount of gold which has been claimed to have agglomerated in the resultant pyrrhotite in some of these experiments appeared too large to have come from within the arsenopyrite itself (Graham *et al.*, 1988). Consequently, the heating of arsenopyrite in the presence of coarse metallic gold was examined to determine the effects of the breakdown of arsenopyrite on gold mobilisation. Clark (1960) in his high pressure experiments found that gold from the tube in which arsenopyrite was contained diffused through arsenopyrite at 660°C and 2k bars. Some of the experiments carried out in Chapter 4 showed gold to be mobile at temperatures of 600°C and higher.

The experiments carried out are summarised in Table 7.1. For comparison, natural gold free arsenopyrite was also heated in sealed evacuated tubes. Between 450 °C and 550°C little alteration appeared to have occurred in the gold free samples. In samples heated above 550°C various degrees of alteration of arsenopyrite to pyrrhotite, löllingite and arsenic occurred (Figure 7.18). At higher temperatures, a
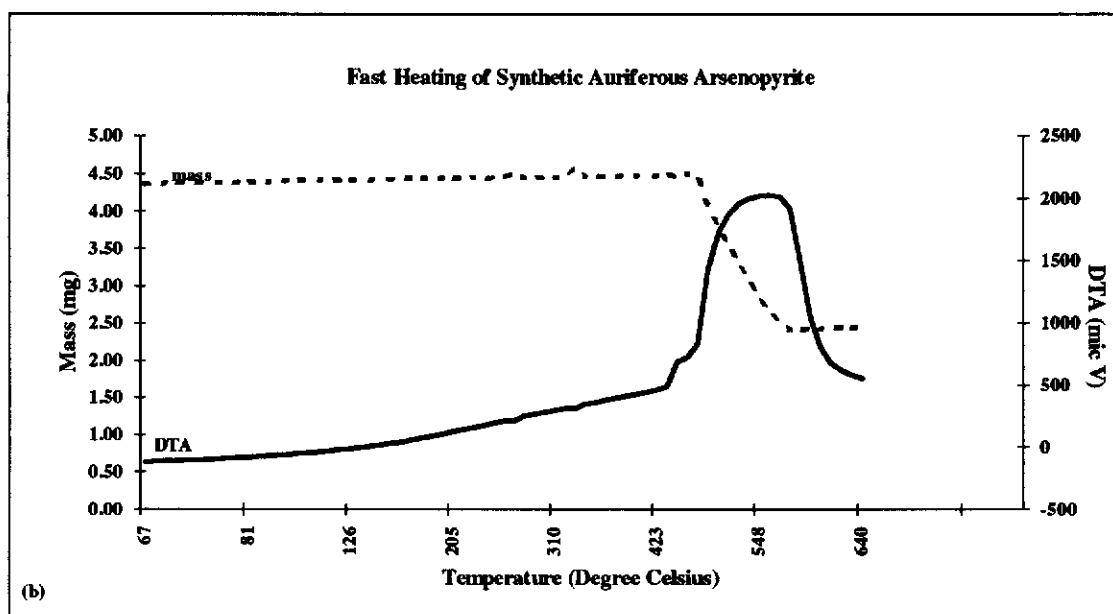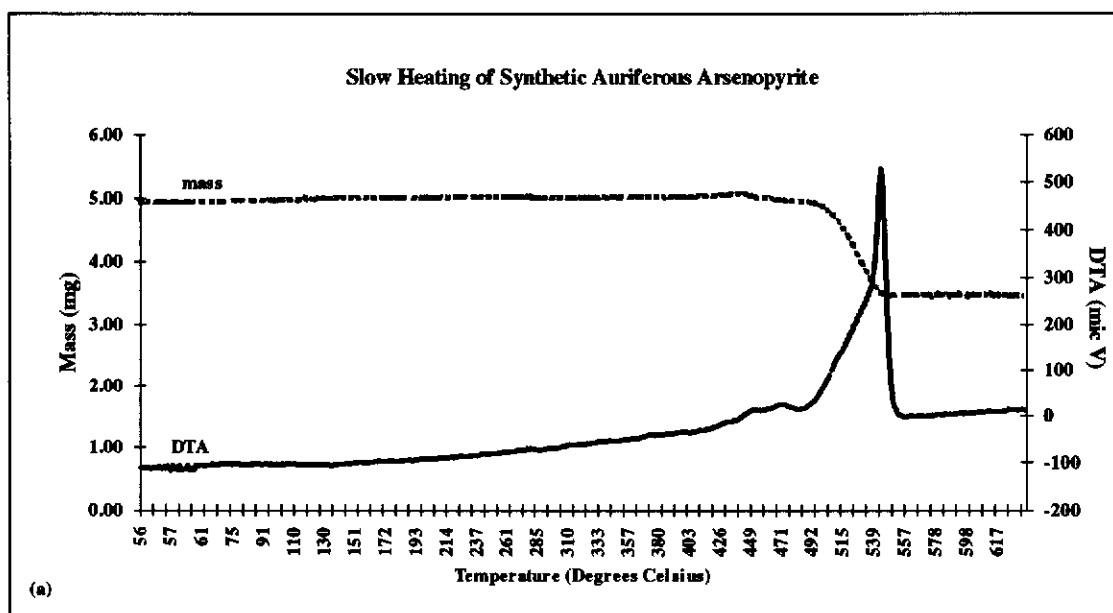
Figure 7.16 Differential thermal and gravimetric analyses of synthetic auriferous arsenopyrite heated at (a) 5°C/min and (b) 50°C/min in air.
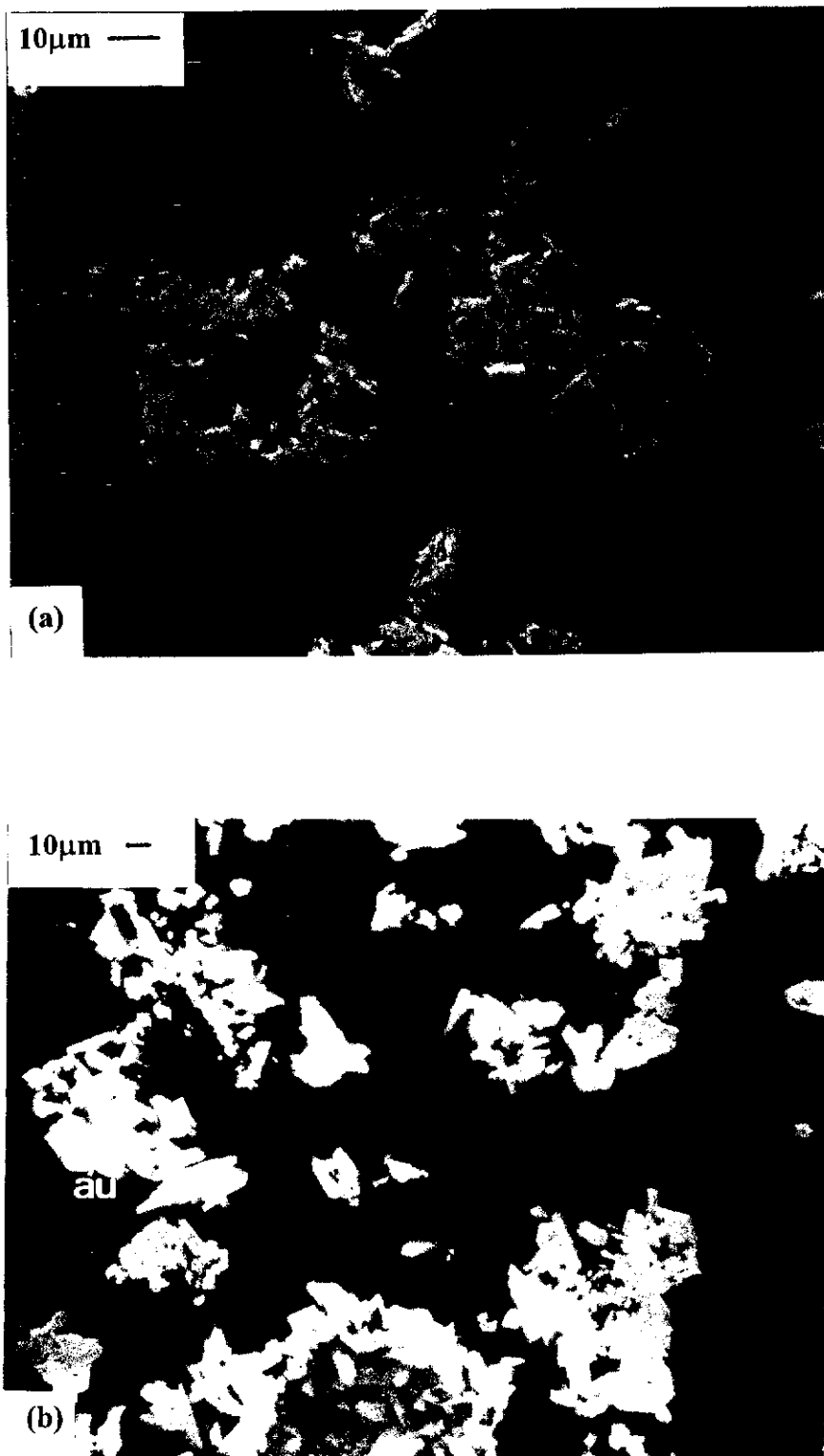
Figure 7.17 Scanning electron micrograph of haematite pseudomorphs (a) after a slow heating (5°C/min) and (b) after a fast heating rate (50°C/min) in air. No gold was visible observed in the slow heated sample. Large conglomerated gold grains (~20μm) were observed on the edge of some aggregates of haematite pseudomorphs in the fast heated sample .
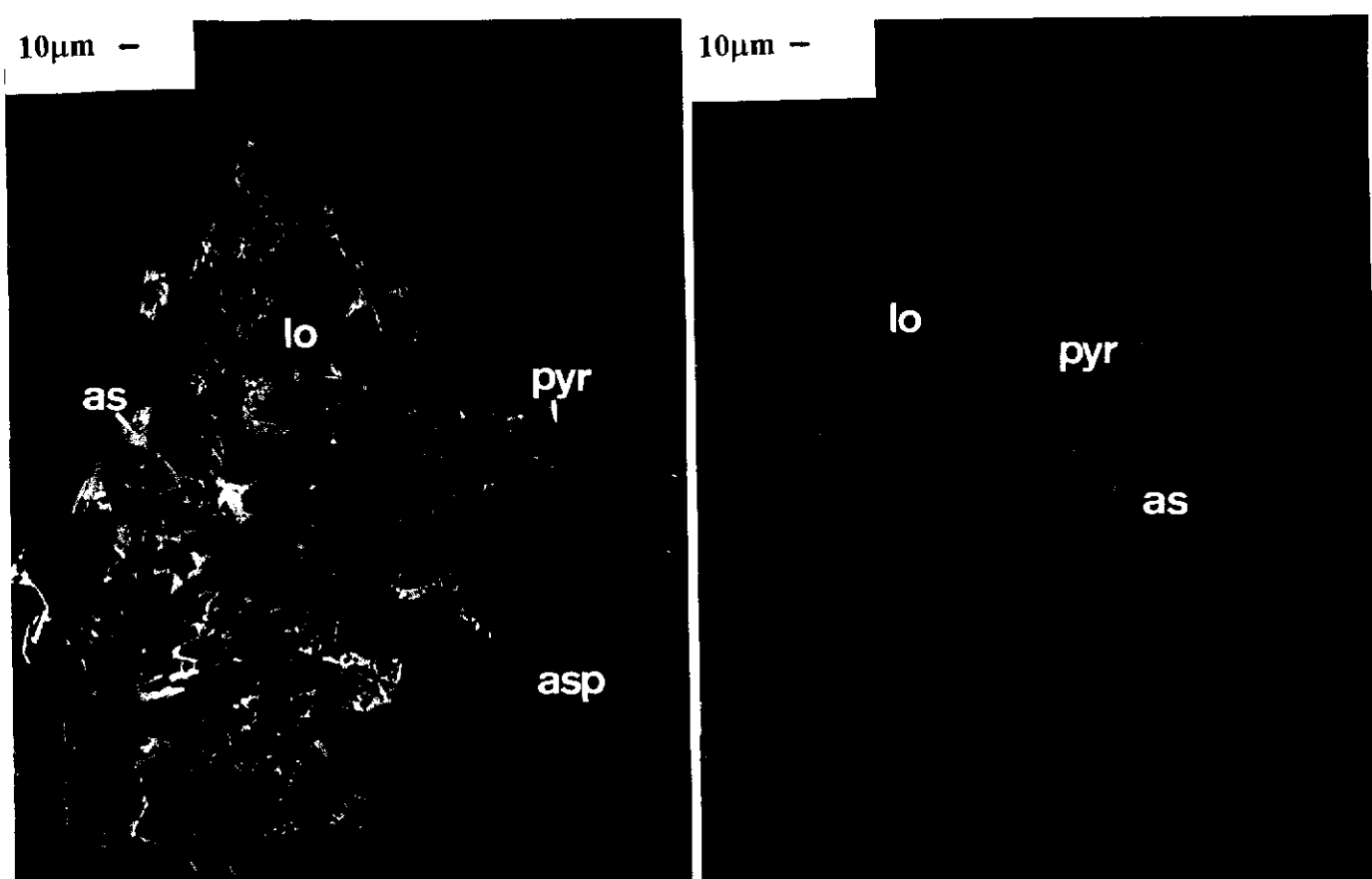
Figure 7.18 Coolgardie arsenopyrite samples heated above 550°C showing alteration of arsenopyrite to pyrrhotite, loellingite and arsenic (vacch1-4).
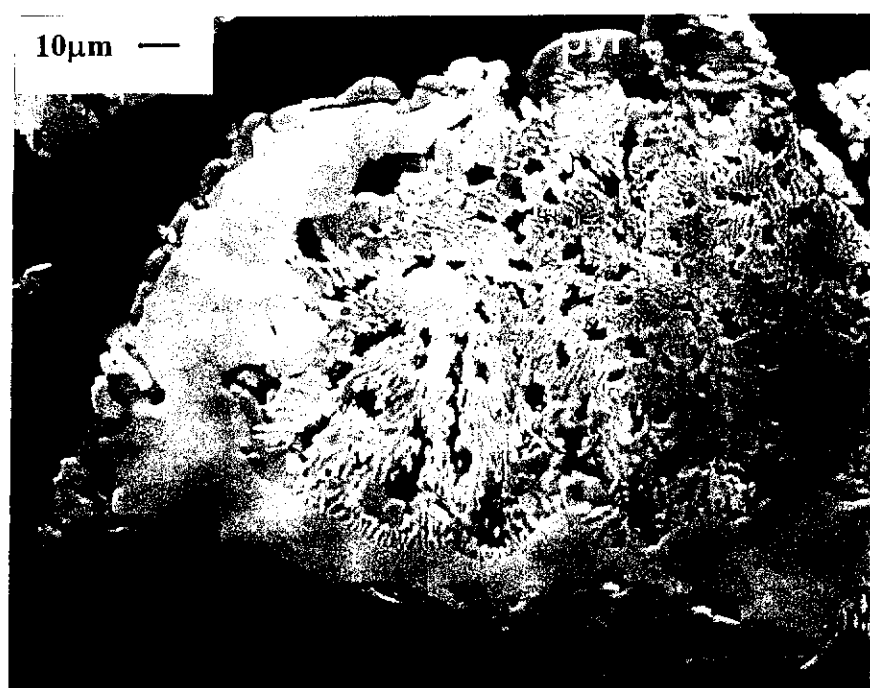
Figure 7.19 Scanning electron micrograph of arsenopyrite heated above 660°C showing a eutectic structure of loellingite and pyrrhotite which have exsolved out on cooling (casp2).

eutectic structure was observed (Figure 7.19) where löllingite and pyrrhotite were soluble in each other.

Examination of the samples containing gold under the SEM showed no interaction between the gold and arsenopyrite at the low temperatures. However, interaction with gold was observed at 500°C (Figure 7.20). The originally smooth gold surface had become pitted. On the surface of pyrrhotite, formed from arsenopyrite, fine round globules of gold could be found.

Table 7.1 - Experiments on the Mobility of Coarse Gold during Arsenopyrite Alteration (carried out in sealed Vycor tubes)

Sample	*Starting Materials (g) Au, S and As present (g)		Temp. (°C)	Period (Hrs)	Products
Casp2	casp 0.5	-	710	12	Asp+lo+pyrr+As
Casp5	casp 0.5	-	542	2	Asp+lo+pyrr+As
Vacch1-4	ch	-	660-690	6	Asp+lo+pyrr+As
Vacch16	ch 0.9807	Au 0.1256	340	3	Asp+Au
Vacch33	ch	Au leaf	340		Asp+Au
Vacch19	ch 0.4905	Au 0.00182	500		Asp + pyrr +As+Au
Vacch37	sh 0.4936,	Au 0.0744, S 0.1298	500	10	Asp+pyrr +As+Au
Vacch36	sh 0.4232,	Au 0.0684 As 0.6761	500	10	Asp + lo +As+Au
Vacch35	ch 0.7094	Au leaf	600	1	Asp + lo +As+Au
Vacch34	ch 0.5536	Au 0.0897, As 0.3966	600 - 660		Asp+lo +As+Au+ S
Vacch5	ch	Au wrapped around ch	660	2 months	Asp+lo+pyrr+As+Au
Vacch8	ch 1.8678	Au 0.4317	600	2	Asp+lo+pyrr+As+Au
Vacch13	ch 0.5097	Au 0.0527	665	1	Asp+ lo + pyrr+As+Au
Vacch35b	sh 0.5263,	Au 0.0666, S 0.0342	650	3	Asp + pyrr+As+Au

*sh - Sheba arsenopyrite; ch - China arsenopyrite; Casp - Coolgardie arsenopyrite

In samples heated above 600°C, gold was more readily mobile. Figure 7.21a shows gold after heating, covering regions of arsenopyrite altered to pyrrhotite. At places where arsenopyrite was unaltered no gold was present. X-ray diffraction studies showed arsenopyrite, arsenic metal, pyrrhotite and löllingite as the major phases. A cross-section is shown in Figure 7.21b where gold had been carried along with the alteration of arsenopyrite to pyrrhotite and löllingite. The degree of alteration varied from grain to grain and many were unaltered. Figure 7.21c shows a close up of
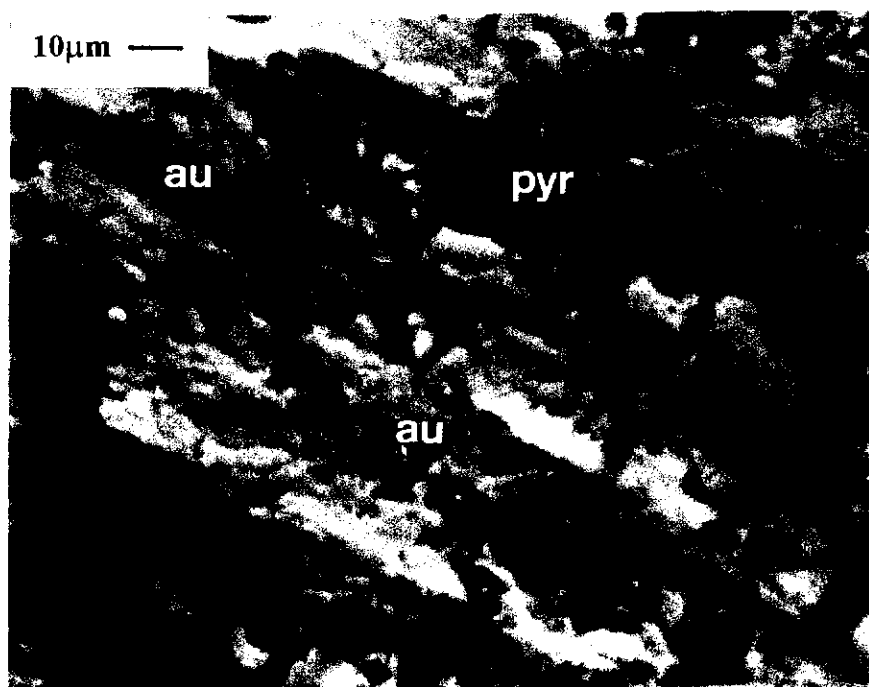
Figure 7.20 Scanning electron micrograph of arsenopyrite partially altered at 500°C to pyrrhotite with gold globules.
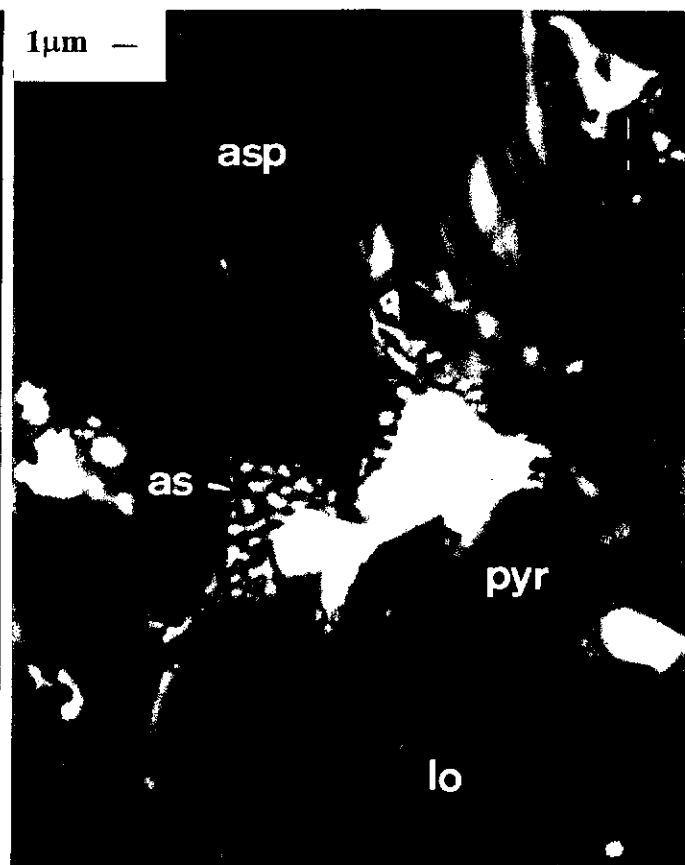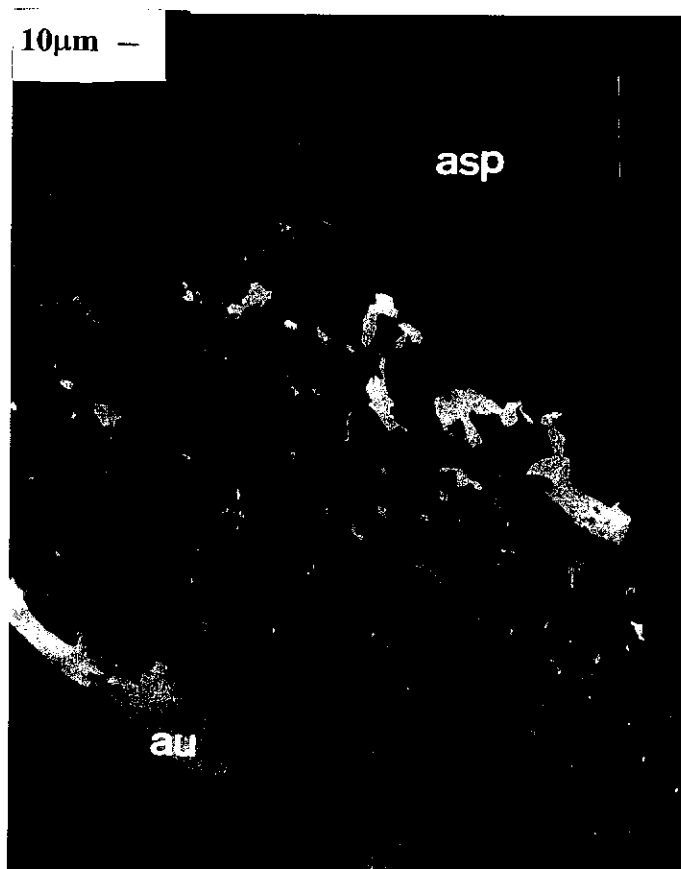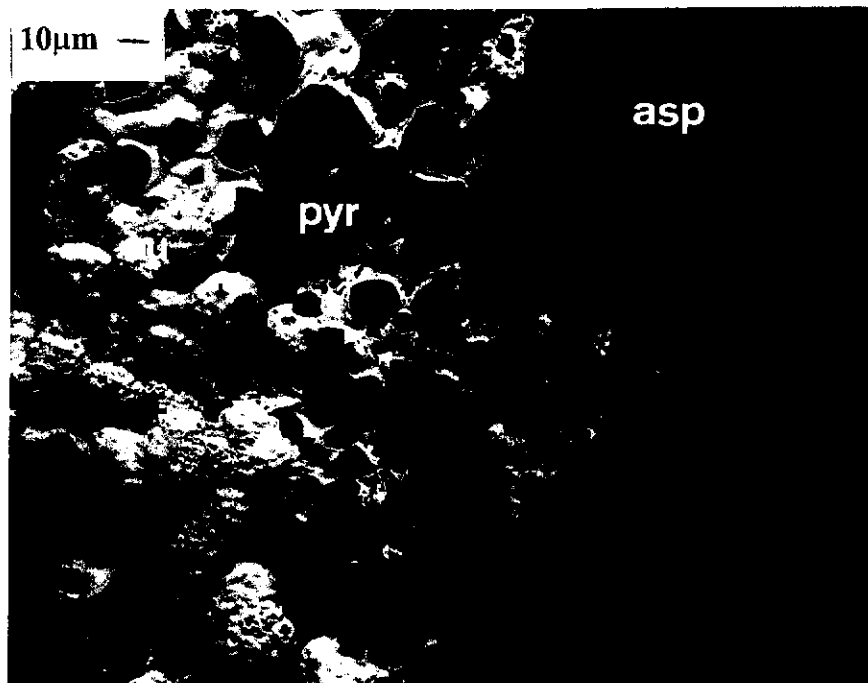
Figure 7.21a Gold deposited after heating, covering regions of arsenopyrite altered to pyrrhotite. At places where arsenopyrite was unaltered no gold was present.(b) A cross-section of grains showing gold made mobile during the alteration of arsenopyrite to pyrrhotite and loellingite. (c) A close up of gold exsolved out of pure arsenic on cooling.

the gold -arsenic eutectic on cooling. No gold and arsenic compound has been reported in the literature, only liquid solutions (Gather and Blachnik, 1976). However, electron microprobe analyses using a broad electron beam gave a composition of approximately $AuAs_{1.8}$, which indicates that this compound may exist at high temperatures. Also present were step-like structures in some directions along the arsenopyrite altering face in the polished sections. In other parts the altering interface was irregular. Arsenic and traces of sulfur vapour, which condensed to a liquid on cooling, were also present on the walls of the vycor tube. No gold was found associated with the condensed gas. The amount of arsenic coming off is a function of temperature. At a given temperature arsenopyrite decomposed until a certain arsenic vapour pressure was reached at which time no more arsenopyrite decomposed. The high quantities of condensed arsenic especially around the gold, indicated that the presence of gold increased the breakdown and distillation of arsenic from arsenopyrite.

The composition of each phase was analysed by electron microprobe. These results are shown in Figures 7.22a to f. Points were probed across a grain from the outer edge to the unaltered arsenopyrite. Points were chosen in order to prevent detection of scattered X-rays from surrounding material and thus to avoid incorrect values, in particular, from coarse gold observed around the rim. The composition of pyrrhotite was constant, with an average Fe and S composition of $Fe_{0.87}S$. The pyrrhotite phase contained no detectable gold. The löllingite phase contained some sulfur with the arsenic and iron. Löllingite can incorporate about 10 mol % FeS_2 (Clark, 1960). No other iron arsenic compounds were observed by XRD or by electron microprobe analyses. The presence of high gold content was generally associated with higher arsenic regions. The breakdown reaction follows the equation

$$FeAsS + Au \rightarrow Fe_{1-x}S + Fe(As,S)_2 + (As,Au) + Au \dotfill (7.4)$$
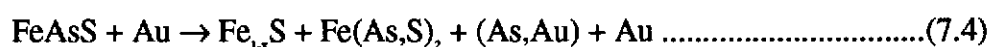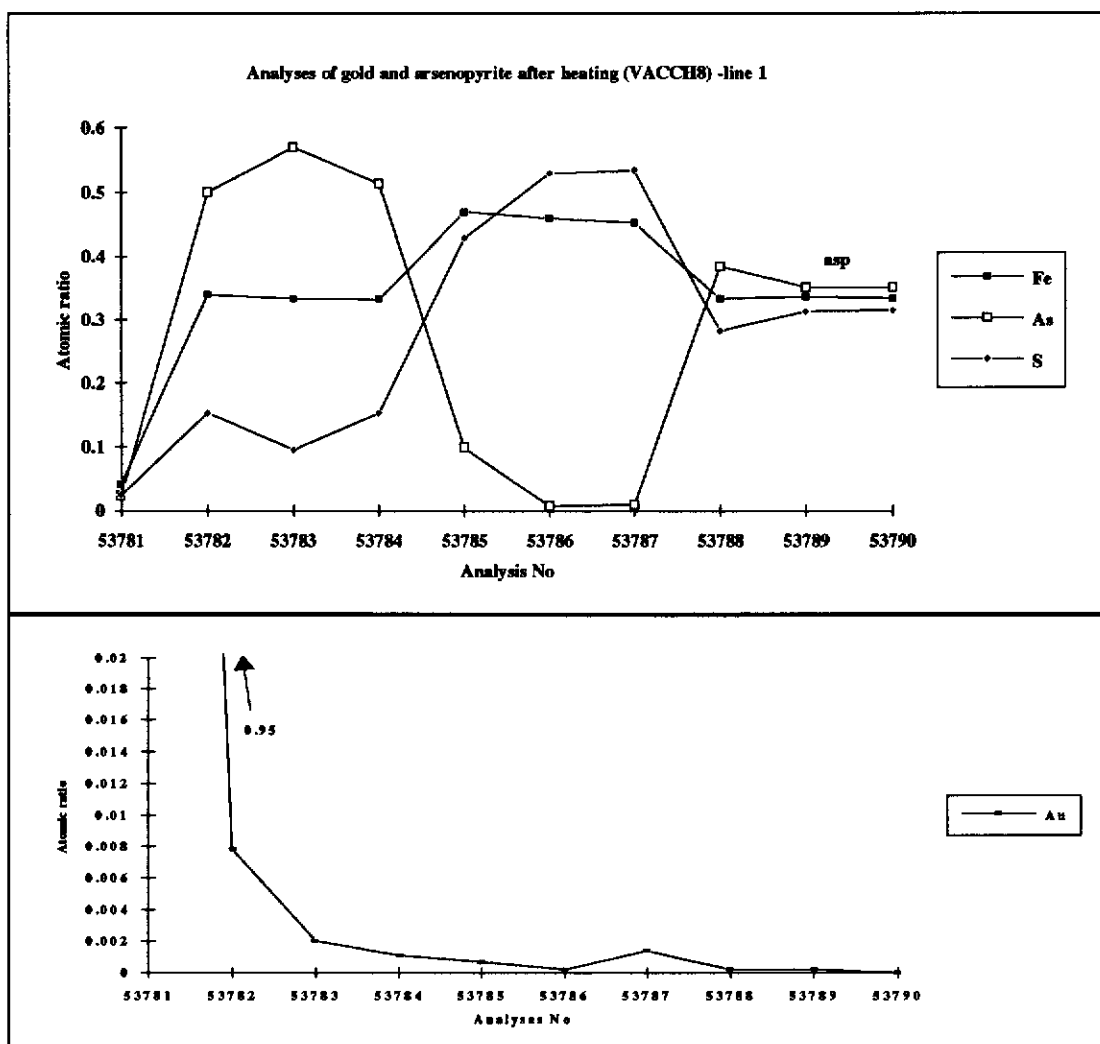
Figures 7.22a to b EPMA analyses across China arsenopyrite grain altering to pyrrhotite and löllingite with gold (vacch8).
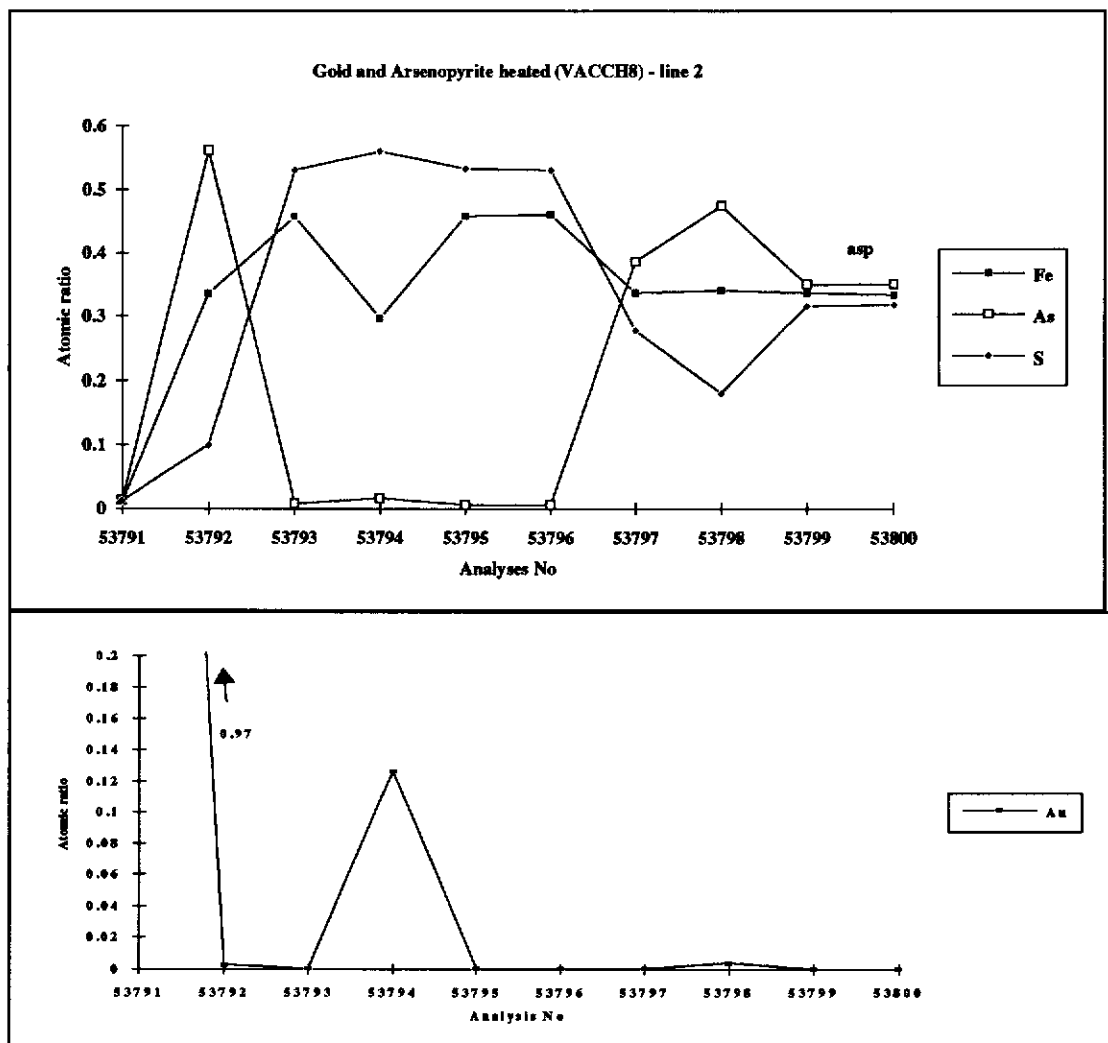
Figures 7.22c to d EPMA analyses across China arsenopyrite grain altering to pyrrhotite and löllingite with gold (vacch8).
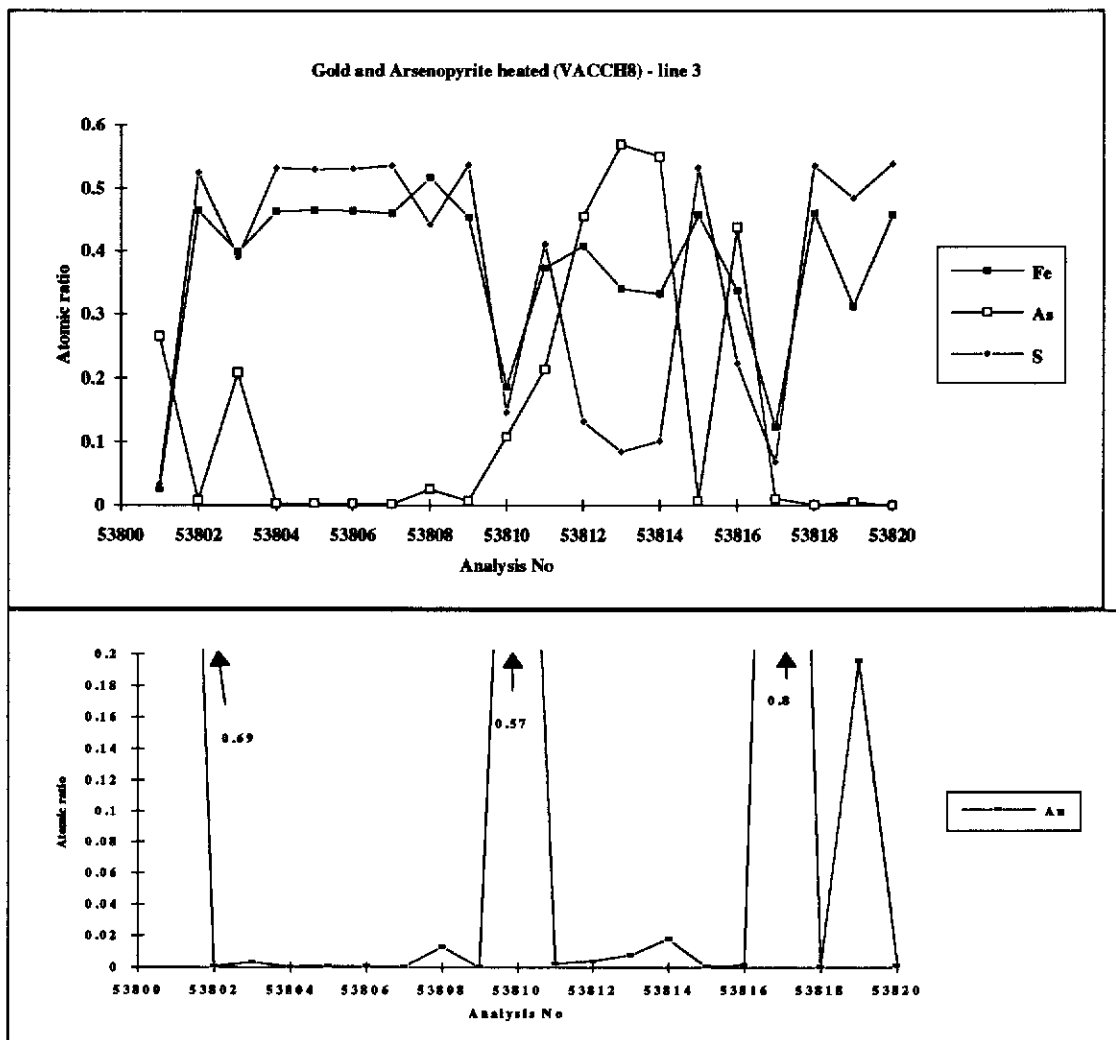
Figures 7.22e to f EPMA analyses across China arsenopyrite grain altering to pyrrhotite and löllingite with gold (vacch8).

The excess iron from arsenopyrite altering to pyrrhotite, as discussed earlier, was taken up with the arsenic to form mostly löllingite. The process was similar to that discussed in Chapter 4 where high pressures were applied to gold tubes containing arsenopyrite. However in the present experiments, the reactions were governed by thermal alteration of arsenopyrite under its own arsenic vapour pressure. The unbalanced chemical reactions involved are shown in Table 7.2.

Table 7.2 Chemical Reactions involving Arsenopyrite

	Reaction	Chemical potential	Temperature range
(1)	$FeAsS = FeAs_2 + FeS + (S,As)_{(l)}$		$\geq 702 \pm 3$
(2)	$FeAsS + As = FeAs_2 + (S,As)_{(l)}$		$\geq 688 \pm 3$
(3)	$FeAsS + S_2 = FeS + (S,As)_{(l)}$	$-23600 + 9.8T (\pm 1500)$	491-702
(4)	$2FeAs_2 + 2FeS + S_2 = 4FeAsS$	$-69900 + 55.6T(\pm 1000)$	25-650

(After Clark, 1960 and Barton, 1969)

Note: None of the phases are stoichiometric

Arsenopyrite, in the presence of gold and excess arsenic, resulted in precipitation of arsenic on unaltered arsenopyrite (Figure 7.23). Gold forming a eutectic texture was observed next to the recrystallised arsenic and arsenopyrite interface as well as on the outer edge of the löllingite crystals. The process can be explained by reaction (2) in Table 7.2 where no reaction of arsenic and arsenopyrite occurs until a temperature above 688°C is reached. Arsenopyrite in the presence of excess sulfur and gold resulted in the breakdown of arsenopyrite to porous pyrrhotite (Figure 7.24). A eutectic texture of gold and arsenic-sulfur was observed around the altered phase with some gold movement into the pores of the pyrrhotite as well as gold being observed at the arsenopyrite altering interface. The alteration of arsenopyrite followed reaction (3) in Table 7.2.

The results reported generally follow the reactions in Table 7.2, except that the actual temperatures for these reactions appear to be reduced. This can probably be
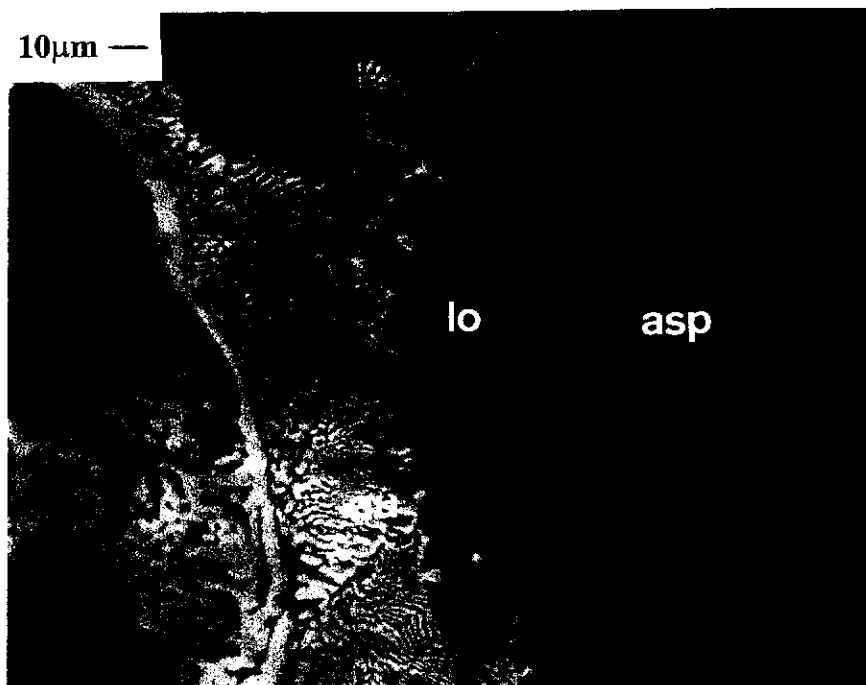
Figure 7.23 Scanning electron micrograph of arsenopyrite after heating in the presence of gold and excess arsenic. The formation of loellingite on unaltered arsenopyrite and arsenic-gold eutectic was observed (vacch34).
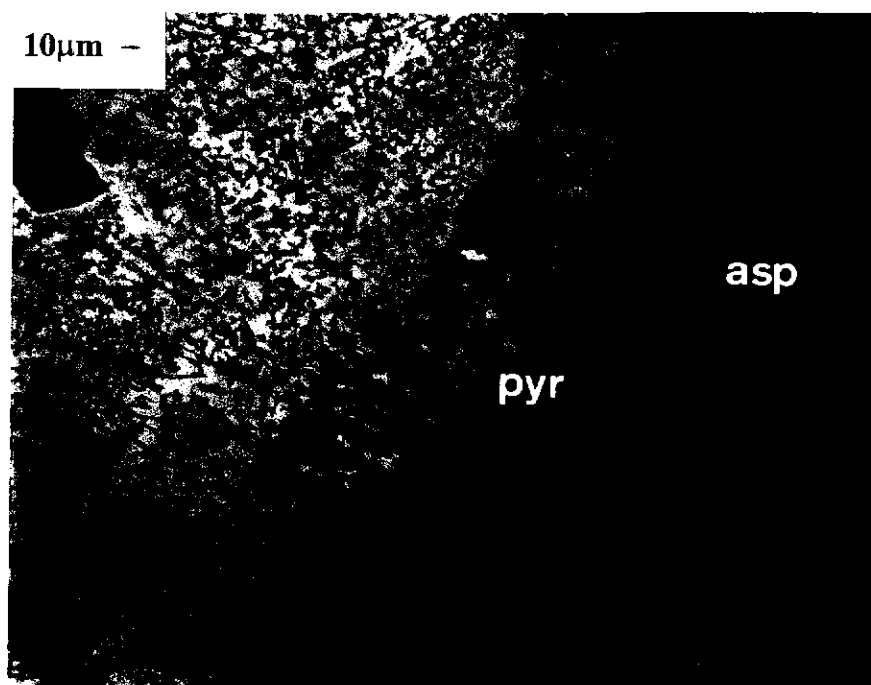
Figure 7.24 Scanning electron micrographs of arsenopyrite after heating in the presence of excess sulfur and gold. The breakdown of arsenopyrite to porous pyrrhotite and the presence of an As-S-Au eutectic were observed. Heated at (a) 600° C (vacch35b) and 500°C (vacch37).

attributed to variations in compositions of arsenopyrite as was illustrated in Figure 7.2. In the presence of gold, the decomposition of arsenopyrite occurred at a lower temperature. The idiomorphic texture observed on some arsenopyrite grains indicates that gold is not soluble in arsenopyrite. The presence of löllingite and pyrrhotite sharing boundaries with each other is puzzling as reaction of löllingite and pyrrhotite to form arsenopyrite is thermodynamically more stable (reaction (4)) at temperatures below 702°C. Above 702°C, the observed eutectic texture in Figure 7.19 indicates that löllingite and pyrrhotite were soluble in each other at high temperatures. The results above indicate that solid state diffusion of gold through arsenopyrite is not favoured and gold mobility is caused primarily by alteration of arsenopyrite as was observed in chapter 4 (section 4.3.5).

7.3.2.5 Non Isothermal Heating of Arsenopyrite with Gold in an Open System

Samples heated in the TG-DTA containing free gold and arsenopyrite with flowing nitrogen at 20°C/min or 40°C/min heating rates also showed gold interactions with arsenic vapour (Figure 7.25). As for arsenopyrite free of gold, the major endothermic peak occurred in the range of 630 to 700°C under conditions favourable for the formation of an arsenic and gold melt. These results indicate that even in an open system, arsenic from arsenopyrite decomposition will react with coarse gold. The flow rate of the nitrogen would most probably affect whether arsenic vapour is in contact with the gold surface for sufficient time. The size of the gold particles in the study would undoubtedly also have some influence.

7.3.2.6 Analysis of As-S-Au system

In view of the observed mobility of gold during arsenopyrite decomposition, experiments were carried out to determine firstly whether the mobility of the gold was caused by the reaction of arsenic alone or the As-S liquid, and secondly at what temperature gold is soluble in these liquid and gas mixtures. The various conditions
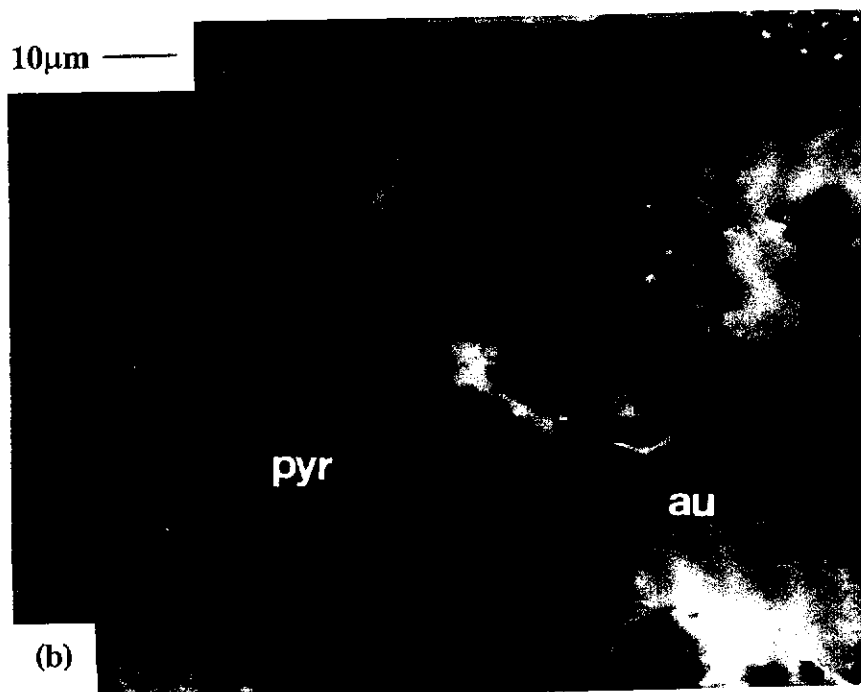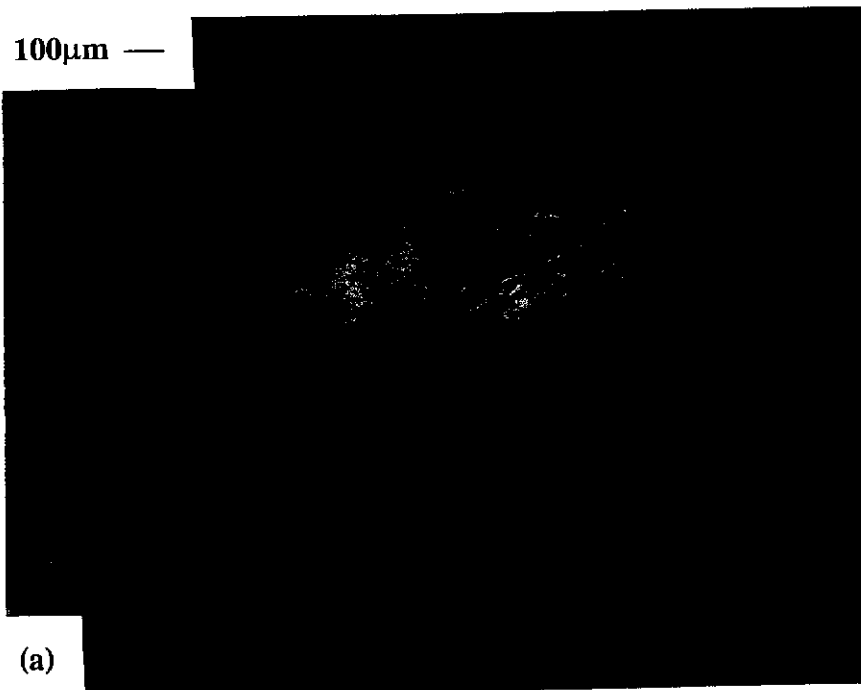
Figure 7.25 Scanning electron micrograph of partially melted gold from reactions with (a) arsenic vapour from arsenic metal and (b) arsenic vapour as a result of alteration of arsenopyrite.

used are shown in Tables 7.3 and 7.4. In the first instance the temperature at which arsenic and gold interact was examined.

Samples which had been heated above 500°C were examined under an optical microscope. The gold in these samples was readily mobilised in the presence of pure arsenic. At lower temperatures (~340°C) the arsenic recrystallised as aggregates on the gold surface. However, no obvious change in gold morphology was observed which indicated that little interaction had taken place. The arsenic vapour pressure over arsenic metal reduces with temperature and so at temperatures around 400°C there would be little As vapour-Au interactions. The reaction of arsenic on gold below 630°C indicates that the As-Au phase diagram of Gather and Blachnik (1976) is not correct.

Examination of samples containing various amounts of sulfur with arsenic at temperatures above 500°C, resulted in less interaction with gold than those in pure arsenic mixtures. The conditions used for the arsenic and sulfur mixtures with gold are shown on the arsenic and sulfur phase diagram in Figure 7.26.
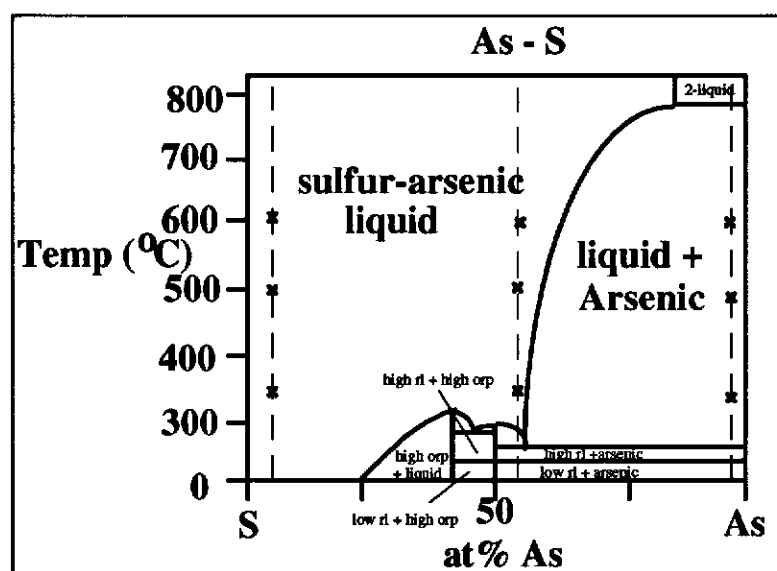
Figure 7.26 The conditions used for the arsenic and sulfur mixtures with gold (crosses) are shown on the arsenic and sulfur phase diagram.

At 340°C to 500°C, in the presence of liquid arsenic-sulfur mixtures, the reaction with gold was much slower. However, on examination under the SEM, fine

Table 7.3 - Arsenic and Gold Mixtures in Sealed Evacuated Vycor Tubes				
Sample	As (g)	Au (g)	Period (Hrs)	Temp (°C)
Vacch18	0.0967	0.1159	3	340
Vacch32	0.2014	0.1500		340grad
Vacch20	0.5548	0.4435		500
Vacch10	0.0905	0.1700		600
Vacch14	0.0962	0.0568	1	600
Vacch15	0.0459	0.0189	1	607

Table 7.4 - Arsenic, sulfur and Gold Mixtures in Sealed Evacuated Vycor Tubes				
Sample	As (At%) - S (At%) mixture (g)	Au (g)	Period (Hrs)	Temp(°C)
Vacch17	As 0.0944, S 0.0977	0.1253	3	340
Vacch22	As10-S90 0.1094	0.014	11	344
Vacch23	As90-S10 0.1986	0.0106	11	344
Vacch24	As52-S48 0.2013	0.0198	11	344
Vacch31	As52-S48	0.0132	12	425
Vacch21	As 0.0826, S 0.0013	0.0172		500
Vacch11	As 0.2211, S 0.0078	0.0557		600
Vacch25	As10-S90 0.1986	0.0119		615
Vacch26	As90-S10 0.1957	0.0158		615
Vacch27	As52-S48 0.1908	0.0176		615
Vacch28	As10-S90 0.2059	0.0242		650
Vacch29	As90-S10 0.1978	0.0226		650
Vacch30	As52-S48 0.1968	0.0194		650

globules of gold were observed (Figure 7.27). The presence of sulfur in the system appeared to retard the action of arsenic on gold at high temperatures. Sulfur has a much higher vapour pressure than arsenic and so would reduce the arsenic vapour concentration. Arsenic sulfide gaseous compounds may also have been present but these do not react with gold. The chemical composition of the liquids produced and whether any gold dissolved remains to be determined. The As:S ratio in the starting materials appeared to have little influence on whether gold reacted. However more gold was made mobile in arsenic rich starting materials.

The results can be explained by plotting the partial pressure of arsenic over arsenic metal (Figure 7.28). Shigematsu (1986) measured the arsenic vapour pressure over arsenopyrite and this is also plotted in Figure 7.28. The arsenic vapour pressure over arsenopyrite is much lower than over arsenic metal, being only detectable above 450°C (i.e. the temperature at which arsenopyrite starts to break down.) Over arsenic metal the arsenic vapour pressure drops off to negligible levels below a temperature of 310°C. No gold is mobile at this temperature or below where the arsenic vapour pressure is low. Also plotted in Figure 7.28 is the sulfur vapour pressure over sulfur. The sulfur vapour pressure exceeds 1 atmosphere pressure at ~400°C and hence, acts as a retardant to the action of arsenic.

7.3.2.7 The Role of Arsenic on Gold Mobility

The structural properties and atomic radii of arsenic and gold were evaluated to find some possible mechanism for arsenic reacting with gold. Gold consists of a face centred cubic lattice with atoms in 12 coordination which are held together by weak metallic bonding. Arsenic, on the other hand, is not represented as a simple packing of spheres because each atom is somewhat closer to three neighbours than to the remainder of the surrounding atoms. The bonding between the four closest atoms forming pyramidal groups is due to the covalent nature of arsenic bonds. Antimony which has a similar structure and falls in the same group in the periodic table as arsenic, forms $AuSb_2$ in nature, whereas gold and arsenic compounds with antimony
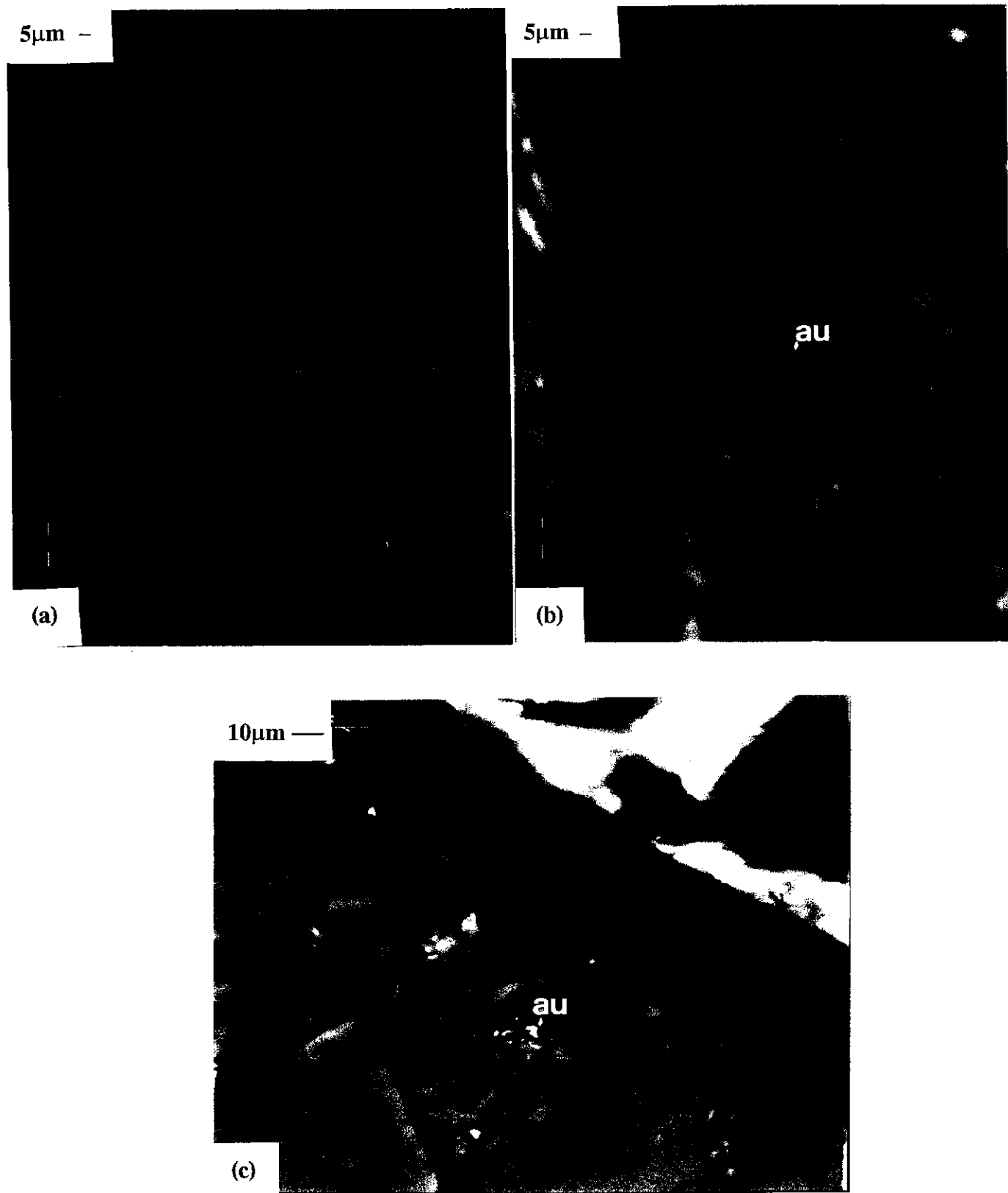
Figure 7.27 Scanning electron micrograph of fine globules of gold in the presence of liquid arsenic-sulfur mixtures after heating between 500°C and 340°C. (a)344°C- Au +As$_{90}$S$_{10}$ mixture, (b) 344°C - Au +As$_{52}$S$_{48}$ mixture, (c) 344°C - Au + As$_{10}$S$_{90}$ mixture
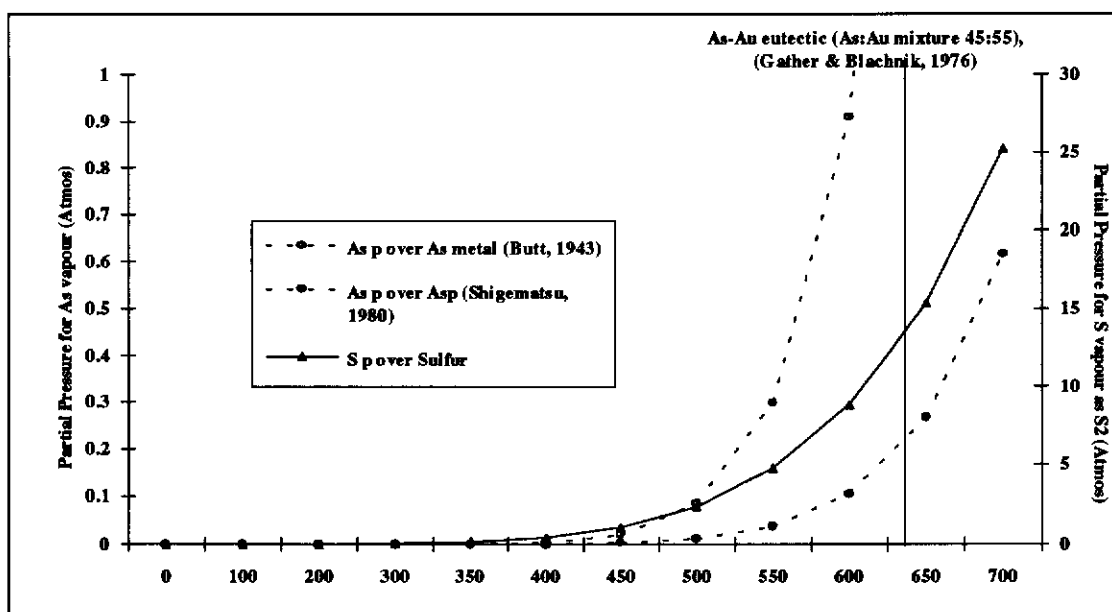
Figure 7.28 Plot of arsenic vapour pressure over arsenic metal and over arsenopyrite against temperature. Sulfur vapour pressure over sulfur is also plotted against temperature on the right axis.

are not known to exist. The atomic radius for gold is 1.44Å whereas for arsenic it is 1.25Å, so a direct substitution of arsenic in the gold structure or vice versa would appear impossible (Hurlbut and Klein, 1977). Copper which is known to form a limited solid solution with gold has an atomic radius of 1.28Å similar to arsenic and so arsenic may be taken up in the gold structure. However, copper has a similar structure to gold. At high temperatures thermal motion in the gold structure may allow accommodation of arsenic atoms. High temperature X-ray diffraction studies would be required to solve this problem.

7.3.3 Breakdown and Agglomeration of Gold in Arsenopyrite

From the previous experiments, the processes involved in the breakdown of arsenopyrite under thermal treatment can be described as follows. When thermal decomposition of arsenopyrite occurs, arsenic vapour is released within the particle and heat absorbed. The thermal decomposition starts around 470°C. The initial breakdown of arsenopyrite to pyrrhotite is topotactic along the b axis of the arsenopyrite structure. The pyrrhotite initially formed changes with temperature and composition depending on other localised reactions taking place. (e.g. exothermic reaction of $As_4 + O_2 \rightarrow As_2O_3$). The arsenic vapour then diffuses to the outer surface where it reacts with the ambient gases or, in an inert atmosphere, escapes. The consumption of arsenic at the surface of the grain drives the diffusion process and the endothermic decomposition is maintained by the transfer of either the combustion heat, from the reaction of arsenic with the ambient gases at the surface, or heat obtained from the furnace. During the breakdown of arsenopyrite some sulfur is released, in addition to arsenic vapour coming off. The amount of arsenic and sulfur in the vapour phase is governed by the type of arsenopyrite heated.

Arsenic-rich arsenopyrite decomposes before sulfur-rich arsenopyrite. The pyrrhotite formed has an Fe:S ratio less than one. The excess iron from the decomposing arsenopyrite forms a metallic iron phase, and the amount will depend upon the composition of the pyrrhotite phase. The excess iron probably migrates

along the vacant iron sites and where other ambient gases are present, probably diffuses to the surface of the grain and reacts with them. An arsenic and sulfur liquid interface as proposed by Swash and Ellis (1986) probably does not exist or is very minor, as any excess iron formed during the breakdown of arsenopyrite would be unstable and react with arsenic or sulfur atoms.

After all arsenic has been removed other ambient gases e.g. O_2 can back mix into the pyrrhotite pores formed and react with the pyrrhotite. Oxygen or other gas will react with any metallic iron phase to form an oxide or other compounds. In an inert atmosphere the product restabilises itself according to temperature. In this process more sulfur may be removed. The local conditions in the decomposing grain are different to those at the surface of the grain or the ambient conditions. The ambient conditions will drive the kinetics.

Mechanism of Gold Agglomeration

The mechanism for the agglomeration of gold in arsenopyrite can be considered in two processes:

(1) First Stage- Exsolution of Gold from Arsenopyrite Structure

In the first stage, gold on interstitial sites in arsenopyrite would be released on the first alteration of the arsenopyrite (e.g. to pyrrhotite). Gold is not soluble and exsolves out in pyrrhotite after arsenic is removed. With the preferential removal of arsenic rather than sulfur the gold is probably carried along with arsenic.

(2) Second Stage - Mobility of Gold

In the second stage it has been demonstrated that the presence of arsenic vapour is sufficient to make the gold mobile. Gold inclusions as well as gold liberated from solid solution migrate by the interaction of arsenic vapour condensing on the gold surface and reducing the melting point of gold (to as low as 500°C) and travels along crystallised pyrrhotite until all arsenic is removed. The amount of mobility would be determined by the surface area of the gold as well as the amount of arsenic

vapour present. Gold will be transported to low energy sites. The arsenic wets the gold surface. The globular shape of gold reduces the surface energy and this is the main cause of the agglomeration once the metal is mobilised. The sulfur vapour pressure is low and if it was too high, gold mobility would be retarded. An arsenic-sulfur liquid phase is not required to carry gold although it may play a role in low temperature systems where arsenic vapour pressure is low.

The presence of coarse gold with arsenopyrite reduces the decomposition temperature. In addition, the melting point of gold is reduced by the presence of arsenic at temperatures lower than those outlined in the As-Au phase diagram of Gather and Blachnik (1976) (shown in Figure 2.7).

7.3.4 Breakdown and Agglomeration of Gold in Pyrite

The previous considerations will also have some relevance to processes involved in the thermal decomposition and agglomeration of gold in pyrite.

In pyrite, gold replaces sulfur (Chapter 6). The behaviour of auriferous pyrite is slightly different from arsenopyrite because of the difference in atomic spacing and crystal chemistry of the two species (Swash and Ellis, 1986).

The decomposition of pyrite follows the endothermic reaction

$$2(1-x)FeS_2 \rightarrow 2Fe_{1-x}S + (1-2x)S_2$$
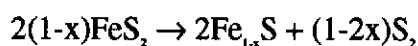
The presence of arsenic means the breakdown of pyrite follows the simplified reaction

$$2Fe(As,S)_2 \rightarrow 2Fe_{1-x}S + As_4 + S_2$$
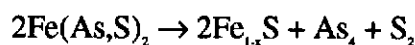
The stoichiometry of pyrrhotite and the presence of an iron phase was not determined. As with arsenopyrite, the gas phases of arsenic and sulfur vapour may combine to give As_4S_4 and As_2S_3 gas. Therefore little arsenic vapour would be present.

Several workers (e.g. Boyle, 1979) have reported that gold coalesces in pyrite at 600°C and possibly at 250°C. However, beam heating of single grains of auriferous

pyrite in the present studies never resulted in any gold agglomeration being observed under the TEM.

The presence of arsenopyrite breaking down with pyrite may help solid solution gold agglomerate in pyrite by the reaction of arsenic in the same way as in arsenopyrite. Alternatively, the arsenic in the pyrite structure may evolve first before sulfur and the local conditions may contain enough arsenic to agglomerate the gold. More studies are required on auriferous pyrites.

7.4 Summary and Conclusions

Using a combination of TG-DTA, EPMA, SEM and TEM techniques, the thermal behaviour of various stoichiometries of arsenopyrite and their decomposition products were studied to provide information on their role in gold mobility. It was found that the decomposition temperature varied slightly with different arsenopyrite stoichiometries. The auriferous arsenopyrite samples analysed had the lowest decomposition temperatures and this may be associated with the presence of gold.

The initial breakdown of arsenopyrite to pyrrhotite was found to be topotactic along the b axis of the arsenopyrite structure with the release of arsenic and some sulfur. The mechanism for this appeared to be a reconstruction process. The existence of an oriented interface of arsenopyrite altering to pyrrhotite probably occurs because of the low surface energy associated with the common structural plane. The excess iron, observed in the formation of pyrrhotite, probably migrates along the vacant iron sites in pyrrhotite and diffuses to the surface of the grain where it forms a metallic iron phase or reacts with ambient gases. The pyrrhotite initially formed changes with temperature and composition depending on other localised reactions taking place. At high pressures of arsenic vapour, an arsenic-sulfur liquid interface as proposed by Swash and Ellis (1986), does not exist or is insignificant.

Electron beam heating of auriferous arsenopyrite in a TEM clearly demonstrated the actual process of gold exsolution and agglomeration. This process was observed in both the auriferous natural and synthetic arsenopyrite samples.

Gold became mobile at the decomposition temperature of arsenopyrite for both synthetic and natural auriferous arsenopyrite samples. At low temperatures, the gold agglomerates as fine particles whereas at high temperatures the agglomerated gold was coarser. Consequently, increasing the temperature resulted in an increased rate of decomposition of arsenopyrite which in turn increased the amount of gold agglomeration. The presence of oxygen increased the rate at which arsenic was removed from the arsenopyrite structure (Chakraborti and Lynch, 1986). A rapid removal of arsenic by oxygen (to form As_2O_3) reduced the size of the gold agglomerated. The rate and the residence time of arsenic vapour within an altering arsenopyrite grain, clearly effected the size of the gold agglomeration. That is, increasing the arsenic vapour pressure increased the size of agglomerated gold and vice versa.

In addition, heating of arsenopyrite in the presence of coarse metallic gold, apart from reducing the decomposition temperature of arsenopyrite, resulted in gold mobilisation at temperatures as low as 500°C. These results revealed that apart from solid solution gold, metallic gold inclusions were also mobile.

The investigation of arsenic-sulfur and gold phase systems showed that the As:S ratio in the starting materials appeared to have little influence on the mobility of gold. However, more gold was mobile in arsenic-rich starting materials at temperatures from 340°C to 500°C. The presence of sulfur in the system appeared to retard the action of arsenic on gold at higher temperatures. In addition, in As-Au mixtures the melting point of gold was less than the 630°C observed by Gather and Blachnik (1976).

Gold did not readily agglomerate in pyrite in the same way as in arsenopyrite. The lack of arsenic and high concentration of sulfur evolving during the breakdown of pyrite tended to reduce arsenic and gold interactions. However, more studies are required to elucidate the behaviour of this system.

The mechanism for the agglomeration of gold in arsenopyrite can be considered in two successive processes. In the first stage, the reconstruction process

involved in arsenopyrite breaking down to pyrrhotite results in interstitial gold being released. Gold on the iron sites in arsenopyrite may remain locked in the pyrrhotite structure. However, gold is relatively insoluble in pyrrhotite. In addition, arsenopyrite does not transform to a low (S-rich) or high (As-rich) temperature polymorph by heat treatment and so, gold will only be liberated when arsenopyrite is chemically altered, for example, to pyrrhotite. The arsenic to sulfur ratio in arsenopyrite does not have a major effect on the breakdown, or on gold mobility. However, the presence of gold affects the breakdown of arsenopyrite by decreasing its decomposition temperature. In the second stage, if the concentration of arsenic vapour is sufficiently high, gold inclusions as well as gold liberated from solid solution will travel along the crystallised pyrrhotite, combining with other gold until all arsenic is removed. The residence time of arsenic determines the size of the gold particles agglomerated. At elevated temperatures gold is readily soluble in arsenic and this lowers the melting point of gold. The mobility of gold is determined by its surface area as well as by the arsenic vapour concentration. Gold will be transported to low energy sites. An arsenic-sulfur liquid phase is not required to carry gold although it may play a role in low temperature systems with low arsenic vapour pressure.

Chapter 8

8.0 SUMMARY AND CONCLUSIONS

The present studies were aimed at a more detailed resolution of the structure of arsenopyrite and to a lesser extent pyrite, the form and location of gold in these minerals, and the mechanisms of gold mobilisation and agglomeration during thermal treatment.

Before studies on the form and mobility of gold could be carried out, a number of aspects of the stoichiometry and structure of arsenopyrite which were inadequately defined had to be evaluated. Consequently, the composition and crystal structure of a number of natural arsenopyrites varying in stoichiometry were analysed.

Detailed microchemical analysis by EPMA of various natural arsenopyrites showed no iron deficiency, casting doubt on the possible substitution of arsenic on iron sites, inferred by some workers. The samples analysed contained little gold, except for the Sheba sample, which contained high concentrations largely as inclusions. An examination of the possible substitution of gold on iron sites in the arsenopyrite structure was inconclusive. Similarly, no definitive conclusion could be reached with respect to the possible substitution of antimony on either iron or arsenic sites.

The crystal structures of arsenopyrites with varying compositions were investigated by X-ray diffraction and convergent beam electron diffraction studies and were refined using the Rietveld method. The presence of one mirror in the whole pattern along the a and c axes, as well as the occurrence of dark bars in the (0k0), (h0l) and (00l) reflections of [001] and [101] CBED patterns for k, l and h+l odd, combined with the observations of a centred rectangular mesh of reflections in the ZOLZ in both patterns, identified the monoclinic point group 2/m and the space group $P2_1/c$ for all arsenopyrite stoichiometries. In addition, the lattice parameters and axial

ratios agreed well with measurements obtained from XRD patterns. Structural analysis of stoichiometric arsenopyrite confirmed Buerger's (1936) arsenopyrite structure as monoclinic P2$_1$/c. All stoichiometries crystallised in this space group and changes observed in the structures by single crystal studies (e.g. Fuess *et al.,* 1987) were due to twinning. Cobalt or other impurities are not required to stabilise this structure for some arsenopyrite compositions, as has been suggested in the literature. In addition, arsenopyrite with a low As:S ratio was not triclinic, contrary to the conclusion of Morimoto and Clark (1961).

An increase in the arsenic to sulfur ratio resulted in an increase in the unit cell dimensions, in agreement with the conclusions first reported by Morimoto and Clark (1961). In the present study, the change in unit cell volume was found to be associated with changes in the iron-centred octahedra, consisting of a slight compression in the (101) direction of the monoclinic cell and an expansion in the (101) plane, together with a slight alteration to the octahedral tilt. Any other differences in structure were too small to be detected. There also appeared to be differences in structure which were not related to stoichiometry as TEM studies often revealed strain or disorder.

Twinning and antiphase domains provide mechanisms for some arsenic and sulfur interchange. Distortions observed in some of the arsenopyrite crystals are possibly due to displacement of the octahedra in the crystal caused by fine scale twinning and antiphase boundaries. However, the presence of clear CBED patterns conforming to the space group P2$_1$/c indicated that twinning is independent of composition. There was no obvious relationship between variation in stoichiometry and structure of arsenopyrite which could provide information as to possible substitution of gold in its structure. However displacements caused by twinning or disorder may help to incorporate gold either on sites or on interstitial sites.

Because of the uncertainty in the abundance of solid solution gold in the natural arsenopyrites available and to provide information on the mechanism by which gold is taken up into the arsenopyrite structure, experiments were carried out to

produce synthetic arsenopyrites containing gold in solid solution from appropriate concentrations of arsenic, sulphur and iron. Various methods were attempted to incorporate gold into the structure of arsenopyrite. These included dry synthesis, an iodine vapour transport method and hydrothermal synthesis.

Metallic gold (Au^0) did not react strongly with arsenopyrites above 500°C, as demonstrated by the sharp boundaries observed between crystallised arsenopyrite and gold in the dry synthesis work. The presence of metallic gold, however, reduced the breakdown temperature at which arsenopyrite decomposed to pyrrhotite and löllingite, as observed by Clark (1960).

Only the samples synthesised from mixtures of iron oxides, arsenic and sulfur under hydrothermal conditions, were successful in incorporating gold in solid solution. Solid solution gold was confirmed by [197]Au Mössbauer data which showed that gold was mostly bonded whether samples were prepared with or without hydrochloric acid in the starting materials. Synthetic auriferous arsenopyrite consisted of acicular grains ranging in size from $2\mu m$ to $50\mu m$. The crystals were mainly euhedral and grew as aggregrates. Analysis of composition by EPMA showed a possible slight iron deficiency in some of the auriferous arsenopyrite grains, but the errors were too high to provide conclusive evidence of gold substitution on the iron sites as proposed by Johan *et al.* (1989).

High gold concentrations in auriferous arsenopyrites synthesised in $HCl-H_2O$ solution were associated with high arsenic to sulfur ratios. In contrast, in arsenopyrite synthesised from dry mixtures of goethite, arsenic and sulfur, the gold concentration appeared to be independent of the As:S ratio and the crystals tended to be more homogeneous and slightly sulfur-rich. The contrast to arsenopyrite synthesised with $HCl-H_2O$ solutions may be related to the form of the gold species in solution, i.e. the presence of $AuCl^{2-}$ species in $HCl-H_2O$ solutions and $Au(SH)^0$, or possibly $Au(SH)^{2-}$, in pure aqueous solutions. Thus, it is possible that under high saline conditions the distribution of gold in arsenopyrite is different from that in low saline conditions for hydrothermal gold deposits.

Structural analyses of the various synthetic auriferous arsenopyrite crystals showed similarities with the natural arsenopyrite samples. However, the unit cell dimensions were larger and some crystals exhibited a loss in symmetry. Rapid crystallisation along the b axis caused some disorder resulting in many crystals exhibiting displacement faults. Shifts in the octahedra resulted in the reordering of the arsenic and sulfur atoms along the displacement plane. The presence of these faults may contribute to high concentrations of gold in the structure. Consequently, stoichiometry alone may have no effect on gold uptake in arsenopyrite.

Pyrite formed during some of the synthesis experiments was also found to contain solid solution gold, and was examined to provide detailed information on the nature of the solid solution process. For both natural and synthetic pyrites examined, the structure appeared not to deviate from cubic pyrite with space group Pa3. Twinning was not observed in CBED patterns. Measured SAED patterns of both non-auriferous and auriferous pyrite showed no significant change in cell dimensions. In addition, the high arsenic content appeared not to have affected cell dimensions. This demonstrated that the structure of pyrite does not change with addition of impurities and that the presence of pseudo-cubic pyrite reported in the literature, may not be controlled by chemical composition. Deviations from the pyrite Pa3 structure may, however, be controlled by temperature as suggested by Bayliss (1977, 1989) and Fleet *et al.* (1989).

To determine the specific location of the gold in the structures, suitable natural and synthetic arsenopyrite and pyrite compounds were examined in detail using Atomic Location by Channelling Enhanced Microanalysis (ALCHEMI). The results demonstrated that some gold and all of the arsenic occurs on the sulfur sites in pyrite and no arsenic occurs on the iron sites. Assuming that a charge exists on the metal and anion pairs, pyrite can be written as $[Fe]^{2+}[S_2]^{2-}$. The presence of arsenic in the structure will result in some anion pairs such as $[AsS]^{3-}$ accompanied, perhaps by Fe^{3+} ions instead of Fe^{2+}. The existence of these anion pairs has been inferred (Tossell *et al.*, 1989). Gold on the sulfur sites may occur as Au^-, Au^0 or Au^+, most probably

combined as an anion pair $[AuAs]^{2-}$ or alternatively as $[AuS]^{-}$. The presence of $[AsS]^{2-}$ pairs would be required to balance the charge of the Fe^{2+} ions for $[AuS]^{-}$ pairs. This would explain the strong association of gold with arsenic-rich pyrites (Cook and Chryssoulis, 1990). Alternatively, the excess charge resulting from the presence of arsenic and gold on the sulfur sites may be compensated for by vacancies in the sulfur sites. Slight sulfur deficiencies in the pyrite structure have been reported by Finklea *et al.* (1976).

The ALCHEMI results for arsenopyrite generally showed no correlation of gold with either the iron or the arsenic-sulfur combined sites. Slight evidence of gold on the iron sites was observed in some data based on the ratio method. These results came from experiments with [101] zone arsenopyrite crystals containing little distortion in their structure. In [101] zone data extensive distortions in the b axis indicated the presence of gold in defects of the arsenopyrite structure. Collectively, the results from EPMA, ALCHEMI and gold Mössbauer spectroscopy imply that some gold is on interstitial sites or in defects in the structure as well as some on iron sites, but not present as fine inclusions. Image contrast and selected-area diffraction also showed no gold inclusions in the crystals studied. Interstitial gold in arsenopyrite is probably situated in gaps between the iron-centred octahedra. The closest bond lengths for iron, arsenic and sulfur atoms to the interstitial gold site were, however, smaller (2.06, 2.11Å,) than the average gold-arsenic (2.386Å) and gold-sulfur (2.290Å) bond lengths cited in the literature. Therefore, to accommodate gold in these positions, some iron, arsenic and sulfur sites may be vacant, or the sites modified by twinning or other defects.

'Invisible' gold is often associated with chemically zoned arsenic rich regions in natural arsenopyrite and pyrite grains (Cook and Chryssoulis, 1990), which reflect non-equilibrium conditions and rapid crystallisation. It therefore seems likely that during rapid crystallisation, gold atoms are trapped at interstitial sites or point defects in the crystal structure, particularly in arsenopyrites. It is possible that in well-crystallised arsenopyrite some gold may be taken up on the iron sites. The difference

in the forms of the gold in pyrite and arsenopyrite is probably related to the differences in crystal structure. Arsenopyrite would be more readily able to accommodate gold in dislocations in its structure than would pyrite.

The thermal behaviour of arsenopyrite and its relationship to the mobility and agglomeration of both solid solution and metallic gold, were examined under different ambient conditions. Using a combination of TG-DTA, EPMA, SEM and TEM techniques, the thermal behaviour of various arsenopyrites and their decomposition products, were studied to provide information on their role in determining gold mobility. Although the thermal decomposition of arsenopyrite to pyrrhotite is similar in all cases, the decomposition temperature increased slightly as the arsenic and sulfur ratio approached stoichiometry from both directions. The auriferous arsenopyrite samples had the lowest decomposition temperatures. The presence of gold in the arsenopyrite structure may have lowered the decomposition temperature of arsenopyrite.

The initial breakdown of arsenopyrite to pyrrhotite was found to be topotactic along the b axis of the arsenopyrite structure with the release of arsenic and some sulfur. The mechanism for this appeared to be reconstructive. The orientation relationship probably occurs because of the low surface energy associated with the common structural plane. The pyrrhotite formed had Fe:S ratios of less than one, leaving an excess of iron in the mass balance. The excess iron probably migrates along the vacant iron sites in pyrrhotite and diffuses to the surface of the grain where it forms a metallic iron phase or reacts with ambient gases. The pyrrhotite initially formed changed composition with temperature depending on other localised reactions taking place. There was no evidence of an arsenic-sulfur liquid interface as proposed by Swash and Ellis (1986).

The behaviour of gold in the presence of arsenopyrite was also studied. Direct evidence for the exsolution and agglomeration of gold in arsenopyrite on thermal treatment was observed. Gold was visually recorded exsolving from the arsenopyrite structure and agglomerating as liquid metal globules on boundaries of

pyrrhotite as the arsenopyrite was chemically altered during thermal treatment under the TEM electron beam.

Gold became mobile at the decomposition temperature of arsenopyrite for both synthetic and natural auriferous samples. At low temperatures, the gold agglomerated as fine particles whereas at high temperatures the agglomerated gold was coarser. Increasing temperature increased the rate of decomposition of arsenopyrite and the degree of gold agglomeration. The presence of oxygen increased the rate at which arsenic was removed from the arsenopyrite structure. However, the consumption of arsenic by oxygen (to form As_2O_3) reduced the size of gold agglomerated. The rate of removal and the residence time of arsenic vapour within an altering arsenopyrite grain clearly affected the size of the gold agglomeration. That is, increasing the arsenic vapour pressure increased the size of agglomerated gold and vice versa.

In addition, heating arsenopyrite in the presence of coarse metallic gold, apart from reducing the decomposition temperature of arsenopyrite, resulted in gold mobilisation at temperatures as low as 500°C. These results indicate that as well as gold from solid solution, metallic gold inclusions were also mobile.

The investigation of arsenic, sulfur and gold phase systems showed that gold was mobile in arsenic-rich starting materials at temperatures from 340°C to 500°C. The presence of sulfur in the system appeared to retard the action of arsenic on gold at higher temperatures (~500°C). In addition, in As-Au mixtures, the melting point of gold was lower than the 630°C observed by Gather and Blachnik (1976).

Gold did not readily agglomerate in pyrite in the same way as in arsenopyrite, because of the deficiency of arsenic. The high concentrations of sulfur evolving during the breakdown of pyrite reduced arsenic and gold interactions.

The agglomeration of gold in arsenopyrite has been shown to occur in two stages. In the first stage, arsenopyrite breaks down to pyrrhotite releasing all solid solution gold, as gold is relatively insoluble in pyrrhotite. Arsenopyrite does not readily undergo a transformation to a lower or higher temperature polymorph and so

gold will only be liberated when arsenopyrite is chemically altered, e.g. to pyrrhotite. The presence of gold as inclusions or in solid solution in arsenopyrite, decreases the decomposition temperature of the host arsenopyrite. Gold is carried along with the arsenic which evolves before sulfur. In the second stage, if the arsenic vapour pressure is sufficient, gold inclusions as well as gold liberated from solid solution, will migrate along the pyrrhotite combining with other gold until all arsenic is removed. The process is facilitated because the arsenic wets the gold surface forming a low temperature eutectic. The mobility of the gold is determined by its surface area as well as the concentration of arsenic vapour present. The residence time of arsenic determines the size of the gold particles agglomerated. An arsenic-sulfur liquid phase is not required to carry gold although it may play a role in low temperature systems where the arsenic vapour pressure is low.

Industrial Implications

High gold contents in solid solution may still be expected in low As:S ratio arsenopyrite despite the general observation in the literature that high solid solution gold concentrations are normally found in arsenopyrite containing high arsenic to sulfur ratios. Wider studies on arsenopyrite ore deposits may resolve this possibility. Both gold in solid solution and that present as inclusions, will be made mobile by arsenic vapour. The present studies have demonstrated the importance of the rate and residence time of arsenic as the key to the removal of gold. Manipulation of these factors should enhance gold extraction in pyrometallurgical practice. Invisible gold in arsenopyrite may be released by a simple heat treatment.

Areas of further work

An examination of the microstructure of gold free arsenopyrite containing a high As:S ratio using HRTEM and comparison with the microstructure of arsenopyrite with a low As:S ratio, may reveal the reason for uptake of impurities such as gold and also provide additional information on the twinning process.

Comparison of both natural and synthetic auriferous arsenopyrites by HRTEM might provide direct evidence of how rapid crystallisation of arsenopyrite occurred and explain the existence of gold in interstitial sites observed in the microstructure. In addition, the question as to whether there are vacancies in the structure of arsenopyrite and pyrite may also be resolved.

Recent developments have enabled an environmental cell pole piece to be installed in some TEM equipment, so that the temperature and gas composition around the sample can be changed and controlled (Doole *et al.*, 1992). It would be valuable to be able to monitor the gold agglomeration process in arsenopyrite by changing the conditions to suit metallurgical operations (e.g. under SO_2 and O_2 atmosphere conditions).

The reactions of arsenic with gold and its effect on gold mobility need to be examined in greater detail. This could be carried out by studying the precipitation of arsenic on gold by LEED and XPS techniques. Such studies would provide information on whether arsenic adopts a preferred orientation to the gold surface, what type of bonding occurs between arsenic and gold, and the amount of solid solution which may take place in either species. The eutectic temperature should also be confirmed.

The limited studies on the pyrite structure carried out here are worthy of considerable extension.

More detailed work is required on the existence of gold complex species in solution at high temperatures.

9.0 REFERENCE LIST

Albinati, A. and Willis, B.T.M. (1982) The Rietveld Method in Neutron and X-ray Powder Diffraction. *J. Appl. Crystal.,* **15**, 361-374.

Amosov, G.M. and Gureev, V. (1970) Experimental Study of Gold Distribution in Sulfides. *Dokl. Akad. Nauk SSSR,* **282**. 1453-1455.

Amosov, G.M., Gureev, V., Tikhomirova, V.I and Konyshok, A.A. (1975) *cited by* Boyle (1979).

Anderson, G.M. and Burnham, C.W. (1967) Reaction of Quartz and Corundum with aqueous Chloride and Hydroxide Solutions at High Temperatures and Pressures. *Amer. J. Sci.,* **265**, 17-27.

Baerlocher, Ch (1986) Zeolite Structure Refinements using Powder Diffraction Data. *Zeolites,* **6**, 325-333.

Bakken, B.M., Hochella, M.F. jr, Marshall, A.F. and Turner, A.M. (1989) High-Resolution Microscopy of Gold in Unoxidized Ore from the Carlin Mine, Nevada. *Econ. Geol.,* **84**, 171-179.

Ballantyne, J.M. and Moore, J.N. (1988) Arsenic Geochemistry in Geothermal Systems. *Geochim. Cosmochim. Acta,* **52**, 475-483.

Bancroft, G.M. and Hyland, M.M. (1990) Spectroscopic Studies of Adsorption /Reduction Reactions of Aqueous Metal Complexes on Sulfide Surfaces, in Hochella, M.F. and White, A.F. (eds.) *Reviews in Mineralogy,* 13, Mineral-Water Interface Geochemistry, 511-558, Amer. Min. Soc., Washington D.C.

Barton, P. B. jr (1969) Thermochemical Study of the System Fe-As-S. *Geochim. Cosochim. Acta,* **33**, 841-857.

Batterman, B. (1969) Detection of Foreign Atom Sites by their X-ray Fluoresence Scattering. *Phys. Rev. Letters,* **22**, 703.

Bayliss, P. (1977) Crystal Structure Refinement of a Weakly Anisotropic Pyrite. *Amer. Mineral.,* **62**, 1168-1172.

Bayliss, P. (1989) Crystal Chemistry and Crystallography of Some Minerals within the Pyrite Group. *Amer. Mineral.,* **74**, 1168-1176.

Bayliss, P. and Stephenson, N.C. (1968) The Crystal Structure of Gersdorffite (III), a Distorted and Disordered Pyrite Structure. *Mineral. Mag.,* **36**, 940-947.

Belevantsev, V.I., Peshchevitskiy, B.I. and Shamovskaya, G.I. (1981) Gold(I) Sulfide Complexes in Aqueous Solution. *cited by* Seward (1982).

Berglund, S. and Ekstrom, T. K. (1980) Arsenopyrite and Sphalerite as T-P indicators in Sulfide Ores from Northern Sweden. *Miner. Deposita*, **15**, 175-187.

Bennett, C.E.G and Graham, J. (1977) New Observations on Natural Pyrrhotites. Part III Thermomagnetic Experiments. *Amer. Mineral.*, **65**, 800-807.

Boiron, M. C., Cathelineau, M. and Trescases, J. J., (1989) Conditions of gold-bearing arsenopyrite crystallization in the Villeranges Basin, Marche-Combrailles Shear Zone, France: A Mineralogical and fluid inclusion study. *Econ. Geol.*, **84**, 1340-1362.

Boisen, M.B. jr and Gibbs, G. V. (1985) Mathematical Crystallography, in Ribbe, P.H. (ed.) *Reviews in Mineralogy*, 15, 406, Amer. Min. Soc., Washington D.C.

Borrmann I. (1941) *cited by* Krishnan (1988).

Boyle, R. W. (1979) The Geochemistry of Gold and its Deposits. *Geol. Sur. Can. Bull.*, **280**, 20-30.

Bragg, W.L. (1913) The Analysis of Crystals by the X-ray Spectrometer. *Proc. Roy Soc.*, **A89**, 468-469.

Brostigen, G. and Kjekshus, A. (1969) Redetermined Crystal Structure of FeS_2 (pyrite). *Acta Chem Scand.*, **23**, 2186-2188.

Brostigen, G. and Kjekshus, A. (1970a) On the Relationships between the Structure types Pyrite, Marcasite and Arsenopyrite. *Acta Chem. Scand.*, **24(8)**, 2983-2992.

Brostigen, G. and Kjekshus, A. (1970b) Bonding Schemes for Compounds with the Pyrite, Marcasite and Arsenopyrite Type Structures. *Acta Chem. Scand.*, **24(8)**, 2993-3012.

Buerger M.J. (1931) The Crystal Structure of Marcasite. *Amer. Mineral.*, **16**, 361-395.

Buerger, M. J. (1936) The Symmetry and Crystal Structure of the Minerals of the Arsenopyrite Group. *Z Krist.*, **95**, p83-113.

Buerger, M. J. (1937) Interatomic Distances in Marcasite and Notes on the Bonding in Crystals of Löllingite, Arsenopyrite, and Marcasite types. *Z Krist.*, **94**, 425-438.

Buerger M.J. (1945) The Genesis of Twin Crystals. *Amer. Mineral.*, **30**, 469-482.

Burg, G. (1930) Natur in Den Pyriten Nicht Sichtbar Enthalten Golde. *Zeitschr. Prakt. Geologie*, **43**, 17-26.

Buseck, P.R. and Self, P. (1992) Minerals and Reactions at the Atomic Scale: Transmission Electron Microscopy, in Buseck P.R. (ed.) *Reviews in Mineralogy*, 27, 123-140, Mineralogical Society of America, Washington D.C.

Butts, A. (1943) *Metallurgical Problems*. 2nd edition .McGraw-Hill Book, New York.

Buxton, B.F., Eades, J.A. Steeds, J.W. and Rackham, G.M. (1976) The Symmetry of Electron Diffraction Zone Axis Patterns. *Phil. Trans. Royal Soc.*, London **A281**, 171-194.

Cabri, L.J. (1988a) *The Role of Mineralogy in Gold Metallurgy.* CANMET, Rep. MSL, 88-51.

Cabri, L.J. (1988b) *New Developments in Determinations of the Distribution of Precious Metals in Ore Deposits.* Proc. Seventh Quadrennial IAGOD Symp. E. Schweizerbart'sche Verslag, Stuttgart, 149-154.

Cabri, L.J. and Chryssoulis, S.L. (1990) Genesis of the Olympias Carbonate Hoted Pb-Zn (Au,Ag) Sulfide Ore Deposit, Eastern Chalkidiki Peninsula, Northern Greece- a Discussion. *Econ. Geol.*, **85**, 651-652.

Cabri, L.J., Chryssoulis, S. L., de Villiers, J. P. R., Laflamme, J. H. G. and Buseck, P. R. (1989) The Nature of 'Invisible' Gold in Arsenopyrite. *Can. Mineral.*, **27**, 353-362.

Cabri, L.J., Harris, D.C., Steward, J.M. and Roland, J.F. (1970) Willyamite Redefined. *Proc. Aust. Inst. Mining Metallurgy*, **233**, 95-100.

Caglioti, G., Paoletti, A. and Ricci, F.P. (1958) Choice of Collimators for a Crystal Spectrometer for Neutron Diffraction. *Nucl. Inst.*, **3**, 223-228.

Campa-Vineta, I.A. (1980) Deformation of Sulfides. *Chem Abstract* CA94(22):135984f.

Cardile, C.M., Cashion, J.D., McGrath, A.C., Renders, P. and Seward, T.M. (1993) [197]Au Mössbauer Study of Au_2S and Gold Adsorbed onto As_2S_3 and Sb_2S_3 Substrates. *Geochim Cosmochim. Acta*, **57**, 2481-2486.

Cathelineau, M. , Boiron, M. C., Holliger, Ph. and Marion, Ph. (1988) Gold-rich Arsenopyrites: Crystal-chemistry, Gold location and State, Physical and Chemical Conditions of Crystallization. *Bicentennial Gold 88*, Melbourne, 235-240.

Chakraborti, N. and Lynch, D.C. (1983) Thermodynamics of Roasting Arsenopyrite. *Metal. Trans.*, **14B**, 239-245.

Chakraborti, N. and Lynch, D.C. (1985) Thermodynamic Analysis of the As-S-O Vapour System. *Can. Metal. Q.*, **24(1)**, 39-45.

Champness, P.E. (1987) Convergent Beam Electron Diffraction. *Mineral Mag.*, **51**, 33-48.

Chang, R. and Zang, J. (1991) Studies of-Gold Poor and Lattice-Gold in some Pyrites. *J. Cent. - South Inst. Min. Metall.*, **22(1)**, 361.

Cheetham, A.K. and Taylor, J.C. (1977) Quantative analysis of Flyash by SIROQUANT. *J.Solid State Chem.*, **21**, 253-275.

Chern, D., Howes, A. and Jacobs, M.H. (1973) Characteristic X-ray Production in Thin Crystals. Z Naturforsch, 28a, 565-571.

Chryssoulis, S.L., Cabri, L.L. and Salter, R.S. (1987) Direct Determination of Invisible Gold, in Salter, R.R, Wyslouzil, D.M. and McDonald, G.W. (eds.) Refractory Sulfide Ores Prog Int. Symp. on Gold Metallurgy. 1. Proc. Metal. Soc. of the Can Inst. Min. Metal., 235-244.

Chryssoulis, S.L. (1989) Ion Probe Microanalysis of Gold in Common Sulfide Minerals and Implication for Enhanced Gold Recovery from Refractory Gold Ores. Surface Science Western Univ. Western Ontario, CANMET Contract Rep. 79037-01-ss, 380.

Chryssoulis, S.L. (1990) Detection and Quantification of "Invisible" Gold by Microprobe Techniques, In Hausen, D.M. (ed.) Gold 90, Salt Lake City, SME-AIME, Littleton, Co USA, 323-332.

Chryssoulis, S.L. and Cabri, L.J. (1990) The Significance of Gold Mineralogical Balances in Mineral Processing. Inst. Min. Metal. (London) Trans. Sec., C99, C1-C10.

Chryssoulis, S. L., Cabri, L. J. and Lennard, W. (1989) Calibration of the Ion Microprobe for Quantitative Trace Precious Metal Analyses of Ore Minerals. Econ. Geol., 84, 1684-1689.

Clark, L.A. (1960) The Fe-As-S system: Phase relations and applications. Econ. Geol., 55, Pt I: 1345-1381, Pt II: 1631-1652.

Cliff, G. and Lorimer, G.W. (1972) Determination of k-factors in Analytical Electron Microscopy. Proc. 5th European Congress on Electron Microscopy, Institute of Physics, Bristol, 140.

Cobble, J.W. (1985) A theory on Trace Arsenic in Geothermal Fluids. Electric Powder Res. Inst EPRI Ap4214 Project 1525-6. cited by Ballantyne and Moore (1988).

Cook, N.J. (1990) Mineralogical Examination of Gold-bearing Samples. CIMM Bulletin, 83(94), 51-55.

Cook, N. J. and Chryssoulis, S. L. (1990) Concentrations of "Invisible Gold" in Common Sulphides. Can. Mineral., 28, p1-16.

Cowan, M.L., Golovchenko, J.A. and Robbins, M.F. (1980) X-ray Standing Waves at Crystal Surfaces. Phys. Rev., 44, 1680-1683.

Cowley, J.M. (1964) The deviation of Structural Information from Absorption effects in X-ray Diffraction. Acta Cryst., 17, 33-45.

Cowley, J.M. (1978) Electron Diffraction 1927-1977, Institute of Physics, Bristol and London, 156.

Doole, R.C., Parkinson, G.M., Hutchison, J.L., Goringe, M.J. and Harris, P.J.F. (1992) A High Resolution, Analytical in-situ Gas Reaction Cell. JEOL NEWS vol. 30E (2), 14-18.

Dowty, E. (1989) ATOMS: *A Computer Program for Displaying Atomic Structures,* IBM version 1.0. Software for Display of Crystal Structures on Personal Computers (available from E. Dowty, 521, Hidden Valley Rd, Kingsport, TN 37663, U.S.A.).

Duncumb, P. (1962) Enhanced X-ray Emission from Extinction Contours in a Single Crystal Gold Filament. *Phil. Mag.,* **7**, 2101.

Eades, J.A., Christenson, K.K. and Andresen, M.L. (1990) Is there a Non-channelling Orientation? in Peachy, L.D. and Williams, D.B. (ed.) Proc. XII Int. Congr. Electron Microscopy. 412-413.

Finklea, S.L.III, Cathey, L.L. and Amma, E.L. (1976) Investigation of the Bonding Mechanism in Pyrite using the Mössbauer Effect. *Acta Crystallogr.,* **A32**, 529-537.

Fleet, M.E. (1970) Structural Chemistry of Marcasite and Pyrite Type Phases. *Z. Krist.,* **142**, 332-346.

Fleet, M.E., Maclean, P.J. and Barbier, G. (1989) Oscillatory-Zoned As-bearing Pyrite from Stratabound and Stratiform Gold Deposits: an Indicator of Ore-fluid Evolution. *Econ. Geol., Gold '88 Monograph.*

Fleet, M.E., Chryssoulis, S.L., Maclean, P.J. , Davidson, R. and Weisener, C.G. (1993) Arsenian Pyrite from Gold Deposits: Au and As Distribution Investigated by SIMS and EMP, and Colour Staining and Surface Oxidation by XPS and LIMS. *Can. Mineral.,* **31**, 1-17.

Francis, C.A, Fleet, M.E., Misra, K. and Craig, J.R. (1976) Orientation of Exsolved Pentlandite in Natural and Synthetic Nickeliferous Pyrrhotite. *Amer. Mineral.,* **61**, 913-920.

Friedl, J., Wagner, F.E., Sawicki, J.A., Harris, D.C., Mandarino, J.A. and Marion Ph. (1992) [197]Au, [57]Fe and [121]Sb Mössbauer Study of Gold Minerals and Ores. *Hyperfine Interactions,* **70**, 945-948.

Fuess, H., Kratz, T., Topel-Schadt, J. and Miehe, G. (1987) Crystal Structure Refinement and Electron Microscopy of Arsenopyrite. *Z. Kristallogr.,* **179**, 335-346.

Fushimi, S. and Webster, A. H. (1969) Growth of Arsenopyrite Single Crystals by the Closed-Tube Iodine Vapor Transport Technique. *Can. Mines Br. Res. Rep.,* **R 216**, 18.

Gadet, M. and Pouradier, J. (1972) Hydrolyse des Complexes del'or(i). *C.R. Acad. Sci. Paris,* **275**, 1061-1064.

Gasparrini, C. (1983) The Mineralogy of Gold and its Significance in Metal Extraction. *CIM Bulletin*, **76(851)**, 144-153.

Gather, A. and Blachnik, M. (1976) The System Gold-Arsenic. *Z. Metallkde.*, **67(3)**, 168-169.

Giese, R.F. and Kerr, P.F. (1965) The Crystal Structure of Ordered and Disordered Cobaltite. *Amer. Mineral.*, **50**, 1002-1014.

Gjonnes, J. and Hoier, R. (1971) Structure Information from Anamalous Absorption Effects in Diffuse Scattering of Electrons. *Acta Cryst.*, **A 27**, 166-174.

Gjonnes, J. and Moodie, A.F. (1965) Extinction Conditions in the Dynamic Theory of Electron Diffraction. *Acta Cryst.*, **19**, 65-67.

Glyuk, D.S. and Khlebnikova, A.A. (1982) Gold Solubility in Water, HCl, HF and Sodium and Potassium Chloride, Fluoride, Carbonate and Bicarbonate Solutions at a Pressure of 1000 Kg/cm^2. *Dokl. Akad. Nauk*, **254**, 190-194.

Goldstein, J.J (1979) Principles of Thin Film X-ray Microanalysis, in Hren, J.J. Goldstein, J.J. and Joy, D.C. (eds.) *Introduction to Analytical Electron Microscopy* Ch3, London, 83-120.

Goodenough, J.B. (1972) Energy bands in TX$_2$ compounds with Pyrite, Marcasite, and Arsenopyrite Structures. *J. Solid State Chem.*, **5**, 144-152.

Goodman, P. (1975) A Practical Method of Three Dimensional Space Group Analysis Using CBED. *Acta Cryst.*, **A31**, 804-810.

Graham, J., Just, J., Dunn, J.G., Nguyen, G. and Avraamides, J. (1988) " Gold Mineralogy", Gold Metallurgy- The Bendigo Conference, Aus. I. M. M., Melbourne (Aust.) 5.

Graham, J., Robinson, B. W. and Walker, R. K. (1989) Gold in Arsenopyrite. *Mineralogy-Petrology Symposium*, Aus. I M. M. Sydney (Aust.), 55-57.

Griffin, W.L., Ashley, P.M., Ryan, C.G., Sie, S.H. and Suter, G.F. (1991) Pyrite Geochemistry in the North Arm Epithermal Ag-Au Deposit, Queensland, Australia: A Proton microprobe Study. *Can. Mineral.*, **29**, 185-198.

Grigor'yeva, T. A. and Sukneva, L. S. (1981) Effects of Sulfur and of Antimony and Arsenic Sulfides on the Solubility of Gold. *Trans. Geokhimiya*, **10**, 1534-1540.

Grimsey, E. J. and Aylmore, M. G. (1990) Roasting of Arsenopyrite, in Hausen, D.M. (ed.) *Gold 90*, Salt Lake City, SME-AIME, Littleton, Co USA, 14.

Groves, D.I. and Foster, R.P. (1992) Archaean Lode Gold Deposits, in Foster, R.P. (ed.) *Gold Metallogeny and Exploration*, 63-102, Blackie, London.

Hager, I. and Hill, R.C. (1970) As-Au Diagram. *Metal. Trans.*, **1**, 2723-31.

Hall, C.R. (1966) On the Production of Characteristic X-rays in Thin Metal Crystals. *Proc. Roy. Soc.*, **A295**, 140.

Hansen, M. and Anderko, K. (1958) *Constitution of Binary Alloys*, 2nd ed., McGraw-Hill Book Co., New York.

Harris, D.C. (1990) The Mineralogy of Gold and its Relevance to Gold Recoveries. *Miner. Deposita*, **25**, S3-7.

Hashimoto, H., Howie, A. and Whelon, M., (1962) Anomalous Electron Absorption Effects in Metal Foils, Theory and Comparison with Experiments. *Roy. Soc.*, **A269**, 80-103.

Hausen, M. (1991) Roasting of Refractory Gold Ore: Literature Survey, in Hausen, D.M. and Park, N.C. (eds.) *Process Mineralogy*, AIME/TMS, New York, 1661-1691.

Hayes, P.C. (1992) A Review of the Mechanisms of Decomposition of Solids and Their Relevance to Extractive Metallurgical Processes. *Mineral Processing and Extractive Metallurgy Review*, **8**, 73-94.

Heinrich, C.A. and Eadington, P.E. (1986) Thermodynamic Predictions of the Hydrothermal Chemistry of Arsenic, and their Significance for the Paragenetic Sequence of some Cassiterite-arsenopyrite-base metal Sulfide Deposits. *Econ. Geol.*, **81**, 511-529.

Henley, K.J. (1975) Gold-ore Mineralogy and its Relation to Metallurgical Treatment. *Minerals Science and Engineering*, **7**, 289-312.

Henley, K.J. (1992) A Review of recent Developments in the Process Mineralogy of Gold. *Extractive Metallurgy of Gold and Base Metals Kalgoorlie*, 177-194.

Henley, K.J. (1989) A Combined Mineralogical/Metallurgical Approach to Determining the Nature and Location of Gold in Ores and Mill Products. *Minerals Engineering*, **2**, 459-470.

Henley, R. W., (1973) Solubility of Gold in Hydrothermal Chloride Solutions. *Chem. Geol.*, **11**, p73-87.

Henley, R.W., Truesdell, A.H. and Barton, P.B. (1984) Fluid-Mineral Equilibra in Hydrothermal Systems. *Rev. Econ. Geol.* **1**, 28-37.

Hewat, A. (1986) Structural Refinements by the Rietveld Method. *Chem. Scr.* **A26**, 119-130.

Hill, R.J. (1992) International Union of Crystallography Commission on Powder Diffraction Rietveld Refinement Round Robin. I Analysis of Standard X-ray and Neutron Data for $PbSO_4$. *J Appl. Cryst.*, **25**, 589-610.

Hill, R.J. and Howard, C. (1986) *A Computer Program for Rietveld analysis of fixed wavelength X-ray and neutron powder diffraction patterns:* version LHPM1, Australian Atomic Energy Commission.

Hill, R.J. and Madsen, I.C. (1987) Data Collection Strategies for Constant Wavelength Rietveld Analysis. *Powder Diffraction,* **2,** 146-162.

Hochella, M. F. Jr., Bakken, B.M. and Marshall, A.F. (1988) *Transmission Electron Microscopy (TEM) of Partially Oxidised Gold Ore, Carlin Mine, Nevada,* in Process Mineralogy vol VII (eds. Vassilious, A.H. Hausen, D.M. and Carson, D.) Warrendale, Pennsylvania, Metall. Soc. Am. Inst. Mining Engineers, 153-155.

Huggins, A.R. (1937) *cited by* Morimoto and Clark (1960).

von Hugo, E., Kohl, H. and Rose, H. (1988) Effect of Delocalised Excitation in Channelling and Related Effects in Analytical Electron Microscopy. *Optik,* **79,** 19-24.

Hulliger, F. and Mooser, E. (1965) Semiconductivity in Pyrite, Marcasite and Arsenopyrite Phases. *J. Phys. Chem. Solids,* **26,** 429-433.

Hurlbut, Jr., C.S. and Klein, C. (1977) *Manual of Mineralogy,* 19th ed, John Wiley&Sons, New York.

Hutchings, R., Loretto, M.H., Jones, L.P. and Smallman, R.E. (1978) Analytical Electron Microscopy, and Workshop, Cornall University, New York, 166.

Hyland, M.M. and Bancroft, G.M. (1989) An XPS Study of Gold Deposition at Low Temperatures on Sulfide Minerals: Reducing Agents. *Geochim. Cosmochim. Acta,* **53,** 367-372.

Jean, G.E. and Bancroft, G.M. (1985) An XPS and SEM Study of Gold Deposition at Low Temperatures on Sulfide Minerals: Concentration by Adsorption/Reduction. *Geochim. Cosmochim. Acta,* **49,** 979-987.

Jean, G.E. and Bancroft, G.M. (1986) Heavy Metal Adsorption by Sulfide Mineral Surfaces. *Geochim. Cosmochim. Acta,* **50,** 1455-1463.

Johan, Z., Marcoux, E., and Bonnemaison, M. (1989) Arsenopyrite Aurifere: Mode de Substitution de Au dans la Structure de FeAsS. *C. R. Acad. Sci. Paris, t.,* **308,** series II, p 185-191.

Jong, W.F. de (1926) *cited by* Clark (1961).

Kalitkina (1971) Consolidation and Disintegration of Gold in Pyrite and arsenopyrite. *Vest. Mosk. Univ. Geol.,* v26(6) 107-110 (Chem. Abstr., v76 143394m).

Kittel, C. (1986) *Introduction to Solid State Physics.* 5th Edition Wiley, 608.

Kjekshus, A. and Rakke, T. (1977) High Temperature Studies of Marcasite and Arsenopyrite Type Compounds. *Acta Chem. Scand.,* A **31**, 517-529.

Klemm, D.D. (1962) Anisotropieeffekte bei kubischen Erzmineralien. *Neues Jahrb. Mineral. Abh.,* **97**, 337-356.

Klemm, D.D. (1965) Synthesen und Analysen in Den Dreiecksdiagrammen FeAsS-CoAsS-NiAsS und FeS_2-CoS_2-NiS_2. *Neues Jahrb. Mineral. Abh.,* **103**, 205-255.

Klempert, S. Ya., Sakhor, D.A. and Khasanov, R. (1973) Submicroscopic Gold in Terek Deposit Pyrite. *Akad. Nauk Usb SSR, Dokl.,* **30(2)**. 42-43. (Chem Abstract v81 15473c).

Klug, H.P. and Alexander, L.E. (1974) *X-ray Diffraction Procedures for Polycrystalline and Amorphous Materials.* John Wiley and Sons, New York.

Knipe, S.W., Foster, R.P. and Stanley, C.J. (1992) Role of Sulfide Surfaces in Sorption of Precious Metals from Hydrothermal Fluids. *Trans. Inst. Min. Metall. (Sect. B: Appl. Earth Sci.).,* **101**, B83-B88.

Knowles, J.W. (1956) Anamalous Absorption of Slow Neutrons and X-rays in Nearly Perfect Crystals. *Acta Cryst.,* **9**, 61.

Kostov, I. (1981) *Mineral Chemistry of Sulfides.* Schweitzerbart'sche Verlagsbuchhandlung, Stuttgart, Germany.

Kravtsova, R.G. and Solomonova, L.A. (1984) Gold in Pyrite from Ores and Metasomatites of the Gold-silver Deposits in the North Okhot'ye Volcanogenic Fields. *GeoChem. Int.,* **22(5)**, 9-14.

Kretschmar, U and Scott, S.D. (1976) Phase Relations involving Arsenopyrite in the System Fe-As-S and their Application. *Can. Mineral.,* **14**, 364-386.

Krishnan, K.M. (1988) Atomic Site and Species Determinations using Channelling and Related Effects in Analytical Electron Microscopy. *Ultramicroscopy,* **24**, 125-142.

Kullerud, G. (1971) Experimental techniques in Dry Sulfide Research, in Ulmer, G.C. (ed.) *Research Techniques for High Pressure and High Temperature,* 289-315, Springer, Verlag.

Kuranti, G. (1941) Synthetic Study of Gold-Bearing pyrite. *cited by* Clark (1960) (Chem. Abstracts v35, 3563).

La Brooy, S.R., Linge, H.G. and Walker, G.S. (1994) Review of Gold Extraction from Ores. *Mineral Engineering,* **7**, 289-312.

Lacroix, A. (1913) Mineralogie de la France et de ses Colonies: Paris, Librairie Polytechnique. Beranger Ch. Ed., **2**, 804.

Lowell, G. R. and Gasparrini, C. (1982) Composition of Arsenopyrite from Topaz Greisen veins in Southeastern Missouri, *Miner. Deposita*, **17**, 229-238.

Lynch, D.F. and Rossouw, C.J. (1987) Non-zeroth Order Laue Zone Effects and ALCHEMI. *Ultramicroscopy*, **21**, 69-76.

Malmros, G. and Thomas, J.O. (1977) Least-Squares Studing Refinement Based on Profile Analysis of Powder Film Intensity Data Measurement on an Automatic Microdensity Meter. *J. Appl. Cryst.*, **10**, 7-11.

Mao, S. (1991) Characterization of Occurrence and Distribution of Invisible Gold in Ore by EPMA, in Michael, J.R and Ingram, P. (eds.) *Microbeam Analysis*, San Franciso Press, Inc. U.S.A.

Marcoux, E., Bonnemaison, M., Braux, C. and Johan, Z. (1989) Distribution de Au, Sb, As et Fe dans l'Arsenopyrite Aurifere du Chatelet et de Villeranges. *C. R. Acad. Sci. Paris, t.*, **308**, serie II, 293-300.

Marion, P., Regnard, J.R. and Wagner, F.E. (1986) Etude de l état Chimique de l'or dans des Sulfures Auriféres par Spectroscopie Mössbauer de [197]Au: *Acad. Sci. Comptes Rendus*, **302**, 571-574.

Marion, P., Monroy, M., Holliger, P., Boiron, M.C., Cathelineau, M., Wagner, F.E. and Friedl, J. (1991) Gold bearing Pyrites: A Combined Ion Microprobe and Mössbauer Spectrometry Approach. in Pagel, F. and Leroy, P. (eds.) *Source, Transport and Deposition of Metals*, Balkema, Rotterdam.

Maslenitsky, L. (1944) On Some cases of Formation of Disperse Gold Segregations in Iron Sulfides, *cited by* Boyle (1979).

McPheat, I.W., Gooden, J.E.A. and Townsend, R. (1969) Submicroscopic Gold in a Pyrite Concentrate. *Proc. Aust. Inst. Min. Met.*, No. **231**, 19-25.

Michel, D., (1989) Morphoscopie de Grains d'or Extraits d'Arsenopyrites; Etude sur la Mine de Fazenda Brazileiro, Bresil. *C. R. Acad. Sci. Paris t.*, **308**, Serie II, 1357-1362.

Mironov, A. G. and Geletiy, V. F. (1978) Experimental Study of Gold Distribution in Sulfides. *Dokl. Acad. Sci. USSR, Earth Sci. Sect.*, **247**, 194-197.

Mironova, G.D., Zotov, A.V. and Gul'ko, N.I. (1984) Determination of the Solubility of Orpiment in Acid solutions at 25-150°C. *Geochim Intl.*, **21**, 53-59.

Mironov, G.D., Geletiy, V.F., Nesterova, I.N. and Tsepin, A.I. (1986) A Radioisotope Study of the Traces of Gold in Sulfides and Magnetite. *Geochim Intl.*, **23**, 117-128.

Mironova, G.D. and Zotov, A.V. (1980) Solubility Studies of the Stability of As(III) sulfide Complexes at 90°C. *Geochem. Intl.*, 17, 46-54.

Morimoto, N. and Clark, L.A. (1961) Arsenopyrite Crystal-Chemical Relations. *Amer. Mineral.*, 46, 1448-1469.

Nakagawa, (1971) *cited by* Ballantyne and Moore (1988).

Narseev and Starova (in Petrovskaya, 1974, *cited by* Boyle, 1979).

Nekrasov, I. Ya, Konyshok, A.A, and Sorokin, V.I. (1982a) Form of Gold(I) in Antimony-Bearing Sulfide Solutions. *Dokl. Acad. Sci. USSR, Earth Sci. Sect.*, 264, 207-210.

Nekrasov, I. Ya and Konyshok, A.A. (1982b) Heteropolynucleate Gold Complexes in Antimony-Bearing Sulfide Solutions. *Dokl. Acad. Sci. USSR, Earth Sci. Sect.*, 266, 185-188.

Neumayr, P., Cabri, L.J., Groves, D.I., Mikucki, E.J. and Jackman, J.A. (1993) The mineralogical Distribution of Gold and Relative Timing of Gold Mineralization in two Archean Settings of High Metamorphic Grade In Australia. *Can. Mineral.*, 31, 711-725.

Neverburg, G.J. (1975) A Procedure, using Hydrofluoric Acid, for Quantitative Mineral Separations from Silicate rocks. *J. Res. U.S. Geol. Surv.*, 3, 377-378.

Nickel, E. H., (1968) Structural Stability of Minerals with the Pyrite, Marcasite, Arsenopyrite and Löllingite Structures. *Can Mineral.*, 9, p311-321.

Okamoto, H. and Massalski, T.B. (1985) The Au-S (Gold-Sulfur) System. *Bull Alloy Phase Diagrams*, 6(6), 518-519.

Otten, M.T. and Buseck, P.R. (1987) The Determination of Site Occupancies in Garnet by Planar and Axial ALCHEMI. *Ultramicroscopy*, 23, 151.

Owen, E.A. and Roberts, E.A.O. (1945) The Solubility of Certain Metals in Gold. *J Inst. Metals*, 71, 213-254.

Parker, H.M. and Whitehouse, W.J. (1932) An X-ray Analysis of Iron Pyrites by the Method of Fourier Series. *Phil. Mag.*, 14, 939-961.

Pennycook, S.J. (1988) Delocalisation Corrections for Electron Channelling Analysis. *Ultramicroscopy*, 26, 239-248.

Pennycook, S.J. and Narayan, J. (1985) Atom Location by Axial-ElectronChannelling Analysis. *Phys. Rev. Lett.*, 54, 1543-1546.

Petruk, W.(1989) Recent Progress in Mineralogical Investigations Related to Gold Recovery. *CIM Bulletin*, 82(931), 37-39.

Post, J.E. and Bish, D.L. (1989) Rietveld Refinement of the Coronadite Structure. *Amer. Mineral.,* **74,** 456-463.

Prince, E. (1981) Comparison of Profile and Intergated-Intensity Methods in Powder Refinement. *J. Appl. Cryst.,* **14,** 157-159.

Prince, E. (1985) Precision and Accuracy in Structure Refinement By Rietveld Method, In Wilson, A.J.C. (ed.), *Structure and Statistics in Crystallography,* Adenine Press, London.

Renders, P.J. and Seward, T.M. (1989a) The Stability of Hydrosulfido- and Sulfido-Complexes of Au(I) and Ag(I) at 25°C. *Geochim Cosmochim. Acta,* **53,** 245-253.

Renders, P.J. and Seward, T.M. (1989b) The Adsorption of Thio Gold(I) Complexes by Amorphous As_2S_3 and Sb_2S_3 at 25 and 90°C. *Geochim Cosmochim. Acta,* **53,** 255-268.

Rietveld, H.M. (1967) Line Profiles of Neutron Powder-Diffraction Peaks for Structure Refinement. *Acta Cryst.,* **22,** 151-152.

Rietveld, H.M. (1969) A Profile method for Nuclear and Magnetic structures. *J. Appl. Cryst.,* **2,** 65-71.

Robins, R.G. (1985) The Aqueous Chemistry of Arsenic in Relation to Hydrometallurgical Processes. *Proc. CIM 15th Ann. Hydrometallurgical Mtg.,* Vancouver, Canada, 19-21.

Robins, R.G. and Jayaweera, L.D. (1992) Arsenic in Gold Processing. *Mineral Processing and Extractive Metallurgy Review,* **9,** 255-271.

Robinson, P.C. (1983) Mineralogy and Treatment of Refractory Gold from the Porgera Deposit, Papua New Guinea. *Trans. Inst Min. Metall.,* **92,** C83-C89.

Robinson, J. J. (1988) The Extraction of Gold from Sulphidic Concentrates by Roasting and Cyanidation. *J.S. Afr. Inst. Min. Metall.,* **88 (4)** 117-130.

Robinson, B.W. and Nickel, E.H (1979) A Useful New Technique for Mineralogy: The Back-scattered-electron/Low Vacuum mode of SEM Operation. *Amer. Mineral.,* **64,** 1322-1328.

Romberger, S.B. (1986) The Solution Chemistry of Gold Applied to the Origin of Hydrothermal Deposits. *Can. Inst Mining Spec.Vol,* **38,** 168-186.

Rossouw, C.J., Turner, P.S., White, T.J. and O'Connor, A.J.(1989) Statistical Analysis of Electron Channelling Microanalytical Data for the Determination of Site Occupancies of Impurties. *Phil. Mag. Lett.,* **60,** 225.

Rossouw, C.J., Potter, D.I and Glanvill, S.R.(1988) Electron Channelling Analysis of Aluminium and Xenon-Implanted Aluminium. *Ultramicroscopy,* **26**, 87-96.

Rossouw, C.J. and Maslen, V.W. (1987) Localisation and ALCHEMI for Zone Axis Orientation. *Ultramicroscopy,* **21**, 277-288.

Rytuba, J.J. and Dickson, F.W. (1977) Reaction of Pyrite + Pyrrhotite + Quartz + Gold with NaCl-H$_2$) Solutions, 300-500°C, 500 to 1500 bars and Genetic Implications. In Problems of Ore Deposition, 4th IAGOD Symposium, Varina, 1974 Vol II Bulgarian Acad. Sciences, Sofia *cited by* Seward (1991).

Sakharova *et al.* (1972,1976) *Cited by* Boyle (1979).

Schneiderhöhn, H. (1930) Mineralchemische und Mikroskopische Beobachtungun an Blei-Zink-und Kieserzen der Deutsch-Bleischarley-Grube/Oberschleisen. *Chem. Erde.,* **5**, 385-395.

Schoonen, M.A.A., Fisher, N.S. and Wente, M. (1992) Gold Sorption onto Pyrite and Goethite: A Ratiotracer Study. *Geochim. Cosmo Chim. Acta,* **56**, 1801-1814.

Schwartz, G.M. (1944) The Host Minerals of Native Gold. *Econ. Geol.* **39**, 371-411.

Scott, S.D. (1974) Experimental Methods in Sulfide Synthesis, in Ribbe, P.H. (ed.) *Reviews in Mineralogy,* 1, Sulfide Mineralogy, S1-S38, Mineral. Soc. Amer., Washington D.C.

Scott, S.D. (1975) Hydrothermal Synthesis of Refractory Sulfide Minerals. *Fortschr. Mineral.,* **52**, 185-195.

Scott, S. D. (1983) Chemical Behaviour of Sphalerite and Arsenopyrite in Hydrothermal and Metamorphic Environments. *Mineral. Mag.,* **47**, 427-435.

Self, P.G. (1992) Computer Modelling of Bloch Waves, in Buseck, P.R. (ed.) Minerals and Reactions at the Atomic Scale: Transmission Electron Microscopy, *Reviews in Mineralogy,* 27, 74-92, Mineral. Soc. Amer.,Washington D.C.

Self, P.G. and Buseck, P.R. (1983) Low Energy Limit to Channelling Effects in the Inelastic Scattering of Fast Electrons. *Phil. Mag.,* **A48**, L21-L26.

Self, P.G., Norrish, K., Milnes, A.R., Graham, J. and Robinson, B.W. (1988) The Negative Peak in Backgrounds of Spectrometers caused by Diffraction of General Radiation Planes in LiF Crystals. *X-ray Spectrometry,* **23**, 45.

Serres, A. (1953) Sur Quelques Compoese Du cobalt et du fer a Paramagnetisme Tres Faible et Constant. *J. Phys. Radium,* **14**, 689-690.

Seward, T.M. (1973) Thio Complexes of Gold and the Transport of Gold in Hydrothermal ore Solution. *Geochim. Cosmochim Acta,* **37**, 379-399.

Seward, T.M. (1982) The Transport and Deposition of Gold in Hydrothermal Systems, in Foster, R.P. (ed.) *Gold '82*, Rotterdam, A.A. Balkama Pub, 165-181.

Seward, T.M. (1989) The Hydrothermal Chemistry of Gold and its Implications for Ore Formation: Boiling and Conductive Cooling as Examples. *Econ. Geol. Mono.*, 6, 398-404.

Seward, T.M. (1992) The Hydrothermal Geochemistry of Gold, in Foster, R.P. (ed.) *Gold Metallogeny and Exploration*, Blackie, London, 37-61.

Sharp, Z. D., Essene, E. J. and Kelly, W. C. (1985) A Re-examination of the Arsenopyrite Geothermometer: Pressure Considerations and Applications to Natural Assemblages. *Can. Mineral.*, 23(4), 517-534.

Shenberger, D.M. (1985) *cited by* Shenberger, D.M. and Barnes, H.L. (1989).

Shenberger, D.M. and Barnes, H.L. (1989) Solubility of Gold in Aqueous Sulfide Solutions from 150°C to 350°C: *Geochim. Cosmochim. Acta*, 53, 269-278.

Shigematsu, K. (1986) Vapour Pressure Measurement of Arsenic Compounds. *Metallurical Review of MMIJ*, 3(2), 49-64.

Shui, H.M. (1991) Occurrence and Distribution of Invisible Gold in a Carlin-type Gold deposit in China. *Amer. Mineral.*, 76, 1964-1972.

Sie, S.H., Ryan, C.G., Cousens, D.R. and Griffin, W.L. (1989) Application of the Proton Microprobe in Mineral Exploration and Processing. *Nucl. Instrum. Meth. Phys Res.*, B40/41, 690-697.

Singh, B. and Gilkes, R.J. (1992) XPAS: An Interactive Computer Program for Analysis of X-ray Powder Diffraction Patterns. *Powder Diffraction*, 7(1), 6-10.

Smith, F.G. (1942) Variation in the Properties of Pyrite. *Amer. Mineral.*, 27, 1-19.

Smyth, J.R. and McCormick, T.C. (1988) Earth Science Applications of ALCHEMI. *Ultramicroscopy*, 26, 77-86.

Spence, J.C.H. and Taftø, J. (1982) Atomic Site and Species Determination using the Channelling Effect in Electron Diffraction, in Johari, O. (ed.) *Scanning Electron Microscopy*, II,. SEM inc., AMF O'Hare, Chicago, 532-539

Spence, J.C.H. and Taftø,J. (1983) ALCHEMI: A New Technique for Locating Atoms in Small Crystals. *J. Microsc.*, 130, 147-154.

Spence, J.C.H., Kuwabara, M. and Kim, Y. (1988) Localisation Effects on Quantification in Axial and Planar ALCHEMI. *Ultramicroscopy*, 26, 103-112.

Spycher, N.F and Reed, M.H. (1989) As(III) and Sb(III) Sulfide Complexes: An Evaluation of Stoichiometry and Stability from Existing Experimental Data. *Geochim. Cosmoch. Acta*, **53**, 2185-2194.

Starling, A., Gilligan, J.M., Carter, A.H.C., Foster, R.P. and Saunders, R.A. (1989) High-Temperature Hydrothermal Precipitation of Precious Metals on the Surface of Pyrite. *Nature*, **340**, 298-300.

Steeds, J.W. (1979) Introduction to Convergent Beam Electron Diffraction, in Hren, J.J., Goldstein, J.L. and Joy, D.C. (eds.) *Introduction to Analytical Electron Microscopy*, Plenium Press, London, 387-422.

Steeds, J.W. and Morniroli, J.P. (1992) Electron Diffraction-SAED&CBED, in Buseck, P.R. (ed.) *Reviews in Mineralogy*, 27, Minerals and Reactions at the Atomic Scale: Transmission Electron Microscopy, Mineral. Soc. Amer., Washington D.C.

Steeds, J.W. and Vincent, R. (1983) Use of High-Symmetry Zone Axes in Electron Diffraction in Determining Crystal point and Space Groups. *J. Appl. Crystallogr.*, **16**, 317-324.

Stephens, J.D., Bryan, S.R. and Roth, D.R. (1990) *Characterisation of Solid Solution Gold Pyrite and Metallurgical Treatment Products by SIMS* in Gold '90 (eds D.M. Hausen, D.N. Halbe, E.U. Petersen and W.J. Tafuri) Soc Min. Metall. Explor Inc, Littleton Colorado, 333-339.

Stillwell, F.L. and Edwards, A.B. (1946) An Occurence of Sub-Microscopic Gold in the Dolphin East Lode, Fiji. *Australasian Inst. Mining Met. Proc.*, **141**, 31-46.

Strathdee, B.A. and Pidgeon, L.M. (1969) Thermal Decomposition and Vapour pressure Measurements on Arsenopyrite and Arsenical Ore. *Trans. CIMM*, **64**, 506-510.

Swash, P. M. (1988) A Mineralogical Investigation of Refractory Gold Ores and their Benefication, with Special Reference to Arsenical Ores. *J. S. Afr. Inst Min. Metal.*, **88(5)**, 173-180.

Swash, P. M. and Ellis, P. (1986) The Roasting of Arsenical gold ores: A mineralogical perspective, in Hausen, D.M. (ed.) *Gold 100*, Proc. Int. Conf. on Gold. vol 2, Extractive Metallurgy of Gold. Johannesburg, SAIMM, 235-237.

Taftø, J. and Liliental, (1982) Studies of the Cation Atom Distribution in $ZnCr_xFe_{2-x}O_4$ Spinel using the Channelling Effect in Electron Induced X-ray Emission. *J. Appl. Cryst.*, **15**, 260.

Taftø J. and Spence J.C.H. (1982a) Crystal Site Location of Iron and Trace Elements in an Mg-Fe Olivine using a New Crystalline Technique. *Science*, **218**, 49-51.

Taftø J. and Spence J.C.H. (1982b) Atomic Site Determination using the Channelling Effect in Electron induced X-ray Emmission. *Ultramicroscopy*, **9**, 243.

Tanaka, M. and Terauchi, M (1985) *Convergent Beam Electron Diffraction.* JEOL Ltd., Tokyo.

Tanaka, M., Terauchi, M and Kaneyama, T. (1988) *Convergent Beam Electron Diffraction* II. JEOL Ltd., Tokyo.

Taylor, J.C. (1985) Quantative analysis of X-ray Diffraction Powder Patterns. *Aust. J. Phys.,* 66, 5712.

Tossell, J.A., Vaughan, D.J. and Burdett, J.K. (1981) Pyrite, Marcasite and Arsenopyrite Type Minerals: Crystal Chemical and Structural Principles. *Phys. Chem. Minerals,* 7, 177-184.

Tossell, J.A. (1980) Electronic Structure of Dichalcogenide and Dipnictide Anions. *Phys. Chem. Solids,* 41, 1047-1052.

Toulmin, P. and Barton, P.B. Jr (1964) A Thermodynamic Study of Pyrites and Pyrrhotite. *Geochim. Cosomchim. Acta.,* 28, 641-671.

Turner, P.S., White, T.J., O'Connor, A.J. and Rossouw, C.J. (1991) Advances in ALCHEMI Analysis. *J. Microsc.,* 162, 369-378.

Turner, P.S. and White, T.J. (1992) On the Determination of Precise k-Factors for AEM. *J. Microsc.,* 166, RP1-RP2.

Van Tendeloo, G. and Amelinckx, S. (1974) Group-Theoretical Considerations Concerning Domain Formation in Ordered Alloys. *Acta Cryst.,* A30, 431-440.

Vaughan, D. J. and Craig, J. R., (1978) *Mineral Chemistry of Metal Sulfides.* Cambridge University Press, London.

Vincent, R., Bird, D.M., and Steeds, J.W. (1984) Structure of AuGeAs Determined by CBED. *Phil. Mag.,* 50A, 765-786.

Vincent, R. and Pretty, S.F. (1986) Phase Analysis in the Ni-Ge-P System by Electron Diffraction. *Phil. Mag.,* 53A, 843-862.

Vincent, R. and Withers, R.L. (1987) Analysis of a Displacive Superlattice in Nickel Arsenide. *Phil. Mag. Lett.,* 56, 57-62.

Vogel, A.I. (1962) *A Text Book of Quantitative Inorganic Analysis* (3rd), Longmans, London.

Wadsley, A.D. (1955) The Crystal Chemistry of Non-stoichiometric Compounds. *Review of Pure and Applied Chemistry.,* Vol 5(3) 165-193.

Wagner, F. E., Marion, Ph and Regnard (1986) Mossbauer study of the the chemical state of gold in gold ores, in Hausen, D.M. (ed.) *Gold 100*, Proc. Int. Conf. on Gold. vol 2, Extractive Metallurgy of Gold. Johannesburg, SAIMM, 435-443.

Wagner, F.E (*pers. comm*) Munich University of Technology, Germany.

Wagman, D.D., Evans, W.H., Parker, V.B., Schumm, R.H., Halow, I., Bailey, S.M., Churney, K.L. and Nuttall, R.L. (1982) The NBS Tables of Chemical Thermodynamic Properties. *J. Phys. Chem. Ref. Data II Supplement 2*.

Wells, J. D. and Mullens, T. E. (1973) Gold-Bearing Arsenian Pyrite Determined by Microprobe Analysis, Cortez and Carlin Gold Mines, Nevada. *Econ. Geol.*, **68**, 187-201.

White, T. and Turner, P. (1992) Zone Axis ALCHEMI, Some Practical Considerations. Practical Notes ACEM-12 &ANZSCB-11. The 1992 Joint Conf. on Electron Microscopy and Cell Biology UWA 10-14 Feb Proceedings.

Wiles, D.B. and Young, R.A. (1981) A New Computer Program for Rietveld Analysis of X-ray Powder Diffraction Patterns. *J. Appl. Cryst.*, **14**, 149-151.

Will, G., Parrish, W. and Huang, T.C. (1983) Rietveld Analysis and Profile Fitting. *J Appl. Cryst.*, **16**, 611-622.

Williams, D.B. (1984) *Practical Analytical Electron Microscopy in Materials Science.* Philips Electronic Instruments Inc., Electron Optics Publishing Group, New Jersey, 153 .

Wood, B.J. and Stren, R.G.J. (1979) Diffuse Reflection Spectra and Optical Properties of Some Sulfides and Related Minerals. *Mineral. Mag.*, **43**, 509-518.

Wood, S.A., Crerar, D.A. and Boresik, M.P. (1987) Solubility of the Assemblage Pyrite-Pyrrhotite-Magnetite-Sphalerate-Garnet-Gold-Stibnite-Bismuthinite-Argentite-Molybdenite in H_2O-NaCl-CO_2 Solutions from 200°C to 350°C. *Econ Geol.*, **82**, 1864-1887.

Wu, X. and Delbove, F. (1989) Hydrothermal Synthesis of Gold-bearing Arsenopyrite. *Econ. Geol.*, **84**, 2029-2032.

Wu, X., Delbove, F. and Touray, J. C. (1990) Conditions of Formation of Gold-rich Arsenopyrite: A Comparison of Synthetic Crystals with Samples from Le Chatelet gold deposit, Creuse, France. *Miner. Deposita*, **25**, [Suppl.], S8-12.

Young, R.A., Mackie, P.E. and Von Dreele, R.B. (1977) Application of the Pattern-Fitting Structure-Refinement Method to X-ray Powder Diffractometer Patterns. *J. Appl. Cryst.*, **10**, 262-269.

Young, R.A. and Wiles, D.B. (1982) Profile Shape Functions in Rietveld Refinements. *J. Appl. Cryst.*, **15**, 430-438.

Young, R.A. (1992) ed The Rietveld Method, Proc. IUCr Commission on Powder Diffraction, Rietveld Analysis Workshop, Petten, The Netherlands, June 1989 Oxford Univ Press. *cited by* Hill (1992).

Zhang, Z., Yang, S. and Yi, W. (1987) Studies of Submicro-Gold and Lattice-Gold in some Minerals. *J. Cent. - South Inst. Min. Metall.,* **18(4)**, 355-361.

Zotov, A.V., Baranova, N.N., Dar'yina, T.G. and Bawnykt, L.M. (1989) Gold(I) complexing in the KCl-H$_2$) system at 450°C and 500 atm. *Geochem. Intl.,* **26**, 66-75.

10.0 APPENDIX

10.1 APPENDIX A - Calibration of Microprobe Conditions

Variations in Current and Voltage

The results presented are the means and standard deviations from over thirty analyses.

Table 10.1 - Composition of Various Arsenopyrites at Different Beam Conditions (atomic ratios normalised)						
Beam Conditions		Coolgardie Low As:S	Mexican Med. As:S	Pine Creek High As:S	Asp200 Std	Pyrite Std
30Kv 40nA	Fe	0.340±0.002	-	0.342±0.001	-	0.339±0.002
	As	0.319±0.008	-	0.357±0.01	-	-
	S	0.340±0.007	-	0.302±0.01	-	0.661±0.002
20Kv 20nA	Fe	0.329±0.002	0.332±0.004	0.331±0.002	0.332±0.001	0.334±0.002
	As	0.323±0.006	0.333±0.003	0.361±0.01	0.318±0.005	-
	S	0.347±0.006	0.335±0.003	0.308±0.01	0.350±0.005	0.666±0.002
20Kv 30nA	Fe	0.335±0.002	-	0.334±0.003	0.331±0.002	0.336±0.003
	As	0.313±0.006	-	0.354±0.007	0.318±0.006	-
	S	0.351±0.005	-	0.312±0.006	0.350±0.006	0.664±0.003
25Kv 20nA	Fe	-	0.331±0.003	-	0.334±0.001	0.335±0.001
	As	-	0.331±0.003	-	0.314±0.002	-
	S	-	0.337±0.003	-	0.351±0.002	0.665±0.001

10.2 APPENDIX B - Rietveld method

An iterative least squares algorithm enables a measured diffraction profile to be compared with the calculated profile for a given model. The calculated counts y_{ci} are determined by summing the contributions from neighbouring Bragg reflections plus the background:

$$y_{ci} = S\Sigma L_k |F_k|^2 \phi(2\theta_i - 2\theta_k)P_k + y_{bi}$$

where
S is a scale factor,

L_k contains the Lorentz, polarisation and multiplicity factors,

F_k is the structure factor,

P_k is the preferred orientation function,

ϕ is the reflection profile function

and y_{bi} is the background intensity at $2\theta_i$

For an assembly of n atoms resting in harmonic potential wells, the structure factor is given by the expression

$$F_k = \sum_{j=1}^{n} f_j \exp(2\pi i.\underline{h}_k.\underline{r}_j - \underline{h}_k.\underline{B}_j.\underline{h}_k)$$

where f_j is the scattering factor of atoms j, and $\underline{h}_k$, $\underline{r}_j$ and $\underline{B}_j$ are matrices representing the Miller indices, atomic coordinates and anisotropic thermal vibration parameters, respectively. The Bragg reflection in a powder pattern constitutes a peak and not a line resulting from a large distribution of wavelengths produced, in combination with a finite mosaic spread of the monochromator, acceptance functions of the collimation systems in the diffractometer and size, strain and shape of the crystallites in the sample. The following are the different parameters used in the refinement.

Background

In the Rietveld program used, the background function is of the form

$$y_b = \sum_{m=-1}^{4} B_m 2\theta_i^m$$

where B_m is one of the six refinable parameters. This works only for diffraction patterns in which there are regions where the Bragg peak contribution is negligible, particularly at high scatter angles.

Peak widths

The peak widths were calculated and refined using the Caglioti, Paoletti and Ricci (1958) equation

$$H_k^2 = (U\tan^2\theta + V\tan\theta + W)$$

where the half width parameters U, V and W are strictly a function of the particle size and strain, collimator divergence angles and monochromator mosaic spread are treated as parameters in the profile refinement.

Profile shape functions

The peak shape in an X-ray powder diffraction pattern is a complex convolution of several sample and instrumental effects and therefore can vary significantly depending on the data collection geometry and type of sample. The pure diffraction maxima have natural profiles determined largely by crystallite-size distribution, crystal structure distortions and spectral distribution in the incident radiation (Klug and Alexander, 1974). Klug and Alexander (1974) identified six functions arising from a typical X-ray diffractometer that modify the pure Bragg diffraction peaks: (1) geometry of the X-ray source, (2) varying displacements of different portions of a flat sample surface from the focusing circle, (3) axial divergence of the x-ray beam, (4) specimen transparency, (5) effects of receiving slits and (6) misalignment of the diffractometer. As a consequence of these effects the shape of the Bragg peaks in powder XRD patterns deviate from Gaussian and therefore a more complex function is required to accurately describe their profiles. Young and Wiles (1982) concluded, after comparing results for a large number of Gaussian, Lorentzian and combined Gaussian and Lorentzian profile functions that the best fit was obtained by the use of combined Gaussian and Lorentzian functions such as pseudo-Voigt and Pearson VII. The use of the pseudo-Voigt function has been recommended and the refinable constant can be interpreted as degree of Lorentzian versus Gaussian character.

Although the Rietveld program gives a number of peak shape options to choose from, the Pseudo-Voigt function was utilised in these experiments. This peak shape function takes into account both the Lorentzian and Gaussian functions.

as

$$PV_{ik} = (g) \, L_{ik} + (1-g) \, G_k$$

where g is a refinable "mixing" parameter.

and

$$G_{ik} = \frac{Co^{1/2}}{H_k \pi^{1/2}} \exp\{CoX_{ik}^2\}$$

where $Co = 4\ln 2$ and $X_{ik} = (2\theta_i - 2\theta_k)/H_k$

and

$$L_k = \frac{C_l^{1/2}}{H_k \pi} \{1 + C_l X_k^2\}^{-1}$$

Least squares procedure

The Rietveld program uses the Newton-Raphson algorithm to minimise the quantity ;

$$\Re = \sum w_i (y_{io} - y_{ci})^2$$

over all data points contributing to the peaks and background.

where $w_i = 1/y_i$ assigned to each observation,

y_{io} = observed (gross) intensity at the ith step,

y_{ci} = calculated intensity at the ith step

and the sum is over all data points.

If x_m are the adjustable parameters in the model, then the normal equations matrix has elements given by:

$$M_{mn} = -\sum 2w_i \left[\frac{(y_{io} - y_{ci})\delta^2 y_{ci}}{\delta x_m \delta x_n} - \frac{\delta y_{ci}}{\delta x_m} \frac{\delta y_{ci}}{\delta x_n} \right]$$

The shifts Δx_m, which will best reduce the residual are then given by:

$$\Delta x_m = \sum_n M_{mn}^{-1} \delta R/\delta x_n$$

where M_{mn}^{-1} is the inverse of matrix M.

The calculated shifts are then applied to the adjustable parameters x_m and a new set of y_{ci} (i.e. a new calculated pattern) are produced. The whole procedure is repeated iteratively until a criterion or completion is met that $\Delta x_m < 0.1\sigma_m$. The values of the parameter esd's, are calculated from the expression:

$$\sigma_m = \left[M_{mm}^{-1} \frac{\sum_i w_i (y_{io} - y_{ic})^2}{N - P} \right]$$

where σ_m is the diagonal element of the inverse matrix, N is the number of observations and P is the number of adjustable parameters.

<u>Criteria of fit</u>

In the Rietveld profile refinement a set of R values is calculated to test the hypothesis that the y_{io} are samples of the scaled y_{ci}; i.e. that the observations are consistent with the model.

The R values observed in the refinement are:

the profile $R_p = \dfrac{\sum |y_{io} - y_{ic}|}{\sum y_{io}}$,

the weighted profile $R_{wp} = \left[\dfrac{\sum\limits_i w_i (y_{io} - y_{ic})^2}{\sum\limits_i w_i y_{io}^2} \right]^{1/2}$,

and the Bragg $R_B = \dfrac{\sum |I_{ko} - I_{kc}|}{\sum I_{ko}}$

where R_B is the 'observed' integrated intensity of reflection k calculated at the end of the refinement after dividing each y_{io} between the contributing peaks according to the calculated intensities I_{kc}.

The expected $R_{exp} = \left[\dfrac{N - P}{\sum\limits_i w_i y_{io}^2} \right]^{1/2}$

The goodness of fit $= \dfrac{\sum_i w_i (y_{io} - y_{ci})^2}{N - P}$

R_B is a measure of the agreement between the observed and calculated Bragg intensities for overlapping reflections and is determined by assuming that they are in the same proportion as their calculated counterparts. Consequently the observed intensities are heavily biased by the structure model and R_B tends to be overly optimistic (Baerlocher, 1986). R_B is an indicator because it depends more heavily on the fit of the crystal structure parameters than do the other agreement indices (Hill and Madsen, 1987).

10.2.1 Application of Rietveld Method

Extensive modifications have been made to the original Rietveld computer program devised by Rietveld (1967,1969). There are several Rietveld refinement programs and packages to date, with the program developed by Wiles and Young (1981) being the most widely used (Post and Bish, 1989). Hill (1992) evaluated the various strategies of Rietveld refinement programs and their precision and accuracy. He found that although high precision was possible for the refinement of a well defined $PbSO_4$ structure, low accuracy was not uncommon in Rietveld analyses. Detailed descriptions and reviews of the Rietveld method have been given by Cheetham and Taylor (1977), Albinati and Willis (1982), Wiles and Young (1981), Taylor (1985), Hewat (1986), Hill and Madsen (1987) Post and Bish (1989) and Young (1992). There have been over 452 publications of Rietveld analyses upto 1990 (Hill, 1992). Limited work has been done on sulfide systems. The most detailed study on sulfides is that of the work carried out by Chang and Zang (1990) who compared auriferous pyrite with non-auriferious pyrite. Their studies showed that auriferous pyrites contained larger unit cell dimensions than nonauriferous pyrites. However the form of gold in their samples was not determined.

10.2.2 Advantages and Disadvantages

A limitation of the Rietveld method is that it is primarily a structure refinement technique as opposed to a structure solution technique. The starting structural model has to be close to the actual structure. In some cases, however partial structure solutions are possible. The advantage of the Rietveld method is that powder XRD patterns are more easily obtained than those for single-crystals. Twinning present in samples is not a problem for powder diffraction studies. Rietveld refinements can yield precise and accurate unit cell parameters as well as quantitative analyses of mixtures. On the other hand, atomic structural parameters (especially temperature factors) are, in general, less accurately determined than those in comparable single crystal studies. Also, sample related problems such as structure

disorder and preferred orientation of crystallites, can effect the accuracy of the Bragg peak intensities, resulting in a poor or incorrectly refined structure.

10.3 APPENDIX C - Bond length and angle calculations

The bond lengths and angles were calculated using two theorems.

(1) For a geometric space the inner product is

$$v \bullet w = vw\cos\theta$$

where θ is the angle between v and w such that $0° \le \theta \le 180°$ and v and w denote the magnitudes of the vectors v and w respectively,

and (2)

$$v \bullet w = [v]_D^t G[w]_D$$

$$= \begin{bmatrix} v_1 & v_2 & v_3 \end{bmatrix} \begin{bmatrix} a \bullet a & a \bullet b & a \bullet c \\ b \bullet a & b \bullet b & b \bullet c \\ c \bullet a & c \bullet b & c \bullet c \end{bmatrix} \begin{bmatrix} w_1 \\ w_2 \\ w_3 \end{bmatrix}$$

$[v]_D^t$ is the transpose $[v_1, v_2, v_3]$ of $[v]_D$,

vector $v = v_1 a + v_2 b + v_3 c$ and vector $w = w_1 a + w_2 b + w_3 c$

and G is the metric matrix.

To illustrate how these equations were used an example is given below.

To calculate the two bond lengths R(As,Fe) and R(S,Fe) and the As-Fe-S bond angle subtended by these two bonds in arsenopyrite, the atomic coordinates and unit cell dimensions were obtained from the Rietveld refined data.

For one natural arsenopyrite samples, the atomic coordinates were

```
for Fe   0.284 -0.006 0.292
    As  -0.148 -0.130 0.131
    S    0.342 -0.131 0.677
```

with unit cell dimensions for the monoclinic unit cell being a = 5.740, b= 5.674, c= 5.761Å and β = 111.53.

The length of each bond equals the magnitude of a vector drawn from the position of the first atom to the second atom. This vector was found by subtracting the vector drawn from the origin to the first atom and the vector drawn from the origin to the second atom.

The Fe atoms occur at the end of a vector $r_1 = 0.284a - 0.006b + 0.292c$, As occurs at the end of $r_2 = -0.148a - 0.130b + 0.131c$ and S occurs at the end of $r_3 = 0.342a - 0.131b + 0.677c$

R(As,Fe) is equal to the length of the vector

$r_2-r_1 = -0.136a - 0.124b -0.161c$

and R(S,Fe) is equal to the length of the vector

$r_3-r_1 = 0.058a -0.125b + 0.385c$

To calculate these bond lengths the metrical matrix must be constructed

since $\alpha = \gamma = 90°$, $a \bullet b = b \bullet c = b \bullet a = c \bullet b = 0$

$a \bullet c = c \bullet a = accos(111.53) = -12.14$
$a \bullet a = a^2 = 32.95$
$b \bullet b = b^2 = 32.95$
$c \bullet c = c^2 = 32.95$

Hence the metrical matrix G for this arsenopyrite crystal is

$$G = \begin{bmatrix} 32.95 & 0 & 12.14 \\ 0 & 32.19 & 0 \\ -12.14 & 0 & 33.19 \end{bmatrix}$$

The v and w in the first equation are both replaced by (r_2-r_1)

$$R(As, Fe)^2 = (r_2 - r_1)(r_2 - r_1) = \begin{bmatrix} -.136 & -.124 & -.161 \end{bmatrix} G \begin{bmatrix} -.136 \\ -.126 \\ -.161 \end{bmatrix}$$

$= 5.812$

and so R(As,Fe) = 2.411Å.

similarly for (r_3-r_1) R(S,Fe) can be obtained as 2.231Å.

To calculate the angle $\theta = <(As-Fe-S)$ the inner product $(r_2-r_1) \bullet (r_3-r_1)$ is required

since

$$(r_2-r_1) \bullet (r_3-r_1) = [r_2-r_1]_D' G [r_3-r_1]_D$$

$$(r_2 - r_1) \bullet (r_3 - r_1) = \begin{bmatrix} -.136 & -.124 & -.161 \end{bmatrix} G \begin{bmatrix} .058 \\ -.125 \\ .389 \end{bmatrix}$$

$$= -0.253$$

$$\cos\theta = (-0.253)/(R(As,Fe)R(S,Fe)) = -0.047$$

$$\theta = 92.7°$$

10.4 APPENDIX D - Tables of Rietveld Refined Data

(Tables 10.2a and b)

Table 10.2a Unit Cell Dimensions (based on space group P2₁/c) and Chemical Composition*

Sample	Sheba	Coolgardie	Paddington	Greenbushes	Mexican	China	Pine Creek	Portugal	Utah
a	5.739±0.003	5.738±0.002	5.739±0.001	5.742±0.001	5.751±0.003	5.755±0.005	5.761±0.000	5.757±0.002	5.762±0.001
b	5.665±0.003	5.668±0.002	5.669±0.005	5.680±0.002	5.682±0.005	5.692±0.005	5.697±0.001	5.695±0.000	5.700±0.001
c	5.760±0.002	5.759±0.002	5.761±0.005	5.764±0.002	5.786±0.003	5.789±0.005	5.788±0.000	5.788±0.001	5.794±0.001
Beta	111.449±0.002	111.398±0.119	111.599±0.125	111.728±0.008	112.368±0.003	112.452±0.008	112.407±0.000	112.490±0.007	112.543±0.005
Volume	174.43±0.15	174.42±0.29	174.26±0.18	174.63±0.14	174.70±0.48	175.27±0.44	175.70±0.14	175.35±0.08	175.82±0.17
Sites Occupancies									
As	0.885±0.005	0.920±0.008	0.912±0.074	0.958±0.013	0.796±0.005	0.812±0.033	0.947±0.000	0.846±0.002	0.819±0.003
S	1.154±0.003	1.078±0.008	1.087±0.074	1.060±0.027	1.323±0.004	1.186±0.031	1.293±0.003	1.154±0.002	1.181±0.003
Chemical Composition									
Fe	0.330±0.002	0.329±0.002	0.332±0.002	0.331±0.002	0.331±0.002	0.331±0.004	0.331±0.002	0.332±0.002	0.331±0.002
As	0.318±0.008	0.323±0.006	0.322±0.007	0.339±0.007	0.331±0.003	0.351±0.007	0.361±0.008	0.363±0.006	0.360±0.007
S	0.352±0.008	0.347±0.006	0.346±0.006	0.331±0.007	0.337±0.003	0.319±0.006	0.308±0.008	0.305±0.006	0.309±0.007
As:S ratio	0.90±0.04	0.93±0.03	0.93±0.04	1.02±0.04	0.99±0.02	1.10±0.04	1.17±0.06	1.19±0.04	1.17±0.05
Coordinates									
Fe									
x	0.279±0.0009	0.282±0.0004	0.281±0.0039	0.286±0.0002	0.277±0.0009	0.277±0.0022	0.281±0.0003	0.279±0.0004	0.280±0.0010
y	-0.004±0.0003	-0.005±0.0002	-0.005±0.0021	-0.008±0.0004	-0.003±0.0018	-0.004±0.0022	-0.005±0.0004	-0.003±0.0003	0.003±0.0052
z	0.289±0.0002	0.291±0.0001	0.291±0.0019	0.291±0.0003	0.290±0.0005	0.294±0.0046	0.290±0.0005	0.291±0.0008	0.293±0.0010
As									
x	-0.150±0.0011	-0.148±0.0004	-0.148±0.0007	-0.149±0.0005	-0.154±0.0008	-0.152±0.0013	-0.150±0.0010	-0.150±0.0004	-0.153±0.0014
y	-0.128±0.0005	-0.130±0.0006	-0.130±0.0000	-0.128±0.0002	-0.129±0.0015	-0.127±0.0057	-0.128±0.0000	-0.129±0.0001	-0.130±0.0015
z	0.132±0.0009	0.132±0.0001	0.133±0.0025	0.130±0.0005	0.134±0.0006	0.133±0.0008	0.131±0.0003	0.134±0.0005	0.131±0.0004
S									
x	0.343±0.0020	0.344±0.0012	0.344±0.0026	0.343±0.0001	0.344±0.0003	0.346±0.0009	0.344±0.0010	0.345±0.0008	0.341±0.0021
y	-0.131±0.0003	-0.131±0.0005	-0.131±0.0012	-0.132±0.001	-0.131±0.0005	-0.131±0.0005	-0.135±0.0027	-0.134±0.0005	-0.134±0.0029
z	0.672±0.0020	0.677±0.0013	0.678±0.0013	0.676±0.0004	0.680±0.0019	0.680±0.0044	0.677±0.0020	0.678±0.0012	0.671±0.0026

* SD's are measured from three refined patterns

Table 10.2b Profile and Agreement Indices for Arsenopyrites Refined by Rietveld

SAMPLE	Sheba	Coolgardie	Paddington	Greenbushes	Mexican	China	Pine Creek	Portugal	Utah
WHH	0.1095	0.0556	0.047	0.2083	0.25	0.191	0.1795	0.2063	0.566
	0.0267	0.0267	0.0056	-0.0591	-0.02	-0.07	0.026	-0.1209	-0.233
	0.0420	0.0420	0.015	0.0448	0.017	0.0539	0.042	0.055	0.073
Peak shape	0.77	0.95	0.86	0.62	0.86	0.45	0.87	0.78	0.58
expected	3.14	3.16	3.26	3.21	3.20	3.30	3.3	3.26	3.14
RP	5.7	5.98	5.55	6.6	9.21	6.21	6.07	6.76	8.1
RWP	7.64	7.71	7.85	9.08	12.32	8.13	8.57	10.18	10.7
GOF	5.91	5.82	5.4	7.98	14.65	6.42	6.76	9.75	11.64
Bragg R	2.1	2.3	3.13	2.82	7.8	3.38	2.33	3.96	4.06
Durtin-Watson									
UW	0.344	0.672	0.596	0.467	0.163	0.49	0.446	0.332	0.267
W	0.416	0.588	0.568	0.387	0.167	0.456	0.412	0.449	0.253

10.5 APPENDIX E - Conference and Publications arising from thesis

1.Aylmore, M.G., Graham, J. and Johnson (1990) Effect of Twinning on Arsenopyrite and its Implications for ALCHEMI. ACEM-12.

2. Aylmore, M.G. and Graham, J.(1992) Arsenopyrite as a Host for Refractory Gold. J. Computer-Assisted Microscopy. **4(4)**, 275-280.

3. Aylmore, M.G. and Graham, J.(1992) A Mineralogical Approach to Auriferous Arsenopyrite, Proceedings of the International Conference on Extractive Metallurgy of Gold and Base Metals, Kalgoorlie, 203-210.

4. Graham, J., Fletcher,A., Walker, G., and Aylmore, M.G. (1992) A Pyrolysis Approach to Refractory Gold Processing, Proceedings of the International Conference on Extractive Metallurgy of Gold and Base Metals, Kalgoorlie, 441-3.

5. Aylmore, M.G., Graham, J. and Johnson (1993) The Nature of Gold in Pyrite and Arsenopyrite Determined using ALCHEMI, ICAM 93 Proceedings, abstract 66-69.